

DISSERTATION ZUR ERLANGUNG DES DOKTORGRADES
DER FAKULTÄT FÜR CHEMIE UND PHARMAZIE
DER LUDWIG-MAXIMILIANS-UNIVERSITÄT MÜNCHEN

Development of an Efficient Crystallisation Scale Up of
Incongruently Soluble Cocrystal Coformers to Produce
High-Quality Crystals
Using the Example of the CL-20/HMX Cocrystal

DIRK HERRMANNSDÖRFER

AUS
STUTTGART

2021

Erklärung

Diese Dissertation wurde im Sinne von § 7 der Promotionsordnung vom 28. November 2011 von Herrn Prof. Dr. Thomas M. Klapötke betreut.

Eidesstattliche Versicherung

Diese Dissertation wurde eigständig und ohne unerlaubte Hilfe erarbeitet.

München, 10.05.2021

Dirk Herrmannsdörfer

Dissertation eingereicht am 20.05.2021

1. Gutachter: Prof. Dr. Thomas M. Klapötke
2. Gutachter: Prof. Dr. Konstantin Karaghiosoff

Mündliche Prüfung am 06.07.2021

It's the questions we can't answer that teach us the most.
Patrick Rothfuss, *The Wise Man's Fear*

Danksagung

Ich danke Prof. Dr. Thomas M. Klapötke für die immer freundliche Betreuung meiner Dissertation. Ebenso dankbar bin ich für die zu jedem Zeitpunkt umgehende Beantwortung jedweder Fragestellung, die ich hatte und für die wissenschaftliche Freiheit, die mir während meiner Promotion eingeräumt wurde. Für die Unterstützung, die mir Dr. Jörg Stierstorfer als Schnittstelle zum Arbeitskreis hat zuteilwerden lassen, gebührt ihm mein Dank. Wenka Schweikert und Stefan Müller gilt mein Dank für unzählige zuverlässige und prompte und zum Teil auch auf Abruf durchgeführte Ramanmessungen. Für wertvolle fachliche Diskussionen möchte ich Dr. Alexander Dresel und insbesondere Konstantin Busch danken. Thomas Heintz und Dr. Michael Herrmann gilt mein Dank für die absolute Handlungsfreiheit und das uneingeschränkte Vertrauen, das mir während meiner Arbeit am Fraunhofer-ICT entgegengebracht wurde. Ich danke unserem Quantachrome Gaspycnometer dafür, dass es zum richtigen Zeitpunkt den Dienst quittierte, sodass wir uns ein richtiges Dichtemessgerät zulegen konnten.

Besonderes Dankes würdig ist Dr. Horst Krause, ohne dessen wegweisende Beratung meine Promotion sicherlich einem verzweigteren Weg gefolgt wäre. Des Weiteren danke ich ihm für wertvolle Kritik zur Verbesserung meiner Dissertation.

Ich danke meine Partnerin Diana aus tiefstem Herzen für ihre unnachgiebige Beharrlichkeit in ihrer Unterstützung bei der Ausarbeitung dieser Arbeit. Ohne ihr Mitwirken wären viele Passagen weit weniger ausgefeilt. Ich danke meiner Familie, insbesondere meinen Eltern Bernadette und Michael, sowie meinen Brüdern Nick und Frank für ihren vorbehaltlosen Rückhalt und ihr Verständnis. Darüber hinaus bin ich für das Erwecken meiner Liebe zur Naturwissenschaft und für ihre absolute Unterstützung während meines Studiums meinen Eltern zutiefst zu Dank verpflichtet.

Table of Content

| | | |
|------|--|-----|
| 1 | Introduction | 1 |
| 1.1 | What is a Cocrystal?..... | 1 |
| 1.2 | The Use of the Phase Diagram..... | 2 |
| 1.3 | Cocrystallisation Techniques | 2 |
| 1.4 | Crystal Quality..... | 3 |
| 1.5 | Cocrystal Applications..... | 4 |
| 1.6 | Energetic Material Classification | 5 |
| 1.7 | Energetic Material Performance Versus Safety..... | 7 |
| 1.8 | Properties of the CL-20/HMX Cocrystal..... | 8 |
| 1.9 | Cocrystallisation Scale Up Challenges..... | 9 |
| 2 | Motivation | 11 |
| 3 | Aim and Objectives | 13 |
| 4 | Summary..... | 15 |
| 5 | Quality Assessment of the Cocrystal | 23 |
| 5.1 | High-Precision Density Measurements of Energetic Materials for Quality Assessment..... | 23 |
| 5.2 | Quality Assessment of the CL-20/HMX Cocrystal Utilising Digital Image Processing..... | 45 |
| 6 | Solubility Determination of the Coformers | 65 |
| 6.1 | Solubility Behaviour of CL-20 and HMX in Organic Solvents and Solvates of CL-20..... | 65 |
| 7 | Cocrystallisation Method: Choice and Development | 97 |
| 7.1 | Investigation of Crystallisation Conditions to Produce CL-20/HMX Cocrystal for Polymer-Bonded Explosives..... | 97 |
| 7.2 | Semibatch Reaction Crystallization for Scaled-Up Production of High-Quality CL-20/HMX Cocrystal: Efficient Because of Solid-Dosing | 119 |
| 8 | Conclusion..... | 137 |
| 9 | Outlook | 140 |
| 10 | Appendix..... | 141 |
| 10.1 | List of Publications | 141 |
| 10.2 | Conference Publications and Presentations..... | 142 |

1 Introduction

1.1 What is a Cocrystal?

The, presumably, first publication on the generation of a cocrystal was published over 175 years ago.¹ The cocrystal of benzoquinone and hydroquinone (quinhydrone), called grünes Hydrochinon by Wöhler, is apparently one of the most beautiful substances in existence¹ (Figure 1).

Das grüne Hydrochinon ist einer der schönsten Stoffe, welche die organische Chemie aufzuweisen hat.

Figure 1: Passage from the 1844 paper "Untersuchungen über das Chinon".

Back then, the concept of cocrystallisation was unknown and quinhydrone was believed to be a single molecule.

But what is a cocrystal? This question is under debate to this date. No IUPAC guideline exists, and the only regulatory department that attempted a classification of cocrystals is the US food and drug administration (FDA), but only for cocrystals containing an active pharmaceutical ingredient (API).² Their first attempt to define the term cocrystal was met with substantial backlash from the scientific community. The counter paper was co-authored by 46 experienced researchers.³ Two main arguments were filed against the proposed cocrystal definition: "solids that are crystalline materials composed of two or more molecules in the same crystal lattice". Not only was it stated that the definition can be ambiguous because every molecular crystal is composed of two or more molecules, but it was also stated that the definition is too restrictive, as it limits cocrystals to molecular components.³ The discussion part of the FDA report, furthermore, makes it clear that solvates are also excluded, even though this is not stated in the definition itself. Several issues arise from these exclusions. Based on this definition, the 2,4,6,8,10,12-hexanitro-2,4,6,8,10,12-hexaazaisowurtzitane (CL-20) ammonium perchlorate (AP) cocrystal,⁴ for example, would not be classified as a cocrystal because of the ionic nature of AP, even though the interactions between CL-20 and AP are undoubtedly non-ionic. Based on the FDA's definition of salts, cocrystals, and polymorphs (which includes solvates), this cocrystal would be unclassifiable. The exclusion of solvates from cocrystals is also problematic. The CL-20 ethylene carbonate (EC) cocrystal⁵ was produced by dissolving CL-20 in EC. Which could classify it as a solvate crystal. This crystallisation was, however, performed at 333.15 K because EC is a solid at room temperature. Would

it, thus, be a cocrystal at room temperature, but a solvate at 333 K? The general consensus of the cocrystal community is generally more in line with the proposed definition of Aitipamula *et al.*³ that all "solids that are crystalline single phase materials composed of two or more different molecular and/or ionic compounds generally in a stoichiometric ratio" should be considered cocrystals. This definition intentionally leaves overlap between salts, solvates and cocrystals.

In 2018, the FDA published a revision of their regulatory classification⁶ in which they have improved the wording, but the exclusion of solvates and ionic compounds is still present. Both definitions have their shortcomings. The flaws of the FDA definition have already been discussed and the definition of Aitipamula seeks to allow some overlap between the definition of a salt and a cocrystal. In the present formulation, however, salts and solvates are fully included in the definition. It seems that merging the two definitions would work best. A definition that says that "cocrystals are predominantly molecular crystals that can contain entities that interact ionically, but also have to have intermolecular interactions between various low-volatile entities that are purely non-ionic and non-covalent in nature" could better describe what Aitipamula and most of the cocrystal community mean by cocrystal. This definition is used in this thesis.

There are also some renowned scientist who advocate the exclusion of solvates from cocrystals⁷ or are opposed to the term cocrystal in its current use in general.⁸ Even the use of a hyphen, as in cocrystal or co-crystal, is agitatedly discussed.^{8,9}

In contrast to the methodology of its definition and spelling, the methodology for the generation of cocrystals in solution is undisputed. And the undoubtedly most useful tools here are the phase diagrams of the cocrystals.

1.2 The Use of the Phase Diagram

For most solution based cocrystallisation techniques, the knowledge of the cocrystal phase regions' positions in the ternary phase diagram

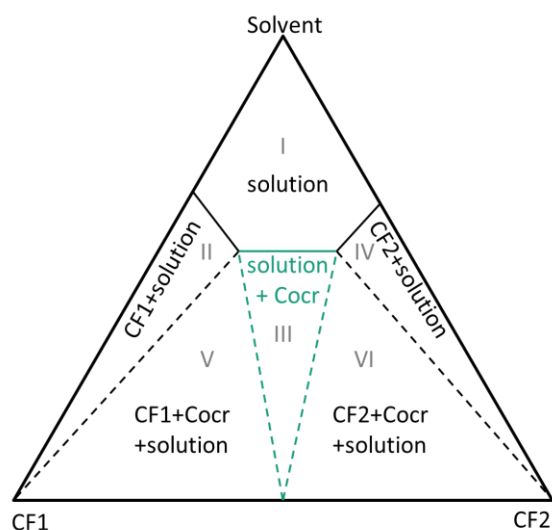


Figure 2: Depiction of a ternary phase diagram of a cocrystal. The cocrystal phase region is marked in green. Solid lines represent solubility curves. The thermodynamically stable composition of each phase region is displayed. Phase regions are marked in gray roman numerals.

(TPD) is of dire importance.^{10,11} Any composition of the two cofomers^a (CF) and the solvent can be represented in the TPD (Figure 2). The solid lines in Figure 2 represent the equilibrium between the solid CF and their solutions at one temperature.¹² Specifically, this means that in region I no solid is present. If, for example, solid is added in a fashion that moves the solution composition into region II, only undissolved CF1 can be present after equilibration. Accordingly, the cocrystal is only formed as the sole thermodynamic product in region III. The size and position of the cocrystal phase region is, among other factors, dependent on the cocrystals stoichiometry and the solubility of the two CF. In reality, the TPD is, therefore, seldom that clear. Oftentimes, the phase solubility diagram (PSD)¹³ is a far more suitable tool for crystallisation design. The PSD shows the equilibrium solubilities of its solid phases as a function of solution concentration of the CF at one temperature.¹³ The PSD in Figure 3 displays a cocrystal system of incongruently soluble CF. The solubility of CF2 is significantly higher than the solubility of CF1. This has shifted the position of the cocrystal phase region. As a result, the solution compositions having the same stoichiometric ratio of CF2:CF1 as the cocrystal are outside the cocrystal phase region (blue line in Figure 3). Such a system is called

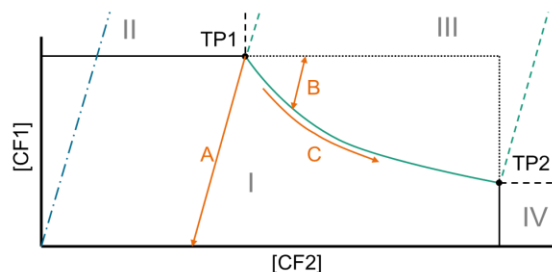


Figure 3: Phase solubility diagram of an incongruently soluble cocrystal. Solid lines represent solubility curves. The blue dash-dot-line represents the solution concentrations where [CF1]:[CF2] is equal to the ratio in the cocrystal. Orange arrows indicate the change in solution concentration during antisolvent or cooling crystallisation (A), reaction cocrystallization (B), and evaporation crystallisation (C). TP are the transition points between phase regions. The gray roman numerals correspond to the same phase regions as in Figure 2.

incongruent.¹⁴ In such a case, excess CF2 must be dissolved to operate a cocrystallisation within the cocrystal phase region. For most systems, this can be avoided by the choice of the right solvent or solvent mixture,¹⁵ as typically the solubility of one CF must be more than ten times higher than the solubility of the other CF for incongruity to occur.¹⁴

While the efficiency of the antisolvent, cooling, and evaporation crystallisation strongly depends on the position of the cocrystal phase region, the position is of less importance for the mechanochemical, reaction, and spray crystallisation.

1.3 Cocrystallisation Techniques

Antisolvent cocrystallisation generates supersaturation of the cocrystal by antisolvent addition to the saturated solution. The solution composition during the experiment follows arrow A in Figure 3. The antisolvent dosing rate can be very precisely matched to the crystallisation rate which enables one to control the supersaturation and, therefore, the crystallisation rate. For incongruent systems, the methods efficiency is limited by the solubility ratio at TP1 and the achievable solubility difference of CF1 between the pure solvent and the final solvent-antisolvent mixture.

Cooling cocrystallisation operates very similar to antisolvent cocrystallisation. The major difference is that the supersaturation is achieved by temperature reduction.

Evaporation crystallisation generates supersaturation by reducing the solvent content of the ternary mixture. For incongruent systems, this means that the fraction of CF2 increases during the crystallisation. The solution composition during the

^a The term cofomer is used in the field of pharmaceutical cocrystals to represent the other component of the cocrystal besides the API. In this thesis, cofomer is used to describe both components of a cocrystal.

experiment follows arrow C in Figure 3. The method's efficiency is, thus, also limited by the solubility ratio of CF1 and CF2 at TP1 as well as their solubility difference between TP1 and TP2. Because the evaporation rate can be adjusted, control over the supersaturation and the crystallisation rate is achievable.

Mechanochemical cocrystallisation techniques subdivide into two categories, liquid assisted grinding and neat grinding. For both methods, cocrystallisation is induced by grinding a mixture of the two (or more) CF together. This is often done via mortar and pestle, but scaled-up production has been carried out using resonant acoustic mixing¹⁶ and bead milling.¹⁷ In liquid assisted grinding (LAG), often also called solvent drop grinding, a (small) amount of antisolvent or solvent is added to the solid mixture. The presence of liquid typically decreases the cocrystallisation time drastically.^{18,19} Both methods gained significant traction in the 1980s and '90s, but the first use of neat grinding and LAG for cocrystallisation for the generation of quinhydrone by Ling and Baker was reported over 125 years ago.²⁰ The efficiency of the methods is high because of the limited use of solvent, but the obtainable crystal size is small because of the permanent milling of the material.

Cocrystallisation methods that utilise solution mediated phase transformation, such as the slurry technique^{21,22} and batch reaction crystallisation^{13,23} (also called reaction cocrystallization by Rodríguez-Hornedo *et al.*²³), have become the most applied cocrystal screening methods.²⁴ Both methods operate strictly within the boundaries of the cocrystal phase region in the ternary phase diagram, and supersaturation of the cocrystal is achieved by adding either one (reaction cocrystallization) or both (slurry technique) CF in solid form to the solution. From a chemical standpoint, both methods classify as "reaction cocrystallisation". Therefore, in this work, the expression "reaction cocrystallization" (RC) coined by Rodríguez-Hornedo *et al.* will be used to describe crystallisation experiments where one or more CF are added to a solution saturated with respect to the cocrystal. The solution composition during batch RC follows arrow B in Figure 3. Excess CF dissolves until the solubility limit of the individual CF is reached. More CF dissolves then when the solution concentration is reduced because of cocrystal formation. As excess solid is used, a higher efficiency can be reached, but the supersaturation cannot be controlled.

A multitude of crystallisation techniques exist that utilise the atomisation of liquid by expelling it

through a nozzle. Among these, spray drying²⁵ is the most prevalent technique for the generation of cocrystals.²⁶ Here, crystals are produced by rapid evaporation of the solvent from the liquid (solution, suspensions, or slurry). Spray drying is considered one of the most desirable methods for the scaled-up production of cocrystals because it is a fast, continuous, one-step process²⁷ and easy to scale up,²⁸ but the fast solidification during spray drying is detrimental to the achievable crystal quality as it facilitates the formation of defects and amorphous states.²⁷

1.4 Crystal Quality

A variety of characteristics can be summarised as the crystal quality. Of these, the crystal morphology, phase purity, point defects, and inclusions are most relevant for this work. All of these attributes are dependent on the growth conditions of the crystal and can, therefore, be optimised to some extent by the selection of the crystallisation parameters, such as the chosen supersaturation and agitation speed as well as the solvent selection. The crystal morphology, called habit, is determined by the relative growth rates of the crystal faces which can be altered by a number of factors. Crystallisation at high supersaturations often results in the formation of needle-like crystals, impurities in the solution can hinder the growth of a certain crystal face, and different solvents often produce different crystal habits.²⁹ Ascorbic acid, for example, exhibits a plate-like habit when grown from water, but needles form from ethanol.³⁰ Three kind of point defects can occur. A small molecule or atom can fill a position in the interstice between the matrix atoms (interstitial point defect), a vacancy point defect is a lattice site from which a molecule or ion is missing, and a substitutional impurity is a foreign atom that occupies the site of a matrix atom. For example, the incorporation of synthesis by-products of CL-20 as substitutional impurities could explain the inability to purify CL-20 above a certain purity level via recrystallisation.³¹ Pockets of solid, liquid, or gas often found in crystals are called inclusions. They can either form during the crystal growth process or can form when a crystal cracks because of internal stress created during growth. Larger crystals and fast growth increase the likelihood of inclusions.²⁹

Depending on the aspect of crystal quality of interest, a variety of analysis methods are established. High performance liquid chromatography (HPLC), nuclear magnetic resonance (NMR) and infrared spectroscopy are good examples for the routine detection of solid

and liquid inclusions or impurities in crystals. Depending on the individual substances, impurities of less than 0.005% total content are detectable with relatively low effort. Phase purity can be precisely determined by Rietveld analysis of powder x-ray diffraction measurements (pXRD). The detection of gas inclusions however requires far more effort and can, for example, be done by performing the crystallisation under pure argon atmosphere and subsequent detection of the enclosed argon via gas chromatography (GC).³² Because of the density difference between gas and crystalline substance (and possibly also between crystalline substance and liquid inclusion) density measurements can also yield information about the crystal defects. An exceptionally useful tool for density determination is the device for measuring the density of particles by flotation, developed by Borne and Patedoye³³ that not only allows for the determination of the density distribution within a batch, but also the separation of the density fractions. This apparatus is, however, very sensitive to external factors as well as internal ones.³² Of the available density determination techniques of solids, gas pycnometry is one of the most user friendly because of the availability of easy to operate consumer grade devices. But, the influencing factors on the accuracy and even the precision of the measurement are not satisfactory explored yet. Another, more direct, way of defect analysis is photomicrography of the particles immersed in a liquid of matching refractive index.^{32,34–36} This procedure reduces surface diffraction on the crystals and thereby highlights internal defects (Figure 4). In most cases, this method was only used as a qualitative tool. And only one group has attempted to obtain quantitative data by manually defining individual

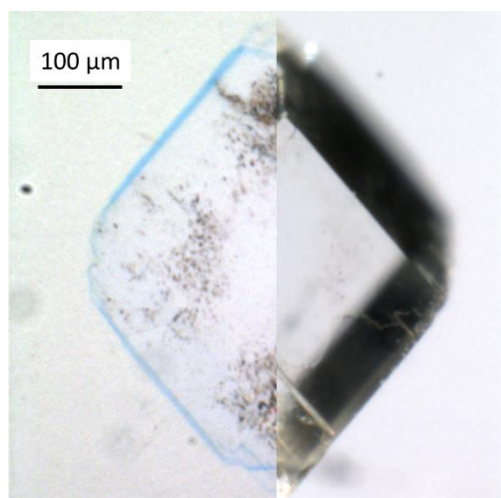


Figure 4: Photomicrograph composite of a CL-20/HMX cocrystal. The left half depicts the crystal immersed in an optically equally dense medium as the crystal, while the right side shows the crystal unimmersed.

crystals and analysing them via digital image processing.^{37,38} The analysis method of choice, of course, is dependent on the desired material characteristics and can, hence, vary with the individual cocrystal application.

1.5 Cocrystal Applications

Cocrystallisation has seen increasing interest recently, mostly because of its ability to modify characteristics of the CF without the need for molecular change to the CF. This resonated most strongly with the pharmacological sector, as evidenced by the over 150 review papers published on API cocrystals over the past decade. Bioavailability,^{28,39} hygroscopicity,⁴⁰ melting point,^{39,41} and permeability⁴¹ are all drug properties that were modified by cocrystallisation. Here, the solubility modification is of the most interest.⁴² Many API are poorly water soluble. This limits the bioavailability of the drug in the human body.⁴⁰ Insufficient bioavailability can result in an overall higher drug dose needed which can increase dose related toxicity and can reduce patient compliance,⁴³ if the drug is approved for distribution at all. The most often employed strategy to increase API solubility is salt formation.⁴⁴ Many API, however, do not possess ionisable functional groups. Other strategies then include the search for more soluble polymorphs, the employment of amorphous material, or the application of ultrafine material.⁴² Cocrystallisation of the API with a highly water soluble CF is a relatively novel, but promising alternative strategy. The increased bioavailability is the result of the dissolution of the soluble CF and the resulting metastable release of the API from the cocrystal into the solution. This supersaturation of the API is more stable than the supersaturation resulting from kinetically produced polymorphs or amorphous material because the CF inhibits crystallisation.²⁶

Because electron-rich donors and electron-poor acceptors can be combined in a single crystal lattice, cocrystallisation has become an interesting concept in the field of molecular electronics. By manipulation of the intermolecular interactions, auspicious features, such as optical waveguide properties, room temperature phosphorescence, two-photon absorption properties and tunable emissions, can be obtained.^{45,46}

The possibility to combine molecules with different characteristics in a crystalline compound that potentially exhibits different properties than the individual CF or a combination of CF properties is also a very interesting aspect of cocrystallisation for the field of energetic materials. Ground breaking work on energetic cocrystals was carried out by the

research group of A. J. Matzger. After initial studies of cocrystals comprised of an energetic and non-energetic CF in 2010,⁴⁷ they published the first cocrystal comprised of two energetic CF in 2011.⁴⁸ Many cocrystals with remarkable characteristics have been published since. The 1:1 cocrystal of diacetone diperoxide with 1,3,5-triiodo-2,4,6-trinitrobenzene, for example, is 60% less sensitive towards impact than both CF, which indicates that cocrystal sensitivity can be lower than the sensitivity of the CF. A cocrystal of CL-20 and AP was described by Gao *et al.*⁴ which exhibits reduced hygroscopy compared to AP and could be an interesting candidate for use in propellants. Furthermore, a study of a melt castable energetic cocrystal was published in 2017.⁴⁹ But the most impactful energetic cocrystal is undoubtedly the 2:1 cocrystal of CL-20 and 1,3,5,7-tetranitro-1,3,5,7-tetrazoctane (HMX) discovered by Bolton *et al.* in 2012.⁵⁰ The paper was cited over 300 times and this cocrystal is subject to the most experimental^{16,17,51-61} and simulation papers⁶²⁻⁶⁶ of all energetic cocrystals. This cocrystal is most likely the major contributing factor to the tremendous rise in interest for energetic cocrystals. The following paragraphs explain the necessary fundamentals of energetic material design and classification to understand why this cocrystal had this much of an impact on the energetic materials community.

1.6 Energetic Material Classification

The field of energetic materials can be divided into three basic categories (pyrotechnics, propellants, explosives) based on the material's properties and the intended purpose. Further subdivisions are possible.⁶⁷

Pyrotechnics typically are mixtures of an oxidising agent, a fuel, and additives. They decompose under non detonative self-sustaining exothermic chemical reaction.⁶⁷ Their primary use is civilian fireworks, but they are, for example, also used to generate smoke to mark landing sites, heat in flares, noise and light in flash bangs, or to provide illumination in military applications.

The primary function of a propellant is the rapid generation of hot gases by combustion. Solid-fuel rockets today are primarily propelled by a mixture comprised mostly of AP and aluminium. While space flight in general has significant detrimental environmental impact, the currently in use solid fuel is by far the most damaging option because of the chlorine content.⁶⁸ Research with the aim to find a replacement of AP is ongoing, but as of yet no true

alternative is available. Candidates of interest currently are ammonium nitrate (AN) and ammonium dinitramide (ADN), but both materials have severe drawbacks, such as, for example, the lower specific impulse achievable by AN and the thermal instability of ADN. Work on the development of novel energy dense oxidisers is carried out.⁶⁹ An alternative to the classical mixture of oxidiser and fuel is the use of secondary explosives as part of the mixture. Propellants with comparable specific impulse to AP mixtures have been reported for a variety of high-performance secondary explosives, such as FOX-7 (1,1-Diamino-2,2-dinitroethylene),⁷⁰ HMX,⁷⁰ and CL-20.⁷¹ The formulations are classified as composite modified double base (CMDB) propellants and are comprised of nitrocellulose and nitroglycerin to which the high explosive and aluminium powder is added.⁷² Such a CMDB containing HMX was used by the US military in their Trident II D-5 submarine launched ballistic missile.⁷² Utilisation of high-performance explosives as part of formulations is also research subject in the field of gun propellants. Triple base propellants typically containing nitrocellulose, nitroglycerin and nitroguanidine are most widely used for tank guns to date.⁷³ The muzzle energy is a deciding factor for the efficacy of modern high performance kinetic energy ammunition like fin stabilised armour piercing discarding sabot rounds. It has been shown that the incorporation of 1,3,5-trinitro-1,3,5-triazinane (RDX) can improve the chemical energy of the propellant and, thus, the muzzle velocity.⁷³

Explosives subdivide into primary and secondary explosives. The classification is based on their designated application. Primary explosives are typically used to initiate secondary explosives, propellants, or pyrotechnic charges because they are sensitive to external stimuli, such as electrical discharge, friction, heat, impact, or light irradiation.⁶⁷ Upon stimulation, the material undergoes a fast transition from deflagration to detonation, which means that decomposition initially proceeds via subsonic heat transfer, but converts into a supersonic shock wave.⁷⁴ The two most common military primary explosives are lead azide and lead styphnate,⁷⁵ but alternatives are investigated because of the detrimental health and environmental effect of the contained lead. Lead-free alternatives have been proposed, such as copper(I) nitrotetrazole (which is already in use as a substitute for lead azide in some applications⁷⁵) or the highly energetic potassium 1,1'-dinitramino-5,5'-bistetrazolate.⁷⁶ Secondary explosives, also called high explosives, generally are less sensitive to detonation initiation than primary explosives. In the

past, secondary explosives were also more powerful than primary explosives, but recently this gap has been bridged for the most part. The utilised secondary explosives are best divided into civilian used and military used explosives. For civilian use, ANFO, a mixture of AN and fuel oil, is the most common explosive in the fields of mining and civil engineering⁷⁷ because it is cheap, safe and easy to handle.⁷⁸ Despite its low detonation velocity and pressure it possesses a high blasting efficiency because of its large volume of gas generated.⁷⁷ The lower detonation velocity is not necessarily a disadvantage as it reduces the amount of fine grain generated around the blast hole. This reduces the material extraction time and depending on the mined good, increases the product value.⁷⁹ Trinitrotoluene (TNT), 1,3,5-trinitro-1,3,5-triazinane (RDX), and HMX are the most commonly used military high explosives. TNT has been in military use for over 100 years now mainly because of its relatively low sensitivity combined with its extremely useful low melting point of 354 K which enables one to produce cast charges.⁸⁰ Composition B, a mixture of TNT and RDX, is the main explosive filling in, for example, artillery projectiles, hand grenades, and land mines. Octol, a mixture of TNT and HMX, is often used as an explosive fill in military application that require more energy than Composition B can provide.⁸¹ HMX is also often used as polymer bonded explosive (PBX) in nuclear ordnance^{81,82} and has been used in naval shells.⁸² A PBX is an explosive material comprised of a crystalline explosive that is bound together in a matrix by a polymer. This procedure can serve several purposes. While TNT is insensitive and shapeable enough to be used as is, HMX and most other high explosives need some form of phlegmatization and shaping matrix. The polymer matrix can be comprised of an elastomer that can absorb shocks for reduced sensitivity, or hard polymers can be utilised to form a rigid PBX that is machinable.⁸² Depending on the utilised polymer, the PBX can be hydraulically pressed to reach bulk densities very close to the theoretical values. The higher density increases the detonation performance. Typically, very high solid loadings of 90-95% by mass are reached. Such high solid loadings can only be achieved if the particle size distribution is carefully designed. In the absence of directing forces, the packing density of loose spheres of equal size can at best reach 63.7%.⁸³ The packing density can be improved by adding smaller particles that fill the voids left between the larger particles. It can be calculated that by mixing spheres of a size ratio of 100:1, a packing density of about 85% can be reached.⁸⁴ Higher space fillings would

require the addition of yet smaller particles. In reality, however, explosive particles typically are neither spheres, nor of uniform size. The particle diameters possess a size distribution after crystallisation. The particle size distribution and its corresponding volume-weighted mean particle diameter $D(4,3)$ ⁸⁵ of a CL-20/HMX cocrystal batch is displayed in Figure 5. Because of this distribution, in praxis, a bimodal size distribution separated by one order of magnitude in size whose particle size distribution curves do not intersect has been shown to produce typically high enough solid loadings. The application of very fine crystals in the PBX can lead to an undesirably high viscosity. For this reason, a pairing of fine and coarse particles of around $D(4,3) = 20 \mu\text{m}$ and $200 \mu\text{m}$ respectively is often the target. Crystals of compact morphology are beneficial to the processability of the PBX because of the detrimental effect of plate-like particles on the viscosity. Plate like particles could decrease the charge density because of inefficient packing which would reduce the performance of the PBX. Furthermore, crystals have a higher chance of contacting each other which also reduces the safety

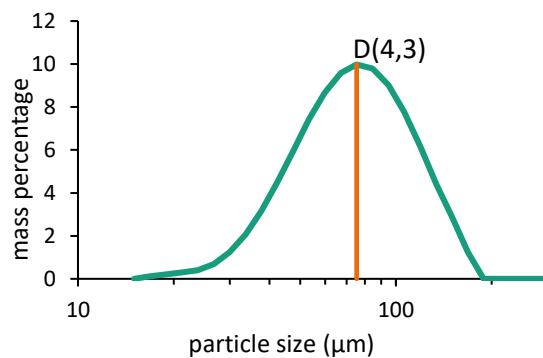


Figure 5: The volume-weighted particle size distribution of a CL-20/HMX cocrystal batch is displayed in green. The orange line represents the volume-weighted mean particle diameter. Because of its intermediate particle size of about $75 \mu\text{m}$, this batch would only be useful as seed crystals.

of the PBX.

1.7 Energetic Material Performance Versus Safety

In the field of military high explosives, improving the lethality of warheads and missiles as well as increasing the jet velocity of shaped-charges are of great interest.⁸⁶ The primary criteria for the selection of a high explosive for these applications are the detonation pressure (p_{Cl}) and the detonation velocity (D).⁸⁶ D is the velocity of the shockwave front traveling through the high explosive during the detonation. This value can be experimentally determined using, for example, optical fibres placed across the charge.⁸⁷ One can also calculate D and p_{Cl} in various ways. One well established method was developed by Kamlet and Jacobs for C-H-N-O explosives.⁸⁸ Here, four quantities are utilised to calculate D and p_{Cl} :

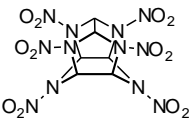
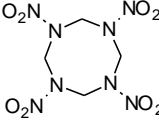
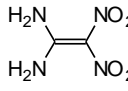
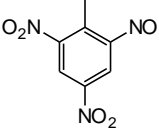
- The number of moles of gaseous detonation products per gram of explosive.
- The average molecular mass of the gaseous products.
- The total heat release during the detonation reaction.
- The loading density of the explosive.

If the crystal density of the explosive is used as the loading density, the D of the explosive itself is determined. In praxis the detonation velocity of a PBX is dependent of the bulk density of the whole charge. An increase in any of the listed quantities will increase D and p_{Cl} . These four quantities give a good indication on how to improve the performance of a high explosive. The number of moles of gaseous products can be improved by oxidising the carbon backbone using nitro groups or by incorporating nitramine groups into the backbone. Ideally, enough oxygen is introduced to oxidise the carbon backbone completely. Substitution of C in the backbone by N not only improves the number of gaseous products per gram, but can also increase the total heat release because of the formation of highly stable N_2 . The total heat release can be increased by introducing ring or cage structures into the molecule because of the resulting strain. The density of an explosive can potentially be increased by utilising the polymorph of highest density. D and p_{Cl} values for selected molecules are displayed in Table 1.^{86,89}

However, the use of these strategies often increases not only the performance of the high explosive, but also its sensitivity.⁸⁹⁻⁹¹ In this context, sensitivity means how much energy has to be transferred to the high-explosive in order to trigger

decomposition. Energy is typically transferred to the high explosive via heating, impact, friction, electric discharge, or light, and the required amount varies for each high explosive depending on the type of energy transfer. This is caused by the multitude of different contributing factors to the explosive's sensitivity. Among other factors, the chemical composition, bonding of functional groups, distribution of charge density, stoichiometry, molecular ordering, grain size, crystal surfaces, presence of imperfections, and the decomposition pathways all contribute to the sensitivity.⁹² A few examples can help understand the complexity of these contributions. The high explosive PETN (2,2-bis[(nitrooxy)methyl]propane-1,3-diyl dinitrate) is unusually susceptible to initiation via laser irradiation. Irradiation with a 1060 nm (1.17 eV) laser can initiate decomposition supposedly by optical excitation of the molecule,⁹³ even though the optical band gap of PETN has been measured to be over 4 eV.⁹⁴ But, the instead proposed purely thermal decomposition in reaction to the irradiation is also unlikely because the calculated activation barrier (146-150 KJ) and the analysed reaction mechanism are inconsistent with the experimental energy of laser initiation (113 KJ).⁹² Another example is the significant sensitivity difference of the two polymorphs β -HMX and δ -HMX. β -HMX is the densest of the four known HMX polymorphs and it is stable at room temperature. When β -HMX is heated to temperatures above 435 K, a phase transformation to δ -HMX occurs.⁹⁵ During this transformation, the molecular ring conformation of HMX changes from chair to boat and the density decreases from 1.90

Table 1: Detonation velocity and detonation pressure of selected high explosives

| name | structure | $D / \text{km s}^{-1}$ | p_{Cl} / GPa |
|-------|---|------------------------|-----------------------|
| CL-20 |  | 9.4 | 41.9 |
| HMX |  | 9.13 | 38.1 |
| FOX-7 |  | 8.61 | 33.8 |
| TNT |  | 7.01 | 20.7 |

to 1.78 g cm^{-3} . It was believed that the resulting cracks and dislocations resulting from this transformation are responsible for the increase in sensitivity. Calculations of the primary decomposition pathways of HMX carried out for an isolated δ -HMX molecule, the molecule placed in an ideal crystal, and on a free surface, however, indicate a different reason for the sensitivity increase. No significant difference in the activation energy between β -HMX and δ -HMX was found for the individual molecule and the molecule placed in the ideal crystal, but a difference of 167 kJ mol^{-1} was found for the activation energy of the N-NO₂ cleavage for the molecule placed on the free surface.⁹² It was speculated that the polar nature of the selected crystal surface of the δ -HMX is responsible for this difference.

Some contributing factors to the sensitivity, such as the chemical composition and the bonding of functional groups, are inherent to an explosive. Other factors, such as the molecular ordering and the crystal surfaces, are dependent on the crystal structure and can change, for example, between polymorphs or between the pure substance and a cocrystal. Other contributing factors, such as the presence of cracks and imperfections, are dependent on the crystal quality. The term imperfections contains a variety of entities,²⁹ (substitutional impurities,³⁴ line defects,^{96,97} surface defects,^{35,98,99} and inclusions.^{32,97,100–102}) that have all been linked to sensitivity increase in high explosives. Of these defects, gas inclusions have been studied the most extensively, and it was demonstrated very impressively by Borne *et al.* that significant improvements in shock sensitivity are possible by reducing liquid and gas inclusions in RDX.^{32,103} The correlation between the void fraction (the amount of inclusions) and the sensitivity of an explosive has been explained by the collapse of these voids when impacted by shock waves and the resulting production of “hot spots”.^{97,100} The concept of hot spots is normally used to describe an area of around $0.1\text{--}10 \mu\text{m}$ that is heated to a temperature above around 700 K that initiates the rapid decomposition of the explosive.⁹⁷ These hot spots can, for example, form within an explosive crystal, in the binder matrix of a PBX, or as the result of gas bubbles in a liquid. The proposed mechanisms of hot spot formation as the result of pore collapse include the adiabatic compression of trapped gas in the void,⁹⁷ the formation of a solid or liquid jet of material that is expelled from one side of the void and slams into the other wall,^{101,104} or viscous or plastic heating of the surrounding matrix material of the void.⁹⁷ Furthermore, mechanisms of hot spots formation have been proposed that do

not require the presence of voids in the crystal or matrix, such as spark discharge, triboluminescent discharge, friction between explosive crystals, localised adiabatic shear of the material during mechanical failure, or viscous heating of material rapidly extruded between impact surfaces.⁹⁷ All these mechanisms have in common that ultimately the decomposition of the explosive is believed to be initiated thermally, but it has recently been proposed that a more broadened view should be adopted to allow for other initiation mechanisms. More in depth analysis is required to increase the understanding of the relative roles of the postulated hot spot formation mechanism.⁹²

The efforts to reduce the sensitivity of munition have gained prominence as the result of many catastrophic explosions that resulted from unintentional initiation by either impact or shock, aboard aircraft carriers, ships, and munition trains.¹⁰⁵ And while the packing and casing of the munition can have a significant effect on the sensitivity, the response of the munition to external stimuli depends to a large extent on the properties of the energetic material.¹⁰⁶

1.8 Properties of the CL-20/HMX Cocrystal

CL-20 has not seen deployment as a high explosive despite its superior D and p_{cl} compared to HMX (Table 1). This is mostly caused by its relatively high sensitivity^{50,107,108} and its polymorphism.¹⁰⁹ Even though four HMX polymorphs are known today, the β -polymorph possesses not only the highest density, but is also the only thermodynamically stable form at normal temperature and pressure. Four of the five known polymorphs of CL-20, however, can coexist at ambient pressure and temperature and can form solution mediated at temperatures between 310 and 328 K .^{110,111} Such transformations could, for example, be induced by the plasticiser used in a PBX. These facile transformations are undesired as they can lead to cracks in the crystals that can negatively affect mechanical properties and sensitivity. In contrast, the CL-20/HMX cocrystal consisting of two molecules CL-20 per molecule HMX does not seem to exhibit polymorphism and no CL-20/HMX cocrystal of different stoichiometry has been observed. The cocrystal is expected to possess a D 100 m s^{-1} higher than HMX and higher explosive power, but was measured to possess the same impact sensitivity as HMX in small-scale drop tests.⁵⁰ These characteristics make it an interesting candidate for the use in military applications that require high D and p_{cl} values. However, further

properties and aspects need to be considered for the application of this cocrystal in PBX charges. The cocrystal inherits some characteristics, such as its toxicology, chemical compatibility, and thermal stability, from its parent molecules, but especially the aspects of practicality need to be specifically evaluated.

1.9 Cocrystallisation Scale Up Challenges

The crystallisation process of the cocrystal must meet the following requirements as the crystals can only then be used in PBX charges. The process must:

- produce compact particles,
- produce particles of tunable size distribution in the size region of 20 μm and 200 μm ,
- produce high-quality crystals (e.g. low inclusion content, no cracks, single crystals, chemically pure,...) and
- be time and material efficient.

While the already discussed need for compact particles of defined size might be somewhat specific to the field of energetic materials, the requirement of high-quality crystals, however, is more universal. In the field of pharmaceutical cocrystals it is necessary to exclude by-products formed or to prevent solvent inclusions,^{112–114} and in the field of molecular electronics higher quality increases the efficacy of the material.^{45,46} The requirement of time and material efficiency is also not unique to energetic cocrystal production and is required because for practical use eventually tonnes of material have to be obtainable in a cost efficient manner. As a first step to test the viability of a system, a scale up to the 100 g-scale is sufficient to produce enough material time efficiently for the production of test PBX charges.

The four requirements must be met by the selection of the three basic crystallisation parameters, the method, the conditions, and the solvent. This selection is limited a priori based on the characteristics of the cocrystal. The desired crystal quality limits which crystallisation methods can be considered. For the scale up of the CL-20/HMX cocrystal, the requirement for crystals of the highest quality means that only methods are considered which are in principle capable of producing high-quality crystals. Furthermore, for cocrystallisation, compared to regular crystallisation, two solubilities have to be considered instead of one. For many cocrystal systems a solvent or solvent mixture is easily

identified that exhibits a beneficial solubility ratio of the CF. This is often the result of the significant chemical difference of the two CF. If one CF is more lipophile while the other CF is more hydrophile an intermediate solvent might level the solubilities. But, more factors have to be considered, such as the overall solubility, possible solvate formation, and the crystal morphology of the crystals grown from this solvent. Solvate formation can make cocrystallisation less reliable or less efficient because the solvate formation is a competing cocrystallisation. A solvent in which both CF are equally insoluble or a solvent that forms fine needles is oftentimes not useful. And in the case of CL-20 and HMX, the chemical composition is very similar; an intermediate solvent might, therefore, not exist. The literature data indicate that CL-20 is far more soluble than HMX. Such a discrepancy has significant impact on the material efficiency. Solvent, condition, and potentially method have to be chosen accordingly.

2 Motivation

Cocrystals are very versatile in their use because of their ability to combine or alter the characteristics of their CF and will see a multitude of applications in the future, but generating the cocrystals introduces additional challenges to the design of a scaled-up crystallisation process compared to the crystallisation of a single component material. So, given the rather recent increase in interest in cocrystals, it is not surprising that scale up attempts are mostly still in their infancy. No scale up has been undertaken in the field of molecular electronics, while the only scale up in the field of energetic cocrystals above the single-digit-gram-range has been carried out for the CL-20/HMX cocrystal by means of spray drying.^{16,61} In the last decade, five API cocrystals, however, have been approved by the FDA.¹¹⁵ Naturally, the exact cocrystallisation procedures are heavily obscured in the patents. The diabetes medication Suglat[®] seems to be obtained from a stoichiometric solution by cooling crystallisation.¹¹⁶ In the patent, Odomzo[®], a cancer medication, is obtained from a batch reaction cocrystallisation with phosphoric acid.¹¹⁷ It can be classified as a cocrystal because the crystal structure indicates that one of the two phosphoric acid entities is present in the crystal lattice in an undissociated form.¹¹⁵ Entresto[®] was approved for the treatment of heart failure. It is comprised of two API molecules (Valsartan and Sacubitril) whose cocrystallisation is, according to the patent, induced by transforming the molecules into their respective sodium salts by sodium hydroxide addition.¹¹⁸ This classifies it as a batch reaction cocrystallisation also. Steglatro[®], which was approved as a diabetes medication, also appears to be obtained by batch reaction cocrystallisation.¹¹⁹ The preparation of Mayzent[®], a treatment for multiple sclerosis, is especially obscured in the patent. It is possible that the cocrystal is obtained either by cooling, evaporation, batch reaction cocrystallisation, or a combination thereof. It is even possible that the crystal is obtained by spray drying.¹²⁰

Even though these scaled-up cocrystallisations have been described, it is yet unknown how universally these methods can be used in the various disciplines. It is, for example, unlikely that spray drying can be used to produce coarse cocrystal for the use in PBX because of the limited achievable particle quality, and even though batch RC seems to be the preferred cocrystallisation method in the pharmaceutical sector so far, it is unclear whether batch RC can be utilised to produce

crystals of high-quality in the 200 μm -range as this was most likely not a requirement for the generation of the API cocrystals. Furthermore, because batch RC does not provide control over the supersaturation during the crystallisation it is reasonable to assume that high-quality crystals cannot be produced in this way for every system. This can also limit its application in the pharmaceutical sector. Cooling crystallisation, on the other hand, should be able to produce high-quality coarse crystals, but might feature unacceptable efficiencies if the CF are incongruently soluble. This is a universal problem of most established crystallisation methods, such as, antisolvent crystallisation and evaporation crystallisation, as they were developed for the crystallisation of a single substance and only one solubility is relevant in this case. For cocrystallisation, however, the solubilities of both CF, that can differ drastically, have to be considered.

A cocrystallisation method must be able to combine good crystal quality with good material efficiency. Depending on the individual use of the cocrystal, further limitations are imposed on the crystallisation process. Especially for the use of cocrystals in the field of energetic materials, but also in the other fields, in-depth research of scalable cocrystallisation methods and their potential for efficiency as well as their capability of high-quality crystal production is required, particularly for the cocrystallisation of incongruently soluble CF. It is quite possible that no established method does suffice for incongruently soluble CF. In that case, alternative methods must be investigated. The scale up of the CL-20/HMX cocrystal for the use in PBX is excellently suited as a sample system for the trial of methods. Not only is this cocrystal of tremendous interest for the energetic materials community due to its lack of polymorphism and its presumed detonation and safety characteristics, but it also imposes a very strict set of limitations on the crystallisation method. Because the CF are likely incongruently soluble, the crystallisation method's capability for efficient crystallisation is tested. And because of the correlation between crystal quality and sensitivity, the highest achievable crystal quality is sought after. This effort should elevate the knowledge of cocrystal analysis methods since methods to evaluate the crystal qualities achieved are required for further development and comparison of the applied cocrystallisation methods. The methods of crystal defects analysis need improvement. None of the established methods can be used to routinely assess the degree of crystal defects quantitatively, especially on the

laboratory-scale. For example, the detection of gas inclusions using GC requires an adaptation of the experimental conditions (e.g. argon atmosphere), the density flotation requires complex equipment and is complex to operate, and the quantitative detection of the degree of crystal defects by immersing the crystals in an optically equally dense medium requires, in its published form, the development of a detection algorithm and extensive manual labour. Given these shortcomings, alternative assessment methods must be found, or existing methods improved in order to be able to carry out routine crystal defect analysis even on a laboratory-scale. One promising method is helium pycnometry. However, in order for it to be useful, it is necessary to know the exact repeatability error of the method as well as the factors that influence the results. At present, only the presumably much larger reproducibility error is known, and no quantification of the possible impact factors has been undertaken. Furthermore, it is unknown whether the measurement results fulfil the prerequisites for the application of statistical tests to compare the results. These uncertainties currently limit the discriminatory power of helium pycnometry to an unusable level.

The transferable knowledge obtained from this cocrystals scale up and its quality analysis should present a strategy that is adaptable to the scale up of other cocrystal systems, not only energetic ones; Furthermore, the improved or developed crystal quality analysis methods should be useful for the analysis of all crystals, not only cocrystals.

The combined results might make it possible that previously unviable cocrystal systems can be implemented.

3 Aim and Objectives

The requirements for the development of the scale up are concentrated in three research questions (RQ). The objectives imposed by the RQ are organised in the form of work packages (WP). The chapters in which the results of the WP are described are displayed in parenthesis after each WP.

RQ1: How can the crystal quality be analysed sufficiently well to allow for the differentiation between and optimisation of the crystallisation methods?

WP1: Suitable analytical methods must be identified or developed in order to be able to quantify and compare the chemical purity, the phase purity and the crystal defects of the crystals of samples even on a laboratory-scale. (chapter 5.1 and chapter 5.2)

RQ2: Which combination of solvent and temperature can produce compact crystals efficiently without the formation of solvates?

WP2: A solvent should be identified either from literature research or experimental work in which CL-20 and HMX are congruently soluble and no solvate formation occurs. Experimental work includes:

- Systematic selection of solvents based on literature data (chapter 6.1)
- Define test conditions (temperature, equilibration time, method, analysis method of the solid (chapter 6.1)
- Identify any solvates that may have formed (chapter 6.1)
- Determination of the solubility ratio at TP1 for the most promising solvents (chapter 7.1)
- Determination of the crystal habitus of cocrystals grown from these solutions (chapter 7.1)

RQ3: Which crystallisation method can produce high-quality cocrystal efficiently and reliably?

WP3: The crystallisation processes known from the literature are to be tested with regard to which methods are basically capable of delivering high-quality crystals reliably and efficiently. This can result in either of the following two scenarios:

- Once an established method has been identified that efficiently and reliably produces high-quality crystals, the method should be scaled-up to the 100 g-scale.

- If no established method is able to produce high-quality crystals with acceptable efficiency and reliability, a method must be developed that can do this. This method must then be scaled-up. (Chapter 7.1 and chapter 7.2)

4 Summary

The content of chapters 5-7 has been published in peer-reviewed scientific journals. For ease of navigation of this thesis, a short summary of the papers is given in this chapter.

High-Precision Density Measurements of Energetic Materials for Quality Assessment

In chapter 5.1, the steps necessary to achieve reproducible density measurements using helium pycnometry are investigated. Because of the lack of reliable data, it was unclear from the literature what its maximum achievable precision is and, thus, it was unclear whether it is useful as a tool for assessing the quality of the CL-20/HMX cocrystal. It was found that even samples of non-hygroscopic material either have to be dried before measurement or flushed extensively in the pycnometer before the measurement, else false density values will be obtained. The density data points are, in principle, normal distributed, which would allow statistical tests to be used to compare samples, but the data are additionally significantly influenced by presumably the semidiurnal atmospheric pressure drift and the weighing error. Statistical tests such as the t-test¹²¹ or ANOVA (ANalysis Of VAriance), therefore, almost always reject the similarity of repeat measurements. An analysis method was, thus, devised that takes these additional disturbances into account. Hence, if strict care is taken during sample preparation, samples whose density differs by as little as 0.001 g cm^{-3} can be differentiated with certainty. This precision is sufficient for the quality analysis of the CL-20/HMX cocrystal.

Quality Assessment of the CL-20/HMX Cocrystal Utilising Digital Image Processing

For the optimisation and comparison of the utilised cocrystallisation techniques, the ability to discriminate the chemical purity and phase purity of cocrystal samples of antisolvent crystallisation, batch RC, and semibatch reaction cocrystallisation (SBRC) was tested in chapter 5.2 using established analytical methods. The chemical purity was determined by HPLC and ^1H NMR, and the solvent inclusion specifically was determined by GC. DSC and pXRD were used to identify the phase purity of

the material. For the analysis of the crystal defects, the previously developed analysis method for helium pycnometry measurements and the results of digital image processing of photomicrographs of crystals immersed in an optically equally dense liquid were utilised. It was found that all crystallisation methods lead to an increased chemical purity of the cocrystal compared to the starting material of about 0.5%, but the prolonged time at 333.15 K for antisolvent crystallisation and SBRC leads to a slight increase (about 0.15%) in decomposition products of CL-20. According to the Rietveld analysis of the pXRD measurements all crystallisation methods yield more than 99.9% phase pure material. Based on the unexpectedly low density difference between the batch RC sample and the other samples and in conjunction with the determined solvent inclusions, the determined chemical purities, and the evaluation of the photomicrographs, it was concluded that batch RC produces crystals with less gas inclusions than antisolvent crystallisation and SBRC. Furthermore, the analysis of the degree of crystal defects based on the photomicrographs shows that SBRC on a pilot plant-scale can produce coarse crystals of equally high quality as antisolvent crystallisation on a laboratory-scale.

Solubility Behaviour of CL-20 and HMX in Organic Solvents and Solvates of CL-20

In chapter 6.1, the best achievable solubility ratio of CL-20 and HMX was investigated to identify solvents that enable efficient cocrystallisation. The solubility determination of CL-20 and HMX in 29 solvents, systematically selected based on the limited literature data, at 293.15 K and 333.15 K as well as solubility determinations of CL-20 and HMX in selected solvent mixtures showed that none of the tested solvents and solvent mixtures exhibits a solubility ratio close to the stoichiometric ratio of the cocrystal. Six novel solvates of CL-20 with 5-methyloxolan-2-one, 1,3-dioxolan-2-one, tetrahydrothiophene-1-oxide, 1,3-dioxolane, butane-2,3-dione, and furan-2-carbaldehyde were discovered. With the exception of furan-2-carbaldehyde, the single crystal structure was determined for all novel solvates, and a novel CL-20 conformation was identified in the tetrahydrothiophene-1-oxide crystal structure. The strict exclusion of solvate-forming solvents from consideration for cocrystallisation had to be revised because, of the ten solvents with the best solubility ratios five are known to form solvates with either

HMX or CL-20. Due to the large difference in solubility between CL-20 and HMX, in most cases the solvate phase region of CL-20 solvates would most likely have no overlap with the cocrystal phase region in which the cocrystallisation is carried out. Therefore, these solvents should generally be able to be used for cocrystallisation.

Investigation of Crystallisation Conditions to Produce CL-20/HMX Cocrystal for Polymer-Bonded Explosives

In chapter 7.1, the capability to form the cocrystal was tested for the ten solvents with the best CL-20/HMX solubility ratio. It was found that only acetonitrile is suited as a solvent, even though it is the solvent of the ten that possesses the worst solubility ratio. Of the other solvents, butane-2,3-dione and dimethyl carbonate did not form the cocrystal reliably, tetramethylurea was chemically incompatible with CL-20, 4-methyloxetan-2-one, 5-propyloxolan-2-one, 5-ethyloxolan-2-one, and 4-methyl-1,3-dioxolan-2-one formed plate-like crystals and cyclohexanone had a poorer solubility ratio than acetonitrile at TP1.

Using acetonitrile, the achievable crystal quality, efficiency, and reproducibility of antisolvent crystallisation, cooling crystallisation, and batch RC were tested, as well as the achievable efficiency of evaporation crystallisation calculated based on the determined phase diagram of CL-20, HMX and acetonitrile. It was found that antisolvent crystallisation, cooling crystallisation and batch RC were capable of producing high-quality crystals, but only antisolvent crystallisation could do this reliably, and robust batch RC experiments yielded only fine crystals of moderate quality. The antisolvent crystallisation suffers from a poor CL-20 efficiency of 25% compared to the achieved efficiency of the batch RC of 55%. An efficiency as high as 79% was achieved for batch RC by recycling the mother liquor twice in consecutively carried out experiments. Solution recycling is, however, not an option for antisolvent crystallisation.

Semibatch Reaction Crystallization for Scaled-Up Production of High-Quality CL-20/HMX Cocrystal: Efficient Because of Solid-Dosing

Because no established cocrystallisation method was able to produce the CL-20/HMX cocrystal efficiently, reproducibly, and in high-quality, the new cocrystallisation method solid-dosing

semibatch RC (SBRC) was developed which is presented in chapter 7.2. Here, the ability of batch RC to add excess CL-20 and HMX to the solution is coupled with the supersaturation control of antisolvent crystallisation to achieve a reliable method that is capable of producing the cocrystal of high-quality efficiently. As the solid-dosing rate must match the crystallisation rate, inline monitoring of the solution concentrations is required. This is achieved by a mid-infrared process spectrometer coupled to an attenuated total reflection (ATR) immersion probe. Coarse cocrystal of comparable quality to crystals produced by antisolvent crystallisation were obtained in the 100 g-range with a CL-20 efficiency of 63%.

References

- (1) Wöhler, F. Untersuchungen über das Chinon. *Justus Liebigs Ann. Chem.* **1844**, 51 (2), 145–163. <https://doi.org/10.1002/jlac.18440510202>.
- (2) Lostritto, R. Regulatory Classification of Pharmaceutical Co-Crystals, Guidance for Industry. *USFDA* **2011**.
- (3) Aitipamula, S.; Banerjee, R.; Bansal, A. K.; Biradha, K.; Cheney, M. L.; Choudhury, A. R.; Desiraju, G. R.; Dikundwar, A. G.; Dubey, R.; Duggirala, N.; Ghogale, P. P.; Ghosh, S.; Goswami, P. K.; Goud, N. R.; Jetti, R. R. K. R.; Karpinski, P.; Kaushik, P.; Kumar, D.; Kumar, V.; Moulton, B.; Mukherjee, A.; Mukherjee, G.; Myerson, A. S.; Puri, V.; Ramanan, A.; Rajamannar, T.; Reddy, C. M.; Rodriguez-Hornedo, N.; Rogers, R. D.; Row, T. N. G.; Sanphui, P.; Shan, N.; Shete, G.; Singh, A.; Sun, C. C.; Swift, J. A.; Thaimattam, R.; Thakur, T. S.; Kumar Thaper, R.; Thomas, S. P.; Tothadi, S.; Vangala, V. R.; Variankaval, N.; Vishweshwar, P.; Weyna, D. R.; Zaworotko, M. J. Polymorphs, Salts, and Cocrystals: What's in a Name? *Cryst. Growth Des.* **2012**, 12 (5), 2147–2152. <https://doi.org/10.1021/cg3002948>.
- (4) Gao, H.; Jiang, W.; Liu, J.; Hao, G.; Xiao, L.; Ke, X.; Chen, T. Study of an Energetic-oxidant Cocrystal: Preparation, Characterisation, and Crystallisation Mechanism. *DSJ* **2017**, 67 (5), 510–517. <https://doi.org/10.14429/dsj.67.10188>.
- (5) Herrmannsdörfer, D.; Stierstorfer, J.; Klapötke, T. M. Solubility Behaviour of CL-20 and HMX in Organic Solvents and Solvates of CL-20. *Energetic Materials Frontiers* **2021**, 2 (1), 51–61. <https://doi.org/10.1016/j.enmf.2021.01.004>.
- (6) Lostritto, R. Regulatory Classification of Pharmaceutical Co-Crystals, Guidance for Industry. *USFDA* **2018**.

- (7) Nangia, A. Pseudopolymorph: Retain This Widely Accepted Term. *Cryst. Growth Des.* **2006**, *6* (1), 2–4. <https://doi.org/10.1021/cg050343e>.
- (8) Desiraju, G. R. Crystal and co-crystal. *CrystEngComm* **2003**, *5* (82), 466. <https://doi.org/10.1039/b313552g>.
- (9) Stahly, G. P. Diversity in Single- and Multiple-Component Crystals. The Search for and Prevalence of Polymorphs and Cocrystals. *Cryst. Growth Des.* **2007**, *7* (6), 1007–1026. <https://doi.org/10.1021/cg060838j>.
- (10) Chiarella, R. A.; Davey, R. J.; Peterson, M. L. Making Co-Crystals The Utility of Ternary Phase Diagrams. *Cryst. Growth Des.* **2007**, *7* (7), 1223–1226. <https://doi.org/10.1021/cg070218y>.
- (11) Chadwick, K.; Davey, R.; Sadiq, G.; Cross, W.; Pritchard, R. The utility of a ternary phase diagram in the discovery of new co-crystal forms. *CrystEngComm* **2009**, *11* (3), 412–414. <https://doi.org/10.1039/b818268j>.
- (12) Purdon, F. F.; Slater, V. W. *Aqueous Solution and the Phase Diagram*; Edward and Arnold & Co, 1946.
- (13) Childs, S. L.; Rodríguez-Hornedo, N.; Reddy, L. S.; Jayasankar, A.; Maheshwari, C.; McCausland, L.; Shipplett, R.; Stahly, B. C. Screening strategies based on solubility and solution composition generate pharmaceutically acceptable cocrystals of carbamazepine. *CrystEngComm* **2008**, *10* (7), 856–864. <https://doi.org/10.1039/b715396a>.
- (14) Alhalaweh, A.; Sokolowski, A.; Rodríguez-Hornedo, N.; Velaga, S. P. Solubility Behavior and Solution Chemistry of Indomethacin Cocrystals in Organic Solvents. *Cryst. Growth Des.* **2011**, *11* (9), 3923–3929. <https://doi.org/10.1021/cg200517r>.
- (15) Rager, T.; Hilfiker, R. Cocrystal Formation from Solvent Mixtures. *Cryst. Growth Des.* **2010**, *10* (7), 3237–3241. <https://doi.org/10.1021/cg100361y>.
- (16) Anderson, S. R.; am Ende, D. J.; Salan, J. S.; Samuels, P. Preparation of an Energetic-Energetic Cocrystal using Resonant Acoustic Mixing. *Propellants, Explos., Pyrotech.* **2014**, *39* (5), 637–640. <https://doi.org/10.1002/prop.201400092>.
- (17) Qiu, H.; Patel, R. B.; Damavarapu, R. S.; Stepanov, V. Nanoscale 2CL-20-HMX high explosive cocrystal synthesized by bead milling. *CrystEngComm* **2015**, *17* (22), 4080–4083. <https://doi.org/10.1039/c5ce00489f>.
- (18) Shan, N.; Toda, F.; Jones, W. Mechanochemistry and co-crystal formation: effect of solvent on reaction kinetics. *Chem. Commun. (Cambridge, U. K.)* **2002** (20), 2372–2373. <https://doi.org/10.1039/b207369m>.
- (19) James, S. L.; Adams, C. J.; Bolm, C.; Braga, D.; Collier, P.; Friščić, T.; Grepioni, F.; Harris, K. D. M.; Hyett, G.; Jones, W.; Krebs, A.; Mack, J.; Maini, L.; Orpen, A. G.; Parkin, I. P.; Shearouse, W. C.; Steed, J. W.; Waddell, D. C. Mechanochemistry: opportunities for new and cleaner synthesis. *Chem. Soc. Rev.* **2012**, *41* (1), 413–447. <https://doi.org/10.1039/c1cs15171a>.
- (20) Ling, A. R.; Baker, J. L. XCVI.—Halogen derivatives of quinone. Part III. Derivatives of quinhydrone. *J. Chem. Soc., Trans.* **1893**, *63* (0), 1314–1327. <https://doi.org/10.1039/CT8936301314>.
- (21) Takata, N.; Shiraki, K.; Takano, R.; Hayashi, Y.; Terada, K. Cocrystal Screening of Stanolone and Mestanolone Using Slurry Crystallization. *Cryst. Growth Des.* **2008**, *8* (8), 3032–3037. <https://doi.org/10.1021/cg800156k>.
- (22) Zhang, G. G. Z.; Henry, R. F.; Borchardt, T. B.; Lou, X. Efficient co-crystal screening using solution-mediated phase transformation. *J. Pharm. Sci.* **2007**, *96* (5), 990–995. <https://doi.org/10.1002/jps.20949>.
- (23) Rodríguez-Hornedo, N.; Nehm, S. J.; Seefeldt, K. F.; Pagan-Torres, Y.; Falkiewicz, C. J. Reaction crystallization of pharmaceutical molecular complexes. *Mol. Pharmaceutics* **2006**, *3* (3), 362–367. <https://doi.org/10.1021/mp050099m>.
- (24) Chen, J.; Sarma, B.; Evans, J. M. B.; Myerson, A. S. Pharmaceutical Crystallization. *Cryst. Growth Des.* **2011**, *11* (4), 887–895. <https://doi.org/10.1021/cg101556s>.
- (25) Vehring, R. Pharmaceutical particle engineering via spray drying. *Pharm. Res.* **2008**, *25* (5), 999–1022. <https://doi.org/10.1007/s11095-007-9475-1>.
- (26) Karimi-Jafari, M.; Padrela, L.; Walker, G. M.; Croker, D. M. Creating Cocrystals: A Review of Pharmaceutical Cocrystal Preparation Routes and Applications. *Cryst. Growth Des.* **2018**, *18* (10), 6370–6387. <https://doi.org/10.1021/acs.cgd.8b00933>.
- (27) Alhalaweh, A.; Velaga, S. P. Formation of Cocrystals from Stoichiometric Solutions of Incongruently Saturating Systems by Spray Drying. *Cryst. Growth Des.* **2010**, *10* (8), 3302–3305. <https://doi.org/10.1021/cg100451q>.
- (28) Rodrigues, M.; Baptista, B.; Lopes, J. A.; Sarraguça, M. C. Pharmaceutical cocrystallization techniques. Advances and challenges. *Int. J. Pharm.* **2018**, *547* (1-2), 404–420. <https://doi.org/10.1016/j.ijpharm.2018.06.024>.
- (29) Mullin, J. W. *Crystallization*, 4. rev.; Elsevier professional, 2001.
- (30) Hassan, S.; Adam, F.; Abu Bakar, M. R.; Abdul Mudalip, S. K. Evaluation of solvents' effect on solubility, intermolecular interaction energies and

- habit of ascorbic acid crystals. *J. Saudi Chem. Soc.* **2019**, *23* (2), 239–248. <https://doi.org/10.1016/j.jscs.2018.07.002>.
- (31) Maksimowski, P.; Skupiński, W.; Szczygielska, J. Comparison of the Crystals Obtained by Precipitation of CL-20 with Different Chemical Purity. *Propellants, Explos., Pyrotech.* **2013**, *38* (6), 791–797. <https://doi.org/10.1002/prop.201300064>.
- (32) Borne, L.; Patedoye, J.-C.; Spycykerelle, C. Quantitative Characterization of Internal Defects in RDX Crystals. *Propellants, Explos., Pyrotech.* **1999**, *24* (4), 255–259. [https://doi.org/10.1002/\(SICI\)1521-4087\(199908\)24:4<255:AID-PREP255>3.0.CO;2-2](https://doi.org/10.1002/(SICI)1521-4087(199908)24:4<255:AID-PREP255>3.0.CO;2-2).
- (33) Borne, L.; Patedoye, J.-C.; Saint-Louis, Institut Franco-Allemand De Recherches De. Device for measuring the density of particles by flotation. US 2008/0011079 A1.
- (34) Borne, L.; Ritter, H. HMX as an Impurity in RDX Particles: Effect on the Shock Sensitivity of Formulations Based on RDX. *Propellants, Explos., Pyrotech.* **2006**, *31* (6), 482–489. <https://doi.org/10.1002/prop.200600066>.
- (35) Borne, L.; Beaucamp, A.; Fendeleur, D. Metrology tools for the characterization of explosive crystal properties. In *International Annual Conference of ICT 1998*; V16.
- (36) Doherty, R. M.; Watt, D. S. Relationship Between RDX Properties and Sensitivity. *Propellants, Explos., Pyrotech.* **2008**, *33* (1), 4–13. <https://doi.org/10.1002/prop.200800201>.
- (37) Kim, J.-W.; Kim, J.-K.; Kim, H.-S.; Koo, K.-K. Characterization of Liquid Inclusion of RDX Crystals with a Cooling Crystallization. *Cryst. Growth Des.* **2009**, *9* (6), 2700–2706. <https://doi.org/10.1021/cg801343b>.
- (38) Kim, J.-W.; Kim, J.-K.; Kim, H.-S.; Koo, K.-K. Application of Internal Seeding and Temperature Cycling for Reduction of Liquid Inclusion in the Crystallization of RDX. *Org. Process Res. Dev.* **2011**, *15* (3), 602–609. <https://doi.org/10.1021/op100334y>.
- (39) Blagden, N.; Berry, D. J.; Parkin, A.; Javed, H.; Ibrahim, A.; Gavan, P. T.; Matos, L. L. D.; Seaton, C. C. Current directions in co-crystal growth. *New J. Chem.* **2008**, *32* (10), 1659. <https://doi.org/10.1039/B803866J>.
- (40) Raheem Thayyil, A.; Juturu, T.; Nayak, S.; Kamath, S. Pharmaceutical Co-Crystallization: Regulatory Aspects, Design, Characterization, and Applications. *Adv. Pharm. Bull.* **2020**, *10* (2), 203–212. <https://doi.org/10.34172/apb.2020.024>.
- (41) Bolla, G.; Nangia, A. Pharmaceutical cocrystals: walking the talk. *Chem. Commun.* **2016**, *52* (54), 8342–8360. <https://doi.org/10.1039/c6cc02943d>.
- (42) Blagden, N.; Matas, M. de; Gavan, P. T.; York, P. Crystal engineering of active pharmaceutical ingredients to improve solubility and dissolution rates. *Adv. Drug Delivery Rev.* **2007**, *59* (7), 617–630. <https://doi.org/10.1016/j.addr.2007.05.011>.
- (43) Kalepu, S.; Nekkanti, V. Insoluble drug delivery strategies: review of recent advances and business prospects. *Acta Pharm. Sin. B* **2015**, *5* (5), 442–453. <https://doi.org/10.1016/j.apsb.2015.07.003>.
- (44) Malamataris, M.; Ross, S. A.; Douroumis, D.; Velaga, S. P. Experimental cocrystal screening and solution based scale-up cocrystallization methods. *Adv. Drug Delivery Rev.* **2017**, *117*, 162–177. <https://doi.org/10.1016/j.addr.2017.08.006>.
- (45) Sun, L.; Zhu, W.; Yang, F.; Li, B.; Ren, X.; Zhang, X.; Hu, W. Molecular cocrystals: design, charge-transfer and optoelectronic functionality. *Phys. Chem. Chem. Phys.* **2018**, *20* (9), 6009–6023. <https://doi.org/10.1039/c7cp07167a>.
- (46) Jiang, H.; Hu, W. The Emergence of Organic Single-Crystal Electronics. *Angew. Chem., Int. Ed. Engl.* **2020**, *59* (4), 1408–1428. <https://doi.org/10.1002/anie.201814439>.
- (47) Bennion, J. C. Multicomponent Crystallization of Energetic Materials. thesis, University of Michigan, Michigan, 2017.
- (48) Bolton, O.; Matzger, A. J. Improved stability and smart-material functionality realized in an energetic cocrystal. *Angew. Chem., Int. Ed. Engl.* **2011**, *50* (38), 8960–8963. <https://doi.org/10.1002/anie.201104164>.
- (49) Bennion, J. C.; Siddiqi, Z. R.; Matzger, A. J. A melt castable energetic cocrystal. *Chem. Commun.* **2017**, *53* (45), 6065–6068. <https://doi.org/10.1039/C7CC02636F>.
- (50) Bolton, O.; Simke, L. R.; Pagoria, P. F.; Matzger, A. J. High Power Explosive with Good Sensitivity: A 2:1 Cocrystal of CL-20:HMX. *Cryst. Growth Des.* **2012**, *12* (9), 4311–4314. <https://doi.org/10.1021/cg3010882>.
- (51) An, C.; Li, H.; Ye, B.; Wang, J. Nano-CL-20/HMX Cocrystal Explosive for Significantly Reduced Mechanical Sensitivity. *J. Nanomater.* **2017**, *2017* (5), 1–7. <https://doi.org/10.1155/2017/3791320>.
- (52) Doblaz, D.; Rosenthal, M.; Burghammer, M.; Chernyshov, D.; Spitzer, D.; Ivanov, D. A. Smart Energetic Nanosized Co-Crystals: Exploring Fast Structure Formation and Decomposition. *Cryst. Growth Des.* **2016**, *16* (1), 432–439. <https://doi.org/10.1021/acs.cgd.5b01425>.
- (53) Gao, B.; Wang, D.; Zhang, J.; Hu, Y.; Shen, J.; Wang, J.; Huang, B.; Qiao, Z.; Huang, H.; Nie, F.; Yang, G. Facile, continuous and large-scale synthesis of CL-20/HMX nano co-crystals with high-performance by ultrasonic spray-assisted electrostatic adsorption method. *J. Mater. Chem. A*

- 2014**, *2* (47), 19969–19974. <https://doi.org/10.1039/C4TA04979A>.
- (54) Ghosh, M.; Sikder, A. K.; Banerjee, S.; Gonnade, R. G. Studies on CL-20/HMX (2:1) Cocrystal: A New Preparation Method and Structural and Thermokinetic Analysis. *Cryst. Growth Des.* **2018**, *18* (7), 3781–3793. <https://doi.org/10.1021/acs.cgd.8b00015>.
- (55) Sun, S.; Zhang, H.; Liu, Y.; Xu, J.; Huang, S.; Wang, S.; Sun, J. Transitions from Separately Crystallized CL-20 and HMX to CL-20/HMX Cocrystal Based on Solvent Media. *Cryst. Growth Des.* **2018**, *18* (1), 77–84. <https://doi.org/10.1021/acs.cgd.7b00775>.
- (56) Wu, Z.; Liu, N.; Zheng, W.; Chen, J.; Song, X.; Wang, J.; Cui, C.; Zhang, D.; Zhao, F. Application and Properties of CL-20/HMX Cocrystal in Composite Modified Double Base Propellants. *Propellants, Explos., Pyrotech.* **2020**, *45* (1), 92–100. <https://doi.org/10.1002/prop.201900245>.
- (57) Xue, X.; Ma, Y.; Zeng, Q.; Zhang, C. Initial Decay Mechanism of the Heated CL-20/HMX Cocrystal: A Case of the Cocrystal Mediating the Thermal Stability of the Two Pure Components. *J. Phys. Chem. C* **2017**, *121* (9), 4899–4908. <https://doi.org/10.1021/acs.jpcc.7b00698>.
- (58) Zhang, M.; Tan, Y.; Zhao, X.; Zhang, J.; Huang, S.; Zhai, Z.; Liu, Y.; Yang, Z. Seeking a novel energetic co-crystal strategy through the interfacial self-assembly of CL-20 and HMX nanocrystals. *CrystEngComm* **2020**, *22* (1), 61–67. <https://doi.org/10.1039/c9ce01447k>.
- (59) Zhang, S.; Zhang, J.; Kou, K.; Jia, Q.; Xu, Y.; Zerraza, S.; Liu, N.; Hu, R. Investigation on the dissolution behavior of 2HNIW·HMX co-crystal prepared by a solvent/non-solvent method in N,N-dimethylformamide at T = (298.15–318.15) K. *J. Therm. Anal. Calorim.* **2019**, *135* (6), 3363–3373. <https://doi.org/10.1007/s10973-018-7502-6>.
- (60) Zhou, S.; Pang, A.; Tang, G. Crystal transition behaviors of CL-20 in polyether solid propellants plasticized by nitrate esters containing both HMX and CL-20. *New J. Chem.* **2017**, *41* (24), 15064–15071. <https://doi.org/10.1039/c7nj03309e>.
- (61) Spitzer, D.; Risse, B.; Schnell, F.; Pichot, V.; Klaumünzer, M.; Schaefer, M. R. Continuous engineering of nano-cocrystals for medical and energetic applications. *Sci. Rep.* **2014**, *4*, 6575. <https://doi.org/10.1038/srep06575>.
- (62) Hang, G.-Y.; Yu, W.-L.; Wang, T.; Wang, J.-T.; Li, Z. Theoretical insights into the effects of molar ratios on stabilities, mechanical properties, and detonation performance of CL-20/HMX cocrystal explosives by molecular dynamics simulation. *J. Mol. Model.* **2017**, *23* (1), 30. <https://doi.org/10.1007/s00894-016-3193-8>.
- (63) Liu, Z.; Wu, Q.; Zhu, W.; Xiao, H. Insights into the roles of two constituents CL-20 and HMX in the CL-20:HMX cocrystal at high pressure: a DFT-D study. *RSC Adv.* **2015**, *5* (43), 34216–34225. <https://doi.org/10.1039/c5ra01829c>.
- (64) Sun, T.; Liu, Q.; Xiao, J.; Zhao, F.; Xiao, H. Molecular Dynamics Simulation of Interface Interactions and Mechanical Properties of CL-20/HMX Cocrystal and Its Based PBXs. *Acta Chim. Sinica* **2014**, *72* (9), 1036–1042. <https://doi.org/10.6023/a14040295>.
- (65) Wang, X. J.; Xiao, J. J. Molecular dynamics simulation studies of the ϵ -CL-20/HMX co-crystal-based PBXs with HTPB. *Struct. Chem.* **2017**, *28* (6), 1645–1651. <https://doi.org/10.1007/s11224-017-0930-2>.
- (66) Zhang, Y.; Gou, R.; Chen, Y. Theoretical insight on effect of DMSO-acetonitrile co-solvent on the formation of CL-20/HMX cocrystal explosive. *J. Mol. Model.* **2021**, *27* (1), 8. <https://doi.org/10.1007/s00894-020-04621-z>.
- (67) Klapötke, T. M. *Chemistry of High-Energy Materials*, 5th, revised and expanded Edition; De Gruyter, 2019. <https://doi.org/10.1515/9783110624571>.
- (68) Dallas, J. A.; Raval, S.; Alvarez Gaitan, J. P.; Saydam, S.; Dempster, A. G. The environmental impact of emissions from space launches: A comprehensive review. *J. Cleaner Prod.* **2020**, *255*, 120209. <https://doi.org/10.1016/j.jclepro.2020.120209>.
- (69) Hermann, T. S.; Klapötke, T. M.; Krumm, B.; Stierstorfer, J. The Reagent-depending Nitration of 1,3-Dihydroxyacetone Dimer. *Z. Anorg. Allg. Chem.* **2017**, *643* (2), 149–151. <https://doi.org/10.1002/zaac.201600397>.
- (70) Xie, W.; Zhao, Y.; Zhang, W.; Liu, Y.; Fan, X.; Wang, B.; He, W.; Yan, Q.-L. Sensitivity and Stability Improvements of NEPE Propellants by Inclusion of FOX-7. *Propellants, Explos., Pyrotech.* **2018**, *43* (3), 308–314. <https://doi.org/10.1002/prop.201700251>.
- (71) Nair, U. R.; Gore, G. M.; Sivabalan, R.; Divekar, C. N.; Asthana, S. N.; Singh, H. Studies on Advanced CL-20-Based Composite Modified Double-Base Propellants. *J. Propul. Power* **2004**, *20* (5), 952–955. <https://doi.org/10.2514/1.8761>.
- (72) Chaturvedi, S.; Dave, P. N. Solid propellants: AP/HTPB composite propellants. *Arabian J. Chem.* **2019**, *12* (8), 2061–2068. <https://doi.org/10.1016/j.arabjc.2014.12.033>.
- (73) Sanghavi, R. R.; Khire, V. H.; Chakraborty, T. K.; Singh, A. Studies on RDX Influence on

- Performance Increase of Triple Base Propellants. *Propellants, Explos., Pyrotech.* **2006**, *31* (4), 318–321. <https://doi.org/10.1002/prop.200600044>.
- (74) Dickson, P. M.; Field, J. E. Initiation and propagation in primary explosives. *Proc. R. Soc. Lond. A* **1993**, *441* (1912), 359–375. <https://doi.org/10.1098/rspa.1993.0066>.
- (75) Mehta, N.; Oyler, K.; Cheng, G.; Shah, A.; Marin, J.; Yee, K. Primary Explosives. *Z. Anorg. Allg. Chem.* **2014**, *640* (7), 1309–1313. <https://doi.org/10.1002/zaac.201400053>.
- (76) Fischer, D.; Klapötke, T. M.; Stierstorfer, J. Potassium 1,1'-dinitramino-5,5'-bistetrazolate: a primary explosive with fast detonation and high initiation power. *Angew. Chem., Int. Ed. Engl.* **2014**, *53* (31), 8172–8175. <https://doi.org/10.1002/anie.201404790>.
- (77) Zganec, S.; Bohanek V.; Dobrilovic M. Influence of a Primer on the Velocity of Detonation of ANFO and Heavy ANFO Blends. *Cent. Eur. J. Energ. Mater.* **2016**, *13* (3), 694–704. <https://doi.org/10.22211/cejem/65006>.
- (78) Sellers, E. J. Controlled blasting for enhanced safety. *J. South. Afr. Inst. Min. Metall.* **2011**, *111* (1), 11–16.
- (79) Shadabfar, M.; Gokdemir, C.; Zhou, M.; Kordestani, H.; Muho, E. V. Estimation of Damage Induced by Single-Hole Rock Blasting: A Review on Analytical, Numerical, and Experimental Solutions. *Energies* **2021**, *14* (1), 29. <https://doi.org/10.3390/en14010029>.
- (80) Meyer, R.; Köhler, J.; Homburg, A. *Explosives*; John Wiley & Sons, 2016.
- (81) Gibbs, T. R.; Popolato, A., Eds. *LASL Explosive Property Data*; Univ. of Calif. Pr, 1980.
- (82) Yan, Q.-L.; Zeman, S.; Elbeih, A. Recent advances in thermal analysis and stability evaluation of insensitive plastic bonded explosives (PBXs). *Thermochim. Acta* **2012**, *537*, 1–12. <https://doi.org/10.1016/j.tca.2012.03.009>.
- (83) Gerber, P. Mechanische Eigenschaften von Matrix-Füllstoffsystemen. Thesis, Universität Fridericiana Karlsruhe, Karlsruhe, 2005.
- (84) Fedors, R. F.; Landel, R. F. An Empirical method of estimating the void fraction in mixtures of uniform particles of different size. *Powder Technol* **1979**, *23* (2), 225–231. [https://doi.org/10.1016/0032-5910\(79\)87011-4](https://doi.org/10.1016/0032-5910(79)87011-4).
- (85) Merkus, H. G. *Particle Size Measurements: Fundamentals, Practice, Quality*; Particle Technology Series, Vol. 17; Springer Netherlands, 2009. <https://doi.org/10.1007/978-1-4020-9016-5>.
- (86) U. R. Nair, S. N. Asthana, A. Subhananda Rao, B. R. Gandhe. Advances in High Energy Materials. *Def. Sci. J.* **2010**, *60* (2), 137–151. <https://doi.org/10.14429/dsj.60.327>.
- (87) Quaresma, J.; Deimling, L.; Campos, J.; Mendes, R. Active and Passive Optical Fiber Metrology for Detonation Velocity Measurements. *Propellants, Explos., Pyrotech.* **2020**, *45* (6), 921–931. <https://doi.org/10.1002/prop.201900197>.
- (88) Kamlet, M. J.; Jacobs, S. J. Chemistry of Detonations. I. A Simple Method for Calculating Detonation Properties of C–H–N–O Explosives. *J. Chem. Phys.* **1968**, *48* (1), 23–35. <https://doi.org/10.1063/1.1667908>.
- (89) Politzer, P.; Murray, J. S. High Performance, Low Sensitivity: Conflicting or Compatible? *Propellants, Explos., Pyrotech.* **2016**, *41* (3), 414–425. <https://doi.org/10.1002/prop.201500349>.
- (90) Mathieu, D. RECENT PROGRESS IN THE PREDICTION OF PERFORMANCES, SENSITIVITIES AND THERMAL STABILITIES OF ENERGETIC MATERIALS USING A SEMI-EMPIRICAL PHYSICS-BASED APPROACH. In *48th int. annul Conf. of Fraunhofer ICT 2017*.
- (91) Zeman, S.; Jungová, M. Sensitivity and Performance of Energetic Materials. *Propellants, Explos., Pyrotech.* **2016**, *41* (3), 426–451. <https://doi.org/10.1002/prop.201500351>.
- (92) Kuklja, M. M. Quantum-Chemical Modeling of Energetic Materials. In *Energetic Materials; Advances in Quantum Chemistry*; Elsevier, 2014; pp 71–145. <https://doi.org/10.1016/B978-0-12-800345-9.00003-9>.
- (93) Aluker, E. D.; Krechetov, A. G.; Mitrofanov, A. Y.; Nurmukhametov, D. R.; Kuklja, M. M. Laser Initiation of Energetic Materials: Selective Photoinitiation Regime in Pentaerythritol Tetranitrate. *J. Phys. Chem. C* **2011**, *115* (14), 6893–6901. <https://doi.org/10.1021/jp1089195>.
- (94) Yu, Z.; Bernstein, E. R. Decomposition of pentaerythritol tetranitrate C(CH₂ONO₂)₄ following electronic excitation. *J. Chem. Phys.* **2011**, *135* (15), 154305. <https://doi.org/10.1063/1.3652893>.
- (95) Herrmann, M.; Engel, W.; Eisenreich, N. Thermal analysis of the phases of HMX using X-ray diffraction. *Z. Kristallogr. Cryst. Mater.* **1993**, *204* (1), 121–128. <https://doi.org/10.1524/zkri.1993.204.Part-1.121>.
- (96) Coffey, C. S. Energy localization in rapidly deforming crystalline solids. *Physical review. B Condens. Matter* **1985**, *32* (8), 5335–5341. <https://doi.org/10.1103/physrevb.32.5335>.
- (97) Field, J. E. Hot spot ignition mechanisms for explosives. *Acc. Chem. Res.* **1992**, *25* (11), 489–496. <https://doi.org/10.1021/ar00023a002>.
- (98) Bellitto, V. J.; Melnik, M. I. Surface defects and their role in the shock sensitivity of

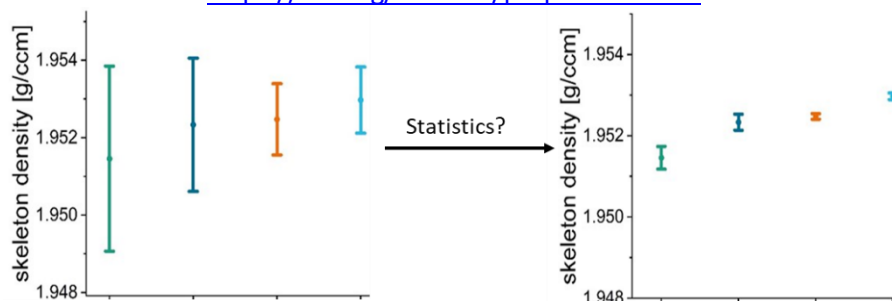
- cyclotrimethylene-trinitramine. *Appl. Surf. Sci.* **2010**, 256 (11), 3478–3481. <https://doi.org/10.1016/j.apsusc.2009.12.060>.
- (99) Czerski, H.; Proud, W. G. Relationship between the morphology of granular cyclotrimethylene-trinitramine and its shock sensitivity. *J. Appl. Phys.* **2007**, 102 (11), 113515. <https://doi.org/10.1063/1.2818106>.
- (100) Borne, L. Influence of intragranular cavities of RDX particle batches on the sensitivity of cast wax bonded explosives. In *Tenth Symposium (International) on Detonation*, 1993; 286-293.
- (101) Dear, J. P.; Field, J. E.; Walton, A. J. Gas compression and jet formation in cavities collapsed by a shock wave. *Nature* **1988**, 332 (6164), 505–508. <https://doi.org/10.1038/332505a0>.
- (102) Lindstrom, I. E. Planar Shock Initiation of Porous Tetryl. *J. Appl. Phys.* **1970**, 41 (1), 337–350. <https://doi.org/10.1063/1.1658345>.
- (103) Borne, L.; Patedoye, J.-C. Crystalline explosive form and preparation process thereof. 2 426 755.
- (104) Maillet, J.-B. MD Simulations of Hot Spots. In *Shock Compression of Condensed Matter 2003*; pp 379–384. <https://doi.org/10.1063/1.1780258>.
- (105) Sikder, A. K.; Sikder, N. A review of advanced high performance, insensitive and thermally stable energetic materials emerging for military and space applications. *J. Hazard. Mater.* **2004**, 112 (1-2), 1–15. <https://doi.org/10.1016/j.jhazmat.2004.04.003>.
- (106) Powell, I. J. Insensitive Munitions – Design Principles and Technology Developments. *Propellants, Explos., Pyrotech.* **2016**, 41 (3), 409–413. <https://doi.org/10.1002/prep.201500341>.
- (107) Nair, U. R.; Sivabalan, R.; Gore, G. M.; Geetha, M.; Asthana, S. N.; Singh, H. Hexanitrohexaazaisowurtzitane (CL-20) and CL-20-based formulations (review). *Combust., Explos. and Shock Waves* **2005**, 41 (2), 121–132. <https://doi.org/10.1007/s10573-005-0014-2>.
- (108) Johnson, N. C. CL-20 sensitivity round robin. *Naval Surface Warfare Center* **2003**.
- (109) Mathieu, J.; Stucki, H. Military High Explosives. *CHIMIA* **2004**, 58 (6), 383–389. <https://doi.org/10.2533/000942904777677669>.
- (110) Goede, P.; Latypov, N. V.; Östmark, H. Fourier Transform Raman Spectroscopy of the Four Crystallographic Phases of α, β, γ and ϵ 2,4,6,8,10,12-Hexanitro-2,4,6,8,10,12-hexaazatetracyclo[5.5.0.0.5,9.0.3,11]dodecane (HNIW, CL-20). *Propellants, Explos., Pyrotech.* **2004**, 29 (4), 205–208. <https://doi.org/10.1002/prep.200400047>.
- (111) Foltz, M. F.; Coon, C. L.; Garcia, F.; Nichols, A. L. The thermal stability of the polymorphs of hexanitrohexaazaisowurtzitane, part II. *Propellants, Explos., Pyrotech.* **1994**, 19 (3), 133–144. <https://doi.org/10.1002/prep.19940190305>.
- (112) Saleemi, A. N.; Steele, G.; Pedge, N. I.; Freeman, A.; Nagy, Z. K. Enhancing crystalline properties of a cardiovascular active pharmaceutical ingredient using a process analytical technology based crystallization feedback control strategy. *Int. J. Pharm.* **2012**, 430 (1-2), 56–64. <https://doi.org/10.1016/j.ijpharm.2012.03.029>.
- (113) Simone, E.; Zhang, W.; Nagy, Z. K. Analysis of the crystallization process of a biopharmaceutical compound in the presence of impurities using process analytical technology (PAT) tools. *J. Chem. Technol. Biotechnol.* **2016**, 91 (5), 1461–1470. <https://doi.org/10.1002/jctb.4743>.
- (114) Douroumis, D.; Ross, S. A.; Nokhodchi, A. Advanced methodologies for cocrystal synthesis. *Adv. Drug Delivery Rev.* **2017**, 117, 178–195. <https://doi.org/10.1016/j.addr.2017.07.008>.
- (115) Roy, P.; Ghosh, A. Progress on cocrystallization of poorly soluble NME's in the last decade. *CrystEngComm* **2020**, 22 (42), 6958–6974. <https://doi.org/10.1039/d0ce01276a>.
- (116) Imamura, M.; Nakashini, K.; Shiraki, R.; Onda, K.; Sasuga, D.; Yuda, M. COCRYSTAL OF C-GLYCOSIDE DERIVATIVE AND L-PROLINE. US 8,097,592 B2.
- (117) Bajwa, J. S.; La Cruz, M. de; Dodd, S. K.; Waykole, L. M.; Wu, R. Salts of N-[6-(cis-2,6-dimethylmorpholin-4-yl)pyridin-3-yl]-2-methyl-4'-(trifluoromethoxy)[1,1'-biphenyl]-3-carboxamide. WO 2010033481.
- (118) Feng, L.; Godtfredsen, S. E.; Karpinski, P.; Sutton, P. A.; Prashad, M.; Girgis, M. J.; Hu, B.; Liu, Y. Pharmaceutical combinations of an angiotensin receptor antagonist and a neutral endopeptidase inhibitor for the treatment of cardiovascular and/or renal diseases. WO 2007056546.
- (119) Ramkinkar, S.; Bhogala, B. K. R.; Khanduri, C. H. ERTUGLIFLOZIN CO-CRYSTALS AND PROCESS FOR THEIR PREPARATION. WO 2016-IB53042.
- (120) Ciszewski, L.; La Cruz, M. de; Karpinski, P. H.; Mutz, M.; Riegert, C.; Vogel, C.; Schneeberger, R. HEMIFUMARATE SALT OF 1- [4- [1- (4 -CYCLOHEXYL-3 -TRIFLUOROMETHYL-BENZYLOXYIMINO) -ETHYL] -2 -ETHYL-BENZYL] -A ZETIDINE-3-CARBOXYLIC ACID. WO 2010080409.
- (121) Student. The Probable Error of a Mean. *Biometrika* **1908**, 6 (1), 1–25. <https://doi.org/10.2307/2331554>.

5 Quality Assessment of the Cocystal

5.1 High-Precision Density Measurements of Energetic Materials for Quality Assessment

Dirk Herrmannsdörfer, Thomas M. Klapötke
Propellants, Explosives, Pyrotechnics **2021**, *46*, 413-427

<https://doi.org/10.1002/prop.202000272>



The following modifications were made to this paper:

- The density measurement data was not included in the supporting information section, because it is 150 pages long.
- Temperatures were changed from °C to K to unitise the style in this work

Abstract: Even though helium pycnometry is considered a very precise method of density determination, its use to analyse factors influencing crystal quality (e.g. solvent inclusions, amorphous states, crystal defects...) is limited due to the unknown inherent accuracy of the method. Previous studies have attempted to identify the best possible accuracy of helium pycnometry. However, no robust method has been proposed to validate even the precision obtained. This means that the often occurring, seemingly random density deviations have never been satisfactorily explained. In this study the influencing factors on density measurements of the CL-20/HMX cocrystal and phase stabilised ammonium nitrate carried out with an AccuPyc 1340 TEC were quantified and a robust method of data analysis was developed to judge with certainty the quality and significance of the data obtained. This study shows that statistical tests such as the t-test and ANOVA cannot be utilised to differentiate between samples or repeat measurements, even though the density data points exhibit a normal distribution. By utilising confidence intervals and quantifying the three major sources of error (sampling error, change in barometric pressure during the measurement, and weight in error), a repeatability of 0.015% was achieved and a method was developed that enables differentiation between samples with a certainty as good as 0.05%.

1 Introduction

The skeleton density of solids is a useful tool in chemical industry and research for the detection of, for example, processing efficacy [1], composition [2], or for characterisation [3]. Specifically in the field of energetic materials, the density can be utilised to calculate the detonation velocity [4], assess the explosive's quality [5], or the success of the generation of a pressed composition.

The skeleton density is most commonly obtained by gas pycnometry which is considered to provide the closest approximation of the skeleton density.[6] Of the available density determination techniques of solids, gas pycnometry is one of the most user friendly due to the availability of easy to operate consumer grade devices lending it an air of simplicity that invites people to regard gas pycnometry as a standard analysis method. The high precision of pycnometry is strongly dependent on the measurement conditions as has been shown previously.[6] And even under optimised conditions, errors to the measurements remain and in-depth analysis is required to judge with confidence whether a repeat measurement is valid and whether one sample is significantly denser than another. Viana *et al.* [6] have published what is probably the most in-depth analysis of the influences on and optimal conditions for pycnometric density determination. Since then, some studies have used ANOVA [7] or confidence intervals [3] to analyse their results, but no fundamental analysis of the statistical character of the pycnometric measurement and the impact of the varying influences on the measurement have been published. So, to this date it is unexplored what the true accuracy of a pycnometric measurement is and whether the nature of the obtained data points even allows for the use of statistical tests. Here we expand on some of the

previously reported challenges to a successful density measurement and the steps to optimise it and present additional challenges and the necessary data analysis of the results. Viana *et al.* [6] concerned themselves mostly with the quest for maximum accuracy of the data and closed their paper with the assessment that for the differentiation of products of different crystallinity, hydration, and polymorphic form very close density values must be compared and that this comparison is greatly influenced by the calibration of the device. Therefore, the first step in optimising gas pycnometric measurements on the quest for highest discriminatory power of samples must be to maximise the precision of repeat measurements but leave reproducibility for future studies. This study aims to explore the precision limits of helium pycnometry by investigating which errors dominate the density measurement, how to minimise these, and whether statistical test such as the t-test and ANOVA are applicable to optimised pycnometric density measurements to allow for statistically backed discrimination between samples under repeat conditions. If sufficient precision is achieved, helium pycnometry can be applicable for the quality assessment of the CL-20/HMX cocrystal discussed in this paper. The solvent content of the cocrystals, which depends on the crystallisation technique, ranges from traces of solvent (C3) through to 0.07 % (C2) and up to 0.3 % (C1), which correlates with an expected density difference of 0.0018 g/cm³ for C3-C2 and 0.0097 g/cm³ for C3-C1. While it is obvious from literature data that a difference of 0.0097 g/cm³ is detectable, it is unclear whether 0.0018 g/cm³ or even smaller differences can be resolved. Detection of such differences would make it possible to utilise gas pycnometry as a valuable tool for quality assessment of energetic materials of highest quality, a role that was formerly reserved for more sophisticated but hard to

operate and time consuming methods such as density flotation.[8]

2 Material and Methods

Sample mass was determined using a Kern 770 analytical balance (accuracy 0.1 mg).

The pycnometer was operated and reports compiled utilising the AccuPyc 1340 Windows Software.

Density measurements were carried out using a micromeritics AccuPyc 1340 TEC 10 cm³. This configuration includes a temperature-controlled Peltier element. The heating/cooling element was set to 292.95 K for all measurements to achieve an average chamber temperature close to 293.15 K. (the chamber temperature can vary depending on the room temperature by about 0.4 K for the measurements presented here). Two chamber inserts can be utilised to reduce the chamber volume from 10 cm³ to 3.5 cm³ and 1 cm³, respectively. Sample cups were fitted with AccuPyc filter caps (10 µm pore diameter) to prevent the fluidation and discharge of sample material during measurements. The basic measurement principal is described elsewhere. [6, 9] He 5.0 was used as measurement gas. Between 1 and 100 purging cycles were carried out before measurement (see supporting information for specifics on each measurement). For most measurements a fixed equilibration time of 60 seconds was utilised.

All utilised statistical methods have been carried out using OriginPro version 2019 9.6.0.172, OriginLab Corporation, Northampton, MA, USA.

ε CL-20 (lot number 573S98) was obtained from SNPE. The chemical purity has been determined via ¹H-NMR and HPLC to be 98.3 and 99.4 %, respectively. Further analysis details are found in the supporting information. β HMX (lot number NSI 00E 000 E004) was purchased from Chemring Nobel. The chemical purity has been determined via ¹H-NMR and HPLC to be 98.7 and 99.3 %, respectively. Further analysis details are found in the supporting information. Ammonium nitrate 99.86% (LA 84802524) was purchased from Borealis Agrolinz Melamine GmbH. The Ni and NH₃ content of the PSAN was 2.5 % and 0.9 %, respectively.

3 Results and Discussion

In the following paragraph challenges to an accurate density measurement of energetic materials and ways to face them are presented. This list is likely not exhaustive, but it is based on the findings of Viana *et al.* [6], the ISO12154, [9]

and the result of the measurements carried out of the abovementioned materials. In all likelihood additional challenges might occur with different materials such as for example extremely porous or amorphous substances. It is important to note that the aim of this study is to maximise the precision of the measurements to push the limit of significant comparison of samples as far as possible. Following the terminology of DIN ISO 2725 [10], if

$$y = m + B + e$$

with y being the measurement result, m the calculated mean, B the laboratory bias under repeatability conditions and e the random error occurring in every measurement under repeatability conditions, most of the optimisations presented here aim to minimise e . Minimising e maximises the precision of the measurements, but has only a partial influence on the accuracy of y . Therefore, samples can only be compared under repeatability conditions i.e. under conditions for which B is constant. It is obvious, that an approach that also minimises B would be preferable. As, however, for example the varying calibration standard volumes in the study of Viana *et al.* [6] have shown, some factors of B are possibly uncontrollable and a statistically sound verification of the accuracy is far beyond the scope of this study.

3.1 Sample Volume

Chamber and reference volume of gas pycnometers are typically calibrated using calibration standards in form of metal spheres. Maximum precision and trueness are achieved when the sample volume is identical with the volume of the calibration standard. Oftentimes, however, the bulk density of a material is significantly lower than its skeleton density. Typically, in these experiments a sample volume of less than half of the calibration standard volume was achieved by filling the sample chamber up to 75% (as specified by the manufacturer) and without compaction of the solid. To be able to estimate the resulting increase in standard deviation the calibration standard of the 3.5 cm³ cell (measurement **K1**) and the calibration standard of the 1 cm³ cell (measurement **K2**) were measured in the 3.5 cm³ cell. Both measurements achieved an identical volume standard deviation of 0.0004 cm³; the density standard deviation of the smaller calibration standard was, however, over three times the standard deviation of the larger calibration standard (0.0088 cm³ and 0.0023 cm³, respectively). This factor 3.8 difference in density standard deviation is the result of the factor 3.4

difference in volume between the standards. One can, therefore, assume that by only obtaining half the calibration volume the standard deviation of the experiments is twice as high as necessary. The achievable sample volume can be increased by compacting the sample (increasing the bulk density) in the process of weighing in and by filling the sample cup higher than the recommended 75% filling height. The recommendation of 75% percent filling height is most likely the attempt of the manufacturer to prevent liability in case of product discharge from the sample cup, as the likelihood of such an occurrence increases with increasing filling height. “Overfilling” the sample cup should, therefore, only be considered if the sample material is certain to not be fluidised by the pressure drop during measurement and if the material is coarse and dense enough to not be carried along by the gas flow. Another very important aspect of the sample volume is that the measured sample density is dependent on the sample volume. Multiple studies [6, 7, 11] show, that with decreasing filling ratio the measured sample density decreases. This trend is shown exemplary in Figure 1 for the measurement of glass beads carried out by micromeritics. [11] Note that the deviation of the obtained density value from the maximum value is larger than the determined density repeatability for a cup filling percentage of under 40% in this test. Furthermore, it is important to note that 100% of cup filled means no more glass beads could fit in the sample cup, but even then, the sample fills only 47 cm³ of the 100 cm³ sample cup. Based on the trend in Figure 1 one can assume, that at least for glass beads the sample volume has a small influence on the obtained density if the sample volume is more than half of the sample cup volume. For maximum comparability it is still advisable to match the

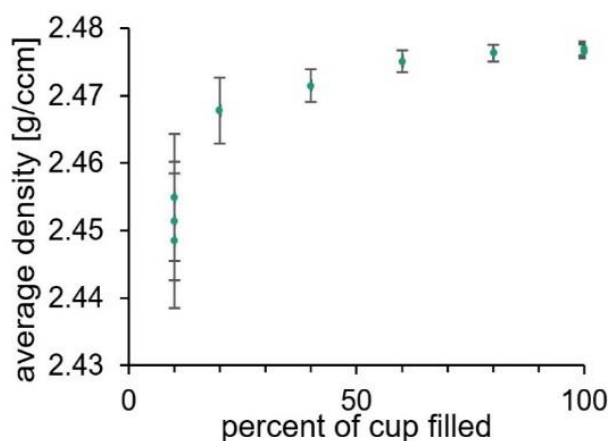


Figure 1: Measured density of glass beads dependent on the percentage of fill of the sample chamber.

weight in as much as possible on repeat measurements and sample comparisons.

3.2 Chamber Volume

It is essential for the density determination that the measurement chamber volume is constant. Many factors can contribute to a change in chamber volume. In some gas pycnometers the sample chamber lid does not exhibit a defined stop. Here it is important to always apply the same torque when closing the lid. Other pycnometers require the application of vacuum grease to the seal. Here a calibration of the sample chamber volume after application should be carried out to accommodate for the change in grease volume. Furthermore, grease must be applied sparingly even when recalibration is carried out to prevent changing chamber volumes over time as the grease might be squeezed out of the chamber over the course of measurements. Other factors can contribute to a change in chamber volume such as scratches in the sample cup or sample remains in or on the sample cup and chamber. Residues in the mg-scale can already be enough to significantly alter the obtained density value. Therefore, manipulation of the sample cup should always be carried out wearing gloves to prevent water and fat deposition, and thorough cleaning should succeed every measurement.

3.3 Calibration

Chamber and reference volume calibration should be carried out with the same level of care as sample measurements. This includes to use the same number of data points (if possible by the programming of the pycnometer) as this increases the quality of the calibration. A calibration should always be verified upon completion. One easy method is to measure the calibration standard. By inserting the standard's volume as the sample mass, a value of 1 g/cm³ is received that is henceforth called “density”. If the determined “density” diverges significantly from 1.0000 g/cm³, recalibration is necessary. Typically, a “density” in the region of 0.9999 and 1.0001 g/cm³ is achievable. An even better validation of the calibration is to utilise an auxiliary volume standard because if the calibration standard itself is damaged or altered, validation with it will still result in seemingly good values. As Viana *et al.* [6] have shown, their calibration standards of the three sample chamber volumes exhibited a correlated increase and decrease in volume over a 6-month period. As it is unlikely that the calibration

standards would concerted increase and decrease in volume (except for temperature effects) it is more likely that changes in the pycnometer itself or in the surrounding conditions are responsible. The only true validation of a density value can, therefore, only be obtained by measuring the same sample in different pycnometers.

3.4 Leak Tightness of the Helium Line

Even though for many substances it is almost irrelevant whether helium or nitrogen is used as measurement gas, it can be very important to ensure that the helium line is free of leakages. This can be most efficiently carried out by utilising specialised portable helium leak detectors. If a helium leak occurs in a non-permanently pressurised part of the helium line, the line will fill with air that is subsequently flushed through the sample chamber in the pycnometer. This can be detrimental if the sample is hygroscopic or reactive towards oxygen or water.

3.5 Room Climate

The room temperature can have a significant impact on the quality of a pycnometric measurement, as the density of most materials is temperature dependent. Ideally a measuring room should be conditioned to 293.15 K and a pycnometer with active temperature control should be employed. If no climatisation is available, varying room temperature in general does not exclude the possibility of high precision measurements. Even under room temperature deviations of 10 K over the course of 24 h, stable density measurements are possible under the condition that the pycnometer is equipped with a heating/cooling device. In Figure 2 the measured "density" of the measurement **K3** of the calibration standard of the 3.5 cm³ cell and the chamber temperature are displayed over the number of data point. The temperature trend is the result of the decreasing room temperature overnight, and the increase in temperature in the morning at around data point 400 was caused by the automated room heating. Even though the room temperature increased by around 5 K over the course of minutes, no influence on the measurement is apparent (the determined "density" of 0.9997 g/cm³ indicates that a calibration was necessary for following precision measurements).

The other influence of temperature - the decrease of material density with increasing temperature - appears to be too weak for the calibration standard to be noticeable here.

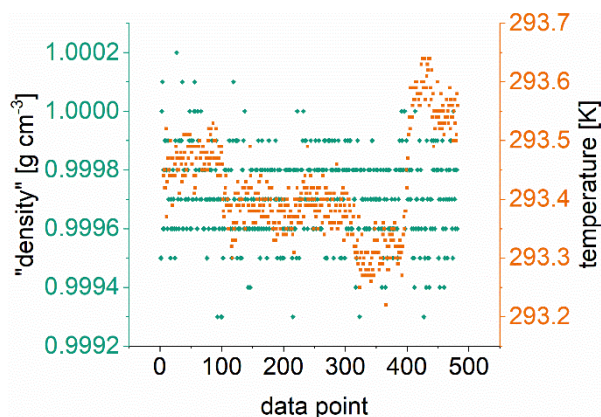


Figure 2: Overlay of the temperature data points (orange squares) and the "density" data points of **K3**.

However, the measurement temperature is not inconsequential. For the cocrystal discussed later, the thermal expansion can be estimated from the cryogenic crystal density of 2.001 g/cm³ at 95 K [12] and the room temperature density of 1.957 g/cm³. By assuming a constant expansion coefficient in this temperature frame, a 1 K temperature difference should amount for a density difference of around 0.0002 g/cm³ which can be quite significant.

3.6 Sample Dryness

Of all the abovementioned factors none is as impactful on the quality of the received data as the sample's water content and none is as counterintuitive. With the exception of the calibration standards all measured samples discussed in this paper exhibited a decrease in measured density over the course of 10 to 400 data points. And while it appears obvious that evaporating water could not be responsible, because water evaporation should decrease the sample volume and, therefore, increase the density over time, the opposite is the case. [6, 7, 9, 13–15] As the pressurised helium is virtually free of water the partial pressure of water is also zero. As a result, even strongly hygroscopic material in most cases will release water if no special care has been taken to ensure sample dryness. The continuous evaporation of water will increase p_1 (pressure after charging the sample chamber with helium) and p_2 (pressure after equilibration of the sample chamber pressure and reference chamber pressure) values. Even though both values are increased, only the increase in p_2 influences the volume determination, as an increase in p_1 only offsets the system pressure. An increased p_2 due to evaporating water during the equilibration period seemingly indicates a lower sample volume and, therefore, a higher sample density. It is for this reason, even though the sample loses volume in form of water, the measured sample volume

increases with each data point, as less and less water evaporates over time. The effect of the evaporated water on the measurement is magnitudes stronger than the effect of the loss of condensed water in the sample, because the volume of the gaseous water is several hundred times larger. Kikuchi *et al.* [15] have written a very comprehensive derivation of the density error due to water evaporation.

Insufficient sample dryness can result in multiple different implications for the result of a density measurement. A too wet sample might not be measurable at all, as too much water evaporates constantly and the equilibrium condition is not met within the permitted time frame. A wet but hygroscopic sample might lose water slowly enough that the equilibration condition is met, but does not reach a constant volume for hundreds of purging/measuring cycles [13] and the obtained density in the end is too high, as the sample has lost mass (and, therefore, volume) since it has been weighed in (this can be remedied by additional weighing of the sample after the density measurement and recalculation of the density based on the new sample mass [9]). Even a non-hygroscopic sample might have substantial amounts of water adsorbed especially if the crystalline structure exhibits cracks or pores. In the following, the density trend over time is discussed for two material systems.

3.6.1 Phase Stabilised Ammonium Nitrate (PSAN)

Ammonium nitrate is hygroscopic. PSAN [16] typically exhibits a water content of around 0.2% after processing. Sample drying in vacuum, however, could be detrimental to the stability of the instituted amine complex. For a good measurement it is, therefore, required to increase the number of purging cycles to eliminate the initial drop in density. Typical measurements of PSAN are displayed in Figure 3. The blue squares (**PSAN1**) and orange triangles (**PSAN2**) data points are two consecutively carried out density measurements on the same sample. The green circles (**PSAN3**) and teal rhombs (**PSAN4**) data points are two consecutively carried out density measurements of a sample of a different PSAN batch. The data gap between measurements is the representation of the ten purging cycles carried out at the beginning of each measurement. Several findings can be derived from the data. The density drift for both samples is around 0.02 g/cm³ with 20% deviation between the two. The

reduction in density appears to exhibit an exponential decline which is congruent with the idea of evaporating water. As a result, no clear endpoint to the drift can be defined. For efficiency reasons it was stated that 60 flushing cycles are sufficient to reduce the density drift to an acceptable level, even though a weak drift appears to be present in the data points of **PSAN4** even after 100 data points. While the **PSAN1** data points exhibit an obvious drift during the whole measurement, the **PSAN3** data points do not. Especially the first 10 data points might mislead an operator to assume density constancy, even though a strong drift is underlying that is just randomly obscured in this case. This highlights the necessity to run measurements of high data point counts when a new material is analysed to end up with a more in-depth insight in the response the material exhibits to the measurement.

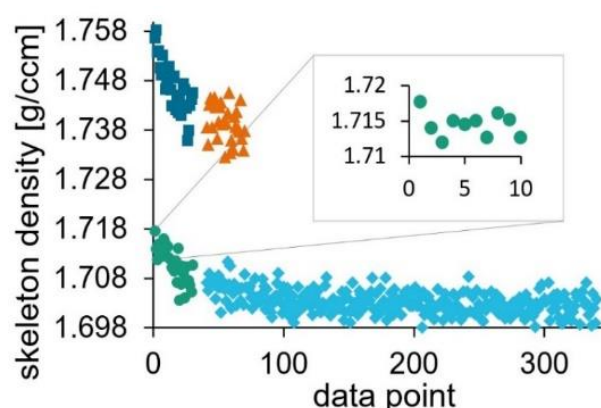


Figure 3: Visualisation of the initial density drift of PSAN. **PSAN2** (orange triangles) is the direct repeat measurement of **PSAN1** (blue squares). **PSAN4** (teal rhombs) is the direct repeat measurement of **PSAN3** (green). The gaps are caused by the 10 flushing cycles before **PSAN2** and **PSAN4**. The first 10 data points of **PSAN3** are magnified.

3.6.2 CL-20/HMX Cocrystal

HMX and CL-20 are non-hygroscopic, insoluble in water, and not easily wettable by water. The cocrystal samples discussed in this paper have been prepared following the previously published procedures. [17, 18] Cocrystal 1 (C1, Figure 6) was obtained by slow phase transformation at 293.15 K in 2-propanole, while cocrystal 2 (C2, Figure 7) was obtained by reaction cocrystallization at 333.15 K in acetonitrile, and cocrystal 3 (C3, Figure 8) was obtained by refined antisolvent crystallisation. The water contents are 0.035 %, 0.028 % and less than 0.02 % for C1, C2 and C3, respectively. Results of the density measurements of the cocrystal samples

C1.1 and **C2.1** are displayed in Figure 4. **C1.1** exhibits a strong density drift (0.008 g/cm^3), while **C2.1** exhibits a drift of 0.0028 g/cm^3 . The drift of **C1.1** seems to persist until around data point 300 which is even longer than the drift observed in PSAN while the drift of **C2** only persists for about 50 data points. The difference in behaviour between **C1.1** and **C2.1** lies most likely in the partially porous nature of **C1.1** as can be seen in Figure 6, while **C2.1** exhibits mostly internal defects and some cracks that propagate through the material. In theory, the drift in density could also be caused by other factors. For example, for **C1.1** a vestige of 2-propanol from the crystallisation process could also explain the behaviour. However, a second density measurement carried out after two days on the very same sample material exhibited again a density drift of 0.004 g/cm^3 which indicates that even though the material is non-hygroscopic it appears to collect water from the air most likely

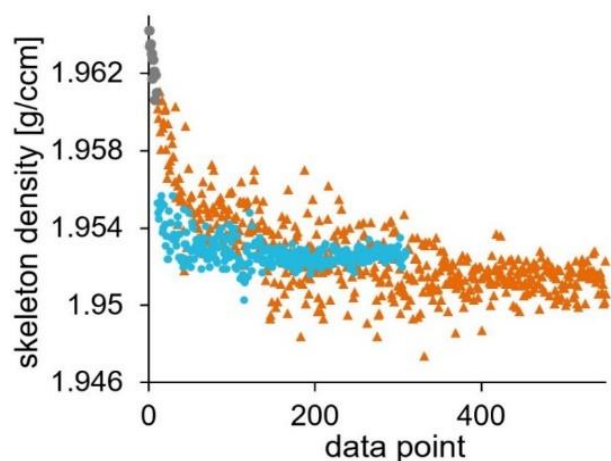


Figure 4: Visualisation of the initial density drift of **C1.1**(orange triangles) and **C2.1**(light blue circles). The first nine data points of **C1.1** are greyed to aid in the comparison of the drift, as **C2.1** was preceded by 10 flushing cycles and **C1.1** of only one.

because of its porous nature.

The data points of **C2.1** start at 10 and the first 10 data points of **C1.1** are displayed in grey in Figure 4 to accentuate that the measurement of **C1.1** was carried out with one flushing cycle, while the measurement of **C2.1** was carried out with ten flushing cycles and to provide better comparability between the two measurements. The reduction of flushing cycles can provide insight into the sample behaviour if the time allows for it, as flushing cycles are around five to ten times faster than measuring cycles. The insight lower flushing cycle numbers can provide is best seen in Figure 5 where the first 150 data points of the measurements of **C1.1** and **C3.1** are displayed.

C3.1 exhibits a substantial drop in density of 0.024 g/cm^3 for the first 10 measurements that is

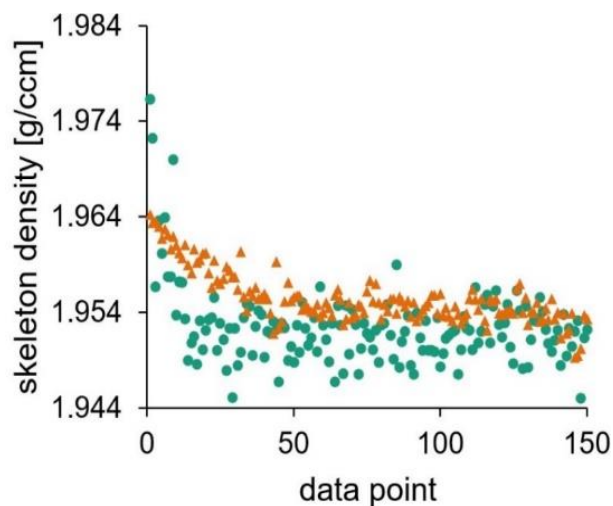


Figure 5: Visualisation of the initial density drift of **C1.1**(orange triangles) and **C3.1**(green).

three times larger than even the drop of **C1.1**. Even with only ten flushing cycles this drop would have been obscured and the sample would have been declared free of any drift. Because **C3.1** is virtually free of defects especially on the surface, the most likely explanation for the sample's density drift is traces of water present as a thin film on the surface

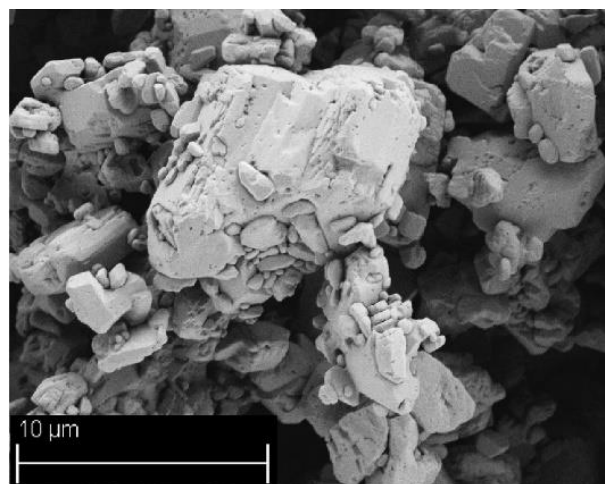


Figure 6: REM image of cocystal 1.

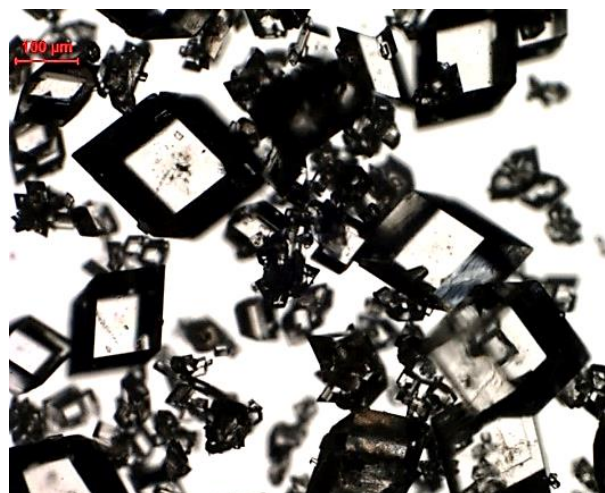


Figure 7: Macroscopic image of typical crystals of cocystal 2.



Figure 8: Macroscopic image of cocystal 3.

of the crystals and the sample cup. The comparably high rate of density reduction during measurement is most likely also the result of the smoothness of the crystal surfaces of **C3.1** compared to **C2.1** and **C1.1**.

These three different drifts that C1, C2, and C3 exhibited, even though they are the same base material, highlight how important it is to adapt the measuring parameters to the sample if highly time efficient measurements are needed. If time is not of the essence, it always pays to increase the number of data points to increase the information content of the data. A reduction of flushing cycles can also serve to increase the information content, as it provides data about the strength of the initial drift of the sample.

3.7 Data Analysis

All the abovementioned strategies aim to improve the quality of the density measurement. In themselves they, however, do not provide certainty that the obtained data is correct. "Correct" is in any event the wrong terminology, as it is obvious from the graphs above that every measurement possesses varying degrees of uncertainty. Aside from the standard deviation of the individual measurement additional errors that affect the repeatability of the measurement can occur. One tends to meet this uncertainty by duplicate measurements and comparison of the obtained average density. A true duplication at this point involves removing the sample from the sample cup, cleaning of the sample cup, and to weigh in the sample anew. Only in doing so the errors stemming from sample inhomogeneities, weight in errors, changes in sample chamber volume, etc. can be statistically comprised. A better way than to simply compare the two received density values is to carry out a true statistical analysis. Thereby one is able to determine whether a difference in the received density averages is likely caused by random

sampling error or an underlying additional source of error. Furthermore, one is able to tell whether the amount of data points even allows for such a differentiation. For a duplicate measurement of one sample a t-test [19] is a fitting method, while for the comparison of multiple samples ANOVA with an appropriate post-hoc method is suitable. While non-parametric methods are also an option, in case of pycnometry, however, all the special requirements that parametric methods demand from the sample data can be met. In the following paragraphs the data requirements for statistical analysis are discussed.

3.7.1 Test for Outliers

It is proven that ANOVA is affected by extreme outliers [20]. The removal of these outliers should always be considered in a proper density measurement, as no reasonable explanation exists why these values should occur aside from freak measurement error. If, however, a multitude of such outliers occur, this might indicate an underlying issue of the measurement. The first three measurements undertaken with the Accupyc II TEC utilised in this study on spheriglass A2227 exhibited an almost bimodal density

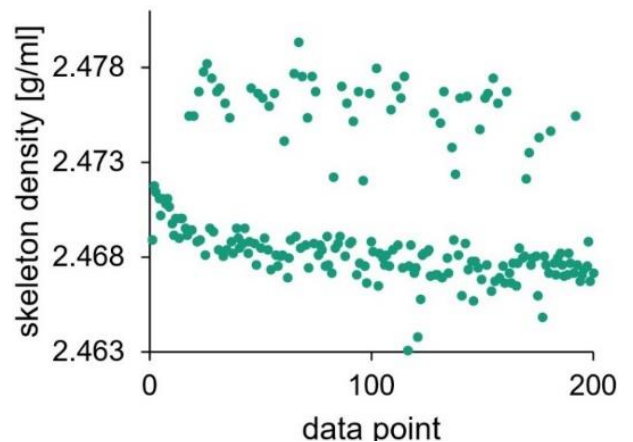


Figure 9: The bimodal distribution of the density measurement of spheriglass A2227 is shown.

distribution as seen in Figure 9.

This effect occurred for three measurements and then disappeared for the following measurements. This was not further studied, but might be related to the gas inclusions close to the surface of the glass beads. Obviously, these extreme outliers are too numerous to be considered freak occurrences and should not simply be removed. The general exclusion of moderate outliers in contrast to extreme outliers is also debatable. A fast and clear visual representation of the data to judge outliers in the data is the box plot. [21] In Figure 10 right, the volume data of **K3** on the left is represented by

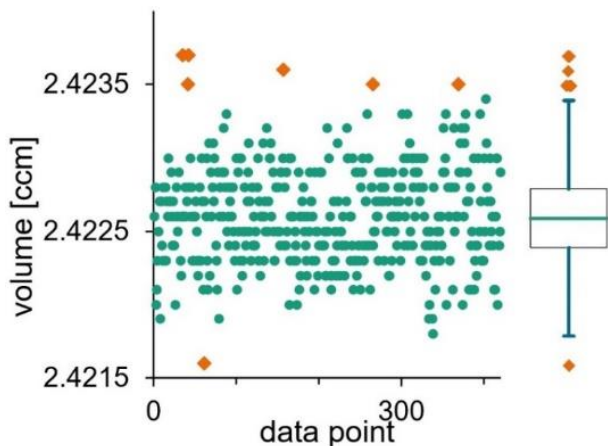


Figure 10: Volume data points of **K3** on the left and the corresponding box plot on the right. Outliers are depicted as orange rhombs.

a box plot. The green horizontal line represents the median of the data, the box represents the position of 50% of the data, the blue so-called whiskers indicate the data that lie within 1.5 times the box height (interquartile range IQR), and the orange rhombs visualise the mild outliers i.e. outliers that lie within the region of 1.5 IQR to 3 IQR. Because the reason of the appearance of these mild outliers is unclear, general removal of the data points might be ill advised. In chapter 3.7.3, however, it is shown that the removal of these mild outliers can significantly improve the normality of the data. Further study is required to develop a general procedure concerning mild outliers.

Based on the gathered data it appears prudent to remove extreme outliers if they appear as singular freak appearances, but to reevaluate the entire measurement if a multitude of extreme outliers occur and to remove mild outliers if appropriate.

3.7.2 Underlying Trends

One prerequisite for any meaningful data analysis in this context is that the data points are free of any permanent drift. Due to the differences in sample densities, for best comparability the volume data drift is regarded. Any meaningful drift analysis requires at least around 100 data points. Seven measurements of the cocrystal batches **C2** and the calibration standard of at least 150 data points were, therefore, analysed. Most measurements exhibit a volume drift of around $1 \cdot 10^{-6} \text{ cm}^3/\text{data point}$ and only two of eight measurements exhibit a drift of around $1 \cdot 10^{-7} \text{ cm}^3/\text{data point}$ (**C2.3, K3**). The volume drift appears to be mostly independent of the measured material, as the smallest ($8 \cdot 10^{-8} \text{ cm}^3/\text{data point}$, **C2.3**) and second largest ($2.7 \cdot 10^{-6} \text{ cm}^3/\text{data point}$, **C2.1**) volume drift was obtained from the same sample in different runs

and the calibration standard achieved an only marginally better drift than average ($2.6 \cdot 10^{-7} \text{ cm}^3/\text{data point}$). Of the seven measurements two exhibited a linear increase in sample volume (**C2.5, K3**), three a linear decline (**C2.1, C2.2, C2.3**), and two measurements showed a change in the algebraic sign of the volume drift (**C2.4, C2.6**). This inhomogeneous behaviour indicates that the volume drift is not a characteristic of the measured sample, but of the pycnometer itself. It is important to determine whether the monotonically decreasing and increasing volume drifts are indefinitely ongoing. Because if they were, this would render such density measurement meaningless, as the achieved density would be dependent on the length of the measurement. To investigate this, a 900 data point (**C3.3**) and a 600 data point (**C3.4**) measurement of **C3** were carried out. These measurements took 45 and 31 hours, respectively. It was thus possible to investigate whether the diurnal and semidiurnal barometric pressure cycles that result in a fluctuation of atmospheric pressure of 0.3 to 3 hPa depending on location [22] with a periodicity of around 12 hours each could be the reason for the volume drift. The utilised barometric pressure data was measured at the meteorological station Karlsruhe located around 10 km from the place of experiment. As the AccuPyc 1340 is fitted with a gage pressure sensor, the actual barometric pressure is of lesser importance compared to the rate of pressure change, because a change of barometric pressure between the determination of p_1 and p_2 will influence the measured pressure difference. A reduction in barometric pressure after the determination of p_1 will lead to a relative increase of p_2 . A higher p_2 normally correlates to a sample of lower volume and, therefore, higher density. An increase in barometric pressure accordingly leads to a lower density. A simple recalculation of the sample density based on modified p_2 data was carried out following the formula

$$\rho(\text{sample}) = \frac{p_2 + \Delta p - p_1}{(p_2 + \Delta p)(V_r + V_c) - p_1 \cdot V_c} \cdot m(\text{sample})$$

with the sample chamber volume (V_c), the reference volume V_r , the initial pressure p_1 , the equilibrium pressure p_2 , Δp the atmospheric pressure change between the measurement of p_1 and p_2 , and the sample mass $m(\text{sample})$ to investigate whether the magnitude of pressure change is sufficient to explain the density fluctuations. The calculation was carried out under the following assumptions. 0.5 hPa/h was chosen as maximum positive and negative pressure change. This value was derived from the actual atmospheric pressure data for the measurements **C3.3** and **C3.4**. It was assumed, that the time frame of the interference of the pressure change is around 0.03 h of the 0.05 h each individual data point determination took. This resulted in a 1.5 pa deviation per measurement between the determination of p_1 and p_2 . p_1 was left unmodified and p_2 was increased or decreased in the calculation to receive the maximum and minimum density values, respectively. The calculation was carried out based on actual p_1 and p_2 values of **C3.3**. The thereby obtained difference in density between maximum and minimum density is 0.0012 g/cm^3 for this specific sample. This is in remarkable agreement with the actual discrepancy within **C3.3** of 0.0013 g/cm^3 . Assuming that the rate of change of the barometric density fluctuation is about the same for most days its influence in dependence of the utilised sample chamber insert and sample volume can be estimated. The measurement **C2.2** can serve as a realistic scenario for the 10 cm^3 cell. Here the sample volume of 4.3 cm^3 fills the sample chamber volume to about 40 % which is a rather good value for most samples due to their low packing density. Here, under the same assumptions as for **C3.3** a density deviation of 0.00025 g/cm^3 is calculated. This is also in good agreement with the amplitude of 0.0002 g/cm^3 of a 4th order regression curve of the measurement **C2.2**. The obtained atmospheric pressure data for **C3.3** and **C3.4** were differentiated and the resulting curves are superimposed with the fitted density curve of the two measurements in Figure 11 to evaluate the

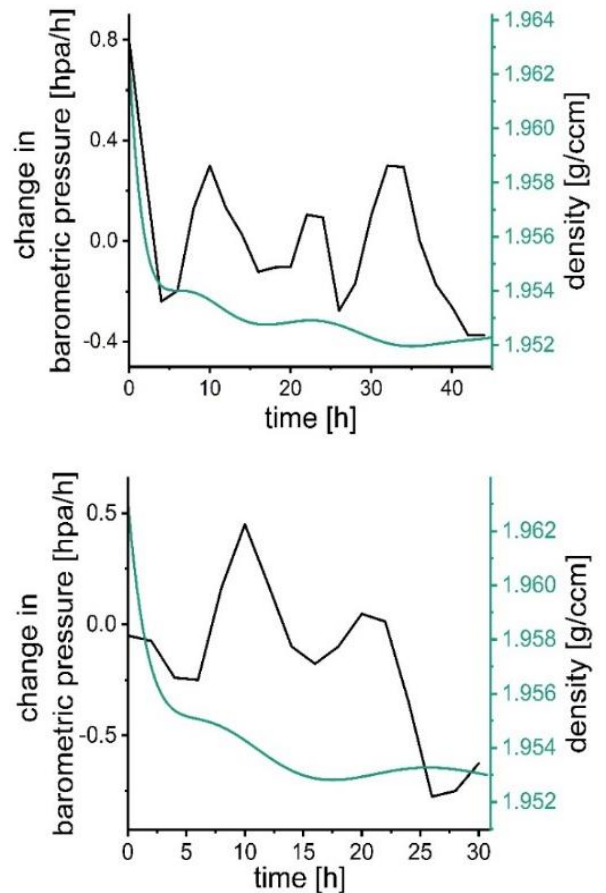


Figure 11: Overlay of the rate of barometric pressure change (black) with the smoothed density data points for **C3.3** (top) and **C3.4** (bottom).

correlation between the obtained density values and the change in barometric pressure.

Both density progressions do not seem to fit the change in barometric pressure. This is best seen in the change in correlation of the global minima of the

density curve of **C3.3** to the barometric pressure change compared to the correlations of the local minima. Also, none of the local minima of the density curve of **C3.4** correlate to the maxima of the barometric pressure change curve. It could be possible that the discrepancies are explained by the spatial distance between the meteorological station and the place of experiment or variations of the length of the individual measurements. Further study is required to explain the lack of correlation.

Table 1: Summary of the obtained p-values from the Shapiro-Wilk test dependent on the applied data treatment

| designat ion | nr. of data points | raw data | raw data detrended | recalculated data | recalculated data detrended | polynomial outliers removed | detrended and outliers removed |
|-----------------|-----------------------|----------|-----------------------|----------------------|-----------------------------------|--------------------------------|--------------------------------------|
| K3 | 481 | <0.01 | 0.26 | 0.20 | 0.50 | 0.20 | |
| C2.2 | 282 | 0.02 | 0.05 | 0.08 | 0.14 | 0.19 | |
| C2.3 | 336 | 0.05 | 0.06 | 0.02 | 0.02 | 0.17 | |
| C2.4 | 150 | <0.01 | 0.01 | <0.01 | 0.01 | 0.25 | |
| C2.5 | 150 | 0.21 | 0.94 | 0.41 | 0.73 | 0.55 | |
| C3.3 | 701 | <0.01 | 0.43 | 0.09 | 0.27 | 0.17 | |
| C3.4 | 416 | <0.01 | <0.01 | 0.28 | 0.45 | 0.42 | |
| average | | 0.04 | 0.25 | 0.16 | 0.30 | 0.28 | |

This, however, does not mean that the calculated influence of the barometric pressure change on the density value is wrong, as this value is derived directly from real pressure change data and is not contradicted by the additional findings. These calculated values can, therefore, still be used for the explanation of some of the occurring error of the density measurements. These values are only valid for stable weather conditions. In case of a superimposed drop or increase of the barometric pressure in addition to the diurnal and semidiurnal barometric pressure cycles a stronger density variation is to be expected. It appears, therefore, advisable to also check the current weather development on performing high precision density measurements, as this might explain an increased drift in measurements or discrepancy between measurements. Furthermore, on the quest for best accuracy one might be tempted to choose stricter equilibration conditions than the standard 35 hPa/min. This could, however, even reduce the accuracy as it increases the measurement time and, therefore, the influence the change in barometric pressure should have on the measurement. It is noteworthy that the influence of the change in barometric pressure should only affect gas pycnometers equipped with gage pressure sensors, as absolute pressure sensors should provide constant pressure values even under changing barometric pressure.

3.7.3 Test for normality

A special requirement of parametric tests is a specific distribution of the data [23] typically a normal distribution.[24] A multitude of test methods for normality exists. Of these it appears that the Shapiro-Wilk test [25] is the most powerful and universal test in most situations. [26, 27] It was shown that for normal distributed data the Type I error rate of the Shapiro-Wilk test is independent from the sample size, [26] but the test power increases strongly for most non normal distributed data with increasing sample size.[26] The most reliable results should, therefore, be expected at larger sample size. Normality of the density data is thus only discussed for measurements of at least 150 data points. Because of the similar nature of each density measurement one can assume that if the majority of density measurements of more than 150 data points satisfies the normality condition, all data points of proper density measurements are random samples of a normally distributed population, even if the individual measurement's normality is rejected. This

assumption might fail if different sample material is probed that

possesses a sufficiently disruptive character to the measurement itself. Which again only highlights the necessity of performing density measurements of high data point count for any new material. Seven data sets were tested for normality utilising the Shapiro-Wilk test. Only data point regions with a linear volume drift of less than $2 \cdot 10^{-6} \text{ cm}^3/\text{data point}$ were used. The obtained p-values (probability values) are summarised in Table 1. Of the seven sets only two passed the test unrefined and one of them barely. This indicates that the raw volume data points are not normally distributed. Four data refinements were carried out to investigate whether an improvement of the data is possible. The underlying linear drift of the data was eliminated in such a fashion that the average volume was conserved. The volume was recalculated based on the sample chamber volume V_c , the reference volume V_r , the initial pressure p_1 , and the equilibrium pressure p_2 following the formula

$$V(\text{sample}) = \frac{p_2(V_r+V_c)-p_1 \cdot V_c}{p_2-p_1}$$

A linear detrending of the recalculated data was undertaken. And the raw data were detrended utilising a regression function typically of 3rd or 4th order while maintaining the average volume followed by removal of all outliers. The comparison of the resulting data sets per measurement allows some conclusions. From Table 1 it is obvious that every data treatment improved the normality of the data on average. The strongest single impact on normality has linear detrending. That recalculation of the data improves the normality seems to indicate that the pycnometer uses additional hidden parameters to calculate the sample volume which influence the normality of the data. Only by combining polynomial detrending

and outlier removal do all measurements pass the test.

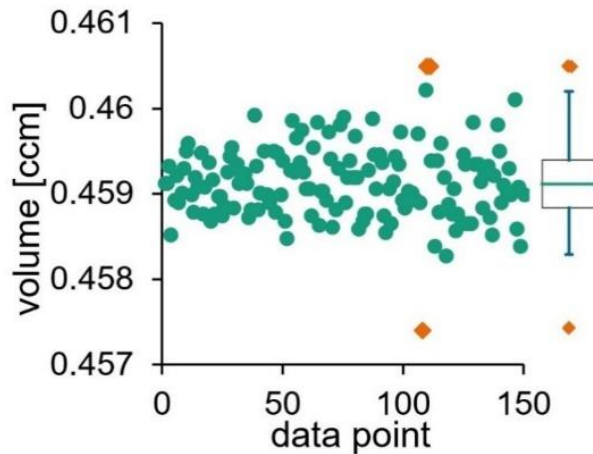


Figure 12: Volume data points of **C2.4** on the left and the corresponding box plot on the right.

The impact of outlier removal can easily be identified at **C2.4**, for which neither the untreated nor the detrended data achieved a satisfactory p-value. On inspecting the box-plot (Figure 12 right) one finds that no extreme outliers are present, but the lower outlier comes close. The removal of this one outlier, however, does not improve the p-value significantly. The additional removal of the two upper outliers increases the p-value of the detrended raw data from 0.01 to 0.23. For this measurement it is easy to identify that the outliers are caused by a disturbance of the measurement and are not part of the regular population. This can be deduced from the temporal closeness of the outliers. This might indicate that every outlier is the result of a disturbance, albeit in many cases a less obvious one. It could, therefore, be argued that every outlier, not only the extreme ones, is to be removed to improve the quality of the data. The poor p-value of **C2.3**, however, can only be marginally improved by removing the eight outliers. As it was discussed in section 3.7.2 likely due to variations in barometric pressure, density measurements possess a periodic fluctuation. Linear detrending only removes part of its influence. For **C2.3** polynomial detrending was, therefore, applied. By polynomial detrending alone a p-value of 0.07 was achieved which is only 0.01 better than linear detrending. By additional removal of the outliers a p-value of 0.17 was achieved which is markedly better than the 0.1 for linear detrending and outlier removal. From Table 1 it can be seen that by removing outliers and the polynomial drift of the data every measurement passes the normality test with typically a quite significant p-value. This indicates

that the density measurement in itself produces normal distributed data points. The normal distribution is, however, heavily influenced by a variety of disturbances. The strengths of these disturbances vary and might lead to measurements that even after post treatment do not fulfil the normality condition. Due to their underlying normality it appears appropriate to extrapolate from the tested measurements that most density measurements are fit for statistical analysis, even though some measurements might benefit from appropriate post treatment such as removal of outliers.

3.7.4 Homoscedasticity

The density's standard deviation of a sample measurement appears to be dependent on the sample volume as discussed in section 3.1, but it also seems to be dependent on additional factors. An unexplainable trend of standard deviation occurred in the study of Viana *et al.* [6]. Here three measurements of mannitol in the 10 cm³ cell have a ten times larger standard deviation than the measurements in the 1 cm³ cell and a 3.5 times larger standard deviation than the measurements in the 3.5 cm³ cell, even though the trend should be reverse. For other tested materials (glass beads and quartz) the expected standard deviation trend was observed. In the present study for C3, four measurements were carried out where between measurements the sample chamber was not opened. Measurements **C3.1** and **C3.2** were carried out directly after one another. Between measurement **C3.2** and **C3.3** as well as **C3.3** and **C3.4**, however, the sample rested within the sample chamber for 34 hours and 96 hours, respectively. Not only did the initial drift interval increase from 10 data point for **C3.1** and **C3.2** to about 200 for **C3.3** and **C3.4**, but also the standard deviations of the regions free of strong drift of **C3.3** and **C3.4** are with 0.001g/cm³ and 0.0009 g/cm³, respectively, distinctly lower than for **C3.1** and **C3.2** with 0.0025 g/cm³ and 0.002 g/cm³, respectively. The reason for this different behaviour is unknown and it is unclear whether it is caused by the sample or the device. A similar behaviour is sometimes observed where during a measurement the standard deviation suddenly increases or decreases. This is displayed in Figure 13 for two measurements of C1. For clarity, **C1.3** is shifted by 300 data points. **C1.2** shows a decrease in standard deviation at about data point 150, while **C1.3** shows an increase in standard deviation at about data point 400. It appears unlikely that the samples

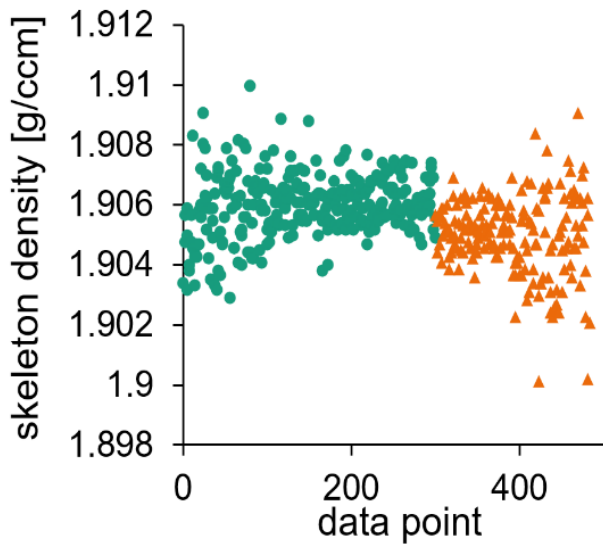


Figure 13: Visualisation of the change in standard deviation within measurements for **C1.2** (green) and **C1.3** (orange triangles).

could exhibit such behaviour and it appears more likely that an external factor, such as a disturbance in the power line, influences the measurements. Direct solar irradiation has disturbed measurements in the past; however, in this case the disturbance has twice started at around midnight which eliminates the sun as causing factor. Besides, the comparably rapid heating of the device by solar irradiation has caused negative density spikes that lasted only around 15 data points instead of a prolonged increase in standard deviation.

Fluctuations in the room pressure were also tested as causing factor. The room's air extraction creates a mild vacuum in the room that is equilibrated through the closed door. It is conceivable that this equilibration causes pressure fluctuations that affect the measurement. Two tests (K4 and K5) during which the air extraction was switched on and off for at least 50 data points each showed, however, no effect of the state of air extraction on the standard deviation of the measurements.

4 Repeatability

All the abovementioned aspects serve to enable one to carry out a density measurement that is statistically sound. And in doing so allow for some certainty about the obtained results and their relevance. One simple validation of the quality of measurements is repeatability of the obtained results. In this case the t-test is a suitable method to judge whether the difference in the result of a repeat measurement is only caused by statistical error due to limited sample number. It has been shown in chapter 3.7.3 that influences on the

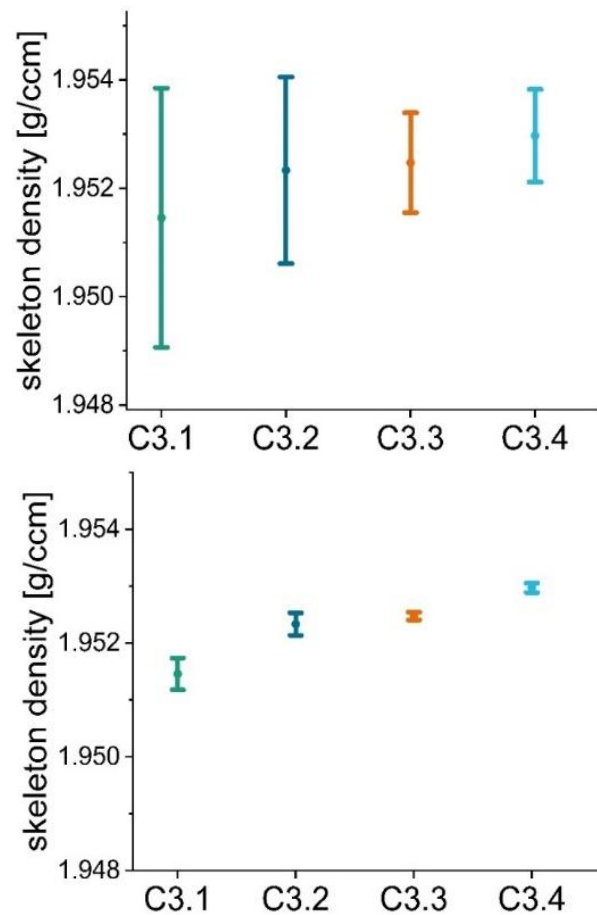


Figure 14: Comparison of the standard deviations of **C3.1-4** (top) and the 95% confidence intervals of **C3.1-4** (bottom).

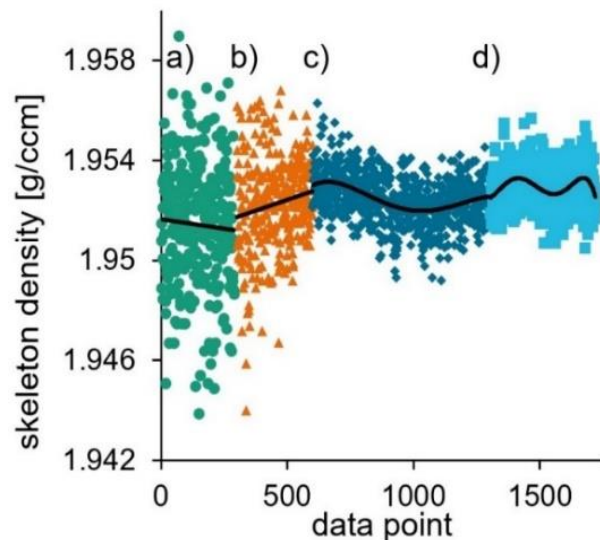


Figure 15: Visualisation of the density progression from **C3.1**(green) to **C3.4**. The measurements **C3.2** (orange triangles), **C3.3** (blue rhombs), **C3.4** (teal squares) have been offset on the x-axis for clarity purposes. Furthermore, at marker a) the first 13 data points of **C3.1** have been omitted, at marker c) the first 198 data points of **C3.3** have been omitted and at marker d) the first 199 data points of **C3.4** have been omitted. Additionally, Measurement **C3.2** was started within 10 minutes after the end of measurement **C3.1**, while 34 h lie between the end of **C3.2** and the start of **C3.3** and 96 h lie between the end of **C3.3** and the start of **C3.4**.

measurements exist that with varying strength influence the data point values and reduce their normality. These influences can also affect the sample average. **C3.1** to **C3.4** are four repeat measurements that have been conducted in the 1 cm³ sample chamber without opening the device. It, therefore, would be expected that the sample averages are statistically insignificantly different. Because of the change in standard deviation that was discussed in chapter 3.7.4 between measurement **C3.2** and **C3.3**, Welch's [28] t-test was used to compare the sample means in pairs, but no ANOVA can be carried out.

Of the pairs only **C3.2** and **C3.3** are identified as originating from the same population with a p-value of 0.19. The power of this test, however, is only 0.38 due to the difference in standard deviations. The lack of sameness of the data means is somewhat surprising when one inspects the raw data or the standard deviation diagram (Figure 14 top), but on considering the 95% confidence intervals [29] of the data (Figure 14 bottom) the result is easily comprehensible. The measurements appear to follow a clear trend of increasing sample density. And this trend could be suspected to cause the lack of similarity. The inspection of the data points, however, draws a different picture (Figure 15). If there was an underlying trend to increase the sample density, it could hardly be explained by evaporation of solvent inclusion as this should lead to a decrease in density during density measurements as discussed in chapter 3.6. Only if the solvent evaporation rate was unchanging over time one could conceive that a slow increase in skeleton density is possible. The data, however, do not support this hypothesis. As discussed for **C3.3** and **C3.4** in section 3.7.2 fluctuations of the barometric pressure over the course of the day can influence the density measurements. This influence might explain most of the variation in density as the difference in average density between **C3.1** and **C3.4** is only 0.0002 g/cm³ larger than the calculated amplitude of the density value resulting from the change in barometric pressure. This pressure drift, however, does not only cause the repeat measurements to be considered different by the t-test, but also the measurements with themselves. This can easily be illustrated by

dividing measurement **C3.3** into ten equal sections of 70 data points and performing ANOVA on them. Of the 44 pairs, for 21 pairs did the Tukey test [30] reject the null hypothesis. The assumed influence of the change in barometric pressure is much smaller for measurements using the 10 cm³ sample cup as has been shown in chapter 3.7.2. Because the standard deviation of the data points is, however, also reduced, repeat measurements in the 10 cm³ sample cup usually also do not pass the t-test. For example, the t-test of the true repeat measurements **C2.2** and **C2.3** rejects the null hypothesis even though the mean difference is only 0.00035 g/cm³. Even on parallel translation of the data points of **C2.3** to achieve a mean difference of 0.0001 g/cm³ the null hypothesis is rejected.

The failure of a typical repeat measurement to pass the t-test simply shows that the random sampling error of the individual data points due to their limited number is not the only considerable error at play. Besides some preventable errors to a density measurement such as insufficient sample dryness, insufficient sample volume, or markedly different measurement temperature, the following errors that will always affect the measurement remain: sampling error, the weight in error, the error caused by variance in sample chamber volume upon opening and reclosing the chamber, the temperature fluctuation, and the drift of barometric pressure. Of these errors the variance of sample chamber volume and the temperature fluctuations did not show any signs of being relevant in face of the other errors present. For the other three errors, their influence on the obtained density value has been calculated and displayed in Table 2 for the 10 cm³ and 1 cm³ sample chamber based on the density measurements discussed in this paper. Insufficient measurements have been carried out in the 3.5 cm³ sample chamber, but there is no indication that this intermediate chamber should not exhibit intermediate errors. The error resulting

from the weight in error was calculated based on a 50% filled sample cup and a sample of density 1.95 g/cm³. The error resulting from barometric pressure change was calculated based on an assumed maximum pressure change rate of 0.5 hPa/h, an interference time of 0.03 h per

Table 2: Summary of the major sources of error dependent on the chamber volume and the number of data points

| chamber volume [cm ³] | nr. of data points | error due to weight in error [g/cm ³] | error due to barometric pressure drift [g/cm ³] | sampling error [g/cm ³] | mean error sum [g/cm ³] |
|-----------------------------------|--------------------|---|---|-------------------------------------|-------------------------------------|
| 10 | 100 | 0.00005 | 0.00013 | 0.00007-0.00012 | 0.0003 |
| | 30 | 0.00005 | 0.00013 | 0.00011-0.00017 | 0.0003 |
| | 100 | 0.00038 | 0.00060 | 0.00024-0.00064 | 0.0014 |
| 1 | 30 | 0.00038 | 0.00060 | 0.00045-0.00131 | 0.0019 |

measurement, an about 50% filled sample cup and a sample of density 1.95 g/cm^3 . The sampling error is represented by half of the 99% confidence interval calculated for all discussed measurements in this paper.

It is noteworthy that, technically, the error due to barometric pressure change is to some extent double counted, if the non-detrended data points are used to calculate the confidence interval. It was found, however, for all tested data that detrending and removing the outliers has no influence on the confidence interval within the accuracy of 0.00001 g/cm^3 . No data treatment seems therefore typically necessary for calculating the confidence interval. These obtained values must be viewed in the correct context. Following the terminology of ISO 5725 [10] the error values only represent the precision one can expect and give little information about the trueness of the values. These obtained errors can only be used to compare samples of similar volume that were measured in close temporal proximity (and calibration) within the same sample chamber i.e. under repeat measurement conditions. [10] Furthermore, the values are valid for samples of density 1.95 g/cm^3 and can easily be converted for samples of different density. All errors, however, are not necessarily translatable. The assumed weight in error of 0.0002 g is most likely the most universal error. The magnitude of the barometric pressure drift is strongly dependent on the latitude of the measurement location.[22] Better error values can be expected closer to the poles and worse values closer to the equator. The obtained confidence intervals, as can be seen, vary widely for different measurements and samples. These values always have to be determined for the substance of interest and cannot be translated.

Given these error values it is obvious why in most cases statistical tests such as t-tests and ANOVA will reject similarity of the measurements, as they are only concerned with the error stemming from the data sampling. An alternative procedure to judge whether repeat measurements can be considered the same or whether one sample is significantly denser than another is hence needed. One practical solution is to calculate the sampling error based on the 99%-confidence intervals of the measurements and add the other two error values to obtain a collective measurement error that can be used to compare samples by checking whether their error bars intersect. If the error bars of repeat measurements intersect, the data can be pooled. This pooled data can then be used to compare different samples. The use of the 99%-confidence interval might be beneficial compared to the 95%

to remedy some of the alpha error accumulation that is bound to appear upon the comparison of a multitude of samples. Obviously, this methodology lacks the statistical backing of a proper test such as a t-test, but it is still significantly better than to just perform a replicate measurement and judge the data based on scientific intuition. Because it utilises far more data provided by the measurement than for example the three-sigma rule, it is possible to differentiate between far more similar samples. The three-sigma rule would be very lenient towards replicate measurements, but would hardly be able to differentiate between different polymorphs for example. There is no need to fall back to the three-sigma rule, because all of the major contributing error factors are accounted for and the error margin is therefore very well known. Based on the collective measurement error one is able to differentiate between samples of 0.001 g/cm^3 density difference with certainty utilising the 10 cm^3 sample cup. Based on the length of the error bars of 0.0003 g/cm^3 for two samples of a true density difference of 0.001 g/cm^3 the error bars of individual measurements of the two samples can intersect if measurements of both samples are maximum eccentric. It is therefore always advisable to carry out measurements in triplicate. The amount of data points appears to have a less significant impact on the error, as the confidence intervals seem to be relatively unchanged between 30 and 100 data points for the 10 cm^3 cell. This means that high precision measurements are possible with relatively short measurement times. And measurements of 100 data points and more are only needed once to assess the samples behaviour during measurement. Furthermore, as the method should only be applied for measurements that were carried out in the same measurement cell with closely matching sample volume, homoscedasticity should be less of an issue here. This comparison should be applicable even under mild discrepancies in the standard deviation of the data sets.

5 Conclusion

This study examined the necessary prerequisites and analysis methods to carry out pycnometric density measurements of energetic materials of highest precision. It was shown that the individual data points of the density measurement are normally distributed, which enables one to apply statistical methods, such as t-test and confidence intervals to the density data. It was, however, also shown that the measurement is always

considerably disturbed presumably by the change of the barometric pressure which causes a density drift over the day, and sometimes disturbed by isolated disturbances that lead to individual outliers. As a result, repeat measurements typically do not pass t-tests or ANOVA even under optimal sample preparation and execution of the measurement, because the sum of the other errors is of the same magnitude as the sampling error. An alternative method to judge the quality of repeat measurements and the significance of density differences has therefore been proposed for general use that considers the contributing errors. Thereby for the first time enabling one to differentiate with certainty between substances that possess density differences of 0.001 g/cm³ (0.05%). It can, however, not be stressed enough that this is the precision of repeat measurements carried out in the same sample chamber with the same calibration. It must not be confused with the accuracy of the obtained density which is affected by even more factors and requires much more effort to be optimised to a level of 0.05%. This means that under repeat measurement conditions even solvent inclusions of the CL-20/HMX cocrystal of 0.04% or gas inclusions of 25 µm in a particle with a diameter of 250 µm are detectable via helium pycnometry, which means it can be a valuable tool in the process of quality and sensitivity improvement for energetic materials.

Acknowledgements

We are grateful the support provided by Dr. Manfred Kaiser and Michael Koch at the Technical Center for Weapons and Ammunition (WTD 91).

Funding Source

This work was supported by the German Ministry of Defense.

References

- 1 Nielsen, A.F., Bertelsen, P., Kristensen, H.G., Hovgaard, L. (2007) Helium pycnometry as a tool for assessment of sealing efficiency in microencapsulation. *J. Pharm. Sci.*, 32 (4-5), 318–327 <https://doi.org/10.1016/j.ejps.2007.08.007>.
- 2 Biolders, C.L., Backer, L.W. de, Delvaux, B. (1990) Particle Density of Volcanic Soils as Measured with a Gas Pycnometer. *Soil Sci. Soc. An. J.*, 54 (3), 822–826 <https://doi.org/10.2136/sssaj1990.03615995005400030034x>
- 3 Taova, T.M., Mal'surgenova, F.M., Alchagirov, B.B., Khokonov, K.L. (2009) The density

- and molar volumes of ternary alloys of cross sections of the sodium-potassium-cesium system technically important temperatures. *High Temp*, 47 (6), 815–821 <https://doi.org/10.1134/S0018151X09060066>
- 4 Kamlet, M.J. and Jacobs, S.J. (1968) Chemistry of Detonations. I. A Simple Method for Calculating Detonation Properties of C–H–N–O Explosives. *J. Chem. Phys.*, 48 (1), 23–35 <https://doi.org/10.1063/1.1667908>
 - 5 Borne, L., Patedoye, J.-C., Spycckelle, C. (1999) Quantitative Characterization of Internal Defects in RDX Crystals. *Propellants, Explos., Pyrotech.*, 24 (4), 255–259.
 - 6 Viana, M. (2002) About pycnometric density measurements. *Talanta*, 57 (3), 583–593 [https://doi.org/10.1016/S0039-9140\(02\)00058-9](https://doi.org/10.1016/S0039-9140(02)00058-9)
 - 7 Stange, U., Scherf-Clavel, M., Gieseler, H. (2013) Application of gas pycnometry for the density measurement of freeze-dried products. *J. Pharm. Sci.*, 102 (11), 4087–4099 <https://doi.org/10.1002/jps.23723>
 - 8 Borne, L. and Ritter, H. (2006) HMX as an Impurity in RDX Particles: Effect on the Shock Sensitivity of Formulations Based on RDX. *Prop., Explos., Pyrotech.* 31 (6), 482–489 <https://doi.org/10.1002/prop.200600066>
 - 9 ISO 12154 (2014) Determination of density by volumetric displacement— Skeleton density by gas pycnometry; .
 - 10 DIN ISO 5725-1 Genauigkeit (Richtigkeit Und Präzision) Von Messverfahren Und Messergebnissen, Deutsches Institut für Normung e.V.
 - 11 Micromeritics Instrument Corp Understanding the Uncertainty and Precision Specifications for the AccuPyc: Application Note 174.
 - 12 Bolton, O., Simke, L.R., Pagoria, P.F., Matzger, A.J. (2012) High Power Explosive with Good Sensitivity: A 2:1 Cocrystal of CL-20:HMX. *Cryst. Growth Des.*, 12 (9), 4311–4314 <https://doi.org/10.1021/cg3010882>
 - 13 Chang, S.-Y., Wang, C., Sun, C.C. (2019) Relationship between hydrate stability and accuracy of true density measured by helium pycnometry. *Int. J. Pharm.*, 567, 118444 <https://doi.org/10.1016/j.ijpharm.2019.06.035>
 - 14 Sun, C.C. (2005) True density of microcrystalline cellulose. *J. Pharm. Sci.*, 94 (10), 2132–2134 <https://doi.org/10.1002/jps.20459>
 - 15 Kikuchi, T., Wang, B.S., Pikal, M.J. (2011) High-precision absolute (true) density measurements on hygroscopic powders by gas pycnometry: application to determining effects of

formulation and process on free volume of lyophilized products. *J. Pharm. Sci.*, 100 (7), 2945–2951 <https://doi.org/10.1002/jps.22521>

16 Engel, W. and Heinisch, H. (2000) Production of phase-stabilized ammonium nitrate for propellants for airbags and rockets. WO 2000018704.

17 Herrmannsdörfer, D., Gerber, P., Heintz, T., Herrmann, M.J., Klapötke, T.M. (2019) Investigation Of Crystallisation Conditions to Produce CL-20/HMX Cocrystal for Polymer-bonded Explosives. *Propellants, Explos., Pyrotech.*, 44 (6), 668–678 <https://doi.org/10.1002/prep.201800332>

18 Herrmannsdörfer, D., Herrmann, M.J., Heintz, T. Advanced approaches to the CL-20/HMX cocrystal, in 47th *Int. Annu. Conf. Fraunhofer ICT*, p. 14.

19 Student (1908) The Probable Error of a Mean. *Biometrika*, 6 (1), 1 doi.org/10.2307/2331554

20 Halldestam, M. (2016) ANOVA –The Effect of Outliers. Uppsala University. Bachelor’s thesis.

21 McGill, R., Tukey, J.W., Larsen, W.A. (1978) Variations of Box Plots. *Am. Stat.*, 32 (1), 12–16 <https://doi.org/10.1080/00031305.1978.10479236>

22 Le Blancq, F. (2011) Diurnal pressure variation: the atmospheric tide. *Weather*, 66 (11), 306–307 <https://doi.org/10.1002/wea.857>

23 Altman, D.G. and Bland, J.M. (1999) Statistics notes: variables and parameters. *BMJ*, 318 (7199), 1667 <https://doi.org/10.1136/bmj.318.7199.1667>

24 Driscoll, P. and Lecky, F. (2001) Article 6. An introduction to hypothesis testing. Parametric comparison of two groups--1. *Emerg. Med. J.*, 18 (2), 124–130 <https://doi.org/10.1136/emj.18.2.124>

25 Shapiro, S.S. and Wilk, M.B. (1965) An Analysis of Variance Test for Normality (Complete Samples). *Biometrika*, 52 (3/4), 591 <https://doi.org/10.2307/2333709>

26 Mendes, M. and Pala, A. (2003) Type I Error Rate and Power of Three Normality Tests. *Pak. J. Inform. and Technol.* (2), 135–139.

27 Öztuna, D., Elhan, A.D., Tüccar, E. (2006) Investigation of Four Different Normality Tests in Terms of Type 1 Error Rate and Power under Different Distributions. *Turk J Med Sci*, 36 (3), 171–176 <https://doi.org/10.3923/itj.2003.135.139>

28 Welch, B.L. (1947) The Generalization of ‘Student’s’ Problem when Several Different Population Variances are Involved. *Biometrika*, 34 (1/2), 28 <https://doi.org/10.2307/2332510>

29 Neyman, J. (1937) Outline of a Theory of Statistical Estimation Based on the Classical Theory of Probability. *Philos. Trans. R. Soc.*, 236 (767), 333–380.

30 Tukey, J.W. (1977) *Exploratory data analysis*, Addison-Wesley Publishing Company, Reading, MA.

Supporting Information for

High-Precision Density Measurements of Energetic Materials for Quality Assessment

Dirk Herrmannsdörfer*,^[a] Thomas M. Klapötke^[b]

[a] *Energetic Materials Fraunhofer Institute for Chemical Technology ICT Joseph-von-Fraunhofer-Str. 7 76327 Pfinztal, Germany*
E-mail: dirk.herrmannsdorfer@ict.fraunhofer.de

[b] *Department of Chemistry Energetic Materials Research Ludwig-Maximilian University of Munich Butenandtstr. 5 - 13 (Haus D) 81377 Munich, Germany*

Analytical Data

NMR Spectra of HMX and CL-20

Purity of the raw material was judged based on the ¹H-NMR data under the assumption, that the impurities possess a comparable hydrogen to carbon, nitrogen, and oxygen ratio as the raw material. This assumption appears reasonable, as the expected impurities of CL-20 are incompletely nitrated by-products and in case of HMX the expected impurity is RDX. Because of the overlap of the signals in the range of 5.7 ppm to 6.3 ppm for HMX and 7.7 ppm to 8.4 ppm for CL-20, respectively these signals were integrated using origin 2019. The obtained integrals for HMX and CL-20 are listed in Table S1. Measurements were carried out using a 400 MHz Bruker spectrometer. For ¹H 16 spectra were summed up. For ¹³C 64 spectra were summed up and proton decoupling was carried out.

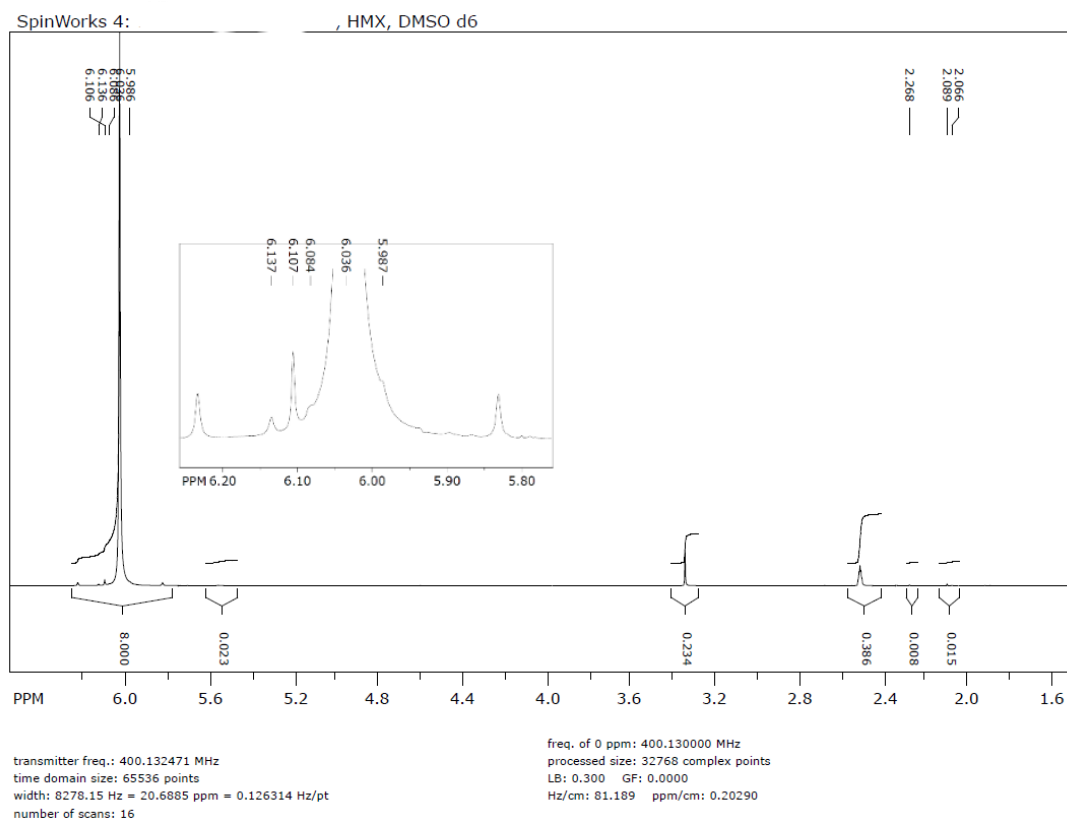


Figure S1: ¹H-NMR spectrum of HMX dissolved in DMSO D6. Signals at 3.3 ppm and 2.5 ppm are caused by incompletely deuterated DMSO.

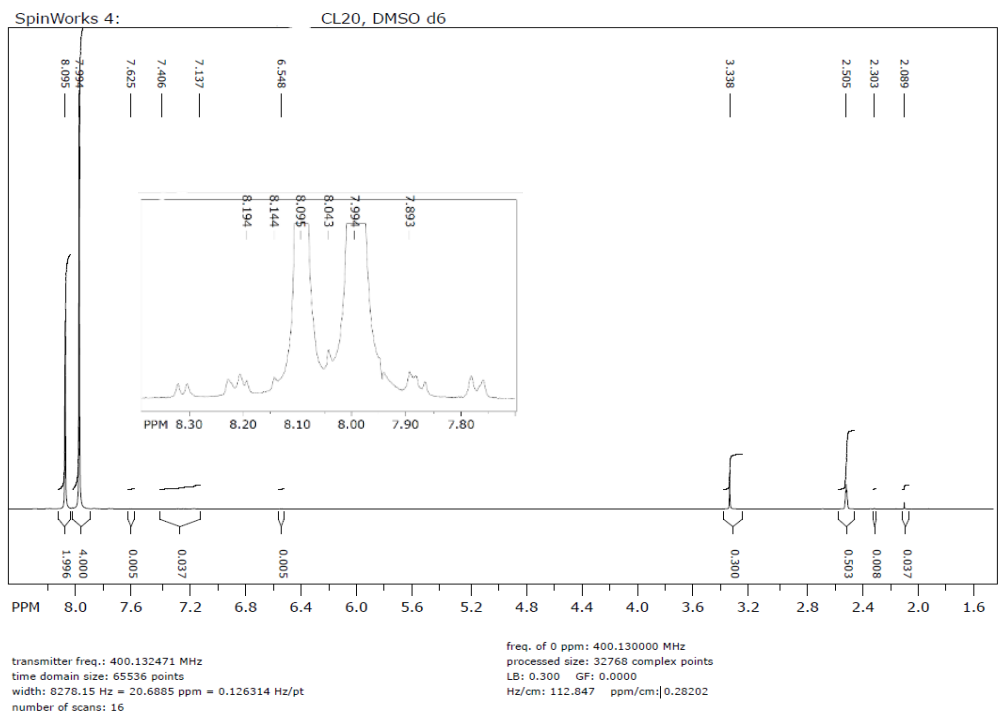


Figure S2: ¹H-NMR spectrum of CL-20 dissolved in DMSO D6. Signals at 3.3 ppm and 2.5 ppm are caused by incompletely deuterated DMSO.

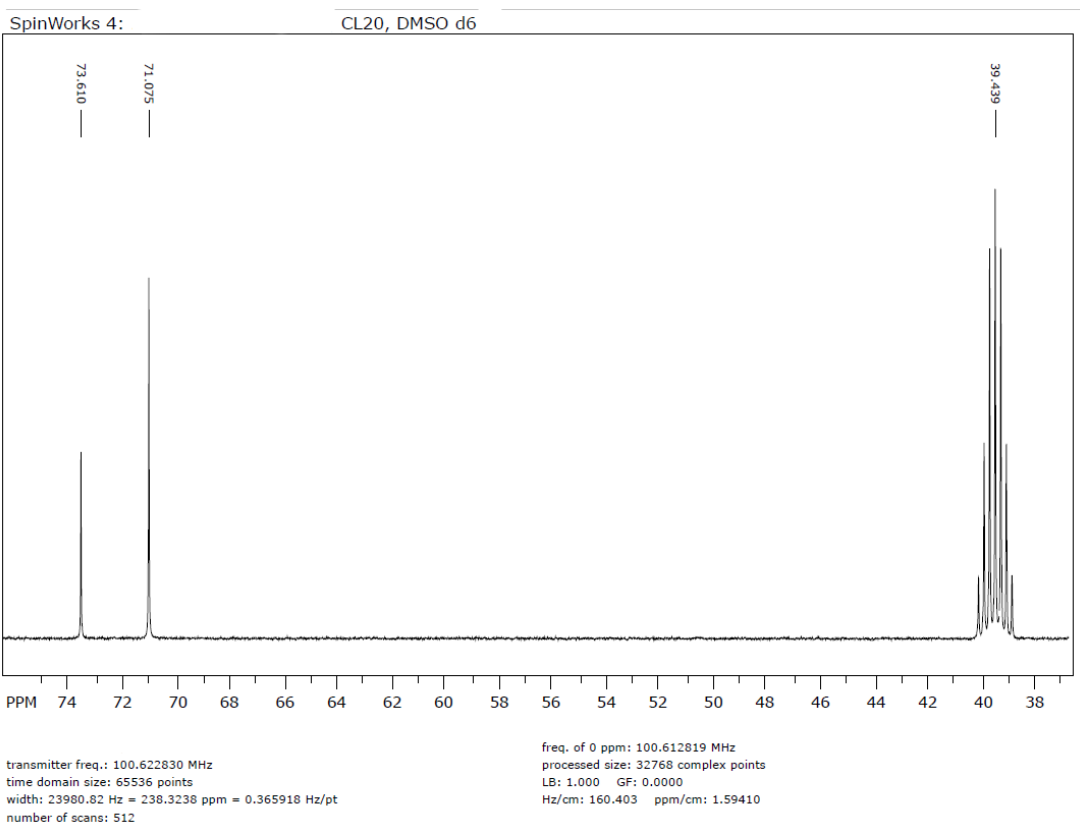


Figure S3: ¹³C-NMR spectrum of HMX dissolved in DMSO D6. The septet at 39.4 ppm is caused by the DMSO.

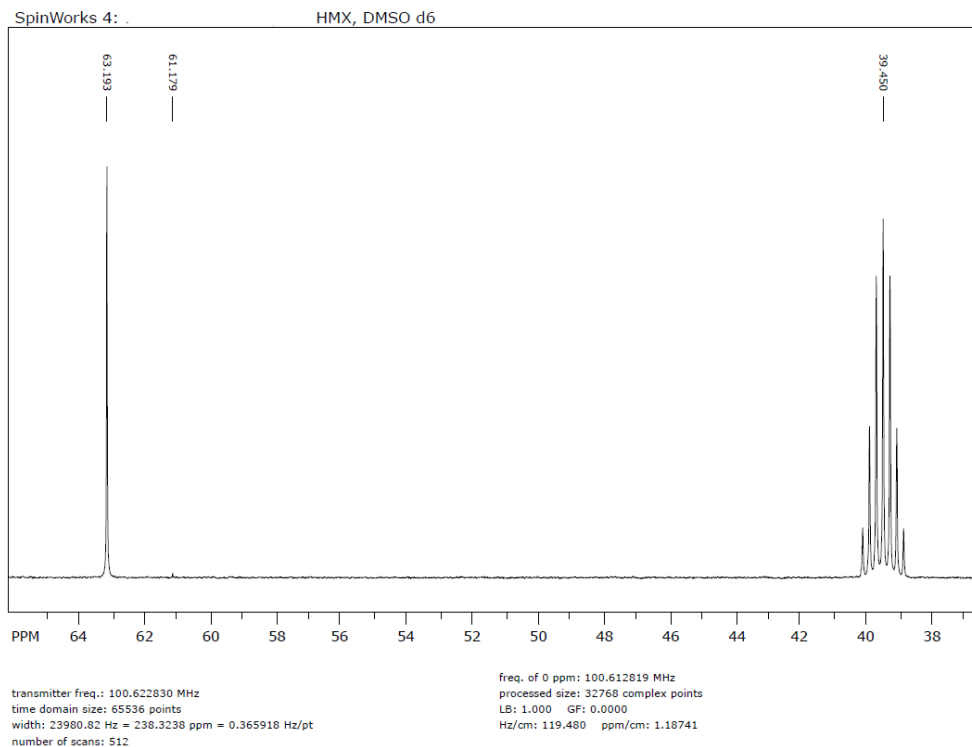


Figure S4: ¹³C-NMR spectrum of CL-20 dissolved in DMSO D6. The septet at 39.4 ppm is caused by the DMSO.

Table S1: Chemical shift and integrals of the ¹H-NMR spectra of the HMX and CL-20 samples

| HMX | | CL-20 | |
|----------------------|----------|----------------------|----------|
| chemical shift [ppm] | integral | Chemical shift [ppm] | integral |
| 2.066 | 0.002 | 2.089 | 0.006 |
| 2.089 | 0.001 | 2.303 | 0.001 |
| 2.268 | 0.001 | 6.843 | 0.001 |
| 5.556 | 0.003 | 7.406 | 0.006 |
| 6.036 | 1.000 | 7.625 | 0.001 |
| 6.107 | 0.005 | 7.892 | 0.001 |
| 6.137 | 0.001 | 7.994 | 0.667 |
| | | 8.043 | 0.001 |
| | | 8.095 | 0.333 |

HPLC Chromatograms of CL-20 and HMX

The chromatograms of HMX and CL-20 were recorded according to the following procedure. Using an Agilent 1100 HPLC system equipped with a binary pump and a diode array detector the injected sample of 1 µl was separated on a Kintex 2.6 µm C18 100 Å 100x4.6 mm column with pre-column. A mixture of acetonitrile and water was used as eluent. The eluent composition was gradually changed over time. Time 1 min: 10% acetonitrile, Time 20 min: 50% acetonitrile, time 22 min: 95% acetonitrile, time 27 min: 95% acetonitrile, time 28 min: 10% acetonitrile, post-time: 11 min. The eluent flow was 0.6 mL/min. The column was heated to 308 K during the analysis. Data analysis was carried out using Agilent ChemStation. The quantification of the impurities was carried out under the assumption, that the impurities exhibit the same responsiveness at the measurement wave length of 255 nm which is reasonable as all the expected impurities are comprised of the same functional

groups as HMX and CL-20. The retention time of HMX was 13.6 min and the retention time of CL-20 23.3 min under these conditions. The retention times and integrals for HMX and CL-20 are listed in Table S2.

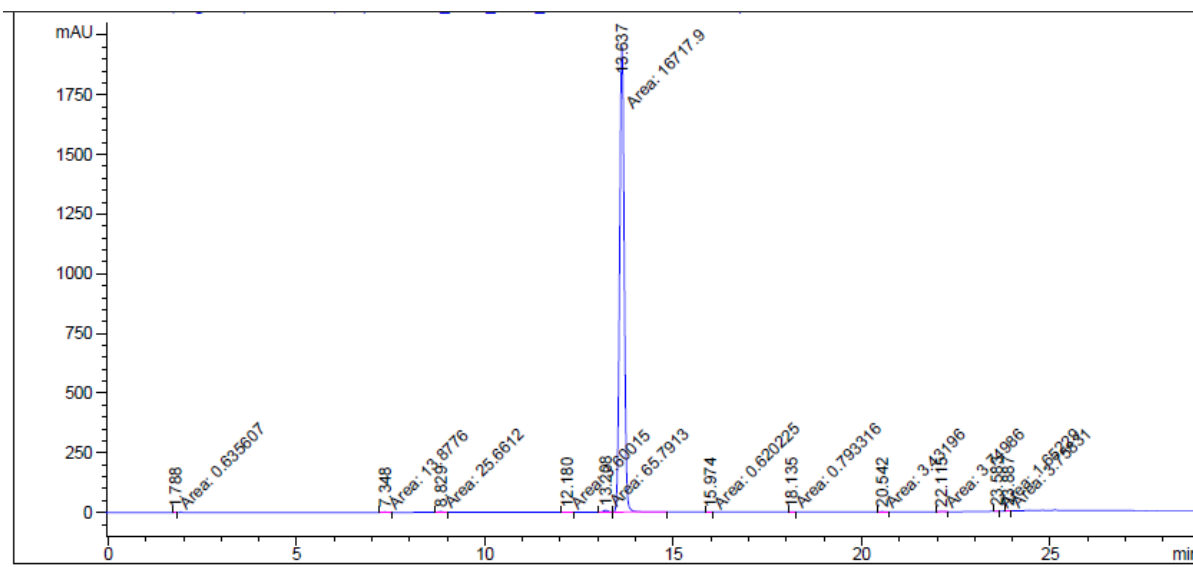


Figure S5: HPLC chromatogram of HMX.

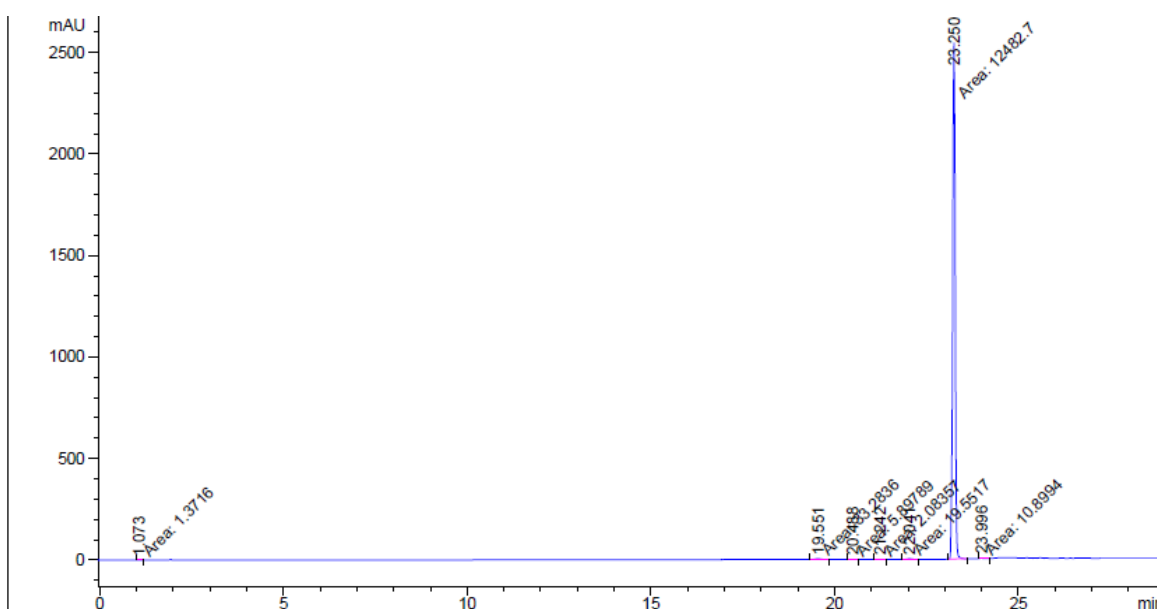


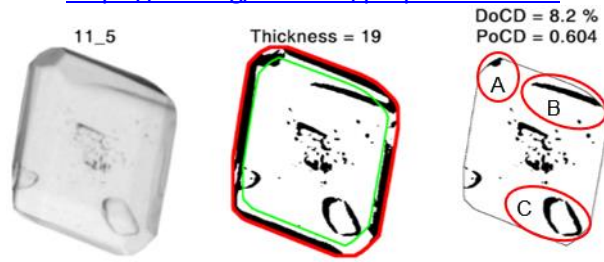
Figure S6: HPLC chromatogram of CL-20.

Table S2: Retention times and integrals of the HPLC chromatogram of the HMX and CL-20 samples

| HMX | | CL-20 | |
|----------------------|----------|----------------------|----------|
| retention time [min] | integral | retention time [min] | integral |
| 7.348 | 0.0008 | 1.073 | 0.0001 |
| 8.829 | 0.0015 | 19.551 | 0.0027 |
| 12.18 | 0.0002 | 20.488 | 0.0005 |
| 13.208 | 0.0039 | 21.242 | 0.0002 |
| 13.637 | 1.0000 | 22.041 | 0.0016 |
| 20.542 | 0.0002 | 23.25 | 1.0000 |
| 22.115 | 0.0002 | 23.996 | 0.0009 |
| 23.583 | 0.0001 | | |
| 23.887 | 0.0002 | | |

5.2 Quality Assessment of the CL-20/HMX Cocystal Utilising Digital Image Processing

Dirk Herrmannsdörfer, Thomas M. Klapötke
Propellants, Explosives, Pyrotechnics **2021**, 46, 4, 522-529
<https://doi.org/10.1002/prep.202000341>



Abstract: The reduction of liquid and gas inclusions in the crystals is an effective strategy for the production of reduced sensitivity high explosives. Assessment of the achieved crystal quality is paramount for the improvement of the crystallisation techniques. Here we present the quality evaluation of the CL-20/HMX cocrystal obtained from semibatch reaction cocrystallization (SBRC), batch reaction cocrystallization (BRC), and antisolvent crystallisation by comparison of the results of digital image processing of photomicrographs of crystals immersed in an optically equally dense liquid, ^1H NMR, HPLC, GC, helium pycnometry, SEM, pXRD, and DSC. It was found that digital image processing is capable of differentiation between crystal qualities of batches that are indistinguishable by all the other listed methods. It presents itself as a very promising tool for crystal quality assessment and improvement. The analysis shows that SBRC can produce coarse crystals of the same quality on a pilot plant-scale as antisolvent crystallisation on a laboratory-scale.

1 Introduction

Reducing the sensitivity of high explosives to improve the safety of storage under combat and non-combat conditions is of special interest in energetic materials research.[1] Many factors, such as surface roughness,[2] morphology,[3] chemical purity,[4] crystallinity,[5] and internal defects [6] have been linked to the sensitivity of high explosives. Internal defects and dislocations, often caused by solvent or gas inclusions, play a major role in determining the sensitivity of the explosive.[7] Because of the density difference between solvent, gas, and explosive, skeletal density could be used as an indirect method to quantify internal defects [7,8] and was used to determine differences in shock response of the explosives dependent on the measured density.[7,9] Another, more direct, way of defect analysis is photomicrography of the particles immersed in a liquid of matching refractive index.[2,4,8,10] This procedure reduces surface diffraction on the crystals and, thereby, highlights internal defects. In the past, this method, however, has only been used as a quantitative indicator by Kim *et al.* [11] by manually defining the crystal boundaries. Now that Lins, Heisel, and Wohlgemuth have developed an algorithm that enables one to automate the detection of crystals and the quantification of the internal defects highlighted by optical immersion,[12] this method can be utilised for quantitative differentiation between batches of different crystal quality far more conveniently. Recently, SBRC a novel crystallisation technique for the scaled-up production of the CL-20/HMX cocrystal has been presented.[13] It promises to combine the crystal quality obtained from antisolvent crystallisation[14] with the efficiency of BRC. To put the obtained crystal quality of SBRC in perspective, here we apply image processing together with a variety of conventional analysis methods to compare the crystal quality obtainable from SBRC with antisolvent crystallisation and BRC.

2 Experimental Section

ϵ -CL-20 (lot number 573S98) was obtained from SNPE. The chemical purity has been determined via ^1H NMR and HPLC to be 98.3 and 99.4%, respectively. Fine β -HMX (lot number NSI 00E 000 E004) was purchased from Chemring Nobel. The chemical purity has been determined via ^1H NMR and HPLC to be 98.7 and 99.3%, respectively. Coarse β -HMX (NSO131, lot number 20173558) was purchased from Euroenco. The chemical purity has been determined via ^1H NMR and HPLC to be 99.4 and 99.9%, respectively. Acetonitrile (ACN) (HPLC grade) was purchased from Carl Roth GmbH, stored over 3 Å molecular sieve, and used as received.

For antisolvent crystallisation, 3000 mg ACN (73.08 mmol) was added to 152 mg fine HMX (0.51 mmol) and 1472 mg CL 20 (3.36 mmol) in 20 mL glass vessels. The solid was dissolved at 343.15 K and 800 rpm for 10 minutes. Subsequently, the solution was cooled to 333.15 K. The seed crystal suspension was added, and the reaction vessels were air tightly connected to the pump tube via teflon fittings. 2000 mg 2-propanol (33.27 mmol) was dispensed over the course of 16.6 h using a Hirschmann ROTARUS VOLUME 50I metering pump equipped with a ROTARUS MKF 12-8 12 channel pump head. During crystallisation, the temperature was kept constant at 333.15 K, and the vessels were agitated at 600 rpm. The solid phase was washed according to the standard washing procedure.[14] Five batches carried out in parallel were mixed to obtain about 1 g of cocrystal.

For BRC, 80.0 g (1.95 mol) ACN was added to 28.0 g coarse HMX (94.5 mmol) and 112.0 g (255.6 mmol) CL 20 in a 250 mL jacketed flask with a rounded bottom. The slurry was agitated at 240 rpm for 2 h at 333.15 K via an overhead stirrer equipped with a paddle stirrer. The stirrer's contour closely matches the inner wall contour of the jacketed vessel. After 2 h, the stirrer was removed and the slurry was transferred into a Büchner funnel using a BRAUN omnifix 100 mL syringe without a

cannula attached to avoid clogging. After the removal of the mother liquor, the product crystals were washed with 30 mL 1:1 2-propanol:ACN, 30 mL 2-propanol:ACN (8:2), 30 mL 2-propanol:ACN (9:1), 30 mL 2-propanol (two times), and 100 mL 2-propanol (once) to ensure the total removal of the mother liquor.

For SBRC, 122 g (2.97 mol) ACN was added to 52.95 g CL-20 (120.8 mmol) and 5.35 g coarse HMX (18.1 mmol) in a 250 mL flat bottomed jacketed flask that was temperature controlled to 333.15 K using a Lauda RC6 CP thermostat. The reaction mixture was agitated by a specially designed captured magnetic stir bar that was propelled via a Heidolph MR Hei-End magnetic stirrer set to 250 rpm. After complete dissolution and thermal equilibration, the seed crystals were added to the solution. The concentration was adjusted to ensure about 10% seed crystal dissolution to reduce surface defects that would reduce the crystal quality. After equilibrium was reached, the solid-dosing of a mixture of 90 g CL-20 (205 mmol), 25 g coarse HMX (84 mmol), and 5 g fine HMX (17 mmol) was started. The solid was dispensed by a LAMBDA Instruments GmbH DOSER 0.2L. A slow stream of pressurised air was vented through the solid-doser to prevent cementation of the solid due to ACN vapours. 1 h after all solid was dispensed, the stirrer was removed and the slurry transferred into a Büchner funnel using a BRAUN omnifix 100 mL syringe without a cannula attached to avoid clogging. The mother liquor was removed, and the product crystals were washed with 30 mL 2-propanol:ACN (8:2), 30 mL 2-propanol:ACN (9:1), and five times with 20 mL 2-propanol to ensure the total removal of the mother liquor. The crystals were dried under ambient conditions. For SBRC1 and 2, a sieve fraction of $D(4,3)=76\ \mu\text{m}$ of a failed SBRC experiment was used as seed crystals. For SBRC3 and 4, a sieve fraction $D(4,3)=132\ \mu\text{m}$ of two mixed failed SBRC batches was used as seed crystals. The two failed batches were also seeded with the same seed crystals as SBRC1 and 2. The crystals of SBRC1 and 2 were, therefore, grown in three steps and the crystals of SBRC3 and 4 are the product of four consecutive growth processes. The crystallisation time for SBRC1,2,3, and 4 was 26 h, 26.5 h, 24 h, and 20 h, respectively.

DSC analysis was carried out using a TA Instruments DSC Q2000 V24.10 build 122. Samples were heated from 298 up to 543 K at the rate of $1\ \text{K}\ \text{min}^{-1}$ in a hermetically sealed aluminium pan. The sample quantity in all experiments was between 0.5 and 1.5 mg.

The bulk density was determined using a micromeritics AccuPyc 1340 TEC $10\ \text{cm}^3$ with He 5.0

as measurement gas. The equilibration pressure change was set to the standard $0.345\ \text{hPa}\ \text{min}^{-1}$. The heating/cooling element was set to 292.95 K for all measurements to achieve an average chamber temperature close to 293.15 K. A calibration of the chamber volumes was carried out before the series of measurements. About 10 g material was weighed in using a Kern 770 analytical balance (accuracy 0.1 mg). 300 flushing cycles ensured total sample dryness during the measurement. Between 50 and 300 data points were collected for each measurement. At least two true repeat measurements were carried out for each sample. Because only 1 g of A1 was available, this density measurement was carried out in the $1\ \text{cm}^3$ measurement cell. It was shown that the required precision needed to compare the batches can only be achieved under repeat measurement conditions in the same sample cell.[15] The offset between the two cells was determined by measuring SBRC3 three times also in the $1\ \text{cm}^3$ cell, and the obtained density value for A1 was adjusted accordingly.

For solvent inclusion determination, about 50 mg samples were dissolved in dry dimethylformamide. $1\ \mu\text{m}$ solution was injected into the Agilent 6890N GC-FID equipped with a DB-624 $60\ \text{m} \times 0.25\ \text{mm}\ \text{ID} \times 1.4\ \mu\text{m}$ film column. The split ratio was 10 and the injection port temperature 503 K. The helium flow was $2\ \text{mL}\ \text{min}^{-1}$ and the column was kept at 323 K for 4 min, then heated up to 353 K with a heating rate of $5\ \text{K}\ \text{min}^{-1}$. From 353 K up to 533 K, the heating rate was $20\ \text{K}\ \text{min}^{-1}$. The detector temperature was 553 K.

Particle diameters were determined with a Malvern Mastersizer 2000 version 5.60 in 2-propanol as dispersion medium. The agitation speed was 2450 rpm. 1.69 was chosen as the refractive index, and the absorption coefficient was selected individually to obtain the best results. Three measurements each consisting of 10000 individual scans were averaged.

X-ray powder diffraction measurements were performed on a D8 Advance from Bruker AXS equipped with a copper tube, two 2.5° Soller collimators, an anti-scatter screen, a flip stick stage, and a silicon strip detector (LynxEye). Samples were milled to a particle diameter of less than $10\ \mu\text{m}$. The reflection range was scanned in $0.01^\circ\ 2\theta$ steps from 10 - $42^\circ\ 2\theta$. Each measurement was accumulated for 20 s. The data were evaluated using Rietveld analysis based on the structure data reported by Bolton *et al.*[16]

^1H NMR analysis was carried out at 300 K and 400 MHz using a Bruker spectrometer. 16 scans were averaged. 0.1 g sample was dissolved in 1 g deuterated dimethyl sulfoxide. Fourier

transformation and phase correction were carried out using SpinWorks 4.2.10.0 ©2019, Kirk Marat. Peak integration was carried out using OriginPro version 2019 9.6.0.172, OriginLab Corporation, Northampton, MA, USA.

HPLC analysis was carried out using an Agilent 1100 HPLC system equipped with a binary pump and a diode array detector. The injected sample of 1 μL was separated on a Kintex 2.6 μm C18 100 \AA 100x4.6 mm column with pre-column. A mixture of ACN and water was used as the eluent. The eluent composition was gradually changed over time. Time 1 min: 10% ACN, time 20 min: 50% ACN, time 22 min: 95% ACN, time 27 min: 95% ACN, time 28 min: 10% ACN, post-time: 11 min. The eluent flow was 0.6 ml min^{-1} . The column was heated to 308 K during the analysis. Data analysis was carried out using Agilent ChemStation. The quantification of the impurities was carried out under the assumption that the impurities exhibit the same responsiveness at the measurement wavelength of 255 nm.

Field emission- scanning electron microscope images were taken by a Zeiss SUPRA 55 VP. The samples were prepared by sputter-coating with Au/Pd (80/20). 1.5 kV was chosen to prevent sample decomposition, but still, some images of higher magnification show the formation of bubbles under the metal coating as the result of the irradiation. The height-to-width ratio was determined from these images by measuring the height of crystals and dividing this value by the length of the crystal face visible. Between 20 and 45 crystals were analysed for each batch.

Impact and friction determination were carried out according to DIN EN 13631-3 and DIN EN 13631-4.

Photomicrographs were taken using a Leica DMC4500 camera equipped with a Leica Z16APO objective. A SCHOTT KL 1500 electronic light source equipped with an Omnilux 15 V/150WGZ-6.35 halogen light bulb was attached to the microscope stand. The images were processed via Leica LAS X software. The image pixel size was 0.702 μm for all taken photomicrographs. This resolution is a compromise between detectable defect size and field of view. It is assumed that defects of the size of 2-5 μm can be resolved via brightfield photomicrographs. Even smaller defects should be visible in dark-field photomicrographs (Figure S19) which could be utilised to compare crystal batches of extremely high-quality. Between 180 and 254 individual images were taken for each batch to ensure statistical significance of the results. The crystals were immersed in a mixture of 1:0.125 mL

1-methyl naphthalene and decane. This mixture was chosen as a compromise between highlighting the internal defects and the crystal edges. If the refractive index matches too well, the edges become undetectable. If, however, the refractive index is mismatched too strongly, the internal defects might be overshadowed by surface refraction of the crystals. The algorithm used for the automated crystal quality analysis was developed by Lins, Heisel, and Wohlgemuth and is available for download.[12] A composite image produced by the algorithm is displayed in Figure 1. The degree of crystal defects (DoCD) and the position of crystal defects (PoCD) [12] is used to judge the crystal quality. These values are obtained individually for every detected crystal. After binarization of the image, the dark area caused by the crystal edge is detected and excluded from analysis. The remaining area of the dark pixels within the crystal boundary is detected, and the DoCD is calculated by dividing the dark area by the crystal area. The PoCD is determined by the position of the dark pixels relative to the centre of the detected crystal. The crystal size is calculated as the equivalent diameter, i.e. the diameter of a circle of equal area. Because these values are calculated based on a binarized two-dimensional image of the crystal, the values have only limited absolute expressiveness, but are an excellent tool for crystal quality comparison, as long as the photomicrographs have been taken under strictly the same circumstances. The dark area resulting from the crystal edges is automatically detected and removed, and typically all dark pixels in the analysed area are caused by internal defects. Three major disturbances (Figure 1), however, occur that influence the determined DoCD (and consequently the PoCD) of a crystal. The distribution and the average of the determined DoCD and PoCD are heavily influenced by these disturbances. Manual removal of detected

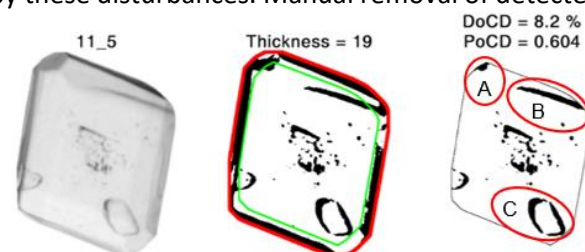


Figure 1: Visualisation of the automated detection process. Left: detected crystal. Centre: binarized image. The edge area that is excluded from detection is highlighted (area between red and green boundary). Right: analysed area of the detected crystal. Visualisation of the three main disturbances of the DoCD and PoCD determination: A) dark spots caused by the flattened edge of the crystals B) dark spots caused by surface defects C) dark spots caused by small crystals lying on the detected crystal.

crystals was, therefore, required. The number of crystals that need to be removed can be drastically reduced if a very strict exclusion of smaller crystals is achieved during classification of the crystals. To be able to estimate the human factor in the process of selecting undisturbed detected crystals and to gain a feeling for the expected deviation of the obtained distributions and averages, two strategies were pursued. In one filter process, all detected crystals were removed that showed even the most minuscule trace of one of the abovementioned disturbances. In another filter process, only severe cases were removed. The resulting average DoCD values are visualised in Figure 2. The average crystal quality improves as expected for all batches by removing the affected crystals. And while the differences between the DoCD values of the untreated and the mildly treated data vary strongly between batches, the difference in DoCD between mildly and severely treated data is far more uniform between batches. This indicates that the removal of strong disturbances improves the quality of the data and that the human factor involved in the removal of the disturbances seems to be weak. In this paper, the obtained DoCD and PoCD distribution of the strictly treated data is utilised for comparisons, because surface defects are here excluded and these defects do not influence crystal purity and density, and their inclusion would, therefore, reduce the correlation to the other analysis methods. But the strict exclusion may overestimate the crystal quality to some degree, because crystals that exhibit internal defects that look like surface defects are excluded. Therefore, half the difference between the DoCD values of mild and severe treatment is assumed as the error interval.

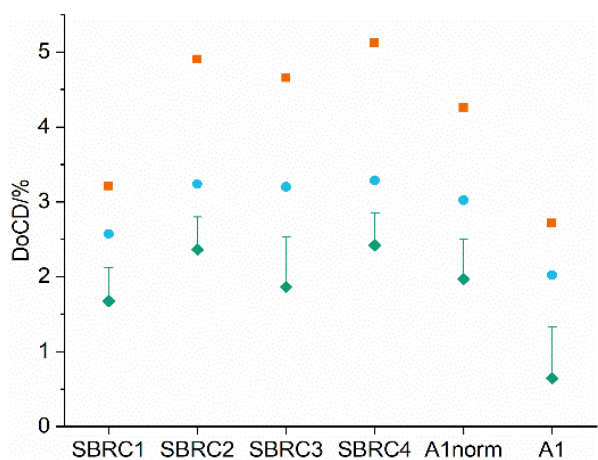


Figure 2: Determined average DoCD values of the crystal batches. Orange squares: no data treatment, teal circles mild data treatment, green diamonds strict data exclusion. Error bars represent half the difference between mild and severe data exclusion.

The SBRC batches were sieved to produce a size fraction close to 150-250 μm . These sieve fractions were used for all analysis. This was done for two reasons. On the one hand, fine particles disturb the analysis of coarser particles in the image processing as shown above, and on the other hand, for assessment of a crystallisation technique, the crystals close to the desired size are of most importance, because these are the crystals grown from the added seed crystals and not the product of secondary nucleation. Only they, therefore, can be used to judge the impact of the seed crystal quality and the seeding procedure on the product crystal quality. Because only 1 g of A1 is available, no sieving could be performed without significant material loss in the process. Here, after image processing, based on the crystal size, a certain amount of data sets was removed to obtain a normal distribution centred around 200 μm . This data ensemble is called A1norm. To retain correlation between the image processing data and the data of the other analysis methods for A1, analysis of the image processing was carried out for the non-normalised data in addition to the normalised data.



Figure 3: Representative photomicrographs of BRC1 (top left), A1 (top right), SBRC1 (mid left), SBRC2 (mid right), SBRC3 (bottom left), and SBRC4 (bottom right).

3 Results

3.1 Conventional approaches

Analysis results are summarised in Table 1. Representative photomicrographs are displayed in Figure 3. All cocrystal batches are more than 99.9% phase pure and exhibit a chemical purity between 99.62% (SBRC1 and 3) and 99.93% (SBRC4) based on HPLC. Based on ^1H NMR, the purity ranges between 98.95% (BRC1) and 99.68% (A1). BRC1's solvent content is almost 20 times higher than the solvent content of SBRC1,2,4 and A1. SBRC3 possesses a slightly higher solvent content than the other SBRC batches. The skeletal density of BRC1 is, based on the determined precision of helium pycnometry,[15] barely significantly less dense than the other batches, whereas SBRC4 is barely significantly denser than the other batches. All densities lie within a 0.002 g cm^{-3} interval and are on average 0.009 g cm^{-3} higher than the density reported by Bolton *et al.*[16] BRC1 possesses the best impact and friction sensitivity of the tested batches. The decomposition onset in DSC analysis of all batches lies within an interval of 1.8 K. SEM images (Figure S1-S6) show that all crystals exhibit a mostly smooth crystal surface.

3.2 Digital Image Processing

The crystals obtained from BRC experiments are too small, irregular, and intergrown to be analysed via image processing.

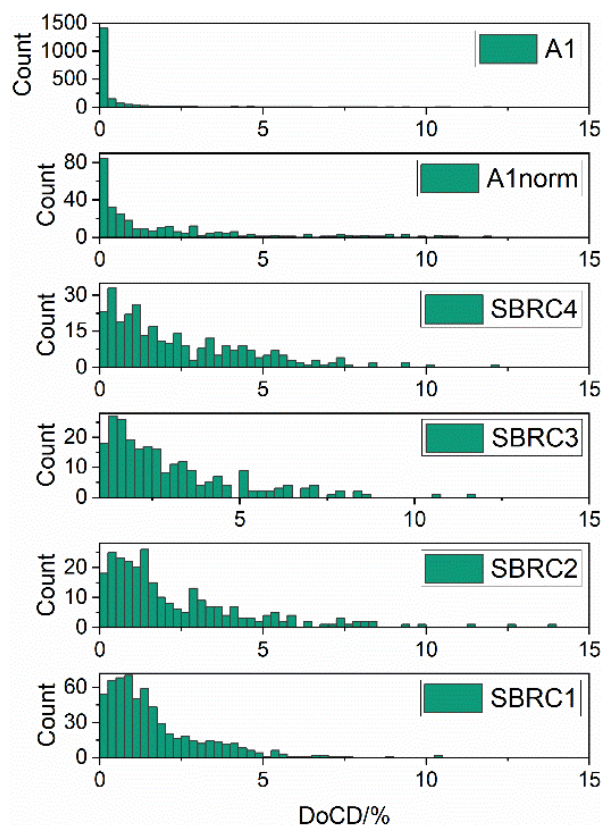


Figure 4: Distributions of DoCD for all batches. All bins are of size 0.25%.

The DoCD and the PoCD of the SBRC and A1 crystals have been analysed and the results are visualised in Figure 2, 4, 5, and Table 2.

The SBRC DoCD distributions can be satisfactorily described by a Weibull distribution.[17] No satisfactory fit, however, was achieved for A1 and A1norm. From Figure 4 it can be seen that A1's and A1norm's distribution maximum is the first bin

Table 1: Analysis data of the cocrystal batches

| | BRC1 | SBRC1 | SBRC2 | SBRC3 | SBRC4 | A1 |
|--------------------------------------|--------|--------|--------|--------|--------|--------|
| purity (^1H)/% | 98.95 | 99.39 | 99.48 | 99.31 | 99.54 | 99.68 |
| purity (HPLC)/% | 99.87 | 99.62 | 99.89 | 99.62 | 99.93 | 99.84 |
| phase purity/% | 100 | 100 | 100 | 99.91 | 100 | 99.93 |
| solvent content/mass% | 0.19 | 0.01 | 0.01 | 0.02 | 0.01 | 0.01 |
| skeletal density/ g cm^{-3} | 1.9533 | 1.9545 | 1.9544 | 1.9540 | 1.9553 | 1.9545 |
| impact sensitivity/Nm | 4.5 | 1.5 | 2 | 2 | 1.5 | 3 |
| friction sensitivity/N | 192 | 120 | 144 | 144 | 160 | 120 |
| decomposition onset/K | 492.05 | 491.85 | 490.25 | 490.95 | 491.15 | 491.15 |
| D(4,3)/ μm | 35 | 163 | 137 | 159 | 179 | 160 |
| height-to-width ratio | n.d. | 0.60 | 0.80 | 0.62 | 0.71 | 0.55 |

Table 2: Image processing data of the cocrystal batches

| | SBRC1 | SBRC2 | SBRC3 | SBRC4 | A1norm | A1 |
|--------------------------------|-------|-------|-------|-------|--------|------|
| Nr. of detected crystals | 1474 | 1282 | 1257 | 1182 | 3071 | 3071 |
| Nr. of evaluated crystals | 610 | 267 | 445 | 301 | 286 | 1963 |
| average DoCD/% | 1.7 | 2.4 | 1.9 | 2.4 | 2.0 | 0.6 |
| error margin of average DoCD/% | 0.4 | 0.4 | 0.7 | 0.4 | 0.5 | 0.7 |
| median of DoCD/% | 1.2 | 1.5 | 1.2 | 1.7 | 0.8 | 0.0 |
| average PoCD | 0.46 | 0.52 | 0.45 | 0.43 | 0.47 | 0.49 |
| median PoCD | 0.43 | 0.51 | 0.44 | 0.41 | 0.46 | 0.46 |

between 0 and 0.25% DoCD, whereas the maxima for the SBRC batches are reached between 0.25 and 1.5% DoCD. SBRC1 possesses the narrowest distribution except for A1. Considering the proposed error margin, the average DoCD of A1 is significantly smaller than the average DoCD of all other batches. The average DoCD of SBRC1 is significantly smaller than the average DoCD of SBRC2 and 4, and the average of A1norm is indistinguishable from the averages of SBRC1,2,3, and 4. The DoCD of A1 and A1norm is strongly crystal size dependent (Figure S17). This can easily be seen from the difference in average DoCD between A1norm and A1 in Figure 2. A1 shows a strong increase in DoCD with increasing particle size. For SBRC1 and 3 a weak increase in DoCD with particle size is observed, but for SBRC2 and 4, a weak decrease in DoCD with increasing particle size is present (Figure S13-S16).

The distribution of PoCD of all batches can be approximated by a normal distribution (Figure S7-S12). Their distribution is visualised as the respective box plot (Figure 5).[18] The distribution of the PoCD is wider for SBRC2 and A1norm than of the rest. The medians of all batches lie close to 0.5 PoCD. Only A1 exhibits PoCD smaller than 0.15 while all batches possess PoCD greater than 0.85.

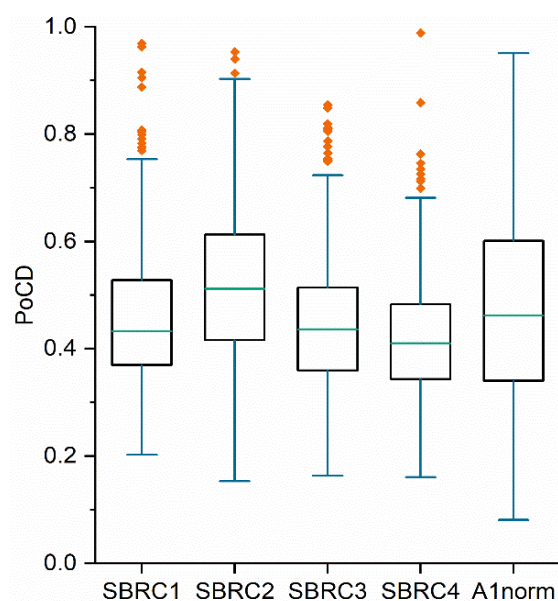


Figure 5: Box plots of the PoCD values of the evaluated batches. The green horizontal line represents the median of the data, the box represents the position of 50% of the data, the blue so-called whiskers indicate the data that lie within 1.5 times the box height (interquartile range IQR), and the orange rhombs visualise the outliers.

4 Discussion

The purity data obtained from HPLC and ^1H NMR are in good agreement (except for BRC1). The average offset between the data of 0.3% is most likely the result of different sensitivities of the two

methods towards the compounds. The lower ^1H NMR purity of BRC1 is the result of its higher ACN content caused by the more rapid crystallisation. The solvent inclusion does not lower the HPLC purity, because ACN is not detected via the HPLC method. Cocrystallisation improves chemical purity compared to the raw material, but the prolonged exposure to elevated temperature during the crystallisations increases signal intensity of some impurity signals, and even new signals occur, in the SBRC experiments (Table S1 and S2). The significantly lower purity of SBRC1 and 3 compared to SBRC2 and 4 is caused by the utilised nickel plated magnetic stir bar, which led to a weak brown discolouration of the crystallin product. For SBRC2 and SBRC4 the stir bar was coated with epoxy resin to prevent any chemical reaction. The varying amounts of impurities seem to not influence the decomposition temperature in DSC measurements. Because of the faster crystallisation of BRC1, RDX impurity can only be found in this cocrystal batch in the ^1H NMR and HPLC. The lower impact sensitivity of BRC1 compared to the SBRC batches might be considered significant, but is most likely the result of the smaller particle size or the more clustered particles. In the past, four BRC batches produced in a similar fashion and of similar particle size possessed an impact sensitivity between 1 and 2 Nm. The impact sensitivity of 4 Nm might, therefore, be anomalous.

Based on studies carried out for RDX where the determined density was linked to the amount of internal defects, [7,8] a strong correlation should be expected between the DoCD values of the cocrystal batches and the determined densities. No such correlation, however, exists between the determined data. The significantly better average and median DoCD values of A1 compared to SBRC1 and the significantly better values of SBRC1 compared to the other SBRC batches disagree with the determined density values. A1 should exhibit the highest density followed by SBRC1. The precision of pycnometric density determination of explosives has been previously studied [15] and based on these results it can be stated with statistical backing that the density of SBRC1 is not significantly different from the density of SBRC2 and SBRC3, and that SBRC4 is slightly, but significantly denser than the other SBRC batches. The measurement error of A1's density determination is larger (0.0012 g cm^{-3} compared to 0.0003 g cm^{-3}) because it was determined in a smaller sample cell. Still, within these limits, A1 cannot possess a significantly higher density than SBRC4. Considering that the average DoCD of SBRC4 is significantly higher than the average DoCD of SBRC1 (and of A1),

this is exactly an inverse correlation between DoCD and skeletal density. Because of a lack of a significant crystal size dependency (Figure S13-S16) of the SBRC experiments, the increase in crystal height seems to be of lesser importance to the DoCD values of these batches. This, consequently, means the DoCD value need not be adjusted for the difference in height-to-width ratio between the batches. The varying height-to-width ratios between batches (Table 1), hence, should not be responsible for the discrepancy between density and DoCD. The relatively high density of BRC1, despite its high solvent content, indicates that A1 and the SBRC batches possess significantly more gas inclusions. This might be the result of the ongoing decomposition of CL-20 during the crystallisation, and BRC1 exhibits, because of the fast crystallisation, considerably less decomposition than SBRC1,2,3 and A1. The higher density of SBRC4 could also correlate with the lower decomposition content compared to the other SBRC batches and A1. This agrees with SBRC4 having the shortest crystallisation time of all SBRC batches. The image processing does not differentiate between gas and liquid inclusions, but in conjunction with density measurement and solvent content determination differentiation seems to be possible.

The PoCD values can give insight into the cause of the crystal defect. Preliminary antisolvent crystallisation batches showed a strong variation of the PoCD. Eccentric defects were the result of crystal edge damage caused by abrasion, while defects located in the centre of the crystals indicated insufficient seed crystal dissolution (Figure S20). The intermediate values for all tested batches in this paper and their substantial standard deviation, however, do not allow for a conclusion based on PoCD.

Based on the various crystal analysis methods, the following statements can be made.

The purification of the raw material by cocrystallisation is to some degree offset by the increased decomposition products present in the cocrystals of A1 and SBRC batches. A reduction of crystallisation time might improve the crystal quality. All SBRC batches are indistinguishable from A1norm via image processing, and no significant difference between the SBRC batches and A1 exists in the other analysis methods (except for the slightly higher density of SBRC4). The average DoCD values of the SBRC batches and A1norm lie around 2% which corresponds to a quite pristine-looking crystal as can be seen from the comparison in Figure S18. SBRC is, thus, capable of producing coarse CL-20/HMX cocrystal in the pilot plant-scale

with the same crystal quality as antisolvent crystallisation in the laboratory-scale. A1, however, exhibits a significantly better average DoCD than the SBRC batches, because of the sizeable amount of smaller crystals with a DoCD of 0%. This means that by applying image processing of photomicrographs a significant differentiation between A1 and the SBRC batches was possible while no established analysis method, with the possible exception of neutron scattering [19] and density flotation, [20] could yield significant results. Great advantages of image processing are that no exotic equipment is needed for the analysis and that extremely small sample quantities are required. This makes this method ideal for the further development of crystallisation experiments, especially in the laboratory-scale. More thorough removal of fine crystals before analysis is required to reduce the DoCD error bar sizes. Even though no image processing of BRC1 was possible and the density is only marginally lower than the densities of the other batches, it is obvious from the photomicrograph (Figure 3) and the SEM image (Figure S6) that the crystal quality is not as good as the crystal quality of the other batches.

5 Conclusion

¹H NMR and HPLC showed that the chemical purity of the obtained cocrystals from antisolvent crystallisation and SBRC is higher than the chemical purity of the raw material. Image processing was used to determine that the DoCD of SBRC is not crystal size dependent but the DoCD of laboratory-scale antisolvent crystallisation is. Furthermore, it was found that SBRC is capable of producing the CL-20/HMX cocrystal in a pilot plant-scale in a size range of 150-250 μm with the same crystal quality as laboratory-scale antisolvent crystallisation. Because of the small required sample mass, digital image processing is a valuable tool for crystallisation optimisation especially in the laboratory-scale and is capable of comparing samples of vastly different production scales. Further work is required to correlate the determined DoCD values with shock sensitivity tests and to reduce the error bars of the average DoCD values.

Acknowledgements

We are grateful for financial support provided by the German Ministry of Defence and the support provided by Dr. Manfred Kaiser and Dr. Michael Koch at the WTD91. Open access funding enabled and organised by Projekt DEAL.

References

- [1]
- [1a] V. J. Bellitto, M. I. Melnik, Surface defects and their role in the shock sensitivity of cyclotrimethylene-trinitramine, *Appl. Surf. Sci.* **2010**, *256*, 3478–3481, <https://doi.org/10.1016/j.apsusc.2009.12.060>;
- [1b] R. H. B. Bouma, W. Duvalois, A. E. D. M. van der Heijden, Microscopic characterization of defect structure in RDX crystals, *J. Microsc.* **2013**, *252*, 263–274, <https://doi.org/10.1111/jmi.12088>;
- [2] L. Borne, A. Beaucamp, D. Fendeleur, Metrology tools for the characterization of explosive crystal properties, in: *Int. Annual Conf. of ICT 1998*, V16.
- [3] H. Chen, L. Li, S. Jin, S. Chen, Q. Jiao, Effects of Additives on ϵ -HNIW Crystal Morphology and Impact Sensitivity, *Propellants, Explos., Pyrotech.* **2012**, *37*, 77–82, <https://doi.org/10.1002/prop.201000014>.
- [4] L. Borne, H. Ritter, HMX as an Impurity in RDX Particles: Effect on the Shock Sensitivity of Formulations Based on RDX, *Propellants, Explos., Pyrotech.* **2006**, *31*, 482–489, <https://doi.org/10.1002/prop.200600066>.
- [5] V. Stepanov, R. B. Patel, R. Mudryy, H. Qiu, Investigation of Nitramine-Based Amorphous Energetics, *Propellants, Explos., Pyrotech.* **2016**, *41*, 142–147, <https://doi.org/10.1002/prop.201500118>.
- [6] R. H. B. Bouma, A. E. D. M. van der Heijden, The Effect of RDX Crystal Defect Structure on Mechanical Response of a Polymer-Bonded Explosive, *Propellants, Explos., Pyrotech.* **2016**, *41*, 484–493, <https://doi.org/10.1002/prop.201500222>.
- [7] A. E. D. M. van der Heijden, R. H. B. Bouma, A. C. van der Steen, Physicochemical Parameters of Nitramines Influencing Shock Sensitivity, *Propellants, Explos., Pyrotech.* **2004**, *29*, 304–313, <https://doi.org/10.1002/prop.200400058>.
- [8] L. Borne, J.-C. Patedoye, C. Spyckerelle, Quantitative Characterization of Internal Defects in RDX Crystals, *Propellants, Explos., Pyrotech.* **1999**, *24*, 255–259, [https://doi.org/10.1002/\(SICI\)1521-4087\(199908\)24:4<255:AID-PREP255>3.0.CO;2-2](https://doi.org/10.1002/(SICI)1521-4087(199908)24:4<255:AID-PREP255>3.0.CO;2-2).
- [9] L. Borne, Influence of intragranular cavities of RDX particle batches on the sensitivity of cast wax bonded explosives, in: *Tenth Int. Symp. on Detonation 1993*, 286-293.
- [10] R. M. Doherty, D. S. Watt, Relationship Between RDX Properties and Sensitivity, *Propellants, Explos., Pyrotech.* **2008**, *33*, 4–13, <https://doi.org/10.1002/prop.200800201>.
- [11] [11a] J.-W. Kim, J.-K. Kim, H.-S. Kim, K.-K. Koo, Application of Internal Seeding and Temperature Cycling for Reduction of Liquid Inclusion in the Crystallization of RDX, *Org. Process Res. Dev.* **2011**, *15*, 602–609, <https://doi.org/10.1021/op100334y>; [11b] J.-W. Kim, J.-K. Kim, H.-S. Kim, K.-K. Koo, Characterization of Liquid Inclusion of RDX Crystals with a Cooling Crystallization, *Cryst. Growth Des.* **2009**, *9*, 2700–2706, <https://doi.org/10.1021/cg801343b>;
- [12] J. Lins, S. Heisel, K. Wohlgemuth, Quantification of internal crystal defects using image analysis, *Powder Technol.* **2021**, *377*, 733–738, <https://doi.org/10.1016/j.powtec.2020.09.015>.
- [13] D. Herrmannsdörfer, T. M. Klapötke, Semibatch Reaction Crystallisation for Scaled-up Production of High-Quality CL-20/HMX Cocrystal: Efficient because of Solid-Dosing, *Cryst. Growth Des.* **2021**, *21*, 1708-1717, <https://doi.org/10.1021/acs.cgd.0c01611>.
- [14] D. Herrmannsdörfer, P. Gerber, T. Heintz, M. J. Herrmann, T. M. Klapötke, Investigation Of Crystallisation Conditions to Produce CL-20/HMX Cocrystal for Polymer-bonded Explosives, *Propellants, Explos., Pyrotech.* **2019**, *44*, 668–678, <https://doi.org/10.1002/prop.201800332>.
- [15] D. Herrmannsdörfer, T. M. Klapötke, High-Precision Density Measurements of Energetic Materials for Quality Assessment, *Propellants, Explos., Pyrotech.* **2021**, *46*, 1-16 <https://doi.org/10.1002/prop.202000272>.
- [16] O. Bolton, L. R. Simke, P. F. Pagoria, A. J. Matzger, High Power Explosive with Good Sensitivity: A 2:1 Cocrystal of CL-20:HMX, *Cryst. Growth Des.* **2012**, *12*, 4311–4314, <https://doi.org/10.1021/cg3010882>.
- [17] W. Weibull, A Statistical Distribution Function Of Wide Applicability, *J. Appl. Mech.* **1951**, *18*, 293–297.
- [18] R. McGill, J. W. Tukey, W. A. Larsen, Variations of Box Plots, *Am. Stat.* **1978**, *32*, 12–16, <https://doi.org/10.1080/00031305.1978.10479236>
- [19] J. T. Mang, C. B. Skidmore, R. P. Hjelm, P. M. Howe, *Quantification of Microstructural Features in Hmx Using Small Angle Neutron Scattering Techniques* 1998, Los Alamos National Lab.
- [20] L. Borne, J.-C. Patedoye, Saint-Louis, Institut Franco-Allemand De Recherches De, *Device for measuring the density of particles by flotation*, US 2008/0011079 A1, 2008.

Quality Assessment of the CL-20/HMX Cocrystal Utilising Digital Image Processing

Dirk Herrmannsdörfer,^{[a]*} Thomas M. Klapötke^[b]

[a] *Energetic Materials Fraunhofer Institute for Chemical Technology ICT Joseph-von-Fraunhofer-Str. 7 76327 Pfinztal, Germany*

[b] *Department of Chemistry Energetic Materials Research Ludwig-Maximilian University of Munich Butenandtstr. 5 - 13 (Haus D) 81377 Munich, Germany*

*Corresponding Author: dirk.herrmannsdoerfer@ict.fraunhofer.de

Content

Table S1: HPLC signals

Table S2: ¹H NMR signals

Figure S1-S6: SEM images

Figure S7-S12: Distributions of PoCD

Figure S13-S17: Size dependency of DoCD

Figure S18: Visualisation of different DoCD

Figure S19: Visualisation of bright-field and dark-field

Figure S20: Comparison of crystal defect positions

Table S1: HPLC signals of the raw product and the cocrystal batches^a

| retention time/min | signal intensity/% | | | | | | | | |
|-----------------------|--------------------|---------------|--------|--------------------|--------|--------|--------|--------|--------|
| | HMX fine | HMX coarse | CL-20 | SBRC1 | SBRC2 | SBRC3 | SBRC4 | BRC1 | A1 |
| 1.1 | | | 0.011 | | | | | | |
| 1.2 | | 0.002 | | 0.009 | | | | | |
| 1.8 | 0.004 | | | | | | | | |
| 7.3 | 0.082 | 0.031 | | | | 0.005 | | 0.012 | |
| 8.8 | 0.152 | | | | | | | | |
| 9.2 | | 0.079 | | | | 0.005 | | 0.018 | |
| 12.2 | 0.021 | | | | | | | | |
| 13.2 ^c | 0.391 | 0.007 | | | | | | 0.003 | |
| 13.6 | 99.266 | 99.882 | | 31.568 | 32.129 | 32.152 | 32.231 | 32.129 | 32.082 |
| 16.0 | 0.004 | | | | | | | | |
| 17.4 | | | | 0.005 ^b | | 0.009 | | | |
| 18.1 | 0.005 | | | | | | | | |
| 19.6 | | | 0.265 | | | | | | |
| 20.3 | | | | | | | | 0.007 | |
| 20.5 | 0.020 | | 0.047 | 0.204 | 0.014 | 0.185 | | | 0.006 |
| 21.2 | | | 0.017 | 0.140 | 0.069 | 0.144 | 0.050 | 0.042 | 0.132 |
| 22.1 | 0.022 | | 0.156 | 0.015 | 0.014 | 0.021 | 0.011 | 0.039 | 0.010 |
| 23.6 | 0.010 | | 99.418 | 68.047 | 67.757 | 67.472 | 67.694 | 67.742 | 67.759 |
| 23.9 | 0.022 | | 0.087 | | 0.007 | 0.006 | 0.008 | 0.010 | 0.006 |

^a Only signals above 0.005% are listed

^b All red numbers are new or more intense signals in the cocrystal batches compared to the raw product.

^c RDX

Table S2: ¹H signals of the raw product and the cocrystal batches^a

| chemical shift/ppm | signal intensity/% | | | | | | | | |
|--------------------|--------------------|------------|-------|-------------------|-------|-------|-------|-------|-------|
| | HMX fine | HMX coarse | CL-20 | SBRC1 | SBRC2 | SBRC3 | SBRC4 | BRC1 | A1 |
| 9.57 | 0.01 | | | | | | | | |
| 8.48 | 0.03 | | | 0.03 | | | | | |
| 8.32 | 0.01 | | | | | | | | |
| 8.14 | | | 0.03 | 0.02 | 0.04 | | 0.01 | 0.03 | 0.03 |
| 8.05 | | | 0.05 | 0.07 ^b | 0.09 | 0.09 | | 0.08 | |
| 8.04 | | | | | | | 0.04 | | |
| 8.03 | | | 98.79 | 59.65 | 59.66 | 59.55 | 59.61 | 59.29 | 59.83 |
| 8.02 | | | | | | 0.01 | | | |
| 7.95 | | | | 0.09 | 0.10 | 0.10 | 0.12 | 0.06 | |
| 7.93 | | | | 0.01 | | 0.01 | | | |
| 7.90 | | | | | | | 0.01 | 0.01 | |
| 7.82 | | | | 0.03 | | 0.02 | | | |
| 7.62 | | | 0.02 | 0.02 | | 0.02 | 0.01 | | 0.02 |
| 7.53 | | | | | | 0.03 | | | |
| 7.39 | | | 0.02 | | | | | | |
| 7.35 | | | 0.02 | | | | | | |
| 7.29 | | | 0.04 | | | | | | |
| 7.27 | | | 0.01 | | | | | | |
| 7.24 | | | 0.05 | | | | | | |
| 7.19 | | | 0.01 | | | | | | |
| 7.18 | | | 0.01 | | | | | | |
| 7.17 | | | 0.16 | | | | | | |
| 7.15 | | | 0.01 | | | | | | |
| 7.03 | | | | 0.03 | | 0.03 | | | |
| 6.55 | | | 0.05 | | | | | | |
| 6.37 | 0.01 | | | | | | | | |
| 6.14 | 0.14 | 0.15 | | 0.04 | 0.06 | 0.05 | 0.06 | 0.06 | 0.06 |
| 6.11 ^c | 0.45 | | | | | | | <0.01 | |
| 6.09 | 0.03 | 0.10 | | 0.03 | 0.05 | 0.04 | 0.01 | 0.03 | 0.03 |
| 6.03 | 98.90 | 99.50 | | 39.74 | 39.82 | 39.77 | 39.93 | 39.66 | 39.85 |
| 5.99 | 0.03 | 0.11 | | 0.06 | 0.07 | 0.06 | 0.08 | 0.04 | 0.04 |
| 5.94 | 0.00 | | | 0.01 | | 0.01 | | | |
| 5.90 | 0.03 | | | | | | | | |
| 5.87 | 0.01 | | | | | | | | |
| 5.80 | 0.01 | | | | | | | | |
| 5.79 | 0.02 | | | | | | | | |
| 5.71 | 0.01 | | | | | | | | |
| 5.56 | 0.12 | 0.07 | | | | | | 0.02 | |
| 4.60 | 0.03 | | | | | | | | |
| 4.28 | | 0.02 | | | | | | | |
| 2.33 | | 0.02 | | | | | | | |
| 2.30 | | | 0.10 | | | | | | |
| 2.27 | 0.06 | 0.03 | | | | | | | |
| 2.15 | | | 0.03 | 0.07 | 0.03 | 0.06 | 0.02 | 0.01 | 0.05 |
| 2.09 | 0.09 | | 0.56 | | | | | | |
| 2.07 | 0.03 | | | 0.05 | 0.04 | 0.06 | 0.05 | 0.66 | 0.06 |
| 1.99 | | | | 0.01 | | | 0.01 | 0.01 | |
| 1.91 | 0.02 | | 0.03 | | | | | | |
| 1.89 | 0.01 | | | | | | | | |
| 1.24 | | | 0.02 | 0.01 | | | 0.01 | 0.01 | |
| 1.15 | 0.01 | | | 0.02 | 0.02 | 0.02 | 0.02 | 0.03 | |

^a Only signals above 0.005% are listed^b All red numbers are new or more intense signals in the cocrystal batches compared to the raw product.^c RDX

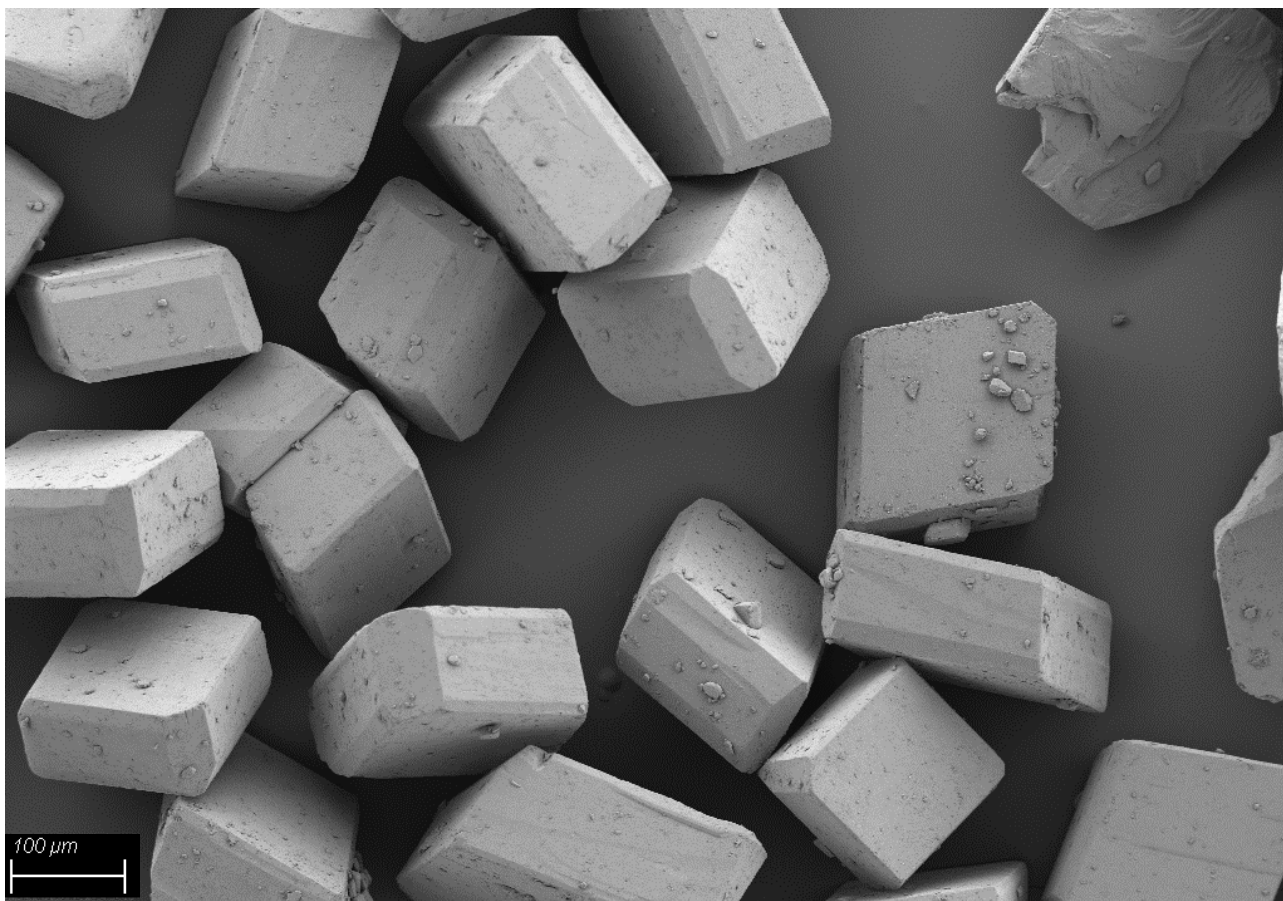


Figure S1: SEM image of SBRC1.

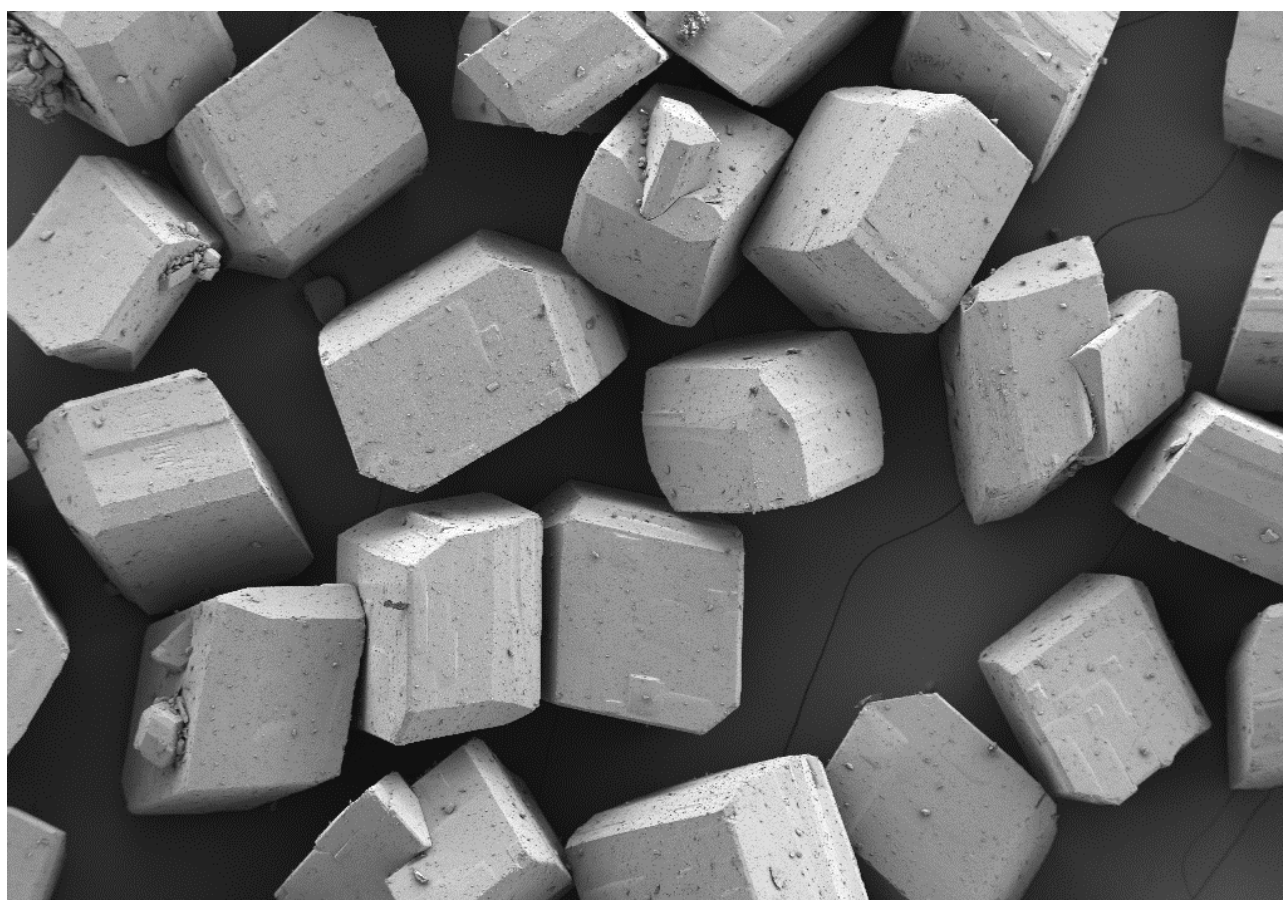


Figure S2: SEM image of SBRC2.

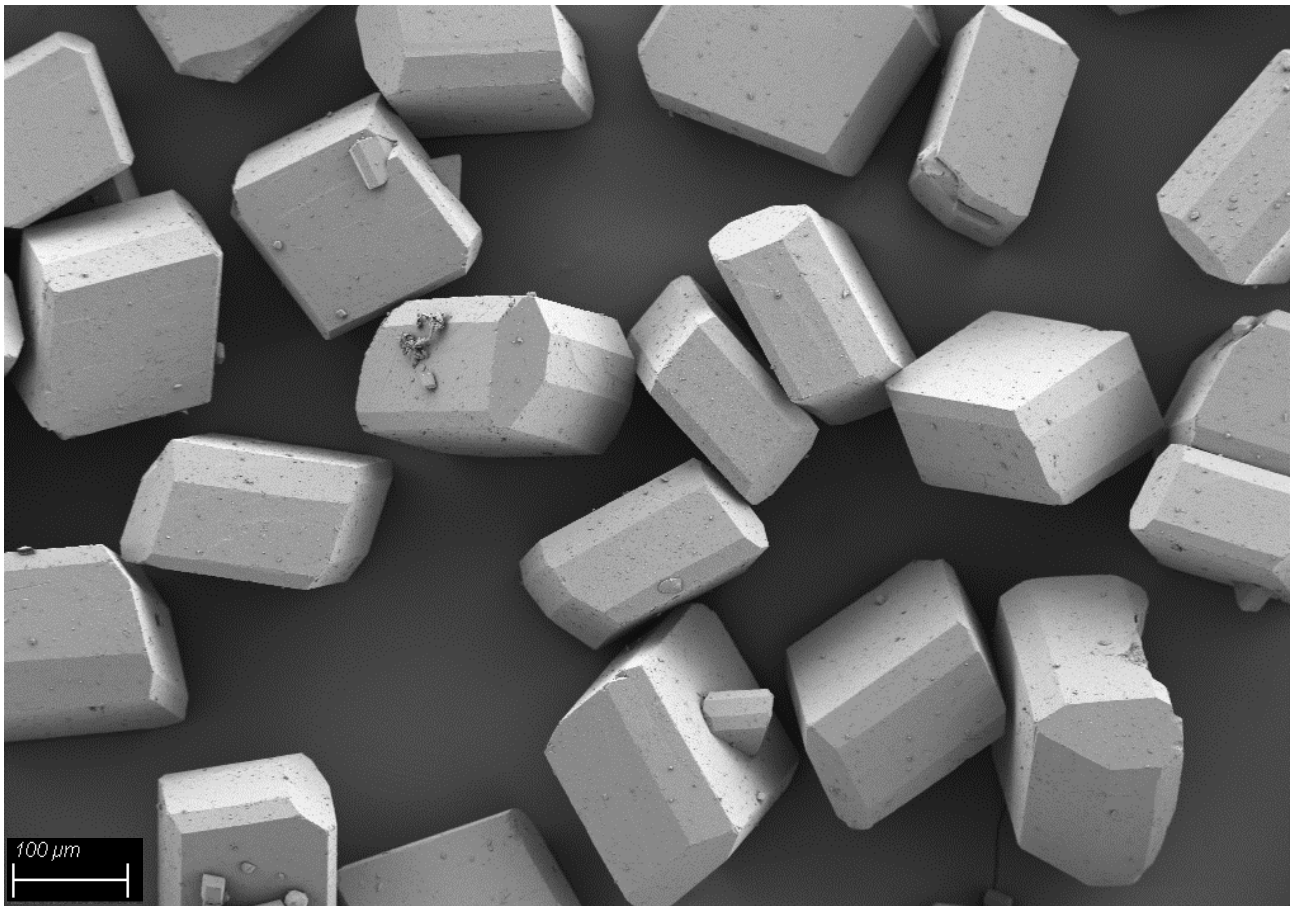


Figure S3: SEM image of SBRC3.

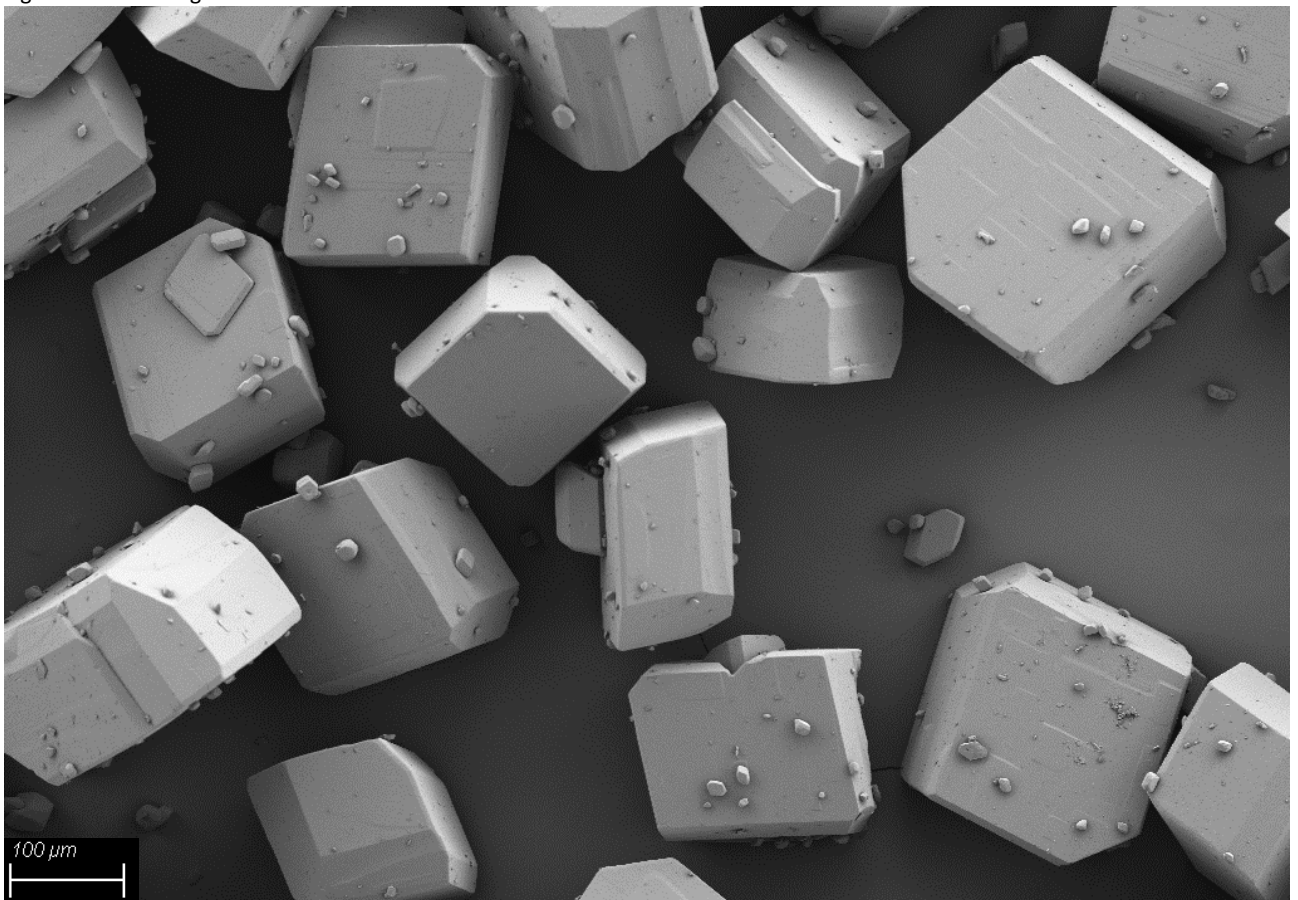


Figure S4: SEM image of SBRC4.

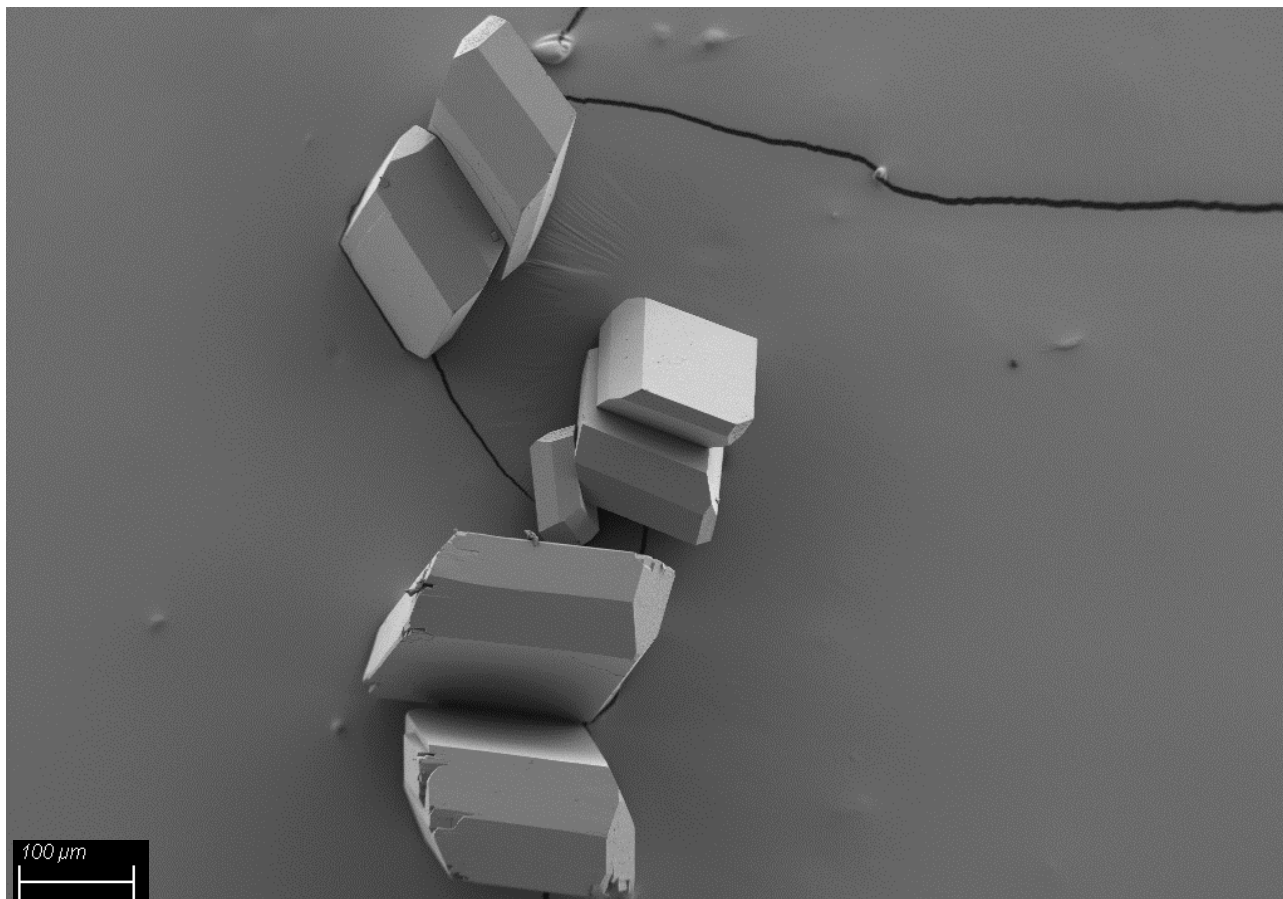


Figure S5: SEM image of A1.

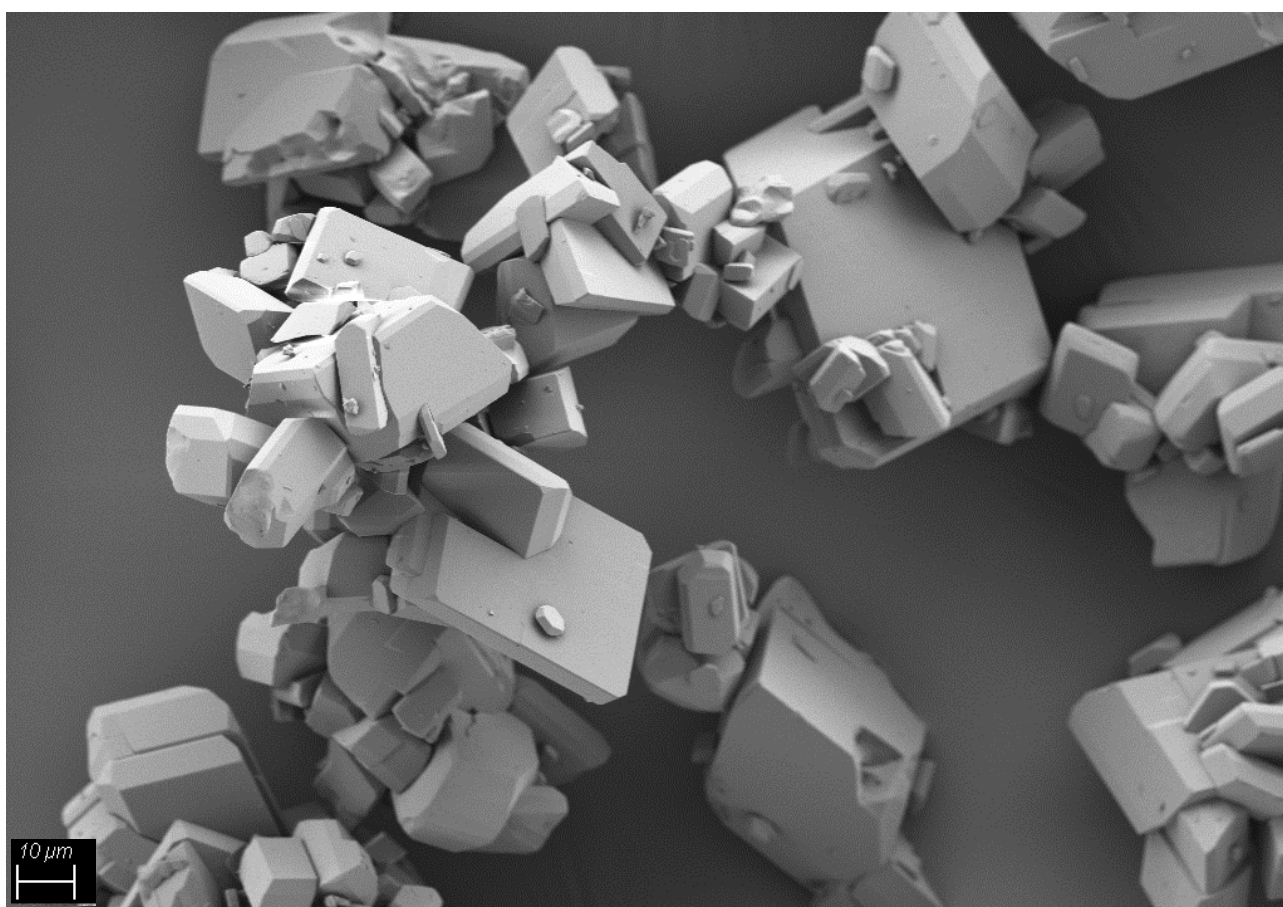


Figure S6: SEM image of BRC1.

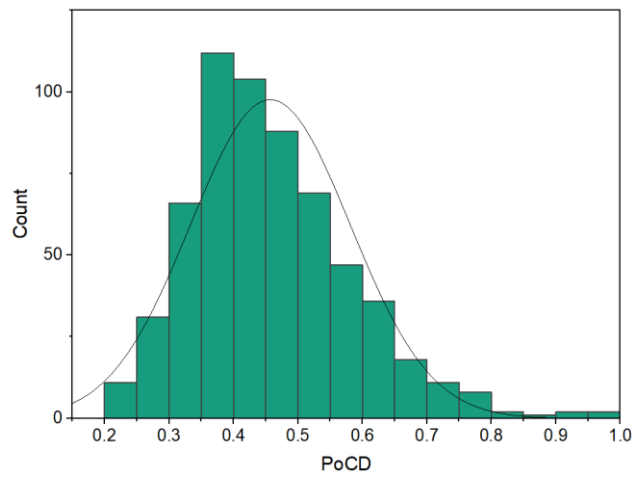


Figure S7: PoCD distribution of SBRC1.

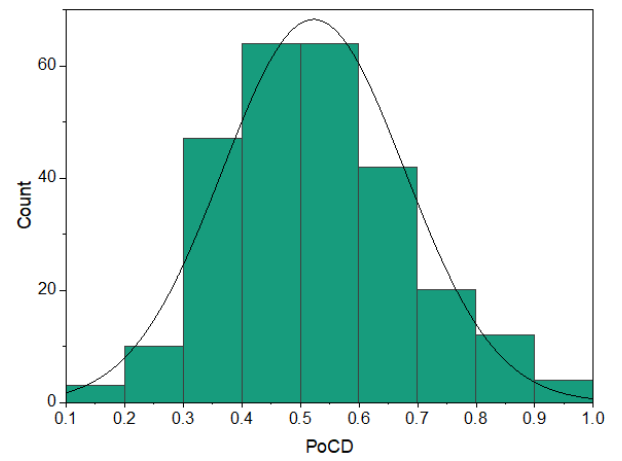


Figure S8: PoCD distribution of SBRC2.

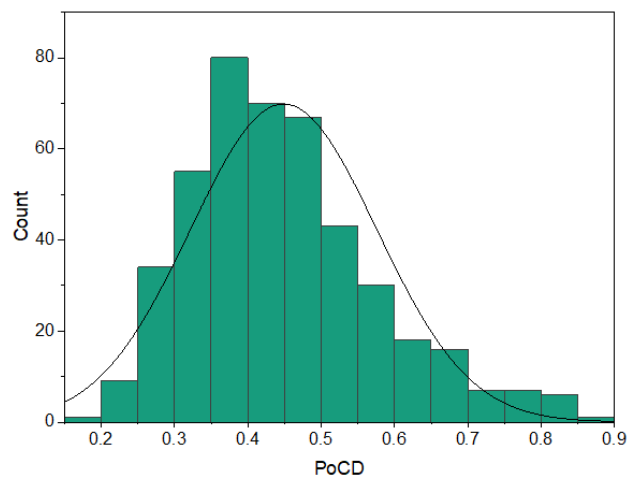


Figure S9: PoCD distribution of SBRC3.

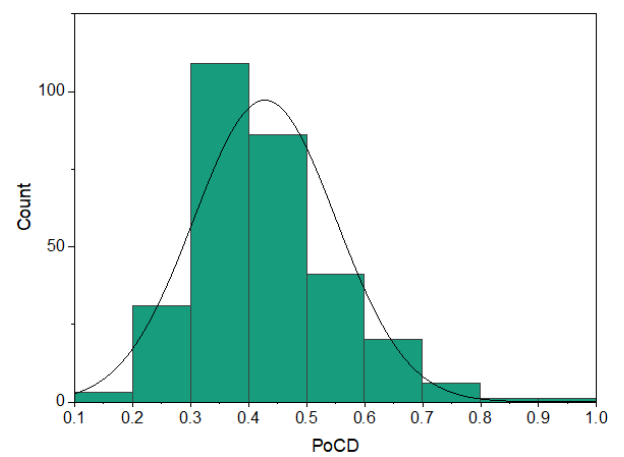


Figure S10: PoCD distribution of SBRC4.

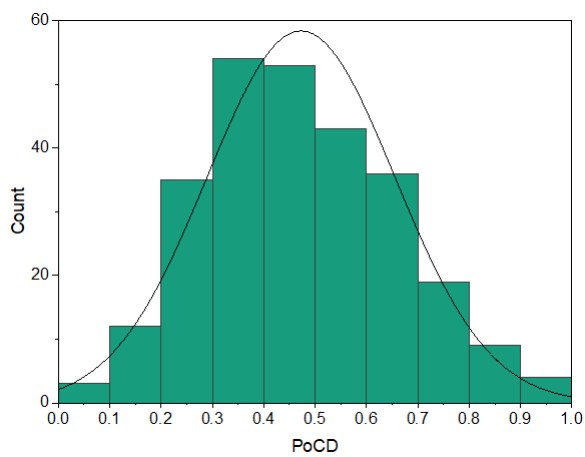


Figure S11: PoCD distribution of A1norm.

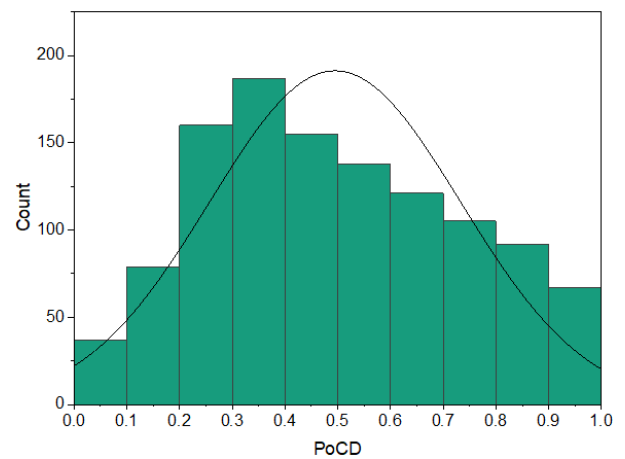


Figure S12: PoCD distribution of A1.

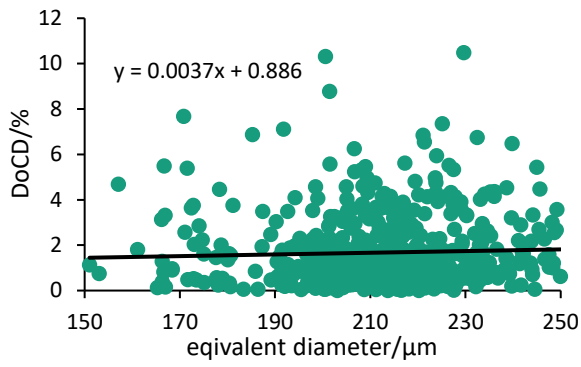


Figure S13: Crystal size dependency of the DoCD of SBRC1.

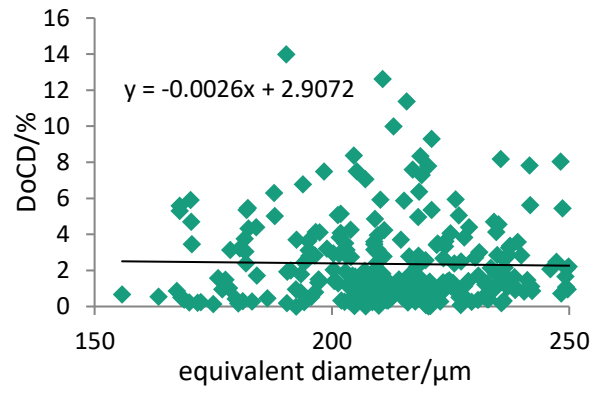


Figure S14: Crystal size dependency of the DoCD of SBRC2.

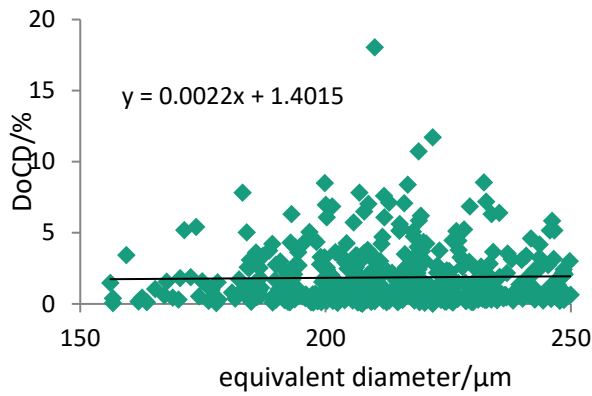


Figure S15: Crystal size dependency of the DoCD of SBRC3.

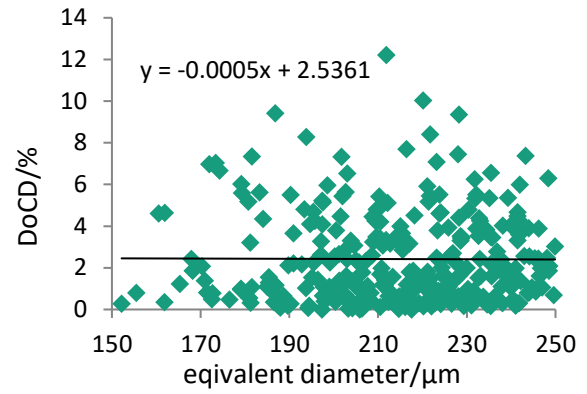


Figure S16: Crystal size dependency of the DoCD of SBRC4.

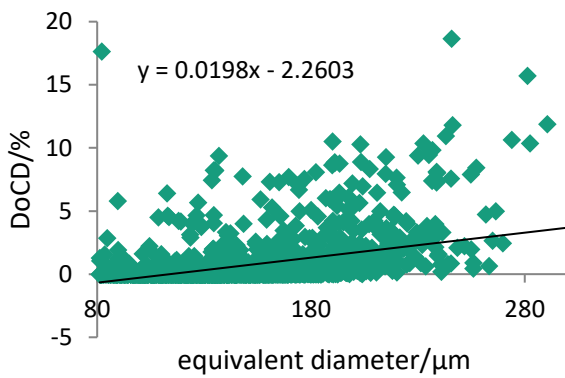


Figure S17: Crystal size dependency of the DoCD of A1.

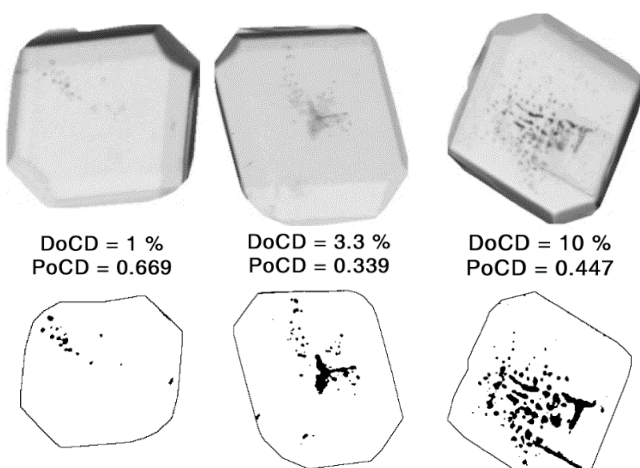


Figure S18: Visualisation of crystals exhibiting 1%, 3.3%, and 10% DoCD.

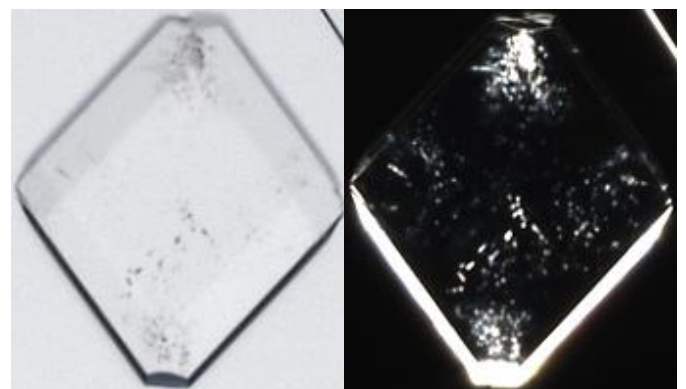


Figure S19: Visualisation of the stronger visibility of defects in dark-field (right) than bright-field (left).

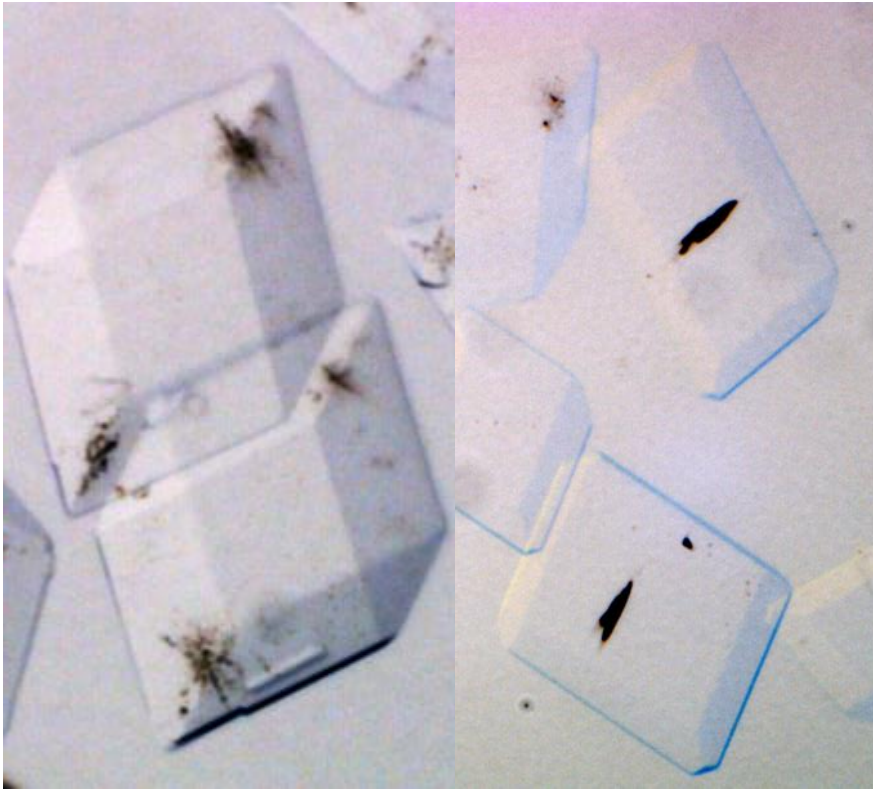


Figure S20: Comparison of crystal defect positions. Defects caused by crystal collisions (left) and defects caused by imperfect seeding (right).

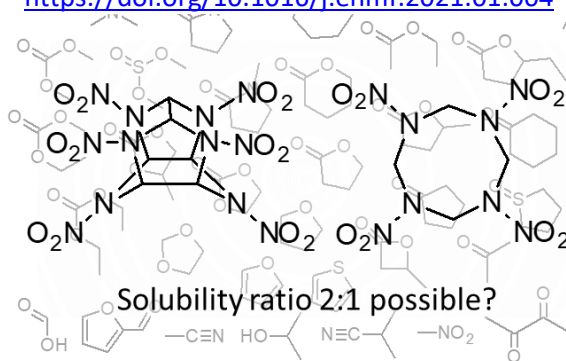
6 Solubility Determination of the Coformers

6.1 Solubility Behaviour of CL-20 and HMX in Organic Solvents and Solvates of CL-20

Dirk Herrmannsdörfer, Jörg Stierstorfer, Thomas M. Klapötke

Energetic Materials Frontiers **2021**, 2, 1, 51-61

<https://doi.org/10.1016/j.enmf.2021.01.004>



Abstract: 2,4,6,8,10,12-Hexanitro-2,4,6,8,10,12-hexaazaisowurtzitane (CL-20) and 1,3,5,7-Tetranitro-1,3,5,7-tetrazoctane (HMX) are promising cocrystal cofomers, but only little solubility data are available. Knowledge about their solubility and solvate formation is essential for the development of cocrystallisation experiments. This paper provides the solubility values of HMX and CL-20 in 29 solvents at 293.15 K and 333.15 K as well as the solubility in five 2-propanol solvent mixtures at 293.15 K. Novel CL-20 solvates of 5-methyloxolan-2-one, 1,3-dioxolan-2-one, tetrahydrothiophene 1-oxide, 1,3-dioxolane, furan-2-carbaldehyde and butane-2,3-dione have been isolated and characterised. For all new solvates, single crystal data were obtained, except for furan-2-carbaldehyde. The novel ϑ -conformation of CL-20 was observed in the tetrahydrothiophene 1-oxide solvate. It was found that none of the tested solvents and likely no existing solvent exhibits a beneficial solubility ratio of CL-20 and HMX in the tested temperature range, exceptionally good solubility ratios are most likely the result of solvate formation, and that solvate forming solvents cannot be categorically excluded from consideration as solvent for cocrystallisation of HMX and CL-20.

1 Introduction

The CL-20/HMX cocrystal is one of the most promising energetic cocrystals due to its reported reduced impact sensitivity compared to CL-20 and the improved detonation properties compared to HMX.¹ A multitude of cocrystallisation methods have been described in literature for this cocrystal. For some of the reported methods, such as spray drying² or liquid-assisted grinding,^{1,3,4} the solubility of the individual cocrystal former is of lesser importance. For solution-based cocrystallisation techniques, such as solvent evaporation,^{1,5,6} antisolvent crystallisation,^{3,7} reaction cocrystallisation,⁷ and cooling crystallisation,⁷ however, detailed knowledge of the size and position of the cocrystal phase region in the corresponding phase diagram is required for the design of a reproducible, efficient, and scalable crystallisation method that can produce coarse compact cocrystal of high-quality. For all conventional solution crystallisation techniques that can be used to produce high-quality crystals, the CL-20 efficiency is severely limited by the position of the cocrystal phase region in the phase diagram.⁷ As the full determinations of the phase diagrams are very time consuming, solubility data of CL-20 and HMX in the respective solvent might be used to assess a solvent's suitability. Further factors influence the suitability of a solvent, such as chemical incompatibility and solvate formation. It has been reported that solvate formation can hinder cocrystallisation.⁸ The aim of this study, therefore, was to identify a solvent that exhibits a beneficial solubility ratio, but does not form solvates with either CL-20 or HMX. In this paper we present the solubility data of CL-20 and HMX in 29 solvents at 293.15 K and 333.15 K as well as in selected solvent mixtures. Furthermore, six novel solvates of CL-20 are described and the single crystal structures of five of them discussed. This

includes the discussion of the novel ϑ -conformation of CL-20.

2 Experimental Section

Table 2 displays the purity and supplier of the utilised solvents. All solvents were used without further purification and stored over 3 Å molecular sieve if used repeatedly. ϵ -CL-20 (lot number 573S98) was obtained from SNPE. The chemical purity was determined via ¹H NMR and HPLC to be 98.3 and 99.4%, respectively. Further analysis details are found in the supporting information. β -HMX (lot number NSI 00E 000 E004) was purchased from Chemring Nobel. The chemical purity has been determined via ¹H NMR and HPLC to be 98.7 and 99.3%, respectively. Further analysis details are found in the supporting information.

2.1 Characterisation Methods

Sample mass was determined using a Kern 770 analytical balance (accuracy 0.1 mg).

Raman spectra were obtained with a Bruker RFS 100/S Raman spectrometer equipped with a 1064 nm ND:YAG-laser operated at 450 mW and a liquid-nitrogen-cooled germanium-detector. The spectra were obtained between 80 and 3500 cm⁻¹ with a spectral resolution of 1 cm⁻¹. 75 scans were accumulated.

For the x-ray diffraction of all compounds, an Oxford Xcalibur3 diffractometer with a CCD area detector was employed for data collection using Mo-K α radiation ($\lambda=0.71073$ Å). By using the CRYCALISPRO software⁹ the data collection and reduction were performed. The structures were solved by direct methods (SIR92,¹⁰ SIR - 97^{11,12} or SHELXS-97^{13,14}) and refined by full-matrix least-squares on F2 (SHELXL^{13,14}) and finally checked using the PLATON software¹⁵ integrated in the WinGX software suite. Non-hydrogen atoms were refined anisotropically and the hydrogen atoms were located and freely refined. The absorptions

were corrected by a SCALE3ABSPACKmultiscan method.¹⁶

DSC analysis was carried out using a TA Instruments DSC Q2000 V24.10 build 122. Samples were heated from 298 up to 543 K at the rate of 5 K min⁻¹ in a hermetically sealed aluminium pan. The sample quantity in all experiments was between 0.5 and 1.5 mg.

TGA was carried out using a TA Instruments TGA Q5000 V3.15 build 263. Samples were heated from 298 up to 573 K at the rate of 5 K min⁻¹ in a platinum pan. The sample quantity in all experiments was between 0.9 and 4 mg.

2.2 Solubility Determination

A moderate excess of HMX or CL-20 was placed in a 6 mL or 20 mL glass vessel. Depending on the expected solubility, between 0.5 g and 15 g solvent/solvent mixture were added. The solution was agitated at 800 rpm and tempered via a Ditabis MKR 23 thermo block mixer equipped with a matching thermo block for the reaction vessels. Typically, after 2 h and 4 h, the solid was sedimented and part of the clear solution removed

by syringe. Enough solution was removed to ensure at least 10 mg evaporation residue. Directly after transfer, the solution mass was determined. The solvent was removed under vacuum and the mass of the remaining solid was determined. The remaining solid in the glass vessel was washed according to the standard washing procedure,⁷ dried, and analysed via Raman spectroscopy. No phase change was detected, except for the solvates discussed later, and α -CL-20 that formed in **27** (total conversion at 293.15 K and 1/3 conversion at 333.15 K) and **25** (traces of α at 293.15 K). A solubility determination was considered successful if the two obtained values differed from one another by less than 5%. This relatively large error margin was chosen because comparison among literature shows that solubility data between different determination setups and especially different raw material varies often by more than 5%.¹⁷ Furthermore, if the determined solubility was less than 0.003 mol kg⁻¹, or the difference in determined solubility was less than 0.001 mol kg⁻¹ the experiment was considered successful independent of the error between the obtained

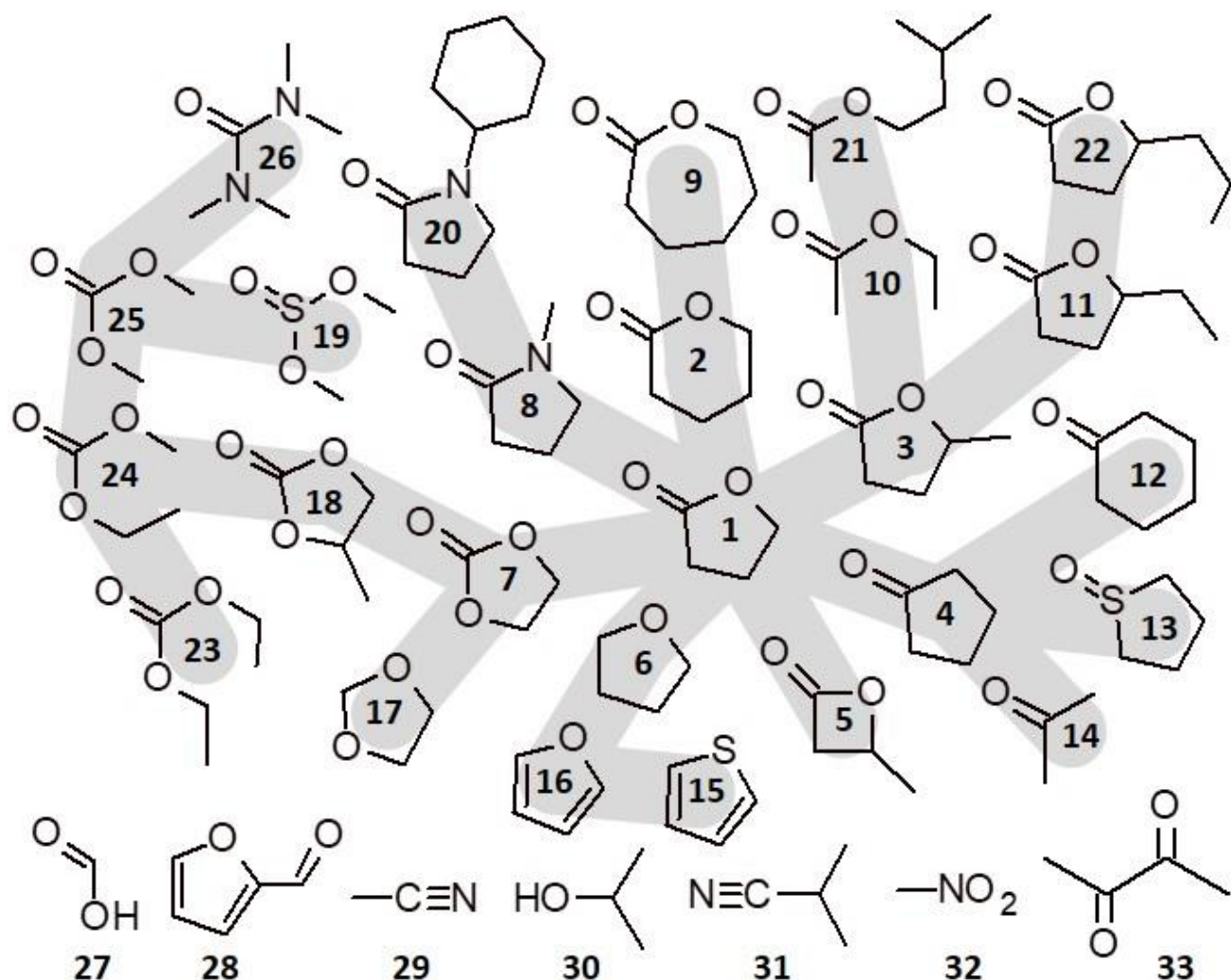


Figure 1: Molecular structure of the utilised solvents. Grey branches visualise the relation of the molecules branching out from 1. The molecules **27** to **33** have not been directly derived in this fashion.

values because of the increase in error due to excessively low solubilities. This procedure was chosen even though it does not provide certainty whether the obtained solubility value truly represents the equilibrium solubility. It is typically preferred to perform an experiment in which the substance in question is dissolved at higher temperature and the solution is subsequently cooled down in addition to the described method.¹⁸ In theory, this provides one with the certainty that the equilibration time was sufficient if the solubility values of both experiments concur. This method is, however, unsuitable for CL-20. For once CL-20 exhibits only a very weak temperature dependency of solubility. In addition, at different temperatures different CL-20 polymorphs can form. It is hence possible that at elevated temperature a polymorphic transformation process occurs which at lower temperature first has to be reversed to form the true equilibrium at this temperature. No solubility data were determined if due to solvate formation the solution completely solidified during the solubility determination. No solubility values have been determined for some solvate forming solvents for this reason. Additionally, no solubility data was determined for **28** and **33**, because discolouration of the obtained solid occurred

after the solvent was evaporated. Solubility values are calculated as molalities b_i according to the formula $b_i = \frac{m_i}{m_j \cdot M_i}$ where m_i represents the solute's mass, M_i represents the solute's molar mass, and m_j represents the solvent/solvent mixture mass. Solvent compositions are calculated as mass fractions w_j according to the formula $w_j = \frac{m_j}{m_j + m_k}$ where m_j and m_k represent the solvent masses.

HMX, CL-20, and their solvates are capable of mass explosion initiated via static electricity, friction or impact. Appropriate care must be taken when handling these materials.

Table 1: Compilation of the available solubility data of CL-20 and HMX

| solvent | CAS Nr. | $b_{\text{HMX}} / \frac{\text{mol}}{\text{kg}}$ | | $b_{\text{CL-20}} / \frac{\text{mol}}{\text{kg}}$ | |
|-------------------------------|----------|---|---|---|---|
| | | 293-298 K | 323-333 K | 293-298 K | 323-333 K |
| 1-Methylpyrrolidin-2-one | 872-50-4 | | | 2.533 ¹⁹ ; 2.622 ²⁰ | 0.776 ¹⁹ ; 2.524 ²⁰ |
| 2-Oxepanone | 502-44-3 | 0.230 ²¹ | | | |
| 4-Methyl-1,3-dioxolan-2-one | 108-32-7 | 0.069 ²² | 0.312 ²² | 1.426 ¹⁹ | 1.723 ¹⁹ |
| 5-Methyloxolan-2-one | 108-29-2 | 0.311 ²¹ | | | |
| Acetic acid | 64-19-7 | 0.001 ²³ | 0.003 ²³ | | |
| Acetic anhydride | 108-24-7 | | 0.007 ²³ | | |
| Acetonitrile | 75-05-8 | 0.068 ²⁴ | 0.147 ²³ | 1.278 ²⁰ | 1.997 ²⁰ |
| Butyl acetate | 123-86-4 | | | 0.730 ¹⁹ | 0.662 ¹⁹ |
| Cyclohexanone | 108-94-1 | 0.034 ²⁴ | 0.240 ²³ | 1.912 ²⁰ | 1.960 ²⁰ |
| Dimethyl sulfoxide | 67-68-5 | 1.924 ²⁴ | 2.296 ²⁴ ; 1.594 ²³ | | |
| Ethane-1,2-diol | 107-21-1 | | | 0.022 ¹⁷ | 0.034 ¹⁷ |
| Ethanol | 64-17-5 | | | 0.014 ¹⁷ ; 0.005 ¹⁹ | |
| Ethyl acetate | 141-78-6 | | | 1.027 ¹⁷ ; 1.141 ¹⁹ ; 1.246 ²⁰ | 0.808 ²⁰ |
| Hexamethylphosphoric triamide | 680-31-9 | 0.047 ²⁴ | | | |
| Methyl acetate | 79-20-9 | | | 1.209 ¹⁹ | 1.438 ¹⁹ |
| N,N-Dimethylformamide | 68-12-2 | | 0.375 ²³ | 1.506 ¹⁹ ; 1.476 ²⁰ | 1.597 ¹⁹ ; 1.860 ²⁰ |
| Nonan-5-one | 502-56-7 | | | 0.399 ¹⁹ | 0.338 ¹⁹ |
| Oxolan-2-one | 96-48-0 | 0.375 ²¹ ; 0.405 ²⁴ ; 0.422 ²⁵ | 0.641 ²⁵ | 0.822 ¹⁹ | 1.296 ¹⁹ |
| Pentan-3-one | 96-22-0 | | | 1.209 ¹⁹ | 1.221 ¹⁹ |
| Propan-2-one | 67-64-1 | 0.095 ²⁴ ; 0.081 ²³ | | 2.159 ¹⁷ ; 2.654 ¹⁹ | |
| Tetrahydro-2H-pyran-2-one | 542-28-9 | 0.219 ²¹ | | | |

2.3 Preparation of Solvates

The following procedure describes the basic course of action for producing the solvates. Because of specifics of the individual solvent, deviations from this procedure were undertaken.

4000 mg of the corresponding solvent were added to an appropriate amount of CL-20 to form a supersaturated solution in a 20 mL glass vessel. The slurry was agitated at 600 rpm at 293.15 K for **3**, **13**, **17** and **33** or 333.15 K for **7** and **28** until conversion occurred. Crystals for single crystal analysis were collected if initially high-quality crystals formed and were stored under mother liquor or Fomblin YR-1800 until measurement. 2000 mg CL-20 (4.56 mmol) were added to the reaction mixture over the course of 48 h to enforce the formation of larger crystals by keeping the supersaturation low. Larger and more defect lean crystals were preferred to facilitate solid-liquid separation. The reaction mixture was divided and the mother liquor of one half was removed via a syringe and filter paper. The solid was dried at room temperature and atmospheric pressure until constancy of mass was achieved. Raman analysis of the dried material was carried out. Raman, TGA, and DSC analysis were carried out with the other half of the collected solid. Here the solid was quickly washed following the standard washing procedure published elsewhere.⁷ The washed solid was only briefly dried to ensure total evaporation of 2-propanol, but prevent excessive solvent evaporation.

3 Results and Discussion

3.1 Solubility Data

Most of the published solubility data for HMX and CL-20 are displayed in Table 1. Of the published solvents, oxolan-2-one (**1**) appears to possess the overall most suitable solubilities of CL-20 and HMX for generating the cocrystal. That is because for cocrystallisation the cocrystal phase region in the solvent must be considered. It is reasonable to assume that the position of the cocrystal phase region correlates with the solubilities of the individual cocrystal formers, as this holds true for other systems.²⁶ One can, therefore, assume that a solubility ratio of CL-20 to HMX of 2:1 would be most beneficial. The ratio 2:1 is proposed because the CL 20/HMX cocrystal is composed of two parts CL-20 per part HMX. Solvent **1** possesses at 333 K a solubility ratio of 2:1 based on the literature solubility data. Solvent **1**, however, also forms solvates not only with HMX,²⁷ but also with CL-20.²⁸ A solvent's ability to form solvates can hinder cocrystal formation,⁸ because solvate formation is

Table 2: Description of materials used in this paper

| chemical | source | purity [%] | design ation |
|--|-------------------|--------------------|--------------|
| 2,4,6,8,10,12-Hexanitrohexaazaisowurtzitan | SNPE | 98.9 ^a | CL-20 |
| Cyclotetramethylenetetranitramin | Chemring Nobel | 99.0 ^a | HMX |
| Tetrahydro-2H-pyran-2-one | Sigma-Aldrich | ≥97.5 ^b | 2 |
| 5-Methyloxolan-2-one | Sigma-Aldrich | 99 ^b | 3 |
| Cyclopentanone | Merck | 99 ^b | 4 |
| 4-Methyloxetan-2-one | Sigma-Aldrich | 98 ^b | 5 |
| Oxolane | Th.Geyer | ≥99.9 ^b | 6 |
| 1,3-Dioxolan-2-one | Aldrich | 98 ^b | 7 |
| 2-Oxepanone | Sigma-Aldrich | 98 ^b | 9 |
| Ethyl acetate | VWR | 99 ^b | 10 |
| 5-Ethylloxolan-2-one | Sigma-Aldrich | ≥98 ^b | 11 |
| Cyclohexanone | Sigma-Aldrich | 99.5 ^b | 12 |
| Tetrahydrothiophene 1-oxide | Sigma-Aldrich | 96 ^b | 13 |
| Propan-2-one | VWR | 100 ^b | 14 |
| Thiophene | Sigma-Aldrich | ≥99 ^b | 15 |
| Furan | Sigma-Aldrich | ≥99 ^b | 16 |
| 1,3-Dioxolane | Sigma-Aldrich | 99 ^b | 17 |
| 4-Methyl-1,3-dioxolan-2-one | Roth | 99.7 ^b | 18 |
| Methoxysulfinyloxymethane | Sigma-Aldrich | 99 ^b | 19 |
| N-Cyclohexyl-2-pyrrolidone | Sigma-Aldrich | 99 ^b | 20 |
| 3-Methylbutyl acetate | Honeywell | 98 ^b | 21 |
| 5-Propyloxolan-2-one | Sigma-Aldrich | ≥98 ^b | 22 |
| Diethyl carbonate | Sigma-Aldrich | ≥99 ^b | 23 |
| Ethyl methyl carbonate | Sigma-Aldrich | 98 ^b | 24 |
| Dimethyl carbonate | Sigma-Aldrich | ≥99 ^b | 25 |
| Tetramethylurea | Sigma-Aldrich | 99 ^b | 26 |
| Formic acid | Sigma-Aldrich | ≥95 ^b | 27 |
| Acetonitrile | Fisher Scientific | ≥99 ^b | 29 |
| 2-propanole | Roth | 99.8 ^b | 30 |
| 2-Methylpropane-nitrile | Sigma-Aldrich | 99 ^b | 31 |
| Nitromethane | LD sportsline | 99.9 ^b | 32 |
| Butane-2,3-dione | Sigma-Aldrich | 97 ^b | 33 |

^a Determined via ¹H NMR and HPLC

^b Provided by suppliers

Table 3: Experimental solubilities of HMX and CL-20 in various solvents at different temperature and pressure $p = 0.1$ MPa

| Solvent | designation | $b_{\text{HMX}} / \frac{\text{mol}}{\text{kg}}$ | | $b_{\text{CL-20}} / \frac{\text{mol}}{\text{kg}}$ | |
|-----------------------------|-------------|---|----------|---|--------------------------|
| | | 293.15 K | 333.15 K | 293.15 K | 333.15 K |
| Tetrahydro-2H-pyran-2-one | 2 | 0.294 | 0.618 | 2.478 | 3.225 |
| 5-Methyloxolan-2-one | 3 | 0.311 | 0.513 | solvate | solvate |
| Cyclopentanone | 4 | 0.101 | 0.155 | 2.207 | 2.385 |
| 4-Methyloxetan-2-one | 5 | 0.145 | 0.246 | 2.118 | 2.036 |
| Oxolane | 6 | 0.014 | 0.020 | 1.433 | 1.511 |
| 1,3-Dioxolan-2-one | 7 | - | 0.442 | - | solvate |
| 2-Oxepanone | 9 | 0.463 | 0.685 | n. d. ^a | 2.054-3.195 ^b |
| Ethyl acetate | 10 | 0.010 | 0.017 | 1.308 | 1.200 |
| 5-Ethyloxolan-2-one | 11 | 0.179 | 0.321 | 2.127 | 2.077 |
| Cyclohexanone | 12 | 0.088 | 0.172 | 1.912 | 1.960 |
| Tetrahydrothiophene 1-oxide | 13 | 1.084 | 1.621 | solvate | n. d. |
| Propan-2-one | 14 | 0.098 | - | 3.097 | - |
| Thiophene | 15 | <0.003 | <0.003 | 0.005 | 0.009 |
| Furan | 16 | 0.003 | - | 0.005 | - |
| 1,3-Dioxolane | 17 | 0.007 | 0.020 | solvate | solvate |
| 4-Methyl-1,3-dioxolan-2-one | 18 | 0.122 | 0.311 | 1.586 | 1.919 |
| Methoxysulfinyloxymethane | 19 | 0.034 | 0.071 | 1.276 | 1.335 |
| N-Cyclohexyl-2-pyrrolidone | 20 | 0.641 | 0.215 | n. d. ^{c)} | n. d. ^{c)} |
| 3-Methylbutyl acetate | 21 | <0.003 | 0.003 | 0.632 | 0.582 |
| 5-Propyloxolan-2-one | 22 | 0.111 | 0.203 | 1.568 | 1.645 |
| Diethyl carbonate | 23 | 0.003 | 0.014 | 0.294 | 0.363 |
| Ethyl methyl carbonate | 24 | 0.007 | 0.014 | 0.475 | 0.559 |
| Dimethyl carbonate | 25 | 0.007 | 0.020 | 0.018 | 0.100 |
| Tetramethylurea | 26 | 0.209 | 0.621 | 2.191 | 2.932 |
| Formic acid | 27 | 0.003 | 0.007 | 0.014 | 0.030 |
| Acetonitrile | 29 | 0.071 | 0.165 | 2.848 | 3.131 |
| 2-Propanole | 30 | <0.003 | <0.003 | 0.002 | 0.002 |
| 2-Methylpropanenitrile | 31 | 0.020 | 0.034 | 1.317 | 1.383 |
| Nitromethane | 32 | 0.024 | 0.071 | 0.500 | 0.860 |

^a n.d. means not determined

^b Extrapolated value from diluted solution, due to excessive viscosity.
Not determined due to excessive viscosity

basically (depending on the preferred definition for cocrystal^{29–32}) a competing cocrystallisation. In the ternary phase diagram of **1**, CL-20, and HMX would,

therefore, coexist at least three cocrystal phase regions which most likely at least partially overlap. It was, hence, attempted to identify alternatives to **1** that also possess a solubility ratio close to 2:1, but do not form solvates. Because of the limited available data, **1** was chosen as the ancestral molecule from which most of the tested molecules are derived by successive exchange of functional

groups or alkyl units (Figure 1). The literature data indicate that the solubility of CL-20 is nearly temperature independent, whereas the HMX solubility increases with increasing temperature. Solubility determinations were, thus, carried out at 293.15 K and 333.15 K. The upper temperature was chosen as a compromise between the better solubility values for HMX at higher temperatures, safety concerns, and the limiting factor of boiling points. The obtained solubility data are displayed in Table 3.

Table 4: Experimental solubilities and reference data of CL-20 in **10** and **12** at different temperatures and pressure $p = 0.1$ MPa

| solvent | $b_{\text{CL-20}} / \frac{\text{mol}}{\text{kg}}$ published in ²⁰ | | experimental $b_{\text{CL-20}} / \frac{\text{mol}}{\text{kg}}$ | | $\Delta b_{\text{CL-20}} / \frac{\text{mol}}{\text{kg}}$ | |
|-----------|--|----------|--|----------|--|----------|
| | 273.15 K | 333.15 K | 273.15 K | 333.15 K | 273.15 K | 333.15 K |
| 10 | 1.246 | 1.212 | 1.308 | 1.200 | 0.062 | -0.012 |
| 12 | 1.933 | 1.969 | 1.912 | 1.960 | -0.021 | -0.009 |

To validate the method, two sets of obtained solubility data of CL-20 are compared to the corresponding measurement data of Cui *et al.*²⁰ The solubility values and deviations of measurement are shown in Table 4. The results indicate the validity of the solubility determination method.

Multiple effects of the solvent molecule structure and its functional groups on the solubilities are apparent. In most cases only the solubility of CL-20 can be discussed, because the HMX solubility is often too low for changes in solubility to be significant in face of the experimental error. The strongest effect on

solubility of CL-20 and HMX in carbonyl compounds with at least one adjacent oxygen has the overall molecular geometry i.e. whether the carbonyl group is situated in a ring. This can most easily be seen in comparing the lactone **3** with the similar acetate **10**. This is the result of the prevalence of the (*Z*)-conformation over the (*E*)-conformation in noncyclic esters. The prevalence was attributed to a minimisation of dipole-dipole repulsion in the (*Z*)-conformation.³³⁻³⁵ As a result, the overall dipole moment of the carboxyl group is weaker in noncyclic esters, because in (*E*)-conformation the individual dipoles align, whereas in (*Z*)-conformation the opposing dipoles weaken the net dipole moment. As the dipole moment is one of the key factors in determining the solubility of CL-20,³⁶ (and presumably also HMX) it is very likely that the difference in dipole moments explains most of the difference in solubility between the tested cyclic and noncyclic esters. The same reasoning can also explain the lower solubilities in the noncyclic carbonates compared to **18**. On the same note, the CL-20 solubility in **2** most likely increases that significantly with increasing temperature because the less stable conformer has a higher dipole moment.³⁷ Increased mobility of the alkyl group is most likely responsible for the solubility reduction of CL-20 in **10** and **21**. Due to the rigid frame of **32** conformational changes, however, cannot explain the significant increase in solubility of CL-20. Also, the solubility increase of CL-20 in **18** is antithetic to the expected reduction in effective dipole moment of **18** with increasing temperature. The solubility changes of CL-20 were typically the result of dipole

moment changes of the solvents with temperature increase. This indicates that CL-20 per se does not exhibit a temperature dependent solubility. In contrast, HMX shows a pronounced increase in solubility with increasing temperature in all tested solvents. Because of the often low HMX solubility in the solvents that exhibited significant CL-20 solubility changes with temperature, no correlation of the HMX solubility to changes in solvent dipole moment can be discerned. On average, the solubility of HMX doubled by increasing the temperature from 293.15 K to 333.15 K. The smallest increase exhibits **20** with an increase of 12% whereas the solubility in **26** almost triples. Of the tested solvents, **13** exhibits at 333.15 K and 293.15 K by far the highest solubility of HMX. The solubility is only surpassed by dimethyl sulfoxide.^{23,24}

Of the tested solvents, **26** and **17** exhibited a slow decomposition of CL-20 in solution both at 293.15 K and 333.15 K. It is documented that CL-20 is chemically incompatible with amines.³⁸ Solvent **20**, a lactam, did not show signs of chemical incompatibility. Apparently, the reported incompatibility also encompasses amides, but potentially not lactams. The observed incompatibility of CL-20 with **17** is likely the result of a high HOMO-energy or a low ionisation potential of **17**, as Thome³⁶ found an unusually high CL-20 solubility for the chemically similar solvent 2,2'-[ethane-1,2-diylbis(oxy)]di(ethan-1-ol) and ascribed it to these attributes. While the two adjacent ether groups common to both molecules in 2,2'-[ethane-1,2-diylbis(oxy)]di(ethan-1-ol) apparently only increased the solubility, the ring geometry in **17** might have increased the effect to a level that enabled destructive levels of interaction.

Of the tested solvents, none have shown excessive viscosities of saturated solutions of HMX. Of the tested solvents **3**, **9**, **13** and **20** have shown viscosities too high for practical application of saturated solutions of CL-20.

3.2 Solvate Formation

Multiple strategies of molecular variation were pursued to identify a solvent that exhibits a similarly good solubility ratio as **1**, but does not form solvates. One strategy was to reduce the energetic

benefit of solvate formation by increasing the side chain of the five-membered lactone ring. The increase in side chain length from **1** up to **22** appears to reduce the tendency of the solvent to produce solvates. While **1** forms solvates with both HMX and CL-20, for **3** only a solvate of CL-20 was observed, and no solvates were formed with **11** and **22**. The increase in side chain length corresponds with a linear decrease in solubility of HMX both at 293.15 K and 333.15 K. The CL-20 solubility however does not follow a clear trend. The reported solubility of CL-20 in **1** and the solubility of the CL-20 solvate in **3** are significantly lower than the CL-20 solubilities in **11** and **22** at 293.15 K. At 333.15 K, compared to 293.15 K the reported solubility of CL-20 in **1** and the solubility of the CL-20 solvate in **3** increase by 58% and 38%, respectively, while the solubility in **11** is unchanged and the solubility in **22** decreases compared to 293.15 K.

Another approach was to vary the lactone ring size hoping to maintain the level of interaction while reducing the energetic benefit of solvate formation. Of the three lactones with varied ring-size, none formed solvates in our solubility tests. The reported CL-20 solubility in **1** is significantly lower than the solubilities in **5**, **2** and **9**. Considering both the trends of the ring size and side chain length dependent CL-20 solubility, it appears very likely that the reported CL-20 solubility in **1** is in fact the solubility of the solvate. The solvate is necessarily less soluble than CL-20 if it is spontaneously formed in a solubility experiment. This leads to an atypically low ostensible solubility and thus to an improved perceived solubility ratio. This is similar to the situation of **7** and **3** which both exhibit a CL-20 solvate to HMX solubility ratio close to that of **1** with 2:1 and 3:1 at 333.15 K, respectively. That the reported solubility of HMX in **1** is not the solubility of the solvate is supported by the fact that even though solvates of HMX with **2**, **4**, **8**, **9**, **13** and **26** are known³⁹⁻⁴¹ these solvates did not form during our solubility tests which makes it likely that the HMX solvate of **1** also did not form in the experiments of Sitzmann *et al.*²⁴ and Svensson *et al.*²¹ Most likely many of the HMX solvates reported are kinetic products, and their formation is in all likelihood only the result of the strong non-equilibrium conditions during their creation such as rapid cooling or fast evaporation of the solvent. It appears, for example, unlikely that HMX forms energetically beneficial solvates with a multitude of benzene and naphthalene derivatives.⁴²

Solvent **20** was also investigated as a more encumbered substitute for **8** to suppress solvate formation. No solvates were observed and a high

HMX solubility was determined. However, no CL-20 solubility could be determined because of excessively high solution viscosity.

All of the solvates discovered in this study were formed during solubility tests. Some solvate formations took several hours under the applied conditions. It is, therefore, very likely that for some tested solvents unknown thermodynamically stable solvate of CL-20 or HMX exist. This becomes clear when one considers that **25**⁴³ and **29**⁴⁴ are known to form CL-20 solvates and **9**³⁹, **13**³⁹, **4**⁴⁰, **8**⁴⁵ and **2**³⁹ are known to form HMX solvates, but no formation of solvate crystals occurred during the solubility tests.

3.3 Solubility ratio

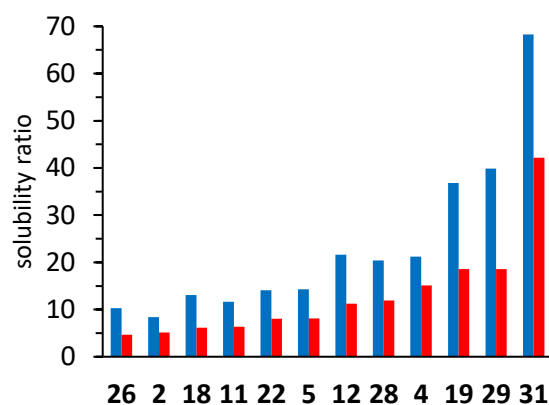


Figure 2: Solubility ratios of CL-20 and HMX at 293.15 K (blue) and 333.15 K (red) in various solvents.

The solubility ratios of CL-20 to HMX are displayed for 293.15 K and 333.15 K in Figure 2. Only solvents that did not form solvates in our tests and exhibited a solubility of HMX of greater than 0.02 mol HMX per kg solvent were used for this comparison. Because of the pronounced solubility increase of HMX with increasing temperature, the solubility ratios at 333.15 K are always improved compared to 293.15 K. On average an improvement of factor 1.8 is achieved.

None of the tested solvents approaches the aimed at solubility ratio of 2:1. A solvent mixture approach was, therefore, investigated, as it has been shown for the cocrystal formers carbamazepine and saccharin that a solvent mixture for example of water and tetrahydrothiophene 1,1-dioxide can result in a more beneficial solubility ratio of the cocrystal formers than in both pure solvents, even though saccharin is more soluble in both solvents.⁸ To investigate whether solvent mixtures can equilibrate the solubility of HMX and CL-20 too, the solubilities were determined in equimolar solvent mixtures (Table 5 and 6). The solvents were chosen for their diversity in functional group and solubility ratio. Furthermore, **29** is known to form a CL-20

solvate and **17** has formed a CL-20 solvate in this study. Solvent mixtures should reduce the chance of solvate formation^{8,46} and having solvate forming solvent in the mixture might provide additional information. As can be seen from Table 5, most solvent mixtures exhibit a solubility ratio close to the arithmetic mean of the individual solvents. Only for the mixture of **5** and **10** a solubility ratio significantly better than the mean, but still worse than the better solubility ratio, was obtained. And in the mixture of **17** and **32** a solubility value significantly worse than in **32** was observed.

Table 5: Comparison of the solubility ratios of CL-20 and HMX in equimolar solvent mixtures with the arithmetic mean and the solubility ratio of CL-20 and HMX in the pure solvents

| solvent A | solvent B | solubility ratio of solvent A | solubility ratio of solvent B | arithmetic mean | obtained solubility ratio |
|-----------|-----------|-------------------------------|-------------------------------|-----------------|---------------------------|
| 5 | 10 | 8 | 71 | 40 | 17 |
| 17 | 5 | n.d. ^{a)} | 8 | - | 13 |
| 17 | 32 | n.d. ^{a)} | 12 | - | 24 |
| 29 | 10 | 19 | 71 | 45 | 34 |
| 29 | 32 | 19 | 12 | 15 | 15 |

^{a)} No solubility ratio of **17** was determinable because of solvate formation.

These results are inconclusive; however, they also do not provide evidence for possible solubility ratio reduction by applying solvent mixtures.

These solubility data represent only one point on the mass fraction dependent solubility curve. For selected solvents, solubilities of HMX and CL-20 were, therefore, determined in varying mixtures with **30** to investigate whether a more favourable solubility ratio can be achieved depending on the solvent mixture ratio (Table 7).

No uniform behaviour of the solubility ratio depending on the mass fraction of 2-propanol in the solvent mixtures is apparent (Figure 3), but no solvent mixture exhibits a decrease of solubility ratio within the solubility region of practical use. No further solubility tests in solvent mixtures were undertaken.

As can be seen from Figure 2, for solvents of reasonably high solubility the solubility ratio of CL-20 and HMX can vary drastically, from 5:1 for **26** up to 42:1 for **31** at 333.15 K, but none of the tested or reported solvents possesses a HMX solubility equal or higher than that of CL-20. This speaks for inherent differences in the solvation and/or lattice enthalpy of the two substances. Because of the lack of data of the lattice enthalpy of HMX and CL-20 and the large margin of error of experimental and calculated data (the reported sublimation enthalpy data of CL-20, for example, from which one could derive the lattice enthalpy differ by over

100 kJ mol⁻¹)⁴⁷ no further analysis of this phenomenon was undertaken.

Table 6: Experimental solubilities of HMX and CL-20 in equimolar solvent mixtures at 333.15 K and pressure p = 0.1 MPa

| solvent A | solvent B | $b_{\text{HMX}} / \frac{\text{mol}}{\text{kg}}$ | $b_{\text{CL-20}} / \frac{\text{mol}}{\text{kg}}$ |
|-----------|-----------|---|---|
| 5 | 10 | 0.093 | 1.578 |
| 17 | 5 | 0.140 | 1.816 |
| 17 | 32 | 0.045 | 1.102 |
| 29 | 10 | 0.051 | 1.750 |
| 29 | 32 | 0.110 | 1.684 |

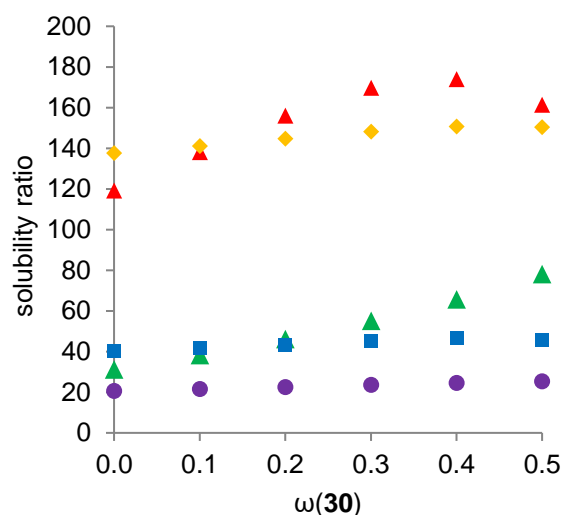


Figure 3: Solubility ratio progression of CL-20 and HMX in various solvent mixtures with **30**. Red triangles **6**, yellow rhombs **10**, green triangles **14**, blue squares **29**, violet circles **32**.

Table 7: Experimental molalities b of CL-20 and HMX in mixtures of liquid solvent with **30** of mass fraction w at 293.15 K and pressure $p = 0.1$ MPa

| Solvent | w_{30} | $b_{\text{CL-20}} / \frac{\text{mol}}{\text{kg}}$ | w_{30} | $b_{\text{HMX}} / \frac{\text{mol}}{\text{kg}}$ | Solvent | w_{30} | $b_{\text{CL-20}} / \frac{\text{mol}}{\text{kg}}$ | w_{30} | $b_{\text{HMX}} / \frac{\text{mol}}{\text{kg}}$ |
|-----------|----------|---|----------|---|-----------|----------|---|----------|---|
| 6 | 1 | 0.002 | 1 | 0.000 | 29 | 0.9318 | 0.011 | 0.9289 | 0.001 |
| | 0.8796 | 0.015 | 0.8822 | 0.001 | | 0.8525 | 0.044 | 0.8538 | 0.002 |
| | 0.7696 | 0.056 | 0.769 | 0.001 | | 0.772 | 0.110 | 0.7727 | 0.002 |
| | 0.6608 | 0.144 | 0.6587 | 0.001 | | 0.6883 | 0.222 | 0.6868 | 0.006 |
| | 0.5498 | 0.316 | 0.5547 | 0.002 | | 0.5907 | 0.410 | 0.5931 | 0.009 |
| | 0.4584 | 0.499 | 0.4546 | 0.003 | | 0.4911 | 0.642 | 0.4943 | 0.015 |
| | 0.3667 | 0.683 | 0.3579 | 0.004 | | 0.3909 | 1.016 | 0.3861 | 0.023 |
| | 0.2656 | 0.897 | 0.2627 | 0.006 | | 0.2715 | 1.477 | 0.2663 | 0.031 |
| | 0.1683 | 1.171 | 0.1715 | 0.007 | | 0.1382 | 2.146 | 0.1408 | 0.051 |
| | 0.0833 | 1.316 | 0.0843 | 0.009 | | 0 | 2.848 | 0 | 0.071 |
| 0 | 1.511 | 0 | 0.013 | | | | | | |
| | | | | 32 | 0.8967 | 0.005 | 0.8947 | 0.001 | |
| 10 | 0.8604 | 0.018 | 0.8591 | 0.001 | 0.7912 | 0.016 | 0.7972 | 0.001 | |
| | 0.7316 | 0.071 | 0.7326 | 0.001 | 0.6331 | 0.054 | 0.6913 | 0.002 | |
| | 0.6162 | 0.163 | 0.6144 | 0.001 | 0.5896 | 0.071 | 0.5953 | 0.003 | |
| | 0.5083 | 0.292 | 0.5061 | 0.002 | 0.4961 | 0.115 | 0.4955 | 0.004 | |
| | 0.4014 | 0.455 | 0.4067 | 0.003 | 0.3952 | 0.175 | 0.3954 | 0.007 | |
| | 0.3109 | 0.621 | 0.3142 | 0.004 | 0.2955 | 0.250 | 0.2968 | 0.010 | |
| | 0.224 | 0.812 | 0.2258 | 0.005 | 0.1978 | 0.323 | 0.177 | 0.016 | |
| | 0.1409 | 0.966 | 0.1448 | 0.006 | 0.098 | 0.432 | 0.0985 | 0.020 | |
| | 0.0704 | 1.213 | 0.0715 | 0.008 | 0 | 0.499 | 0 | 0.024 | |
| | 0 | 1.308 | 0 | 0.009 | | | | | |
| 14 | 0.9032 | 0.023 | 0.9023 | 0.000 | | | | | |
| | 0.7918 | 0.108 | 0.8048 | 0.001 | | | | | |
| | 0.7065 | 0.184 | 0.7062 | 0.002 | | | | | |
| | 0.6084 | 0.483 | 0.6068 | 0.005 | | | | | |
| | 0.5107 | 0.715 | 0.5097 | 0.010 | | | | | |
| | 0.4105 | 1.224 | 0.4069 | 0.018 | | | | | |
| | 0.3086 | 1.633 | 0.307 | 0.029 | | | | | |
| | 0.1971 | 2.285 | 0.2073 | 0.046 | | | | | |
| | 0.0975 | 2.630 | 0.104 | 0.069 | | | | | |
| | 0 | 3.097 | 0 | 0.098 | | | | | |

3.4 Solvent selection for cocrystallisation

Considering the abundance of solvate forming solvents, that often solvents either form HMX or CL-20 solvates, that for eight of the ten best solvents for HMX solvates are known, and that some tested solvents might possess undiscovered solvates, the strict exclusion of solvate forming solvents from consideration for CL-20/HMX-cocrystal generation needs to be reevaluated. It is proposed that the possible formation of thermodynamic stable HMX solvates in general constitutes a far greater hindrance to the formation of the cocrystal than possible CL-20 solvate formation, because one would most likely operate a cocrystallisation for efficiency reasons close to the HMX/cocrystal phase boundary in the ternary phase diagram which is most likely the phase region of the HMX solvate phase. A solution composition for crystallisation close to the HMX phase boundary seems reasonable, because all tested, and possibly all solvents in general, exhibit a far worse solubility ratio than 2:1 in the tested temperature range. Even solvents that spontaneously produce CL-20 solvate can, therefore, be considered for cocrystallisation. It is very likely that many of the reported solvates of HMX are kinetic products that would hence possess a higher solubility than pure HMX. These kinds of solvates would most likely not disturb the cocrystallisation process, and these solvents are most likely suited for consideration for cocrystallisation. Because CL-20 is in all solvents far more soluble than HMX, it appears that the most promising candidates for consideration as solvent for solution based cocrystallisation of CL-20 and HMX are the solvents exhibiting the best solubility ratio that do not form thermodynamically stable HMX solvates. Based on these findings, for the solvents that exhibited the best solubility ratios, cocrystallisation tests have been carried out and published.⁷ Absolute solubility, chemical compatibility, and crystal morphology narrowed the selection down to **29** in these tests.⁷ Because of the temperature dependency of the HMX solubility high-boiling solvents might be of special interest for further crystallisation experiments, as at even higher temperatures than 333.15 K better solubility ratios should be achievable and other solvents than **29** might become viable.

3.5 Solvate characterisation

Solvents **3**, **7**, **13**, **17**, **28**, **33** have formed solvates with CL-20 in our solubility tests. Except for the **28** solvate, for all solvates single crystals suited for x-ray structural analysis were obtained. As can be

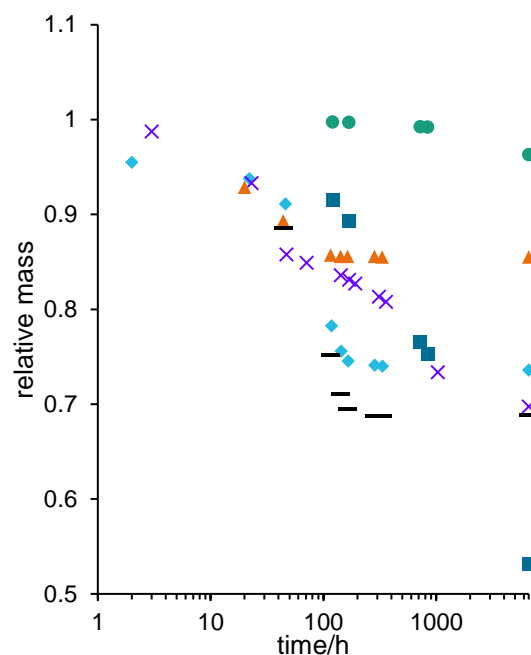


Figure 4: Mass loss of the solvates at 293 K and 0.1 hPa. With the CL-20 solvates of **7** in green circles, **13** in blue squares, **17** in orange triangles, **3** in violet crosses, **33** in teal diamonds and **28** in black dashes.

seen from Figure 4, where the normalised mass loss over time is displayed for the solvate crystals under atmospheric conditions, aside from the solvate of **7** none of the solvates are stable under atmospheric conditions. The **17** solvate reached total desolvation the fastest with 116 h followed by the **28** and **33** solvates with 166 h. Between 1031 and 6600 h, the **3** solvate reached total desolvation, while the **13** solvate still retains a vestige amount of solvent after 6600 h.

Because of the instability of the solvates, no pure material aside from the individual crystals for single

Table 8: Desolvation onsets during the TGA of the solvates

| | first desolvation onset [K] | second desolvation onset [K] |
|-----------|-----------------------------|------------------------------|
| 3 | 308 | 333 |
| 28 | 311 | -- |
| 17 | 319 | -- |
| 33 | 325 | -- |
| 13 | 345 | -- |
| 7 | 371 | 423 |

Table 9: Endothermic heat flow during the DSC analysis of the solvates

| | first endothermic peak (max heat flow) [K] | second endothermic peak (max heat flow) [K] |
|-----------|--|---|
| 13 | 326 | -- |
| 17 | 341 | -- |
| 28 | 359 | -- |
| 33 | 361 | -- |
| 3 | 380 | -- |
| 7 | 418 | 445 |

crystal structure determination could be obtained. Further analysis was carried out with fresh solvate material that was washed following the standard washing procedure and dried quickly to minimise the desolvation. The solvate of **13** desolvated completely during the washing. To obtain samples for analysis, this material was then only dried on filter paper to remove most of the adherent solution. Raman spectra, DSC diagrams, and TGA diagrams of the washed samples are found in the supporting information.

Even though all solvates dissociate at room temperature except for the **7** solvate, during TGA analysis sharp desolvation temperatures significantly higher than room temperature were determined (Table 8). The two-step mass loss of the **3** solvate during the TGA starting at a very mild 308 K but proceeding stronger between 335 K and 367 K correlates well with the initial rapid mass loss at atmospheric conditions and the following slower

mass loss. The **7** solvate also exhibits a two-step mass loss that correlates well with two distinct endothermic signals in the DSC diagram (Table 9). All solvates except for the **13** solvate exhibit a typically broad endothermic signal in the DSC measurement 14-72 K higher than the desolvation onset in the TGA. This is attributed to the desolvation and evaporation of the solvent. The **13** solvate, however, exhibits an endothermic signal 20 K lower than the desolvation onset which could indicate a phase change before desolvation occurred. The **13** solvate, furthermore, is the only compound that exhibits a significantly lower decomposition temperature both in the TGA and DSC measurement than pure CL-20. The comparison of the temperature dependent mass loss curves (Figure S13) show that evaporation of solvent and decomposition of CL-20 fade into each other only for the **13** solvate.

The single crystal data of the five novel solvates of CL-20 are discussed in the following, and the crystallographic information are displayed in Table 10.

In the crystal structure (orthorhombic, $P2_12_12$) of CL-20:**33**, there is one and a half independent **33** present for every independent CL-20. The "half" **33** is situated on the border of the asymmetric unit acting as an inversion centre. This molecule is disordered about its position in the crystal lattice and its contact is limited to four weak $O\cdots H-C$ interactions (ca. 2.5-2.6 Å) with two adjacent CL-20.

Table 10: Crystallographic information for the five CL-20 solvates

| | 3 | 7 | 13 | 17 | 33 |
|--------------------------|---------------------------------------|--------------------------------------|---------------------------------------|--------------------------------------|--|
| space group | $P\bar{1}$ | Cc | $P2_1/c$ | $P2_1/c$ | $P2_12_12$ |
| crystal system | Triclinic | Monoclinic | Monoclinic | Monoclinic | Orthorhombic |
| $a/\text{\AA}$ | 7.1967(7) | 15.8685(5) | 12.6725(4) | 8.9577(3) | 21.5458(8) |
| $b/\text{\AA}$ | 12.1864(10) | 20.1229(6) | 33.1797(16) | 12.6281(4) | 12.5600(5) |
| $c/\text{\AA}$ | 15.9929(16) | 22.9923(8) | 18.0049(6) | 15.6248(6) | 8.0755(3) |
| $\alpha/^\circ$ | 100.573(7) | 90 | 90 | 90 | 90 |
| $\beta/^\circ$ | 102.412(8) | 90.246(3) | 92.411(3) | 96.746(4) | 90 |
| $\gamma/^\circ$ | 106.818(8) | 90 | 90 | 90 | 90 |
| $V/\text{\AA}^3$ | 1265.1(5) | 7341.8(4) | 7563.8(5) | 1755.2(2) | 2185.3(5) |
| Z | 2 | 16 | 4 | 4 | 4 |
| $\rho/\text{g ccm}^{-3}$ | 1.676 | 1.905 | 1.593 | 1.939 | 1.724 |
| T/K | 110 | 110 | 293 | 115 | 113 |
| stoichiometry | 1:2 | 1:1 | 2:9 | 1:1 | 2:3 |
| chemical formula | $C_6H_6N_{12}O_{12} \cdot 2C_5H_8O_2$ | $C_6H_6N_{12}O_{12} \cdot C_3H_4O_3$ | $2C_6H_6N_{12}O_{12} \cdot 9C_4H_8OS$ | $C_6H_6N_{12}O_{12} \cdot C_3H_6O_2$ | $2C_6H_6N_{12}O_{12} \cdot 3C_4H_6O_2$ |
| CL-20 conformation | ε | γ | $\xi + \vartheta$ | ε | γ |
| R_1 | 0.057 | 0.0401 | 0.0667 | 0.0286 | 0.031 |
| CCDC | 2049488 | 2049491 | 2049489 | 2049492 | 2049490 |

Hence, no significant interaction between the two independent **33** molecules is present. CL-20, assuming the conformation found in γ -CL-20, forms a zig-zag chain of strong O \cdots H-C interactions (2.3 Å) along the *b*-axis in which each molecule is related to the next by inversion symmetry. The **33** are bound to this chain on alternating sides by moderate O \cdots H-C interactions (ca. 2.4 Å). These chains form a layer structure in the *bc*-plane, which is linked in *c* direction only by weak O \cdots H-C interactions (2.6 Å) between CL-20 molecules.

The conformation found in γ -CL-20 is also observed in the crystal structure (monoclinic, *Cc*) of CL-20:**7**, where four independent CL-20 and four independent **7** are present in the asymmetric unit. Two of the CL-20 each possess two strong O \cdots H-C interactions (2.2 Å). Of the independent **7** molecules, three possess each two to three moderate O \cdots H-C interactions (ca. 2.3-2.4 Å), while the other **7** only exhibits weak O \cdots H-C interactions (ca. 2.5-2.6 Å). This might explain the two-step mass loss during the TGA. The molecules are arranged in alternating single stack zig-zag layer in the *ab*-plane (Figure 5).

CL-20:**3** (in a 1:2 ratio) has been found to crystallise in the triclinic crystal system ($P\bar{1}$), in which CL-20 exhibits the conformation found in ε -CL-20. Because of the chirality of **7**, two independent **7** are present in the unit cell. Both positions, however, are disordered, as at both positions both enantiomers can be found in the crystal. From Figure 6 it can also be seen that one position exhibits significantly stronger interactions than the other. This asymmetry is most likely the reason for the two-stage desolvation observed during the TGA.

The layered nature of the overall structure becomes evident when viewed down the *a*-axis (Figure 7). **3** is arranged in a zig-zag layer while CL-20 is arranged in a flat plane.

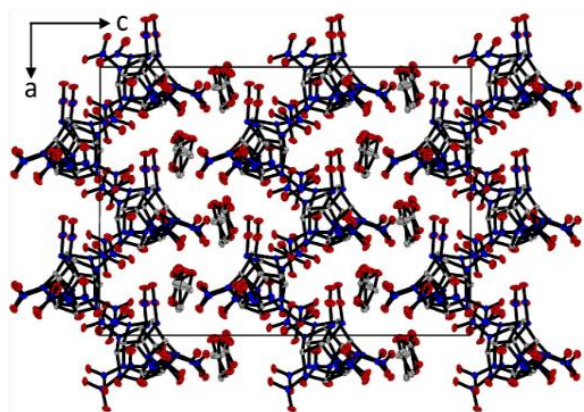


Figure 5: The layered arrangement observed in CL-20:**7**. Hydrogens are omitted for clarity.

The conformation found in ε -CL-20 is also observed in the crystal structure (monoclinic, $P2_1/c$) of CL-20:**17**. CL-20 and **17** form an alternating layer system in the *ab*-plane that is connected in three dimensions with moderately

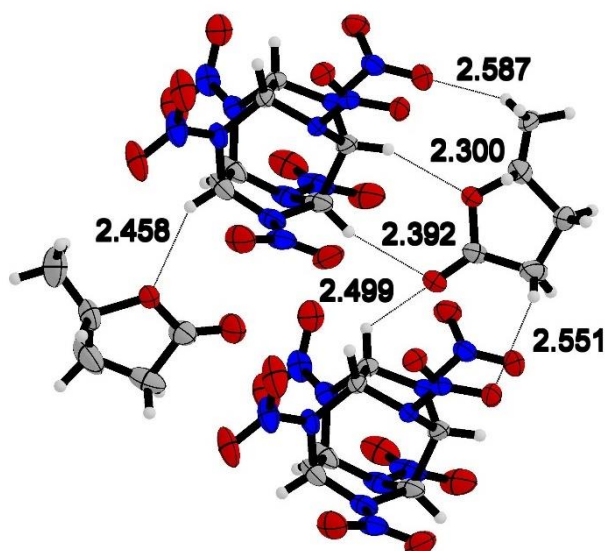


Figure 6: The intermolecular O \cdots H-C interactions between CL-20 and the two independent molecules of **3**. Contact length is displayed in Å. Only contacts of less than VdW radius - 0.1 Å are displayed. One interaction of length 2.6 Å is omitted for both positions for clarity reasons. Thermal ellipsoids are set to 50% probability.

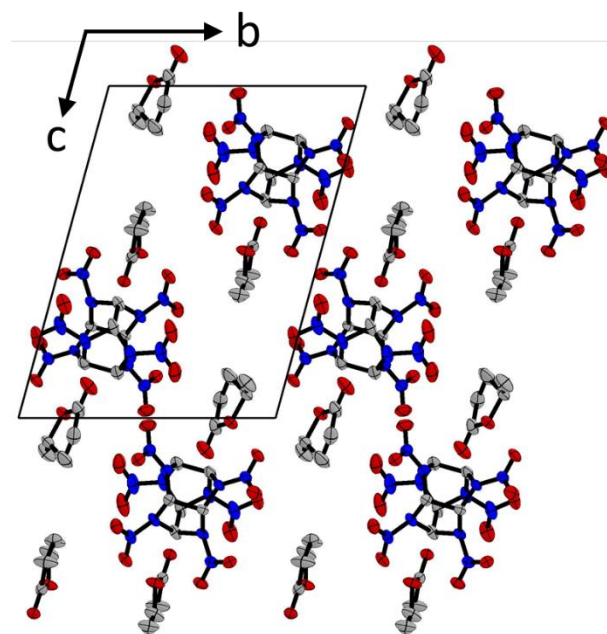


Figure 7: The layered arrangement observed in CL-20:**3**. Hydrogens are omitted for clarity. Thermal ellipsoids are set to 50% probability.

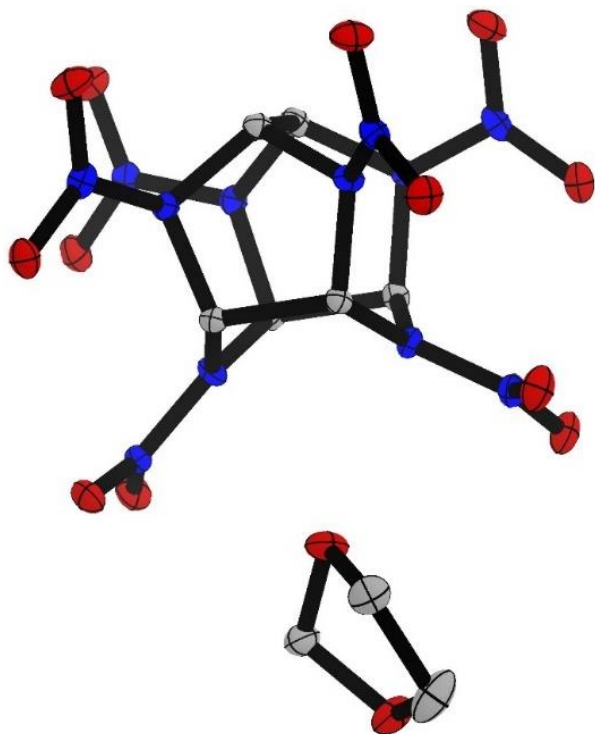


Figure 8: Visualisation of the lack of strong interaction between the acetal group of **17** and the nitramine groups of CL-20. Hydrogens are omitted for clarity. Thermal ellipsoids are set to 50% probability.

weak O \cdots H-C interactions (ca. 2.4-2.5 Å). One molecule **17** acts as the donor in the strongest O \cdots H-C interactions (2.38 Å). No short contact exists between the oxygens of **17** and the nitramine groups of CL-20. This indicates that the destabilising interaction observed in solution is most likely not present in the crystal structure. A destabilising interaction of the acetal group's oxygen lone pairs with the σ^* orbital of the nitramine group might cause the decomposition in solution. As the σ^*

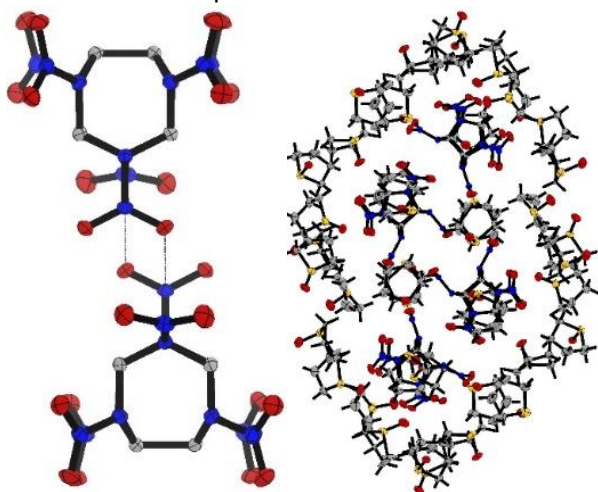


Figure 9: N \cdots O interaction between CL-20 forming an inversion centre (left). Hydrogens are omitted for clarity. Thermal ellipsoids are set to 50% probability. Visualisation of the enveloping cluster of **13** around the four CL-20 around the inversion centre.

orbitals of the N-N-bonds extend from CL-20 in line with the bonds themselves, solvent **17** would need to be positioned in extension of the N-N-bonds. From Figure 8 it can be seen, however, that **17** is situated between the nitramine groups. No significant interaction of the oxygen lone pairs of **17** with the σ^* orbitals of the N-N-bonds is, therefore, possible.

The CL-20:**13** solvate's crystal structure (monoclinic, $P2_1/c$) is formed by two independent CL-20 molecules and nine independent **13** molecules of which one is disordered. This structure comprises clusters of four CL-20 situated over inversion centre that are isolated from each other by a layer of **13** (Figure 9). The **13** molecules, therefore, form a 3 D net throughout the crystal. The nine independent molecules of **13** all exhibit different levels of O \cdots H-C interactions ranging from one to four interactions and 2.2 up to 2.6 Å. The

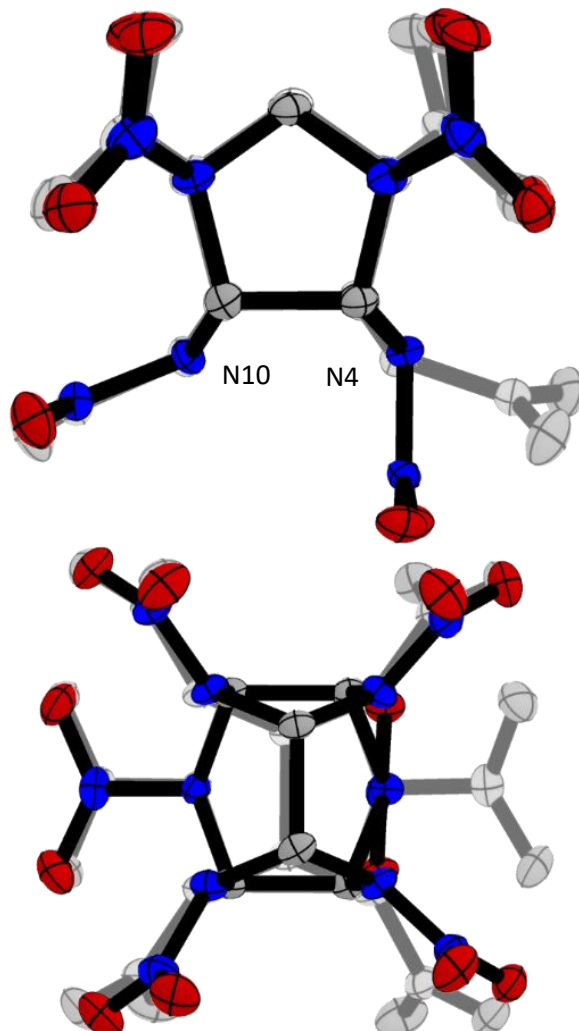


Figure 10: Superposition of the two independent CL-20 in the CL-20:**13** solvate displayed from two angles. The molecule that adopts the conformation found in ξ -CL-20 is displayed in grey. Thermal ellipsoids are set to 50% probability. Hydrogens are omitted for clarity.

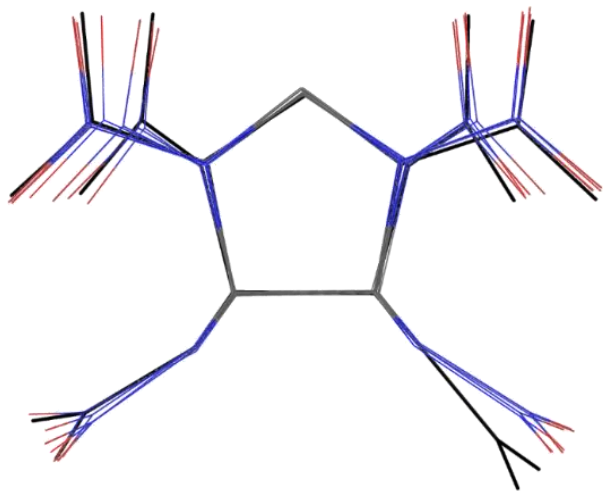


Figure 11: Superposition of the undescribed CL-20 conformations with the conformation found in ϵ -CL-20 (black). Hydrogens are omitted for clarity.

weakest bonded **13** only possesses one moderate interaction (2.4 Å). The difference in intermolecular bonding strength of all nine **13** explains the wide temperature range over which desolvation occurred in the TGA. One of the independent CL-20 adopts the conformation found in ξ -CL-20. This conformation has previously only been found in two additional crystal structures aside from ξ -CL-20.^{48,49} The other CL-20 in the crystal structure of the CL-20:**13** solvate crystal, however, exhibits a conformation (Figure 10) that was believed to be sterically unfavourable^{50,51} and has never previously been described. Hence, a novel ϑ -conformation was discovered. The conformation is similar to the conformation of CL-20 in the ξ -phase, but the nitramine group situated at N4 (Figure 10) is in endo position. The resulting lone pair repulsion seems to be mitigated by the quite severe out-of-plane bend angle (44°) of the nitramine group relative to the six-membered ring plane (Figure 10). Only two other CL-20 conformation are known to date that exhibits an endo orientation of N4 or N10: ϵ -CL-20 and η -CL-20.⁵² The solvate's crystal structure gives no obvious indications why this highly unusual conformation occurs. The CL-20 in question possesses O...N interactions with an inversion symmetrical CL-20 (Figure 9). This interaction is weak (2 · 3.1 Å) compared to similar interactions found in ϵ -CL-20 (2.8 and 3.1 Å) and ξ -CL-20 (2 · 2.6 Å). This interaction is, therefore, most likely not responsible for the unusual conformation and the unusually low decomposition temperature of the solvate. During research concerning the novelty of the ϑ -conformation, five CL-20 containing cocrystals were found that all seem to contain CL-20 in an also undescribed conformation.^{52–55} The

conformation closely resembles ϵ -CL-20. Here, however, the six-ring nitramine groups both exhibit exo orientation (Figure 11) instead of endo-exo orientation found in ϵ -CL-20.⁵⁰ While the nitramine group at N4 is endo bent by 2° in ϵ -CL-20, the nitramine groups at N4 are bent between 14° and 25° exo in the undescribed conformation. The first crystal containing this conformation was, to the best of our knowledge, published by Urbelis, Young, and Swift in 2015.⁵⁵

4 Conclusion

The solubility of CL-20 and HMX was determined in 29 solvents at 293.15 K and 333.15 K and 5 ternary mixtures at 293.15 K. The strong temperature dependency of the HMX solubility was confirmed and a, for the most parts, temperature independence of the CL-20 solubility was found. Furthermore, it was found that HMX is always far less soluble than CL-20 with a solubility ratio ranging from 5:1 for **26** at 333.15 K up to 210:1 for **21** at 293.15 K. Solubility ratios that appeared to be closer to 2 were only found when a CL-20 solvate was formed. Because of the abundance of reported solvate forming solvents and the unfavourable solubility ratio it is proposed that for cocrystallisation of the CL-20/HMX cocrystal only solvents that form thermodynamic stable HMX solvates might be excluded from consideration. In a study based on this work, it was found that only acetonitrile was a suitable solvent for the crystallisation at 333 K. But, based on the strong temperature dependency of the HMX solubility, at higher temperatures other solvents might also be applicable. The analysis of the five obtained crystal structures of the six new solvates of CL-20 revealed a novel CL-20 conformation that is thought to be energetically unfavourable but might provide further insight into the potential energy surface of the CL-20 conformations.

ACKNOWLEDGMENT

We are grateful for financial support provided by the German Ministry of Defence and the support provided by Dr. Manfred Kaiser and Dr. Michael Koch at the WTD91.

References

1. Bolton O, Simke LR, Pagoria PF, Matzger AJ. High Power Explosive with Good Sensitivity: A 2:1 Cocrystal of CL-20:HMX. *Cryst. Growth Des.* 2012;12(9):4311–4.
2. An C, Li H, Ye B, Wang J. Nano-CL-20/HMX Cocrystal Explosive for Significantly Reduced

- Mechanical Sensitivity. *J. Nanomater.* 2017;2017(5):1–7.
3. Anderson SR, am Ende DJ, Salan JS, Samuels P. Preparation of an Energetic-Energetic Cocystal using Resonant Acoustic Mixing. *Propellants, Explos., Pyrotech.* 2014;39(5):637–40.
 4. Qiu H, Patel RB, Damavarapu RS, Stepanov V. Nanoscale 2CL-20-HMX high explosive cocystal synthesized by bead milling. *CrystEngComm* 2015;17(22):4080–3.
 5. Sun S, Zhang H, Liu Y, Xu J, Huang S, Wang S, et al. Transitions from Separately Crystallized CL-20 and HMX to CL-20/HMX Cocystal Based on Solvent Media. *Cryst. Growth Des.* 2018;18(1):77–84.
 6. Ghosh M, Sikder AK, Banerjee S, Gonnade RG. Studies on CL-20/HMX (2:1) Cocystal: A New Preparation Method and Structural and Thermokinetic Analysis. *Cryst. Growth Des.* 2018;18(7):3781–93.
 7. Herrmannsdörfer D, Gerber P, Heintz T, Herrmann MJ, Klapötke TM. Investigation Of Crystallisation Conditions to Produce CL-20/HMX Cocystal for Polymer-bonded Explosives. *Propellants, Explos., Pyrotech.* 2019;44(6):668–78.
 8. Rager T, Hilfiker R. Cocystal Formation from Solvent Mixtures. *Cryst. Growth Des.* 2010;10(7):3237–41.
 9. *CrysAlisPro*: Oxford Diffraction Ltd; 2009.
 10. Altomare A., Cascarano G., Giacovazzo C., Guagliardi A. SIR-92, A program for crystal structure solution. *J. Appl. Crystallogr.* 1993;26:343.
 11. Altomare A., Burla M. C., Camalli M., Cascarano G., Giacovazzo C., Guagliardi A., et al. *J. Appl. Crystallogr.* 1999;32:115–9.
 12. Altomare A., Cascarano G., Giacovazzo C., Guagliardi A., Moliterni A. G. G., Burla M. C., et al. SIR97, program for solving and refining crystal structures 1997.
 13. Sheldrick G. M. *Acta Crystallogr., Sect. A* 2008;64:112–22.
 14. Sheldrick G. M. *SHELX-97*: University of Göttingen; 1997.
 15. Spek A. L. *PLATON, A Multipurpose Crystallographic Tool*: Utrecht University; 1999.
 16. *SCALE3 ABSPACK – An Oxford Diffraction program*: Oxford Diffraction Ltd; 2005.
 17. Holtz E von, Ornellas D, Foltz MF, Clarkson JE. The Solubility of epsilon-CL-20 in Selected Materials. *Propellants, Explos., Pyrotech.* 1994;19(4):206–12.
 18. Zimmerman JHK. The Experimental Determination of Solubilities. *Chem. Rev.* 1952;51(1):25–65.
 19. internal report.
 20. Cui C, Ren H, Huang Y, Jiao Q. Solubility Measurement and Correlation for ϵ -2,4,6,8,10,12-Hexanitro-2,4,6,8,10,12-hexaazaisowurtzitane in Five Organic Solvents at Temperatures between 283.15 and 333.15 K and Different Chloralkane + Ethyl Acetate Binary Solvents at Temperatures between 283.15 and 323.15 K. *J. Chem. Eng. Data* 2017;62(4):1204–13.
 21. Svensson L, Nyqvist J-O, Westling L. Crystallization of HMX from γ -butyrolactone. *J. Hazard. Mater.* 1986;13(1):103–8.
 22. Fuhr I, Mikonsaari I, editors. *Production and characterization of insensitive explosive*; 2004.
 23. Gibbs TR, Popolato A, editors. *LASL Explosive Property Data*. Berkeley, Calif.: Univ. of Calif. Pr; 1980.
 24. Sitzmann ME, Foti S, Misener CC. *SOLUBILITIES OF HIGH -EXPLOSIVES: REMOVAL OF HIGH EXPLOSIVE FILLERS FROM MUNITIONS BY CHEMICAL DISSOLUTION*. White Oak. Maryland; 1973.
 25. internal report.
 26. Good DJ, Rodríguez-Hornedo N. Solubility Advantage of Pharmaceutical Cocystals. *Cryst. Growth Des.* 2009;9(5):2252–64.
 27. van der Heijden AEDM, Bouma RHB. Crystallization and Characterization of RDX, HMX, and CL-20. *Cryst. Growth Des.* 2004;4(5):999–1007.
 28. Millar DIA, Maynard-Casely HE, Allan DR, Cumming AS, Lennie AR, Mackay AJ, et al. Crystal engineering of energetic materials: Co-crystals of CL-20. *CrystEngComm* 2012;14(10):3742.
 29. Aitipamula S, Banerjee R, Bansal AK, Biradha K, Cheney ML, Choudhury AR, et al. Polymorphs, Salts, and Cocystals: What’s in a Name? *Cryst. Growth Des.* 2012;12(5):2147–52.
 30. Bond AD. What is a co-crystal? *CrystEngComm* 2007;9(9):833.
 31. Desiraju GR. Crystal and co-crystal. *CrystEngComm* 2003;5(82):466.
 32. Stahly GP. Diversity in Single- and Multiple-Component Crystals. The Search for and Prevalence of Polymorphs and Cocystals. *Cryst. Growth Des.* 2007;7(6):1007–26.
 33. Blom CE, Günthard HH. Rotational isomerism in methyl formate and methyl acetate; a low-temperature matrix infrared study using thermal molecular beams. *Chem. Phys. Lett.* 1981;84(2):267–71.
 34. Wennerstrom H, Forsen S, Roos B. Ester group. I. Ab initio calculations on methyl formate. *J. Phys. Chem.* 1972;76(17):2430–6.
 35. Wang X, Houk KN. Theoretical elucidation of the origin of the anomalously high acidity of

Meldrum's acid. *J. Am. Chem. Soc.* 1988;110(6):1870–2.

36. Thome V. *Computer Simulationen als Hilfsmittel zur Kristallisation polymorpher organischer Substanzen am Beispiel von HNIW*. thesis. Heidelberg; 2004.

37. Philip T, Cook RL, Malloy Jr. TB, Allinger NL, Chang S, Yuh Y. Molecular mechanics calculations and experimental studies of conformations of .delta.-valerolactone. *J. Am. Chem. Soc.* 1981;103(9):2151–6.

38. *SNPE Safety Data Sheet of CL-20*.

39. Selig W. New adducts of octahydro-1,3,5,7-tetranitro-1,3,5,7-tetrazocine (HMX). *Propellants, Explos., Pyrotech.* 1982;7(3):70–7.

40. George RS, Cady HH, Rogers RN, Rohwer RK. Solvates of Octahydro-1,3,5,7- Tetranitro- 1,3,5,7-tetrazocine (HMX). Relatively Stable Monosolvates. *Ind. Eng. Chem. Prod. Res. Dev.* 1965;4(3):209–14.

41. Selig W. *Some 1:1 complexes of cyclomethylenetetranitramine (HMX) and their application to the estimation of HMX in admixture with RDX*; 1964.

42. Selig W. Adducts of 1,3,5,7-Tetranitro-1,3,5,7-Tetraazacylooctane (HMX). *Explosivstoffe* 1969;17(4):73–86.

43. Shen F. The pseudosymmetric crystal structure of 2,4,6,8,10,12-hexanitrohexaazaisowurtzitane dimethyl carbonate (2/3), C₂₁H₃₀N₂₄O₃₃. *Z. Kristallogr. New Cryst. Struct.* 2019;234(3):387–9.

44. Pan B, Dang L, Wang Z, Jiang J, Wei H. Preparation, crystal structure and solution-mediated phase transformation of a novel solid-state form of CL-20. *CrystEngComm* 2018;20(11):1553–63.

45. Haller TM, Rheingold AL, Brill TB. Structure of the 1/1 complex between octahydro-1,3,5,7-tetranitro-1,3,5,7-tetrazocine (HMX), C₄H₈N₈O₈, and N-methyl-2-pyrrolidinone (NMP), C₅H₉NO. *Acta Crystallogr C Cryst Struct Commun* 1985;41(6):963–5.

46. Sun X, Yin Q, Ding S, Shen Z, Bao Y, Gong J, et al. (Solid + liquid) phase diagram for (indomethacin + nicotinamide)-methanol or

methanol/ethyl acetate mixture and solubility behavior of 1:1 (indomethacin + nicotinamide) cocrystal at T=(298.15 and 313.15) K. *J. Chem. Thermodyn.* 2015;85:171–7.

47. Dorofeeva OV, Suntsova MA. Enthalpy of formation of CL-20. *Comp. Theor. Chem.* 2015;1057:54–9.

48. Aldoshin SM, Aliev ZG, Goncharov TK, Korchagin DV, Milekhin YM, Shishov NI. New conformer of 2,4,6,8,10,12-hexanitro-2,4,6,8,10,12-hexaazaisowurtzitane (CL-20). Crystal and molecular structures of the CL-20 solvate with glyceryl triacetate. *Russ Chem Bull* 2011;60(7):1394–400.

49. Zyuzin IN, Aliev ZG, Goncharov TK, Ignatieva EL, Aldoshin SM. Structure of a bimolecular crystal of 2,4,6,8,10,12-hexanitro-2,4,6,8,10,12-hexaazaisowurtzitane and methoxy-NNO-azoxymethane. *J. Struct. Chem.* 2017;58(1):113–8.

50. Foltz MF, Coon CL, Garcia F, Nichols AL. The thermal stability of the polymorphs of hexanitrohexaazaisowurtzitane, Part I. *Propellants, Explos., Pyrotech.* 1994;19(1):19–25.

51. Sysolyatin SV, Lobanova AA, Chernikova YT, Sakovich GV. Methods of synthesis and properties of hexanitrohexaazaisowurtzitane. *Russ. Chem. Rev.* 2005;74(8):757–64.

52. Aliev ZG, Goncharov TK, Dashko DV, Ignat'eva EL, Vasil'eva AA, Shishov NI, et al. Polymorphism of bimolecular crystals of CL-20 with tris[1,2,5]oxadiazolo[3,4-b:3',4'-d:3'',4''-f]azepine-7-amine. *Russ. Chem. Bull.* 2017;66(4):694–701.

53. Tan Y, Yang Z, Wang H, Li H, Nie F, Liu Y, et al. High Energy Explosive with Low Sensitivity: A New Energetic Cocrystal Based on CL-20 and 1,4-DNI. *Cryst. Growth Des.* 2019;19(8):4476–82.

54. Yang Z, Wang H, Ma Y, Huang Q, Zhang J, Nie F, et al. Isomeric Cocrystals of CL-20: A Promising Strategy for Development of High-Performance Explosives. *Cryst. Growth Des.* 2018;18(11):6399–403.

55. Urbelis JH, Young VG, Swift JA. Using solvent effects to guide the design of a CL-20 cocrystal. *CrystEngComm* 2015;17(7):1564–8.

Solubility Behaviour of CL-20 and HMX in Organic Solvents and Solvates of CL-20

Dirk Herrmannsdörfer,^{[a]*} Jörg Stierstorfer,^[b] Thomas M. Klapötke^[b]

[a] *Energetic Materials Fraunhofer Institute for Chemical Technology ICT Joseph-von-Fraunhofer-Str. 7 76327 Pfinztal, Germany*

[b] *Department of Chemistry Energetic Materials Research Ludwig-Maximilian University of Munich Butenandtstr. 5 - 13 (Haus D) 81377 Munich, Germany*

*Corresponding Author: dirk.herrmannsdoerfer@ict.fraunhofer.de

Content

Figure S1-6: DSC diagram of the solvates

Figure S7-12: Raman spectra of the solvents

Table S1: Observed vibration bands of the solvates

Figure S13: Temperature dependent mass loss of the solvates

Figure S14-17: NMR spectra of CL-20 and HMX

Table S2: Chemical shift and integrals of the ¹H NMR spectra of the HMX and CL-20 samples

Figure S18-19: HPLC chromatograms of CL-20 and HMX

Table S3: Retention times and integrals of the HPLC chromatogram of the HMX and CL-20 samples

Size: 0.8080 mg
Method: HR5 bis 270°C, Air

DSC

Instrument: DSC Q2000 V24.10 Build 122

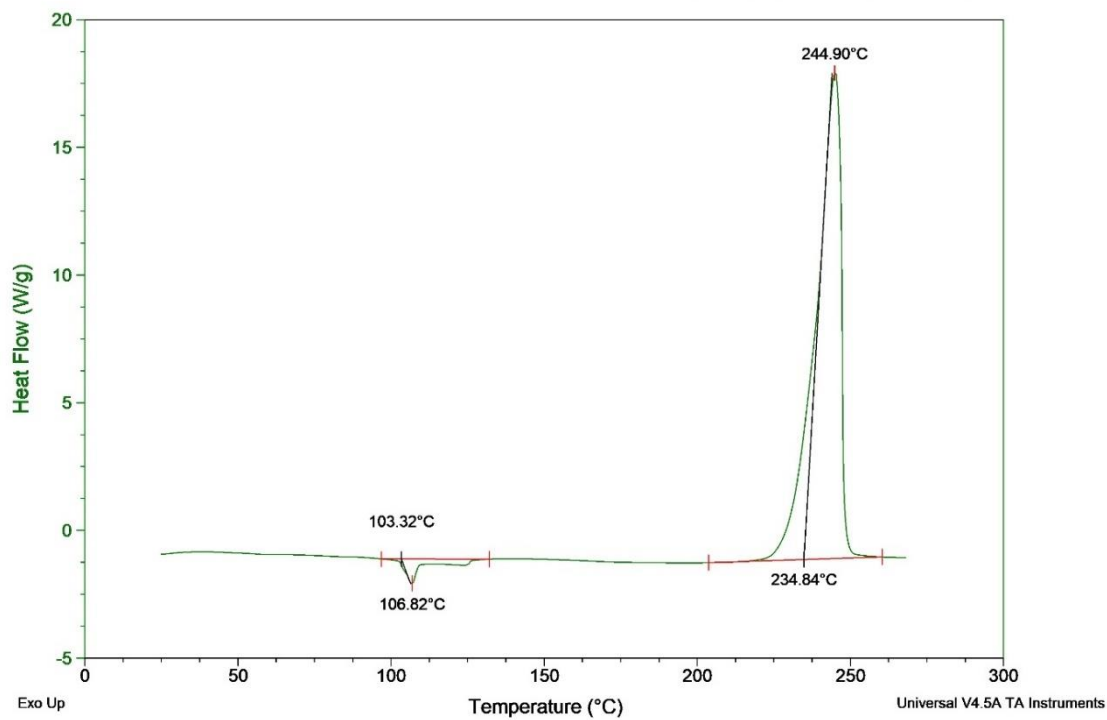


Figure S1: DSC diagram of the **3** solvate (heating rate 5K/min).

Size: 0.7890 mg
Method: HR5 bis 270°C, Air

DSC

Instrument: DSC Q2000 V24.10 Build 122

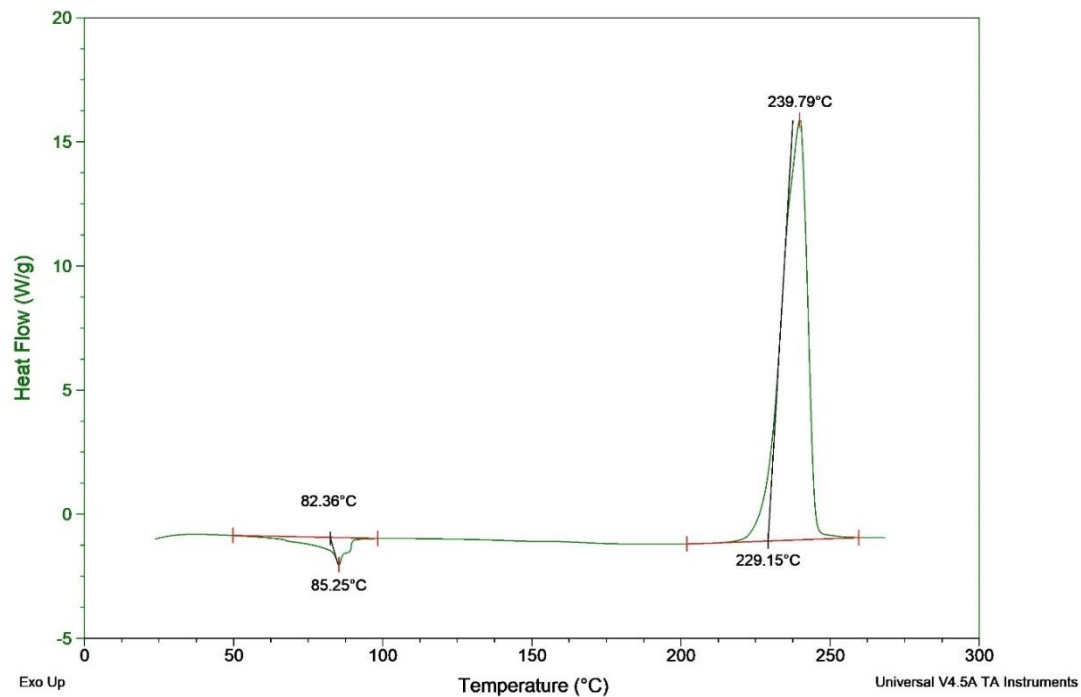


Figure S2: DSC diagram of the **28** solvate (heating rate 5K/min).

Size: 0.9640 mg
Method: HR5 bis 270°C, Air

DSC

Instrument: DSC Q2000 V24.10 Build 122

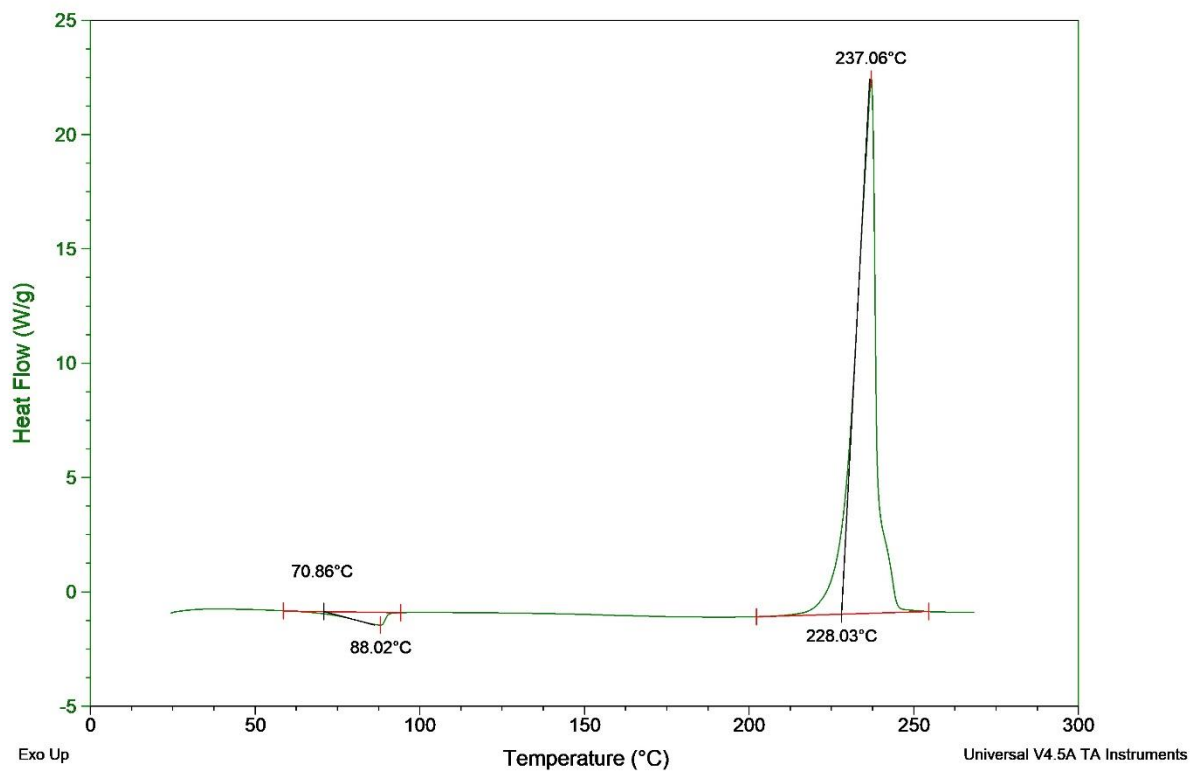


Figure S3: DSC diagram of the **33** solvate (heating rate 5K/min).

Size: 0.9580 mg
Method: HR5 bis 270°C, Air

DSC

Instrument: DSC Q2000 V24.10 Build 122

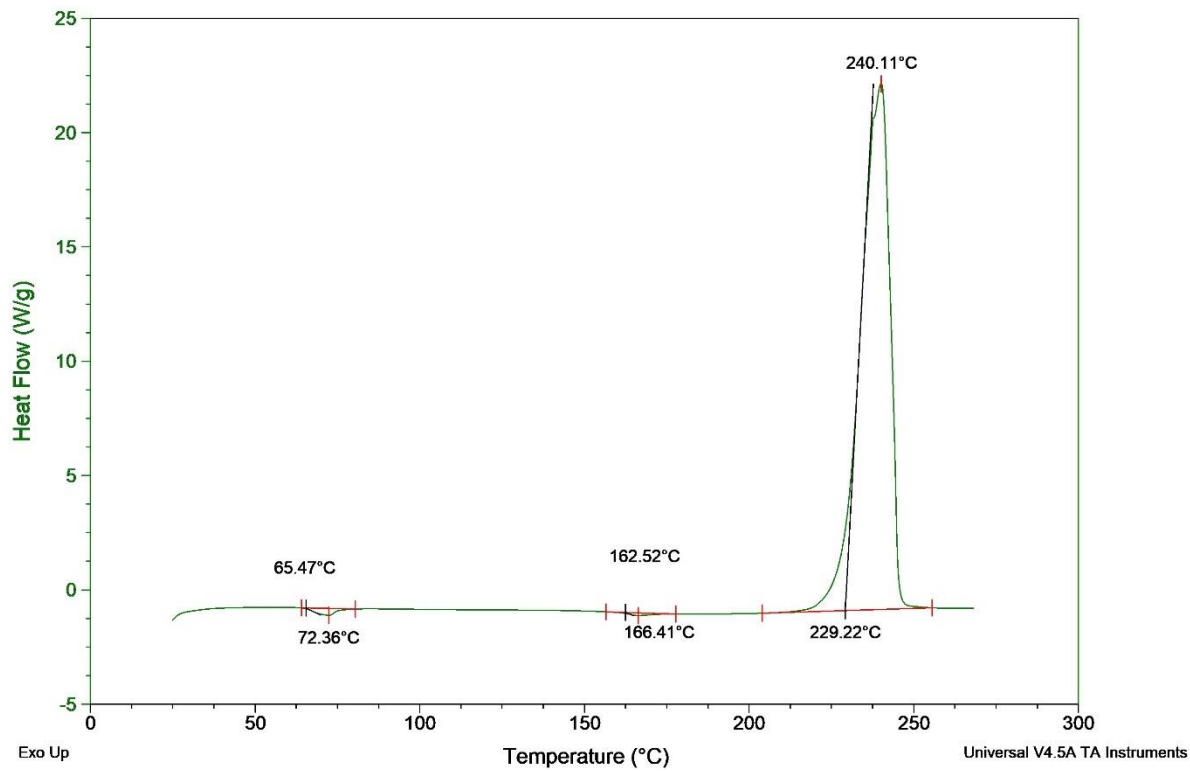


Figure S4: DSC diagram of the **17** solvate (heating rate 5K/min).

Size: 0.8680 mg
Method: HR5 bis 270°C, Air

DSC

Instrument: DSC Q2000 V24.10 Build 122

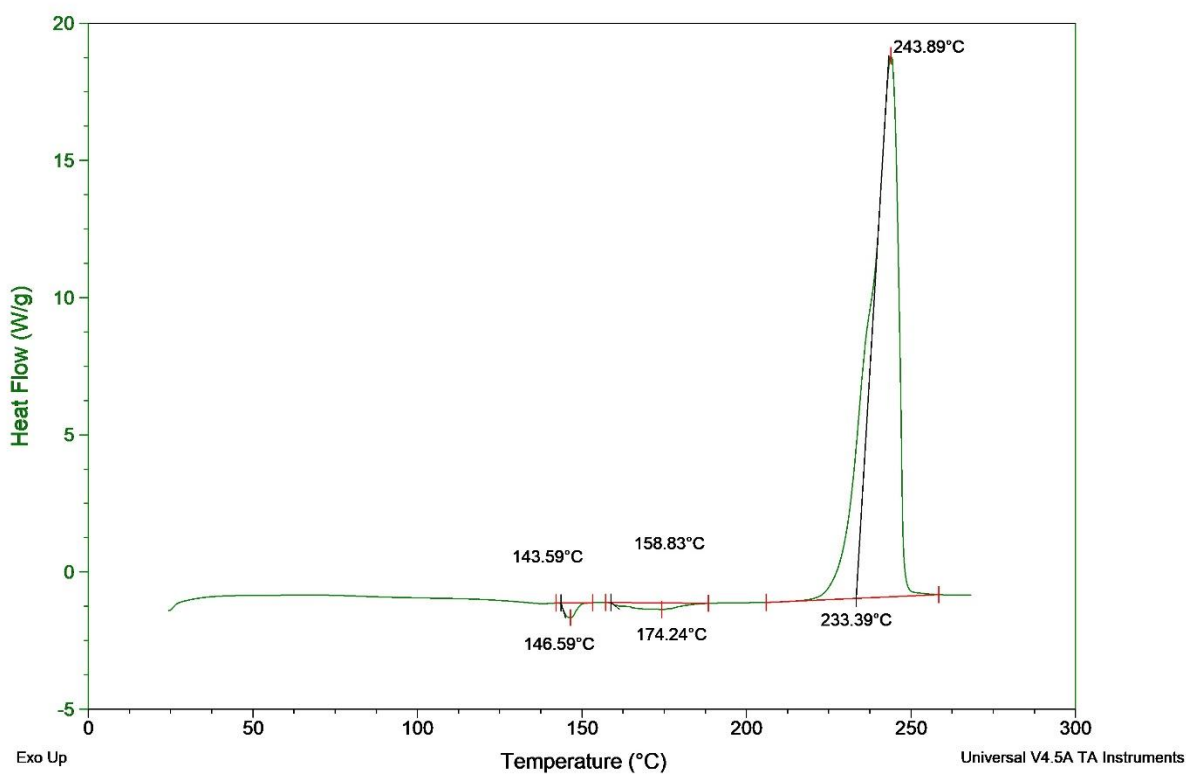


Figure S5: DSC diagram of the 7 solvate (heating rate 5K/min).

Size: 1.4590 mg
Method: HR5 bis 270°C

DSC

Instrument: DSC Q2000 V24.10 Build 122

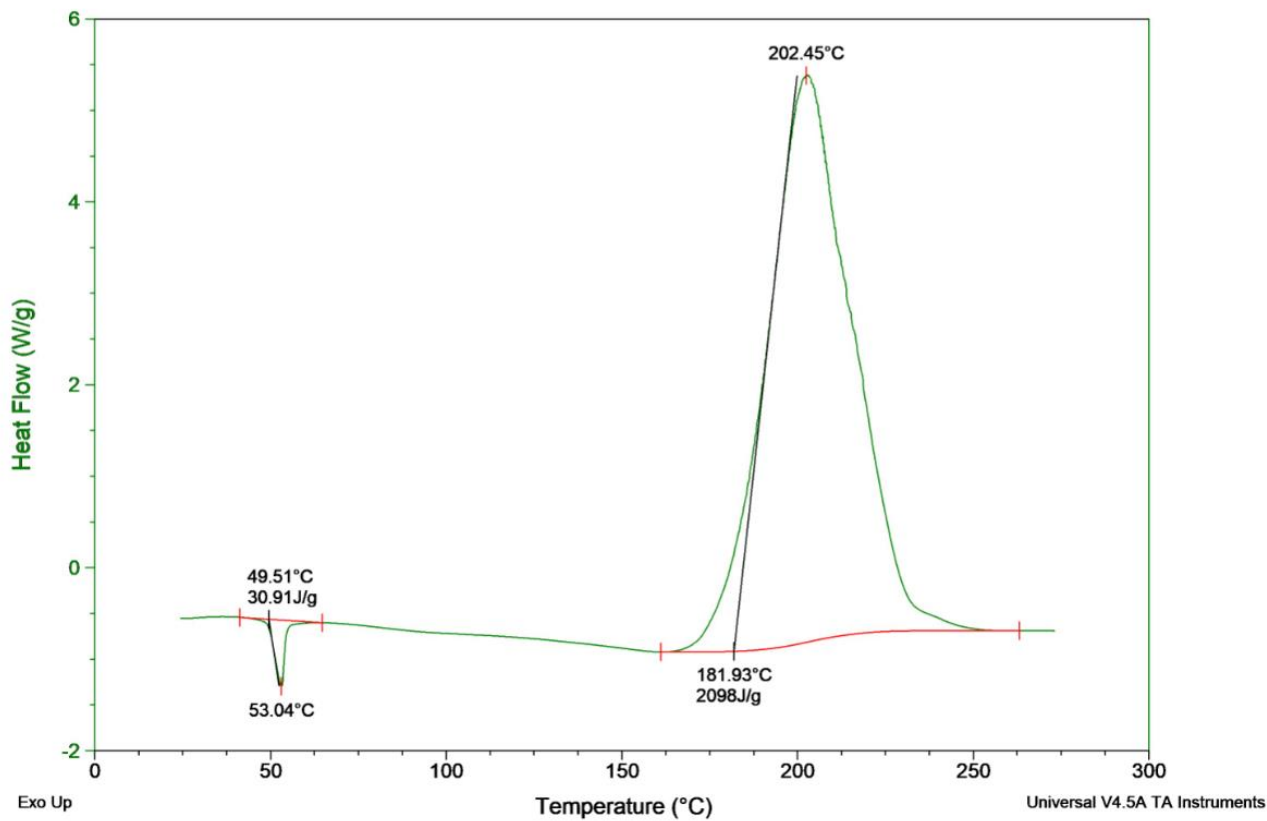


Figure S6: DSC diagram of the 13 solvate (heating rate 5K/min).

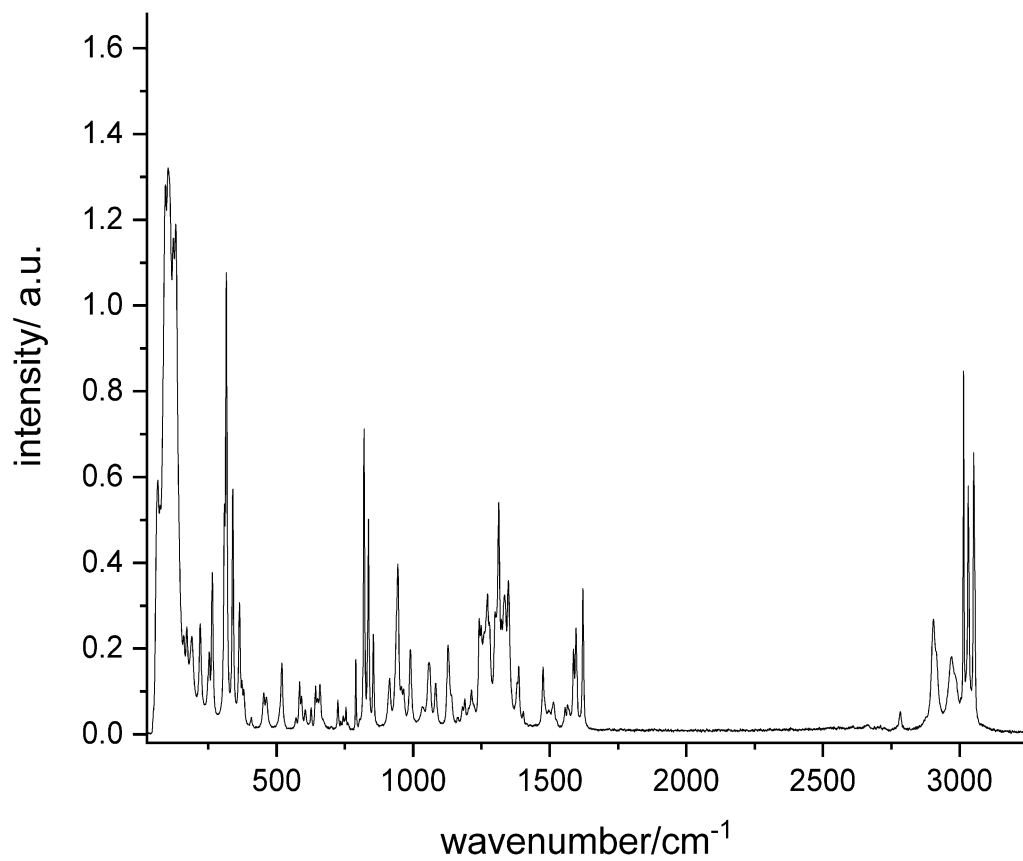


Figure S7: Raman spectrum of the **17** solvate of CL-20.

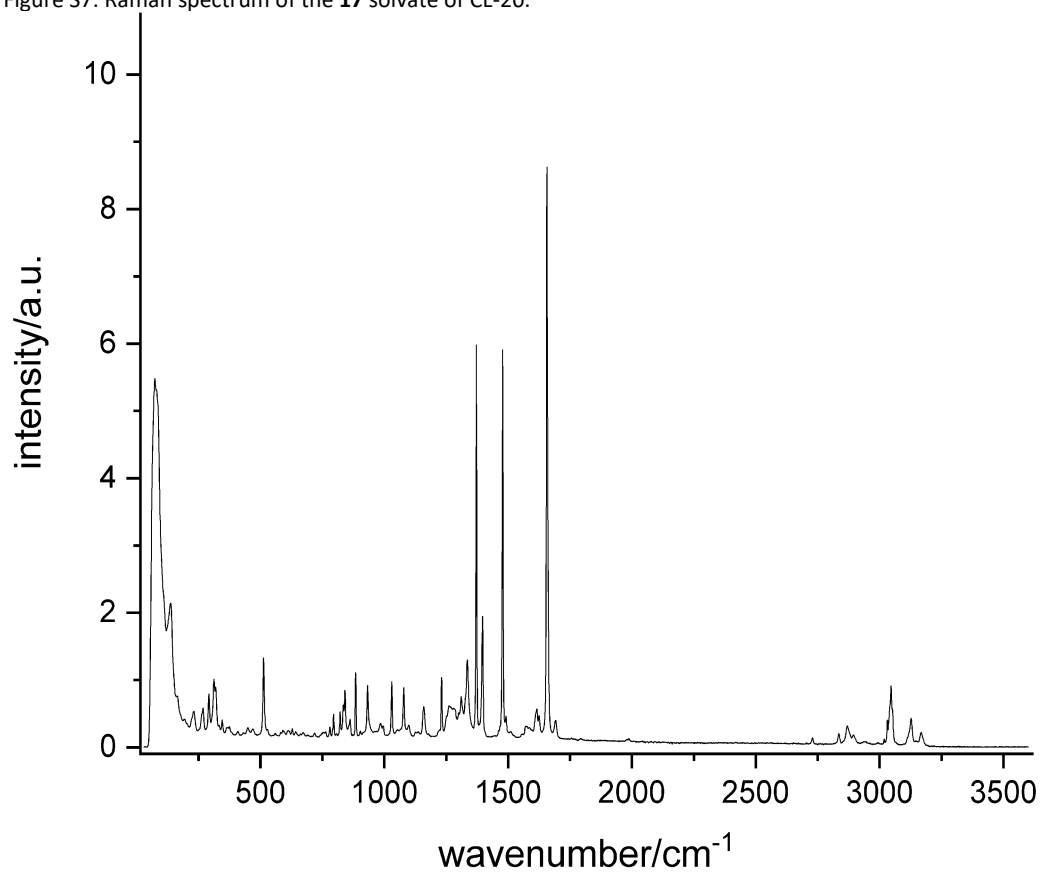


Figure S8: Raman spectrum of the **28** solvate of CL-20.

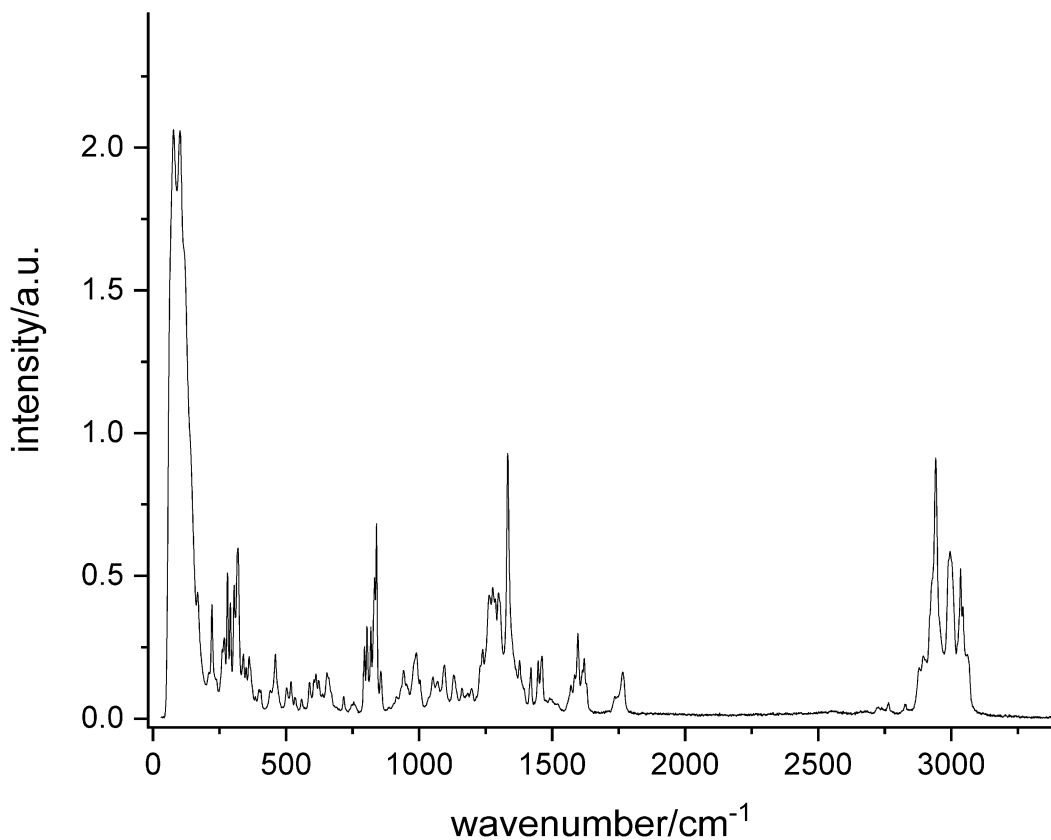


Figure S9: Raman spectrum of the **3** solvate of CL-20.

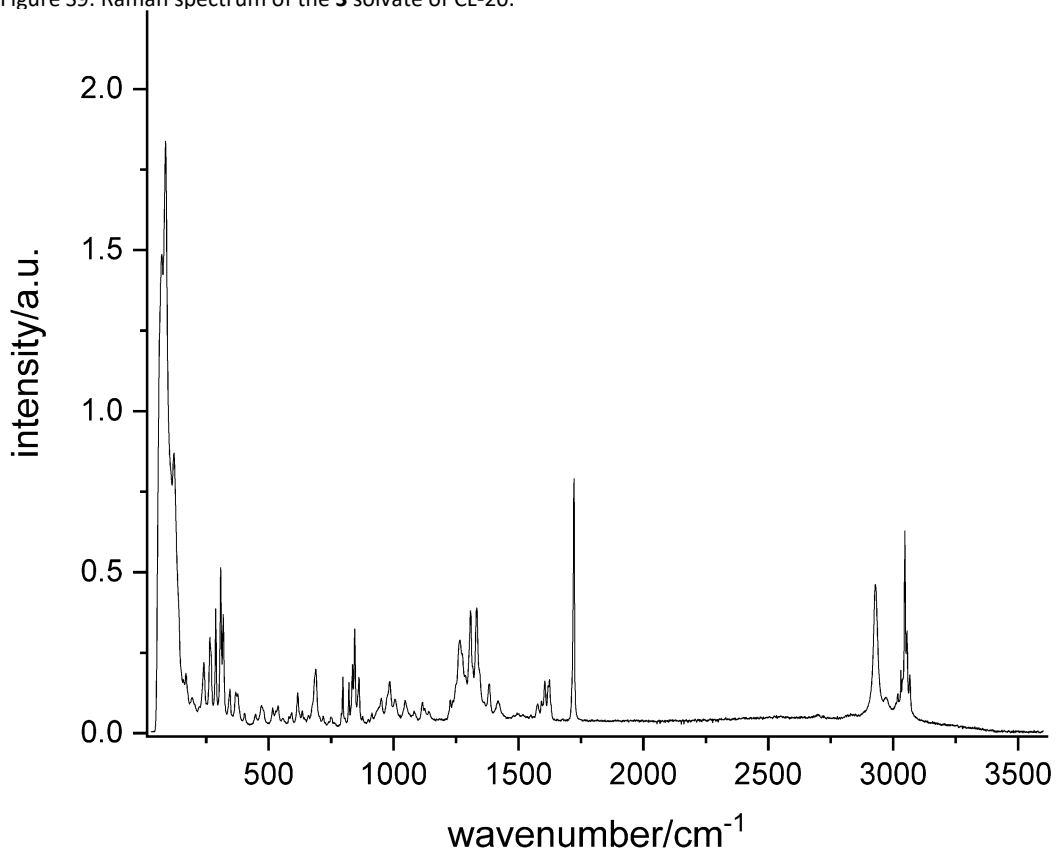


Figure S10: Raman spectrum of the **33** solvate of CL-20.

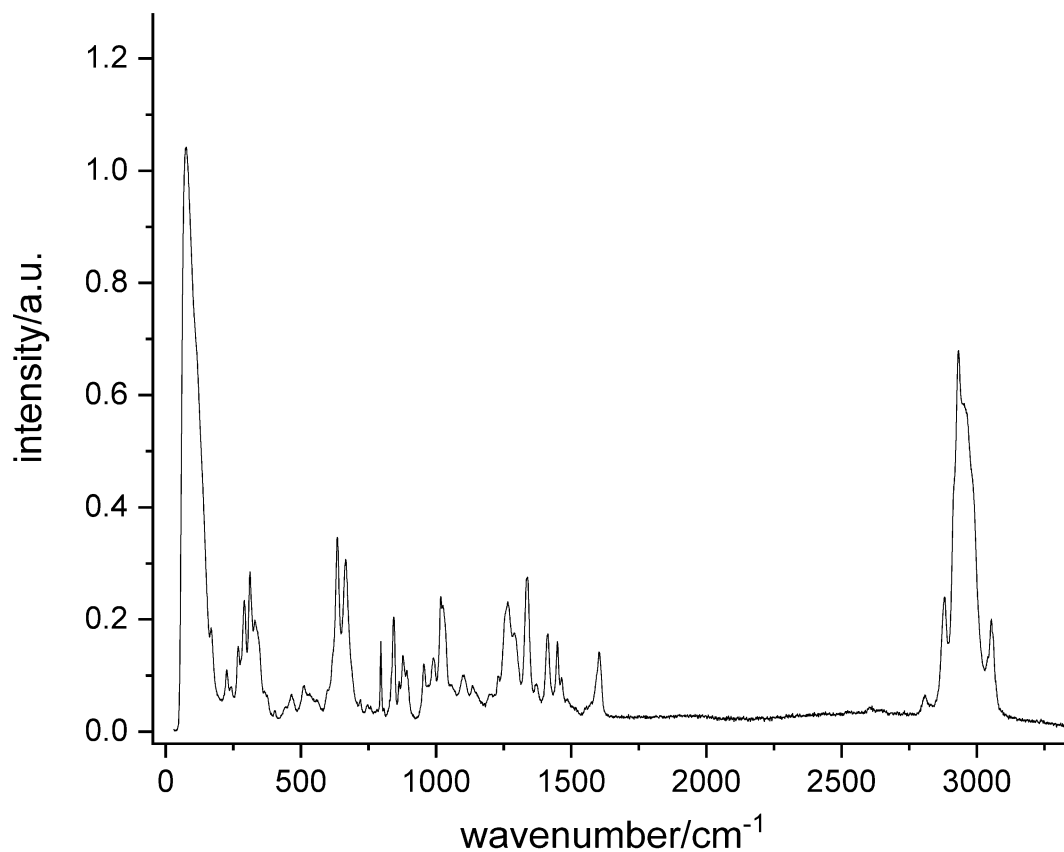


Figure S11: Raman spectrum of the **13** solvate of CL-20.

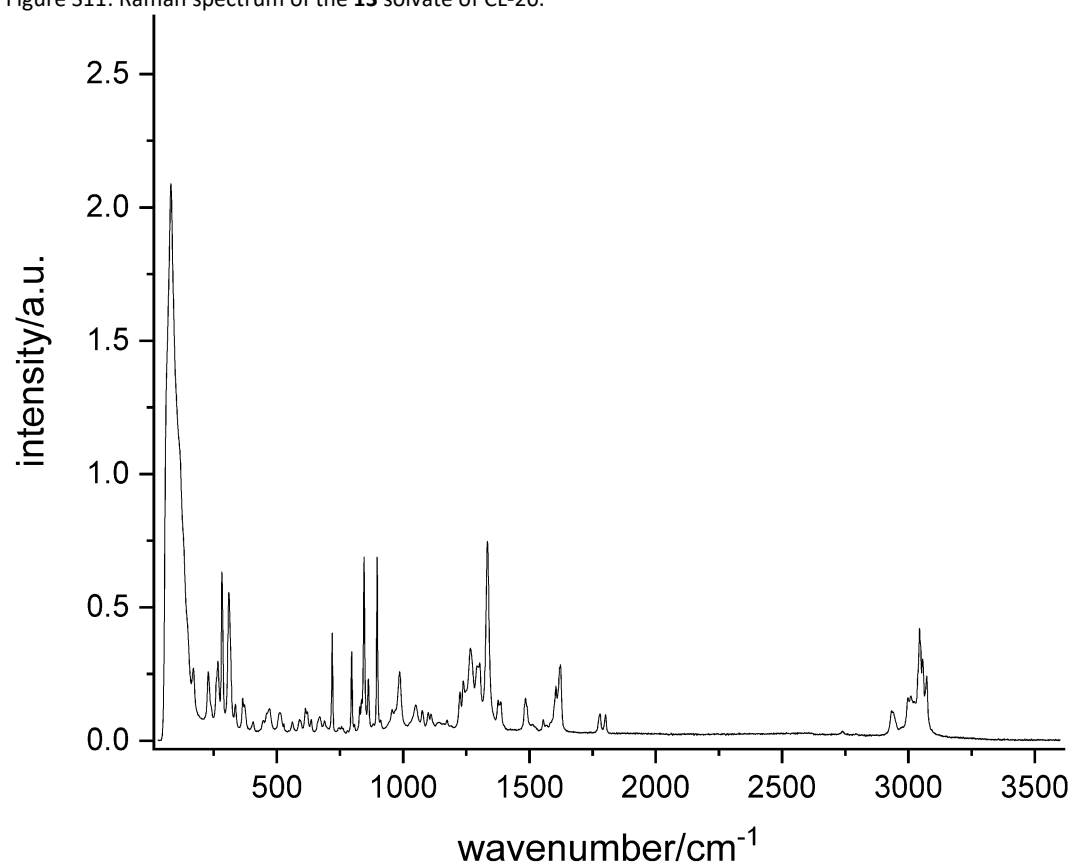


Figure S12: Raman spectrum of the **7** solvate of CL-20.

Table S1: The Observed Vibration Bands of the Solvates in cm⁻¹a)

| 17 | | 28 | | 3 | | 33 | | 13 | | 7 | |
|------|--------|------|-------|------|--------|------|-------|------|--------|------|--------|
| 65 | s | 74 | s | 77 | vs | 72 | vs | 75 | vs | 64 | vs, sh |
| 73 | s | 80 | s, sh | 102 | vs | 87 | vs | 110 | vs | 81 | vs |
| 93 | vs | 137 | w | 118 | vs, sh | 121 | vs | 168 | w | 117 | vs |
| 103 | vs | 231 | vw | 168 | m | 159 | w | 226 | vw | 170 | w |
| 107 | vs, sh | 263 | vw,sh | 222 | m | 169 | w | 242 | vw | 229 | w |
| 122 | vs | 269 | vw | 261 | w | 194 | vw | 268 | w | 261 | w, sh |
| 131 | vs | 292 | vw | 268 | w | 241 | w | 291 | w | 267 | w |
| 160 | w | 312 | vw | 280 | m | 265 | w | 312 | m | 283 | vs |
| 171 | w | 319 | vw | 291 | m | 288 | m | 330 | w | 310 | s |
| 190 | w | 345 | vw | 305 | m | 308 | s | 465 | vw | 336 | vw |
| 220 | w | 512 | vw | 320 | s | 345 | vw | 511 | vw | 365 | w |
| 253 | w | 795 | vw | 340 | w | 368 | vw | 635 | m | 372 | vw |
| 265 | m | 821 | vw | 350 | vw | 377 | vw | 666 | m | 406 | vw |
| 309 | s | 834 | vw | 362 | w | 404 | vw | 720 | vw | 447 | vw |
| 316 | vs | 841 | vw | 385 | vw | 448 | vw | 795 | w | 460 | vw |
| 340 | s | 857 | vw,sh | 398 | vw | 471 | vw | 844 | w | 470 | vw |
| 364 | w | 862 | vw | 406 | vw | 517 | vw | 863 | vw | 512 | vw |
| 373 | vw | 884 | vw | 441 | vw | 529 | vw | 877 | vw | 528 | vw |
| 380 | vw | 932 | vw | 460 | w | 538 | vw | 892 | vw | 561 | vw |
| 408 | vw | 984 | vw | 503 | vw | 556 | vw | 955 | vw | 590 | vw |
| 453 | vw | 1030 | vw | 519 | vw | 581 | vw | 990 | vw | 613 | vw |
| 463 | vw | 1078 | vw | 534 | vw | 592 | vw | 1018 | w | 621 | vw |
| 519 | vw | 1098 | vw | 559 | vw | 617 | vw | 1025 | w, sh | 637 | vw |
| 571 | vw | 1159 | vw | 589 | vw | 635 | vw | 1101 | vw | 670 | vw |
| 584 | vw | 1231 | vw | 605 | vw | 684 | w, sh | 1134 | vw | 689 | vw |
| 591 | vw | 1251 | vw,sh | 613 | vw | 689 | w | 1231 | vw | 719 | m |
| 605 | vw | 1261 | vw,sh | 623 | vw | 719 | vw | 1265 | w | 757 | vw |
| 626 | vw | 1268 | vw,sh | 654 | vw | 750 | vw | 1289 | w, sh | 796 | m |
| 643 | vw | 1279 | vw,sh | 661 | vw,sh | 797 | w | 1338 | m | 807 | vw |
| 650 | vw | 1286 | vw,sh | 717 | vw | 836 | w | 1371 | vw | 828 | vw |
| 659 | vw | 1300 | vw | 795 | w | 844 | m | 1413 | w | 835 | w |
| 725 | vw | 1310 | vw | 804 | w | 861 | w | 1449 | w | 845 | vs |
| 735 | vw | 1327 | vw,sh | 819 | w | 877 | vw | 1464 | vw | 863 | w |
| 744 | vw | 1335 | vw | 833 | m | 914 | vw | 1603 | w | 897 | vs |
| 754 | vw | 1372 | s | 840 | s | 951 | vw | 2808 | vw | 911 | vw |
| 790 | w | 1396 | w | 856 | vw | 1006 | vw | 2881 | w | 957 | vw |
| 820 | vs | 1477 | s | 942 | vw | 1047 | vw | 2932 | vs | 986 | w |
| 836 | m | 1491 | vw | 952 | vw | 1082 | vw | 2955 | vs, sh | 1050 | vw |
| 854 | w | 1616 | vw | 982 | w, sh | 1116 | vw | 3054 | w | 1076 | vw |
| 914 | vw | 1625 | vw | 989 | w | 1124 | vw | | | 1099 | vw |
| 944 | m | 1657 | vs | 1004 | vw | 1140 | vw | | | 1110 | vw |
| 957 | vw | 1693 | vw | 1052 | vw | 1227 | vw | | | 1174 | vw |
| 965 | vw | 2729 | vw | 1069 | vw | 1266 | w | | | 1226 | w |
| 990 | w | 2835 | vw | 1131 | vw | 1275 | w, sh | | | 1238 | w |
| 1034 | vw | 2870 | vw | 1161 | vw | 1288 | w, sh | | | 1266 | m |
| 1058 | vw | 2894 | vw | 1198 | vw | 1308 | m | | | 1292 | w |
| 1082 | vw | 3018 | vw | 1240 | w | 1317 | w, sh | | | 1303 | w |
| 1128 | w | 3031 | vw | 1264 | m | 1333 | m | | | 1333 | vs |
| 1140 | vw | 3041 | vw,sh | 1277 | m | 1343 | w, sh | | | 1376 | w |
| 1180 | vw | 3047 | vw | 1287 | m | 1383 | vw | | | 1387 | vw |
| 1189 | vw | 3052 | vw | 1299 | m | 1419 | vw | | | 1481 | vw,sh |
| 1214 | vw | 3127 | vw | 1305 | m, sh | 1577 | vw | | | 1484 | w |
| 1242 | w | 3167 | vw | 1333 | vs | 1592 | vw | | | 1491 | vw,sh |
| 1249 | w | | | 1378 | w | 1605 | w | | | 1555 | vw |
| 1260 | w | | | 1421 | vw | 1619 | vw | | | 1604 | w |
| 1272 | w | | | 1448 | w | 1624 | w | | | 1619 | w |
| 1279 | w | | | 1462 | w | 1722 | vs | | | 1623 | w |
| 1300 | w | | | 1571 | vw | 2929 | m | | | 1779 | vw |
| 1313 | s | | | 1585 | vw | 2971 | vw | | | 1801 | vw |
| 1323 | w | | | 1597 | w | 3019 | vw | | | 2934 | vw |
| 1334 | w | | | 1614 | vw | 3031 | w | | | 2998 | w |
| 1348 | m | | | 1621 | w | 3037 | w | | | 3010 | w |
| 1381 | vw | | | 1629 | vw | 3047 | s | | | 3044 | m |
| 1386 | vw | | | 1736 | vw | 3055 | m | | | 3048 | m |
| 1403 | vw | | | 1766 | vw | 3066 | w | | | 3056 | m |
| 1475 | vw | | | 2764 | vw | | | | | 3072 | w |

| | | | |
|------|-------|------|-------|
| 1513 | vw | 2828 | vw |
| 1556 | vw | 2879 | vw |
| 1565 | vw | 2895 | w |
| 1587 | w | 2927 | m, sh |
| 1596 | w | 2990 | m, sh |
| 1621 | w | 2996 | s |
| 2783 | vw | 3002 | m, sh |
| 2904 | w | 3035 | m |
| 2915 | w | 3044 | m |
| 2970 | w | 3060 | w |
| 2984 | vw,sh | | |
| 3014 | vs | | |
| 3032 | s | | |
| 3051 | s | | |

a) v = very, s = strong, m = medium, w = weak, sh = shoulder

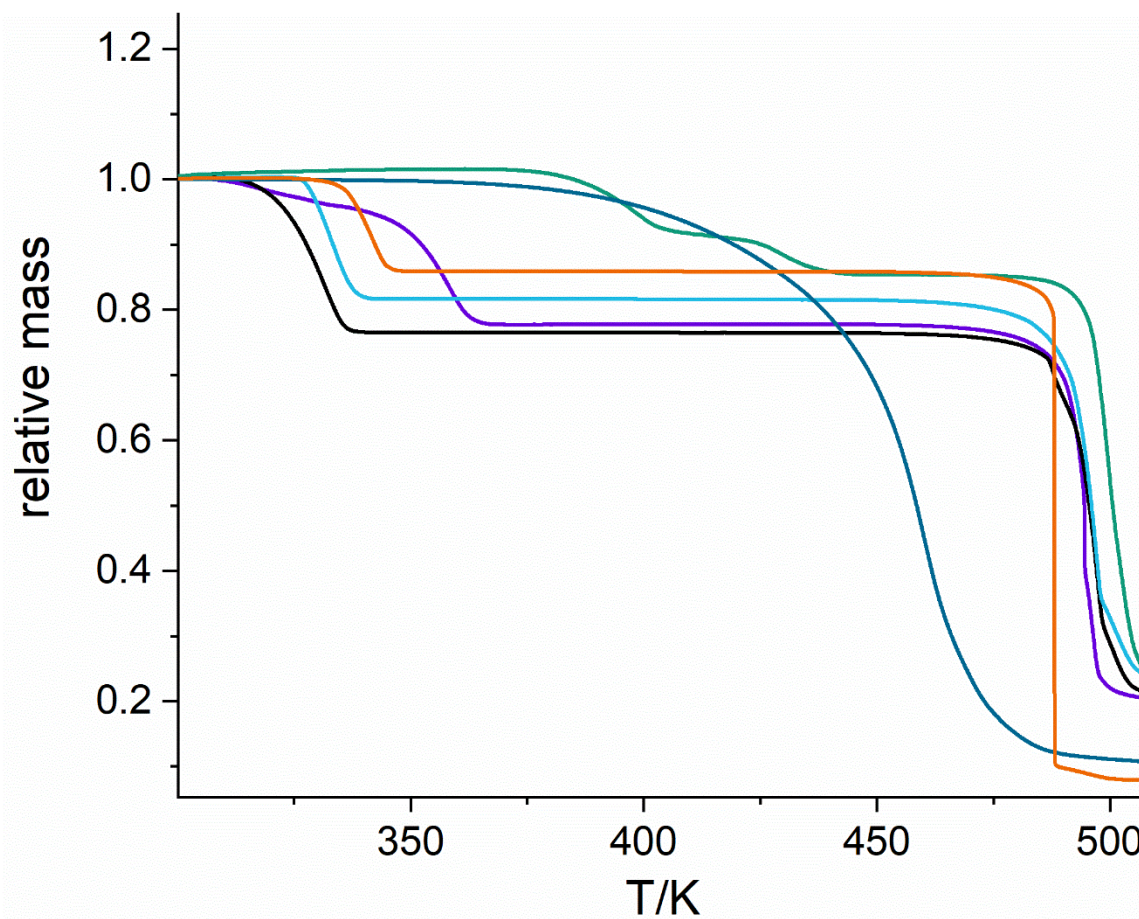


Figure S13: Temperature dependent mass loss of the solvates. With the CL-20 solvates of **7** in green, **13** in blue, **17** in orange, **3** in violet, **33** in teal and **28** in black.

NMR measurement of HMX and CL-20

Purity of the raw material was judged based on the ^1H NMR data under the assumption, that the impurities possess a comparable hydrogen to carbon, nitrogen, and oxygen ratio as the raw material. This assumption appears reasonable, as the expected impurities of CL-20 are incompletely nitrated by-products and in case of HMX the expected impurity is RDX. Because of the overlap of the signals in the range of 5.7 ppm to 6.3 ppm for HMX and 7.7 ppm to 8.4 ppm for CL-20, respectively these signals were integrated using origin 2019. The obtained integrals for HMX and CL-20 are listed in Table S1. Measurements were carried out using a 400 MHz Bruker spectrometer. For ^1H 16 spectra were summed up. For ^{13}C 64 spectra were summed up and proton decoupling was carried out.

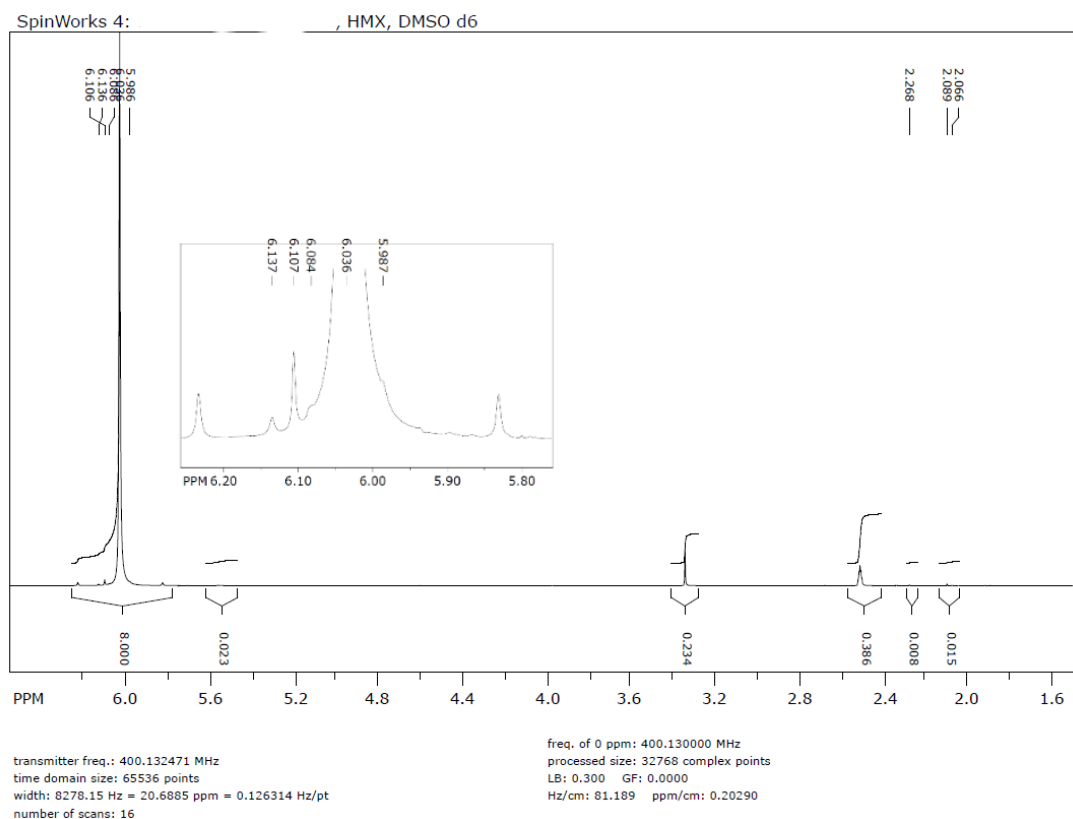


Figure S14: ^1H NMR spectrum of HMX dissolved in DMSO D6. Signals at 3.3 ppm and 2.5 ppm are caused by incompletely deuterated DMSO.

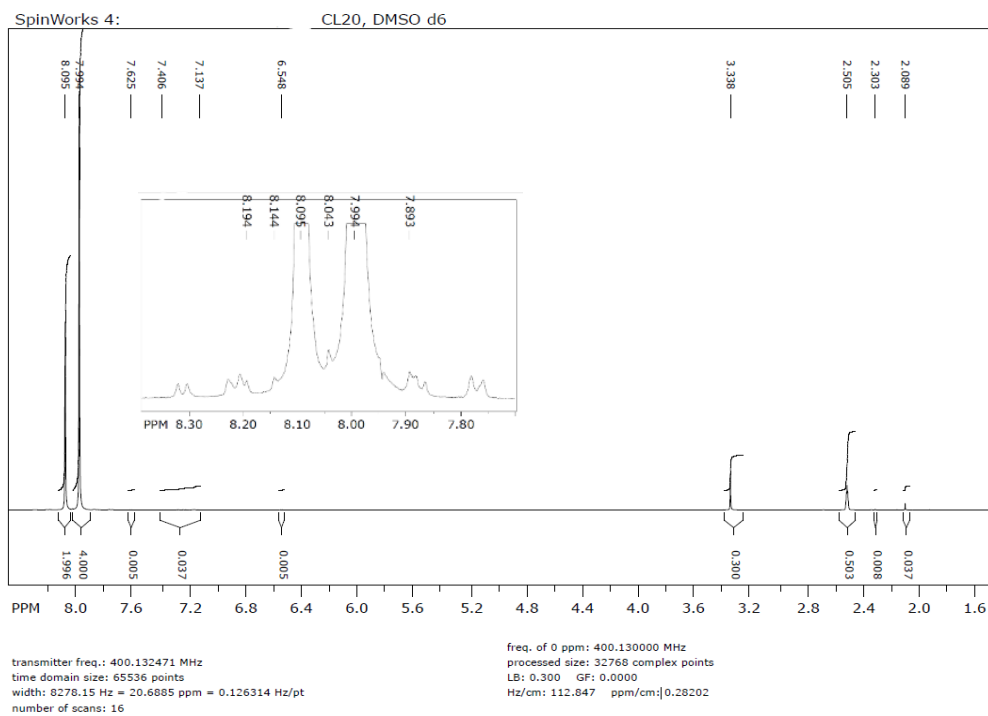


Figure S15: ¹H NMR spectrum of CL-20 dissolved in DMSO D6. Signals at 3.3 ppm and 2.5 ppm are caused by incompletely deuterated DMSO.

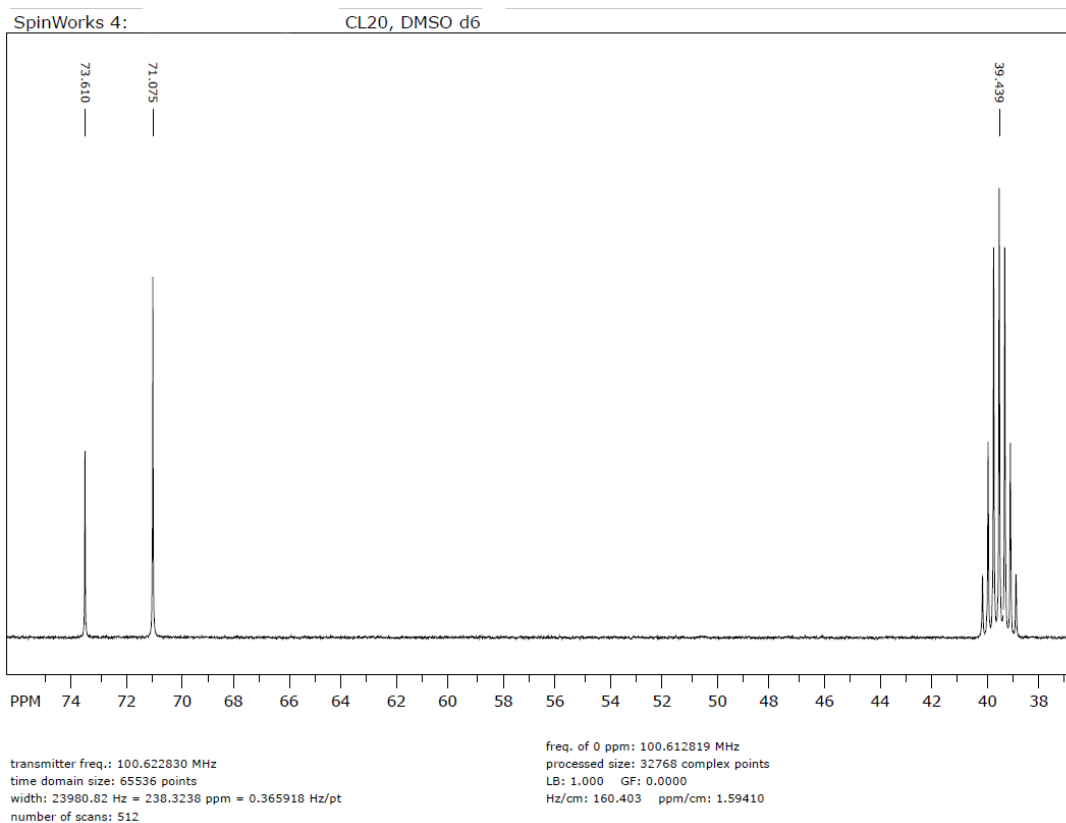


Figure S16: ¹³C-NMR spectrum of HMX dissolved in DMSO D6. The septet at 39.4 ppm is caused by the DMSO.

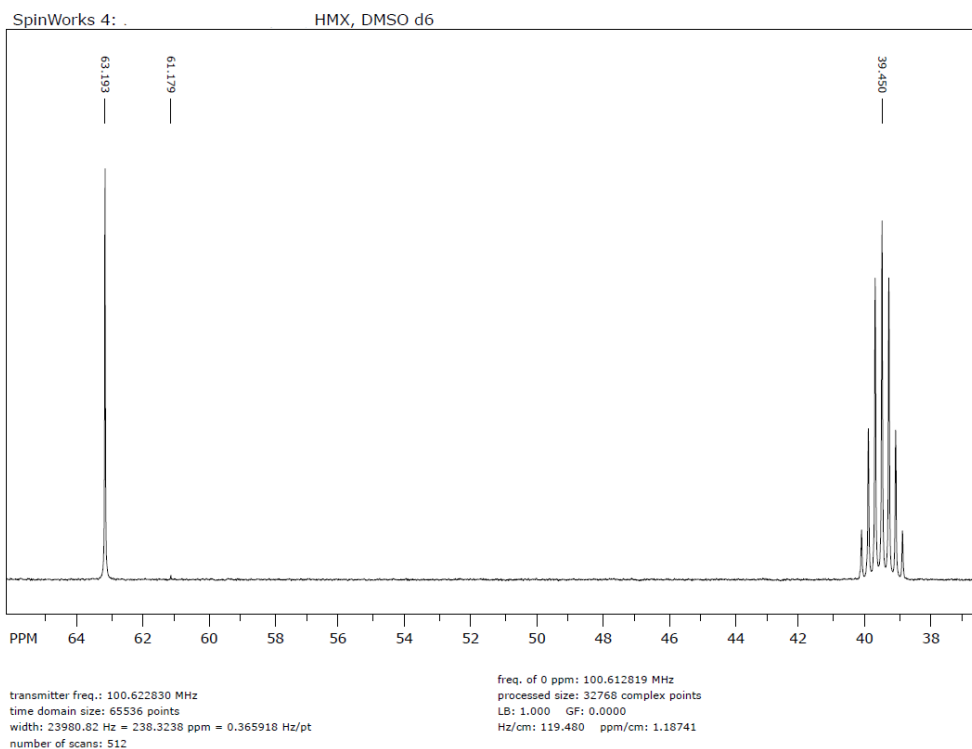


Figure S17: ^{13}C -NMR spectrum of CL-20 dissolved in DMSO D6. The septet at 39.4 ppm is caused by the DMSO.

Table S2: chemical shift and integrals of the ^1H NMR spectra of the HMX and CL-20 samples

| HMX | | CL-20 | |
|----------------------|----------|----------------------|----------|
| chemical shift [ppm] | integral | Chemical shift [ppm] | integral |
| 2.066 | 0.002 | 2.089 | 0.006 |
| 2.089 | 0.001 | 2.303 | 0.001 |
| 2.268 | 0.001 | 6.843 | 0.001 |
| 5.556 | 0.003 | 7.406 | 0.006 |
| 6.036 | 1.000 | 7.625 | 0.001 |
| 6.107 | 0.005 | 7.892 | 0.001 |
| 6.137 | 0.001 | 7.994 | 0.667 |
| | | 8.043 | 0.001 |
| | | 8.095 | 0.333 |

HPLC chromatograms of CL-20 and HMX

The chromatograms of HMX and CL-20 were recorded according to the following procedure. Using an Agilent 1100 HPLC system equipped with a binary pump and a diode array detector the injected sample of 1 μ l was separated on a Kintex 2.6 μ m C18 100 \AA 100x4.6 mm column with pre-column. A mixture of acetonitrile and water was used as eluent. The eluent composition was gradually changed over time. Time 1 min: 10% acetonitrile, Time 20 min: 50% acetonitrile, time 22 min: 95% acetonitrile, time 27 min: 95% acetonitrile, time 28 min: 10% acetonitrile, post-time: 11 min. The eluent flow was 0.6 mL/min. The column was heated to 308 K during the analysis. Data analysis was carried out using Agilent ChemStation. The quantification of the impurities was carried out under the assumption, that the impurities exhibit the same responsiveness at the measurement wave length of 255 nm which is reasonable as all the expected impurities are comprised of the same functional groups as HMX and CL-20. The retention time of HMX was 13.6 min and the retention time of CL-20 23.3 min under these conditions. The retention times and integrals for HMX and CL-20 are listed in Table S2.

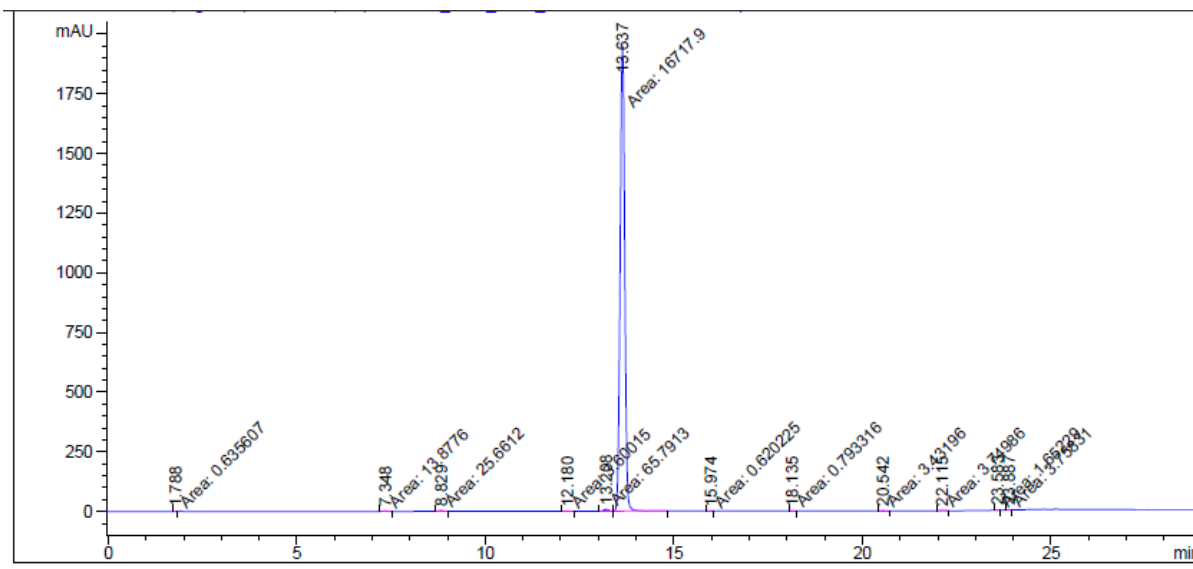


Figure S19: HPLC chromatogram of HMX.

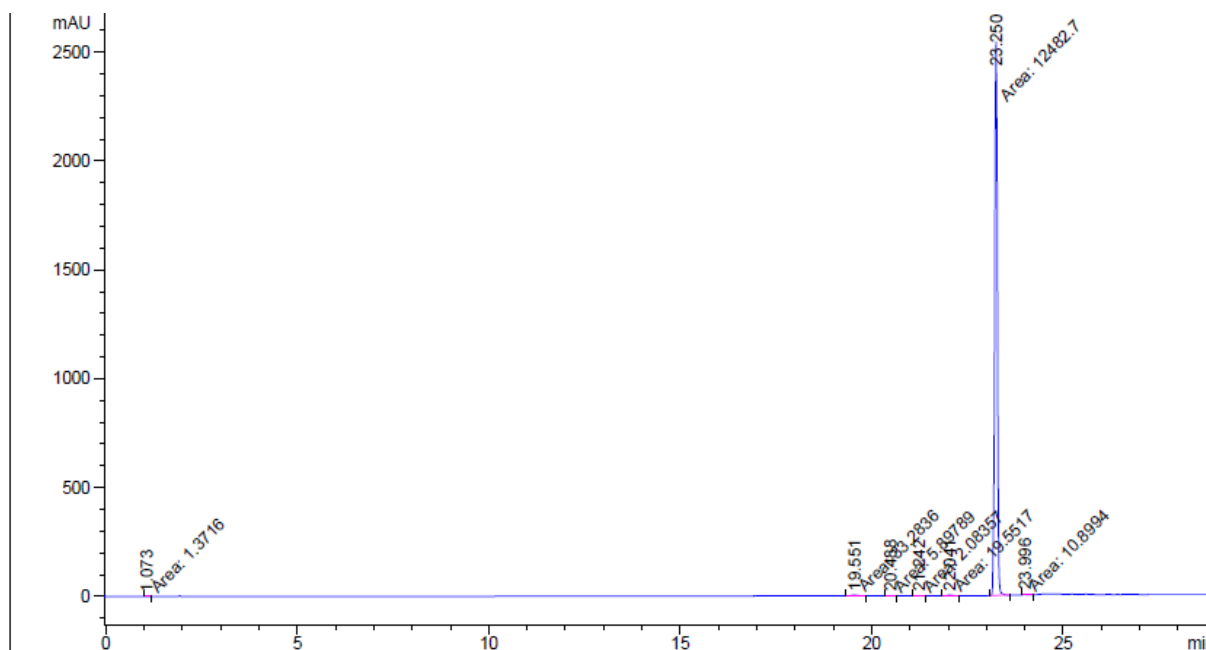


Figure S18: HPLC chromatogram of CL-20.

Table S3: retention times and integrals of the HPLC chromatogram of the HMX and CL-20 samples

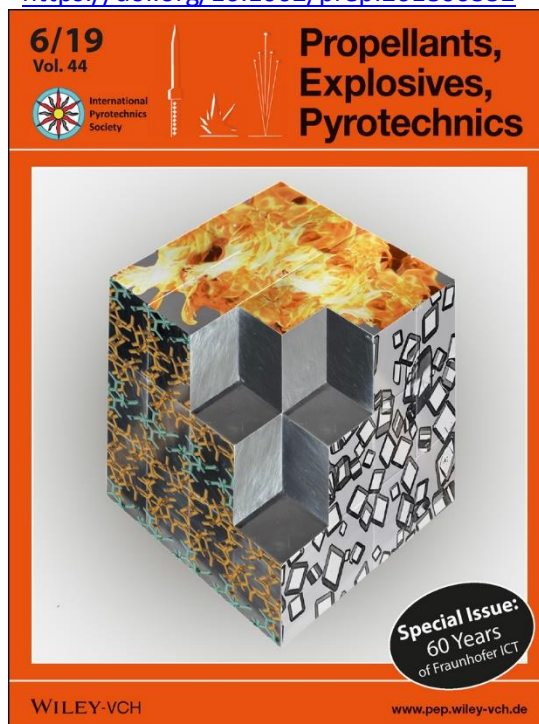
| HMX | | CL-20 | |
|----------------------|----------|----------------------|----------|
| retention time [min] | integral | retention time [min] | integral |
| 7.348 | 0.0008 | 1.073 | 0.0001 |
| 8.829 | 0.0015 | 19.551 | 0.0027 |
| 12.18 | 0.0002 | 20.488 | 0.0005 |
| 13.208 | 0.0039 | 21.242 | 0.0002 |
| 13.637 | 1.0000 | 22.041 | 0.0016 |
| 20.542 | 0.0002 | 23.25 | 1.0000 |
| 22.115 | 0.0002 | 23.996 | 0.0009 |
| 23.583 | 0.0001 | | |
| 23.887 | 0.0002 | | |

7 Cocrystallisation Method: Choice and Development

7.1 Investigation of Crystallisation Conditions to Produce CL-20/HMX Cocrystal for Polymer-Bonded Explosives

Dirk Herrmannsdörfer, Peter Gerber, Thomas Heintz, Michael J. Herrmann, Thomas M. Klapötke
Published as cover story in *Propellants, Explosives, Pyrotechnics* **2019**, 44, 6, 668-678

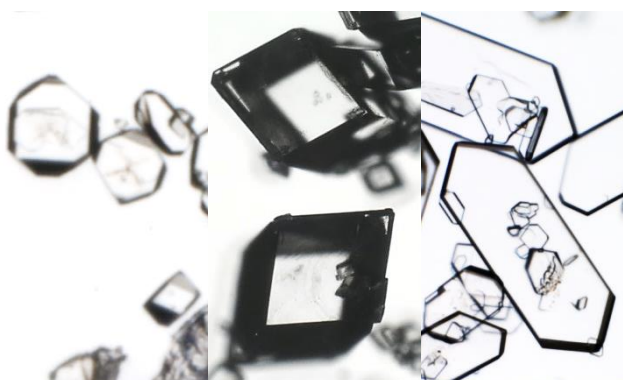
<https://doi.org/10.1002/prop.201800332>



Dirk Herrmannsdörfer, Peter Gerber, Thomas Heintz, Michael J. Herrmann, Thomas M. Klapötke, Cover Picture: Investigation Of Crystallisation Conditions to Produce CL-20/HMX Cocrystal for Polymer-bonded Explosives, *Propellants, Explosives, Pyrotechnics* **2019**, 44, 6, 661-661. Copyright Wiley-VCH GmbH.

Reproduced with permission.

<https://doi.org/10.1002/prop.201980601>



The following modifications were made to the paper:

- Typing errors were corrected
- Temperatures were changed from °C to K to unitise the style in this work

Abstract: Since its discovery in 2012, multiple techniques to generate the CL-20/HMX cocrystal have been published. However, as yet no assessment or trial has been reported of crystallisation methods capable of producing the cocrystal in a size region and production scale suitable for its use in polymer bonded explosives (PBX). This paper provides insight into the selection of suitable crystallisation methods, solvent selection and process optimisation with a focus on the efficient production of high-quality cocrystals for use in PBX. Through extensive solvent screening, acetonitrile was identified as the best solvent for solution-based crystallisation, due to its capability to produce compact parallelepipedic crystals and its comparably wide cocrystal phase region. Crystallisation conducted at 333.15 K was found to increase the conversion rate and the material efficiency compared to room temperature. By application of an advanced seeding procedure, high-quality cocrystals in the size region of 180-250 μm were produced in laboratory-scale antisolvent and cooling crystallisations. By pilot-plant-scale batch reaction cocrystallization, cocrystals with a volume-weighted mean diameter of 33 μm were produced in quantities of 250 g per day.

1 Introduction

2,4,6,8,10,12-hexanitro-2,4,6,8,10,12-hexaazaisowurtzitane (CL-20) outperforms 1,3,5,7-tetranitro-1,3,5,7-tetrazoctane (HMX) in terms of detonation velocity, oxygen balance, and explosive power. [1], [2] However, it has not seen any widespread use in high explosives formulations because of its comparably high mechanical sensitivity. [2], [3], [4]

One way to approach the sensitivity issue of CL-20 was presented by Bolton *et al.* in the form of the 2:1 CL-20/HMX cocrystal. [3] There is still ongoing debate in the scientific community about what kind of species should be called cocrystals. [5], [6] Here we adopt the proposed definition of Aitipamula *et al.* [5] “*cocrystals are solids that are crystalline single-phase materials composed of two or more different molecular and/or ionic compounds generally in a stoichiometric ratio*” knowing that this definition partly overlaps with the definitions of salts and solvates. The CL-20/HMX cocrystal is reported to possess comparable impact sensitivity to HMX and to exceed HMX in terms of detonation velocity. [3] This cocrystal is therefore a promising candidate to succeed HMX as the state-of-the-art high explosive. Multiple techniques are presented in the literature to generate the cocrystal: Antisolvent crystallisation, [7] spray flash evaporation, [8] spray drying, [9] solvent evaporation, [3], [10], [11] ultrasonic spray-assisted electrostatic adsorption, [12] liquid-assisted grinding, [3], [7], [13] and reaction cocrystallisation. [10] The term reaction cocrystallization (RC) was coined by Rodríguez-Hornedo *et al.* [14] and describes cocrystallisation utilising the solubility difference between the cocrystal and the individual cocrystal components. For use of the cocrystal in PBX, special requirements concerning morphology and crystal size distribution need to be achieved in order to ensure processability of the PBX. The

following product parameters were therefore chosen:

- Crystals of compact morphology are beneficial to the processability of the PBX, due to the detrimental effect of plate-like particles on the viscosity.
- A crystal size distribution with a volume-weighted mean diameter (d_m) in the region of 200 μm must be accessible, as the desired explosive loadings of 85-90 % typically require the application of a bimodal particle size distribution that is separated by one order of magnitude. The application of very fine crystals in the PBX can lead to an undesirably high viscosity. For this reason, a pairing of 20 μm and 200 μm for d_m is often the target.
- As sensitivity to shock and impact tends to depend on crystal quality (gas/liquid inclusions, voids, dislocations,...) [15], a crystallisation process capable of producing high-quality crystals is preferred.
- Due to the cost of CL-20, the crystallisation method must either exhibit a good CL-20 efficiency or CL-20 must be easily recyclable from solution.

Based on the defined product parameters, the list of applicable crystallisation methods narrows down to antisolvent crystallisation, cooling crystallisation, reaction cocrystallization and evaporation crystallisation, since other methods generally offer only limited options to control crystal size and crystal quality. In this paper we describe the steps needed to develop a cocrystallisation process capable of producing CL-20/HMX cocrystals in the 100 g-range with tuneable crystal size, compact morphology and high crystal quality. In particular, the following four steps are presented:

- Definition of product parameters
- Selection of crystallisation process
- Solvent selection

- Optimisation of process parameters

2 Experimental Section

All solvents were reaction grade or higher and were stored over 3 Å molecular sieve. CL-20 (lot number 573S98) was obtained from SNPE. HMX (lot number NSI 00E 000 E004) was purchased from Chemring Nobel.

2.1 Characterisation Methods

Raman spectra were obtained with a Bruker RFS 100/S Raman spectrometer equipped with a 1064 nm ND:YAG-laser operated at 450 mW and a liquid- nitrogen-cooled Germanium-detector. The spectra were obtained between 80 and 3500 cm^{-1} with a spectral resolution of 1 cm^{-1} .

X-ray powder diffraction measurements were performed on a D8 Advance from Bruker AXS, equipped with a copper tube, two 2.5° Soller collimators, an anti-scatter screen, a flip-stick stage, and a silicon strip detector (LynxEye). The data was evaluated using Rietveld analysis based on the structure data reported by Bolton *et al.* [3]

Macroscope images were taken with a Leica DFC420 camera equipped with a Leica Z16APO objective. The images were processed via Leica QWin V3 software.

Particle diameters were determined with a Malvern Mastersizer 2000 version 5.60 with a heptane-lecithin mixture as a dispersion medium. The agitation speed was 2450 rpm. Prior to every measurement, injected samples were ultrasonicated for 2 minutes with 60 % intensity. 1.69 was chosen as the refractive index and the absorption coefficient was selected individually to obtain the best results. Three measurements, each consisting of 10000 individual scans, were averaged.

HPLC measurements were performed with an Agilent 1100 equipped with binary pumps and a diode array detector detecting at 225 nm. A Kintex 2.6 μm C18 100 Å 100x4.6 mm column with a Phenomenex precolumn was used with water:acetonitrile (1:1) as eluent at a flow rate of 0.6 mL/min at a column temperature of 308 K. Analysis was carried out using a ChemStation for LC 3D systems Rev. B.01.03.

Laboratory-scale experiments were agitated and temperature controlled using a Ditabis MKR 23 thermo block mixer equipped with a matching thermo block for the reaction vessels.

2.2 Solubility Determination

A moderate excess of HMX or CL-20 was placed in a 6 mL glass vessel. Depending on the expected

solubility, between 0.5 g and 3 g solvent were added. The solution was agitated at 800 rpm and tempered via a Ditabis MKR 23 thermo block mixer equipped with a matching thermo block for the reaction vessels for 5 hours. The solid was sedimented and the clear solution removed by syringe. Directly afterwards the solution mass was determined. The solvent was removed under vacuum and the mass of the remaining solid was determined.

2.3 Standard Washing Procedure

The product solid phase of laboratory-scale crystallisation experiments was washed consecutively with three solutions with decreasing solubilities of CL-20 and HMX to avoid precipitation from the solution and excess dissolution of the solid. The typical washing procedure was 1 mL 2-propanol:acetonitrile (8:2), 1 mL 2-propanol:acetonitrile (9:1), and 5-10 times 1 mL 2-propanol.

2.4 Phase Solubility Diagram

The phase diagrams were obtained via the static method. [16] For PC and DMC, excess CL-20 and HMX was agitated at 800 rpm and 333.15 K. Typically 1 g of solvent was used. All slurries were seeded with cocrystal after 5 h. After at least 5 d the solid was sedimented and an aliquot of the clear solution was removed by syringe and diluted with acetonitrile (ACN). The CL-20 and HMX concentrations were measured by HPLC. The solid phase was washed according to the standard washing procedure. The solid phase was characterised by Raman spectroscopy.

For ACN at 333.15 K and 293.15 K, and ACN:2-propanol (1:1) mixture, DMC and butane-2,3-dione at 333.15 K, excess CL-20 and cocrystal was agitated at 800 rpm and no additional seeding was carried out. Except for the substitution of HMX by cocrystal, the previously described procedure was applied. The altered procedure was intended to eliminate the need for additional seeding and, in the case of DMC and butane-2,3-dione, ensure that slow cocrystallisation rates did not hinder the equilibration.

2.4 Seeding Procedures

In self-seeded laboratory-scale experiments the supersaturated mixture was agitated at 800 rpm at 333.15 K for 24 h before antisolvent was added. Over the 24 h period, large crystals (500-700 μm) formed because of the moderate supersaturation (1.2) and thus low nucleation rate. The large crystals

were rounded during the process due to the agitation. The fragments acted as seed crystals in the subsequent crystallisation.

In externally seeded laboratory-scale experiments 500 mg ACN (12.2 mmol) was added to 6.4 mg HMX (22 μmol) and 221.6 mg CL-20 (505.7 μmol) in a 6 mL glass vessel. The solid was dissolved at 343.15 K and 800 rpm for 10 minutes to ensure total dissolution of CL-20 and HMX. In preliminary experiments, it was found that overheating the crystallisation solution by 10 K increases the metastable zone width, so that without seeding no crystallisation occurs during antisolvent and cooling crystallisations. Subsequently, the solution was cooled to 293.15 K, 5.0 mg cocrystal was added and the dispersion agitated at 800 rpm for 10 minutes. By this method 90 % of the seed crystal mass was dissolved and the seed crystals gained a fresh surface with few defects. 60 μl of this suspension were swiftly transferred to the previously prepared reaction solution using a 20-200 μl VWR Collection Standard Line single channel mechanical air displacement micropipette.

In seeded RC experiments no HMX was used in the seed solution and accordingly more cocrystal was used. Furthermore, the reaction mixture was not heated to 343.15 K.

2.5 Antisolvent Crystallisation

3000 mg ACN (73.08 mmol) was added to 152 mg HMX (0.51 mmol) and 1472 mg CL-20 (3.36 mmol) in 20 mL glass vessels. The solid was dissolved at 343.15 K and 800 rpm for 10 minutes. Subsequently, the solution was cooled to 333.15 K. The seed crystal suspension was added and the reaction vessels were air-tightly connected to the pump tube via teflon fittings. 2000 mg 2-propanol (33.27 mmol) was dispensed over the course of 16.6 h using a Hirschmann ROTARUS VOLUME 50I metering pump equipped with a ROTARUS MKF 12-8 12 channel pump head. During crystallisation the temperature was kept constant at 333.15 K and the vessels were agitated at 600 rpm. The solid phase was washed according to the standard washing procedure. Every experiment was carried out in parallel at least threefold. The solid phase was characterised by Raman spectroscopy.

For internally seeded and unseeded crystallisation experiments in ACN no heating to 343.15 K and no addition of seed crystal suspension was undertaken.

For crystallisation experiments in propylene carbonate the same procedure was applied as in unseeded crystallisation experiments in ACN,

except that 3000 mg propylene carbonate (29.39 mmol), 123 mg HMX (0.42 mmol) and 1276 mg CL-20 (2.91 mmol) were used.

2.6 Cooling Crystallisation

3000 mg ACN (73.08 mmol) was added to 152 mg HMX (0.51 mmol) and 1472 mg CL-20 (3.36 mmol) in a 20 mL glass vessel. The solid was dissolved at 343.15 K and 800 rpm for 10 minutes. Subsequently, the solution was cooled to 333.15 K. The seed solution was added. During the crystallisation the temperature was decreased to 293.15 K over the period of 5 to 30 h according to the temperature curves mentioned in chapter 3.2.2. The vessels were agitated at 800 rpm. The solid phase was washed according to the standard washing procedure. Every experiment was carried out in parallel at least threefold. The solid phase was characterised by Raman spectroscopy.

For cooling crystallisation with adapted solution composition, 119 mg HMX (0.40 mmol) and 1472 mg CL-20 (3.72 mg) was used. Linear cooling over the period of 16.6 h and natural cooling over the period of 25 h was applied.

2.7 Batch Reaction Cocrystallization

In intermediate-scale crystallisation experiments carried out in ACN at 293.15 K, ACN at 333.15 K and cyclohexanone at 333.15 K the excess of solid was chosen as 600 mg/mL of solution. This choice was made to ensure comparability between the solvents. The experiments were agitated using a CAT R60 overhead stirrer fitted with a 3 cm three-blade propeller stirrer, and temperature controlled using a Lauda RC6 CP thermostat fitted to the 50 mL jacketed reaction vessel. For ACN at 293.15 K 13.30 g ACN (324.0 mmol) was added to 2.172 g HMX (7.33 mmol) and 12.373 g CL-20 (28.24 mmol). For ACN at 333.15 K 13.30 g ACN (324.0 mmol) was added to 2.275 g HMX (7.68 mmol) and 14.577 g CL-20 (33.27 mmol). For cyclohexanone at 333.15 K 14.50 g cyclohexanone (147.7 mmol) was added to 2.148 g HMX (7.26 mmol) and 15.686 g CL-20 (35.79 mmol). The reaction mixture was agitated at 440 rpm. An aliquot of 400 μl of seed slurry prepared from 0.500 g cyclohexanone (5.09 mmol), 0.0240 g cocrystal and 0.329 g CL-20 (0.75 mmol) was added to the cyclohexanone slurry after 3 h. After 2 h or 18 h for ACN at 293.15 K, 1 h for ACN at 333.15 K and 18 h for cyclohexanone, the stirrer was removed and the slurry transferred into a Büchner funnel using a BRAUN omnifix 100 mL syringe without a cannula attached to avoid clogging. The mother liquor was removed and the

product crystals were washed with 10 mL 2-propanol:ACN (8:2), 30 mL 2-propanol:ACN (9:1) and five times with 10 mL 2-propanol to ensure the total removal of the mother liquor. The product crystals were dried under vacuum and Raman spectra were collected to determine the purity.

The pilot plant crystallisation was carried out in three consecutive batches. The mother liquor of the first batch was reused in the second as well as the third batch. With each filtration process to remove the product crystals mother liquor is lost. To compensate, with each batch the solid load was reduced by 10 g, and 1 g of ACN was added. For the first batch 80.0 g (1.95 mol) ACN was added to 28.0 g HMX (94.5 mmol) and 112.0 g (255.6 mmol) CL-20 in a 250 mL jacketed flask with a rounded bottom. The slurry was agitated at 240 rpm for 2 h at 333.15 K via an overhead stirrer equipped with a paddle stirrer. The stirrer's contour closely matches the inner wall contour of the jacketed vessel. After 2 h the stirrer was removed and the slurry was transferred into a Büchner funnel using a BRAUN omnifix 100 mL syringe without a cannula attached to avoid clogging. After the removal of the mother liquor, the suction filter was moved to another vacuum side-arm flask, the mother liquor was transferred back into the reaction vessel, and the product crystals washed with 30 mL 1:1 2-propanol:ACN, 30 mL 2-propanol:ACN (8:2), 30 mL 2-propanol:ACN (9:1), 30 mL 2-propanol (two times) and 100 mL 2-propanol (once) to ensure the total removal of the mother liquor. The same procedure was applied for batch 2 and 3, but using 22.5 g (76.0 mmol) HMX and 67.5 g (154 mmol) CL-20, and 20.0 g (67.5 mmol) HMX and 60.0 g (137 mmol) CL-20 respectively. The product crystals were dried under vacuum and Raman and XRD measurements were carried out to determine the purity.

3 Results and Discussion

3.1 Solvent Selection

3.1.1 Solubility

The solubilities of HMX and CL-20 play an important role in the selected crystallisation methods. The CL-20/HMX cocrystal is composed of two parts CL-20 per part HMX and the molecular mass of CL-20 is approximately 1.5 times the molecular mass of HMX. Hence, as a first approach to identify a suitable solvent for cocrystallisation, a solvent was sought which exhibits a three times better solubility of CL-20 than HMX, because it is reasonable to assume that a better solubility ratio corresponds to a more favourable cocrystal phase

region in the ternary phase diagram. [17] Once a matching solvent is identified, the cocrystal phase region could be determined. Based on the available solubility data, [18] it was concluded that HMX is always far less soluble than CL-20, and exhibits a temperature-dependent solubility. Based on these findings, solubility screenings were conducted at 293.15 K and 333.15 K. The upper temperature was chosen as a compromise between the better solubility values for HMX at higher temperatures, safety concerns and the limiting factor of boiling point. A detailed analysis of the gathered solubility data will be published elsewhere. For this work it suffices to state that CL-20 did not exhibit a significant temperature-dependent solubility. The best solubility ratios of CL-20 and HMX were therefore obtained at 333.15 K. The twelve solvents with the best solubility ratio at 333.15 K are listed in Table 1.

Table 1: Solubilities of CL-20 and HMX with solubility ratios in different solvents at 333.15 K

| | [HMX] (g/ g solvent) | [CL-20] (g/ g solvent) | Solubility ratio |
|--------------------------|-------------------------|---------------------------|---------------------|
| ACN | 0.049 | 1.372 | 28 |
| β -butyrolactone | 0.073 | 0.892 | 12 |
| butane-2,3-dione | 0.006 | 0.068 | 11 |
| cyclohexanone | 0.051 | 0.859 | 17 |
| dimethyl carbonate | 0.006 | 0.044 | 7 |
| ϵ -caprolactone | 0.137 | 0.9-1.4 ^a | 7-10 |
| formic acid | 0.001 | 0.007 | 7 |
| γ -heptalactone | 0.060 | 0.721 | 12 |
| γ -hexalactone | 0.095 | 0.910 | 10 |
| propylene carbonate | 0.092 | 0.841 | 9 |
| thiophene | 0.001 | 0.004 | 4 |
| tetramethylurea | 0.184 | 1.285 | 7 |

^a Extrapolated value from diluted solution, due to excessive viscosity.

Of these solvents ϵ -caprolactone was excluded from further studies due to its high solution viscosity. Formic acid and thiophene were neglected because of their low solubility.

3.1.2 Cocrystal analysis

Raman spectra were obtained from all crystallisation experiments. The product composition was determined via reconstruction of the recorded spectra with pure sample spectra of CL-20, HMX and cocrystal. Unless specifically indicated, all the following crystallisations yielded pure cocrystal.

3.1.3 Cocrystal Formation

As the ternary phase diagram of HMX, CL-20 and solvent was unknown for all solvents, the solubility data of pure CL-20 and HMX (Table 1) for the solvents in question was used as the solution composition to determine the capability of the solvent to produce cocrystal. In unseeded experiments all solvents with the exception of dimethyl carbonate, butane-2,3-dione and tetramethylurea produced pure cocrystal within 72 h. Dimethyl carbonate produced a mixture of β HMX and ε CL-20, butane-2,3-dione produced β CL-20, and in tetramethylurea cocrystal formation as well as a partial decomposition of CL-20 took place, which led to a red discoloration of the solution and gas development. The decomposition is not unexpected due to the incompatibility of CL-20 and amines. [19] To eliminate the possibility that slow conversion into the cocrystal was the reason for the non-conversion in butane-2,3-dione and dimethyl carbonate, phase diagram determinations starting with excess cocrystal were carried out. Dimethyl carbonate and butane-2,3-dione again produced a respective mixture of β HMX and ε CL-20, and of β HMX, β CL-20, ε CL-20 and cocrystal after 72 h. Given these seemingly contradicting results for butane-2,3-dione, a mixture of excess HMX and excess CL-20 in butane-2,3-dione was agitated at 333.15 K for 14 d. Here a mixture of ε CL-20 and cocrystal was obtained. These results might indicate a complex phase diagram and low conversion rates in this solvent, which are both undesirable attributes for the cocrystallisation. Due to their adverse properties butane-2,3-dione, dimethyl carbonate and tetramethylurea were eliminated from consideration for cocrystallisation and no further experiments were carried out with these solvents.

Table 2: Width-to-height ratios of cocrystal obtained from different solvents

| | Width-to-height ratio |
|------------------------|-----------------------|
| ACN | 2 |
| β -butyrolactone | 8 |
| butane-2,3-dione | 3 |
| cyclohexanone | 2 |
| γ -heptalactone | 8 |
| γ -hexalactone | 8 |
| propylene carbonate | 6 |
| tetramethylurea | >10 ^a |

^a estimated value – as the plates were so thin, no side view was achievable.

3.1.4 Morphology

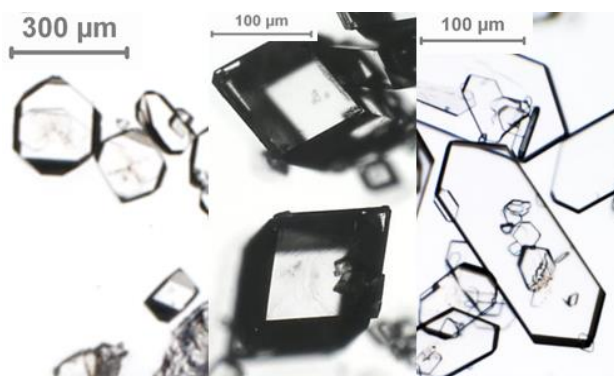


Figure 1: Morphology of cocrystals obtained from cyclohexanone (left); morphology of cocrystals obtained from ACN, butane-2,3-dione and tetramethylurea (centre) and morphology of cocrystals obtained from β -butyrolactone, γ -heptalactone, γ -hexalactone and propylene carbonate (right).

In the preliminary tests three basic cocrystal morphologies were obtained (Figure 1). β -butyrolactone, γ -heptalactone, γ -hexalactone and propylene carbonate produced elongated hexagonal plate-like crystals, cyclohexanone produced irregular capped parallelepipedic crystals, and ACN, butane-2,3-dione and tetramethylurea produced parallelepipedic crystals. Representative images of the cocrystals obtained for all tested solvents are found in the supporting information.

The approximate width-to-height ratios derived from macroscopic images is summarised in Table 2. The longest distance between two parallel sides of the largest crystal face was chosen as the width. The ratio values are strongly dependent on the crystallisation condition [3] and are only used as a rough estimate to judge the merit of a solvent.

The hexagonal elongated shape of the crystals produced in β -butyrolactone, γ -heptalactone, γ -hexalactone and propylene carbonate is undesirable. As the crystal habit can change with the crystallisation conditions, [20] propylene

carbonate was chosen for further studies. Of the four solvents, it possesses the best solubility and width-to-height ratio. Thus, the only remaining solvents for consideration are ACN, cyclohexanone and propylene carbonate.

3.1.5 Transition Concentration

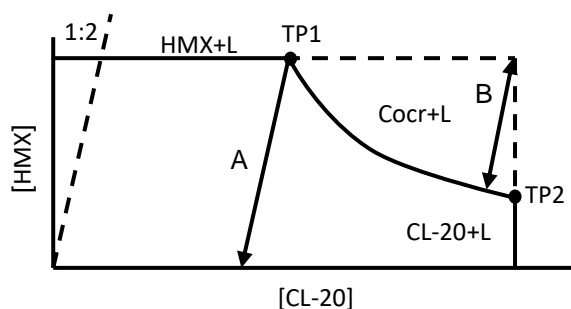


Figure 2: Schematic phase solubility diagram for a system where the cocrystal is more soluble than HMX.

Even though a phase diagram only represents equilibrium conditions, and crystallisation occurs under non-equilibrium conditions, the phase diagram is a powerful tool for finding optimal crystallisation conditions. The phase solubility diagram (PSD, Figure 2) describes the regions of thermodynamic stability of the cocrystal and the individual components. The transition points (TP1, TP2, Figure 2) [16], [21] are the boundaries of the cocrystal phase region at which the solution, the solid cocrystal and one solid individual component are in thermodynamic equilibrium. The concentrations in Figure 2 are expressed in terms of moles of CL-20 or HMX per gram solvent. The diagonal dashed line therefore indicates the stoichiometric composition of the cocrystal. Figure 2 illustrates the case where the cocrystal has a higher solubility than HMX in pure solvent. Ideally the cocrystal should be less soluble than the reactants, because the cocrystal is only the thermodynamically favoured crystallisation product within the cocrystal phase region. In that case the cocrystal can be formed from solution of a 2:1 CL-20:HMX stoichiometric composition and no excess of one of the two is required. Where the cocrystal is more soluble than one of the components a TP as close as possible to the stoichiometric composition of the cocrystal is preferred, as that minimises the excess of one of the components needed to reach the cocrystal phase region.

In ACN, cyclohexanone and propylene carbonate the cocrystal is more soluble than HMX. Hence the TP1 serves as an indicator for the quality of the solvent. The TP1 values for the three solvents and the corresponding solubility ratios are summarised in Table 3.

Table 3: Solution concentrations with solubility ratio of CL-20 and HMX at TP1 in different solvents at 333.15 K

| | TP1 [HMX] (g/g _{solvent}) | [CL-20] (g/g _{solvent}) | Solubility at TP1 |
|---------------------|---|--------------------------------------|----------------------|
| ACN | 0.054 | 0.424 | 8 |
| cyclohexanone | 0.015 | 0.605 | 40 |
| propylene carbonate | 0.060 | 0.374 | 6 |

The TP1 solubility ratios do not correlate well with the solubility ratios presented in Table 1. In cyclohexanone and propylene carbonate the HMX solubility decreases with increasing CL-20, while in ACN the HMX solubility increases. It is apparent that besides the solubility of the pure cocrystal components, their interaction in solution plays an important role in determining the position of the cocrystal phase region. The solubility data of the pure cocrystal components can therefore only act as a rough tool for judging the merit of a solvent. The implications of these TP1 values for the applicability of the solvents in the different crystallisation methods need to be individually addressed, due to the fundamental differences in the crystallisation techniques.

In antisolvent and cooling crystallisation the supersaturation is generated by the transition from a cocrystal phase region of higher solubility to a cocrystal phase region of lower solubility, either by adding an antisolvent or by cooling. For maximal efficiency of the process a large difference in solubility between the two phase regions is required. As the solubility of the cocrystal is higher than the solubility of HMX in all three solvents, the maximum possible yield of cocrystal per gram solvent is determined by the TP1 HMX solubility. In Table 4 the theoretical maximum yield of cocrystal for the three solvents for cooling and antisolvent crystallisation is summarised under the simplification that the final HMX solubility in any case is zero (arrow A in Figure 2). Additionally, the corresponding CL-20 efficiencies are presented in Table 4, i.e. the ratio of CL-20 found in the cocrystal divided by the CL-20 needed to reach TP1.

Given that the cocrystal yields and the CL-20 efficiencies are hypothetical limit values that in practice cannot be achieved [22], cyclohexanone is deemed unfit for antisolvent and cooling crystallisation, due to the low CL-20 efficiency. At best for every gram of CL-20 found in the cocrystal more than ten grams of CL-20 remain in solution.

In batch RC excess CL-20 and HMX is used. In a very simplified manner the crystallisation process follows the double arrow B in Figure 2. The excess reactants are constantly dissolved while the cocrystal crystallises. The cocrystal yield is therefore

Table 4: Theoretical maximum cocrystal yields and CL-20 efficiencies for cooling and antisolvent crystallisation at 333.15 K in different solvents

| | cocrystal yield ($\text{g}_{\text{cocrystal}}/\text{g}_{\text{solvent}}$) | CL-20 efficiency (%) |
|---------------------|--|-------------------------|
| ACN | 0.22 | 38 |
| cyclohexanone | 0.06 | 7 |
| propylene carbonate | 0.24 | 48 |

not directly dependent on the cocrystal solubility curve, but on the excess of reactant. In Table 5 cocrystal yields and CL-20 efficiencies for an excess of 0.5 g and 1 g reactant mixture per g solvent are presented for the three solvents.

The CL-20 efficiency values in Table 5 clearly indicate that for RC the position of TP1 and the corresponding solubility ratio are of less importance compared with antisolvent and cooling crystallisation. In addition, higher cocrystal yields and CL-20 efficiencies are achievable.

For evaporation crystallisation both TP1 and TP2 are of relevance, because in all tested solvents the cocrystal is more soluble than HMX. During evaporation and the resulting crystallisation of cocrystal, the solution concentration of CL-20 therefore increases. The endpoint of the evaporation crystallisation is therefore determined by TP2. Due to its superior solvent properties TP2 was only determined for ACN. The theoretical cocrystal yield and CL-20 efficiency are 0.22 g cocrystal per g ACN and 38 % respectively.

The phase diagrams for ACN, ACN/2-propanol, propylene carbonate and propylene carbonate/2-propanol are provided in the supporting information.

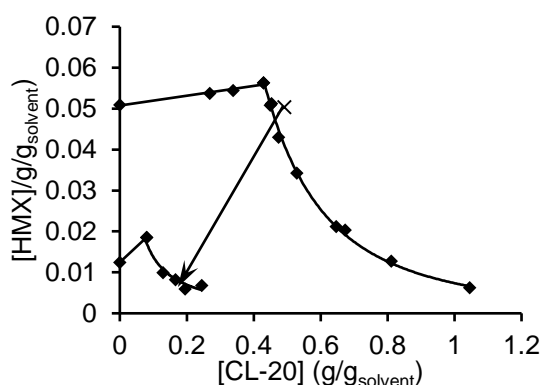


Figure 3: The arrow visualises the crystallisation path in the PSD for antisolvent crystallisations in ACN at 333.15 K. X indicates the starting solution composition.

3.2 Crystallisation Experiments

3.2.1 Antisolvent Crystallisation

Table 5: Cocrystal yields and CL-20 efficiencies for RC at 333.15 K in different solvents and different solid excess

| | cocrystal yield ($\text{g}_{\text{cocrystal}}/\text{g}_{\text{solvent}}$) | | CL-20 efficiency (%) | |
|---------------------|--|---------|-------------------------|---------|
| | xs 0.5g/g | xs 1g/g | xs 0.5g/g | xs 1g/g |
| ACN | 0.5 | 1 | 63 | 85 |
| cyclohexanone | 0.5 | 1 | 51 | 74 |
| propylene carbonate | 0.5 | 1 | 67 | 89 |

Antisolvent experiments were carried out in ACN at 333.15 K with 2-propanol as antisolvent. To ensure that the solution composition does not exit the cocrystal phase region it is beneficial to determine the PSD for the starting and end solvent mixture. The PSD for CL-20 and HMX in ACN and ACN/2-propanol (1:1 mass ratio) and the solution compositions during the crystallisation are presented in Figure 3. The solution composition trajectory in antisolvent crystallisation differs from the trajectory in cooling crystallisation because over the course of the antisolvent crystallisation experiment the solution volume increases, which consequently also changes the concentration of CL-20 and HMX. Figure 3 shows that for this 2-propanol fraction the final solution composition would be close to TP2 and CL-20 might crystallise. A ratio of 3:2 ACN to 2-propanol was therefore chosen as the final solvent composition.

Following this procedure, the cocrystal yield achieved is 0.166 g cocrystal per g ACN and the CL-20 efficiency is 25 %. Cocrystals with a width-to-height ratio between 2 and 1.2 were obtained. The width-to-height ratio did not exhibit a correlation to the controlled crystallisation parameters. Three seeding strategies were explored: no seeding, self-seeding and the addition of seed crystals. Macroscopic images of three representative crystal batches are shown in Figures 4-6.

In unseeded crystallisation experiments conducted in parallel, in some reaction mixtures randomly malformed cocrystals occurred (Figure 4, right). Furthermore, no reproducible crystal sizes were obtained.

The self-seeding experiments reveal that within the metastable region slow nucleation of the cocrystal occurs. This procedure produced high-quality cocrystals; however, it is inefficient in producing cocrystals with a defined crystal size distribution. On the one hand, the initial supersaturation is used up to produce unusably large crystals in the range of 700 μm , which reduces

the cocrystal yield by 36 mg/g, and on the other

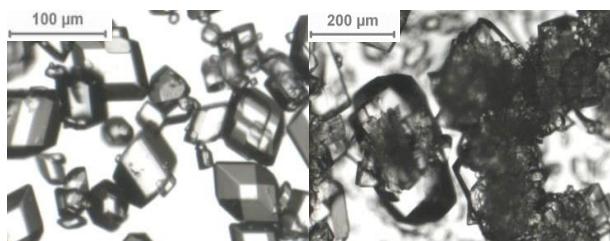


Figure 4: Cocrystal obtained from unseeded antisolvent crystallisation in ACN at 333.15 K

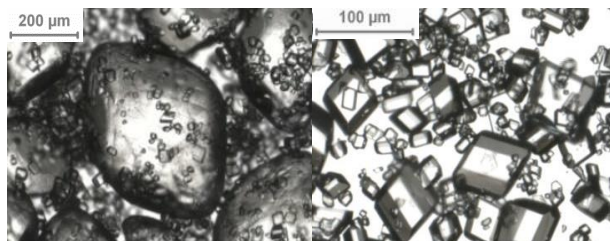


Figure 5: Coarse cocrystal formed over 24 h with finer cocrystals formed during the self-seeded antisolvent crystallisation in ACN at 333.15 K (left). Cocrystals formed during the self-seeded antisolvent crystallisation in ACN at 333.15 K (right).



Figure 6: Cocrystal formed in externally-seeded antisolvent crystallisation in ACN at 333 K.

hand, due to the random nature of nucleation and the following abrasion, the number of seed crystals and therefore the final size distribution of the cocrystal cannot be controlled.

To control the final crystal size, external seeding was applied. To reduce crystal defects on the surface and the amount of internal defects of the seed crystals, the seed crystals were about 90 % dissolved prior to use. This serves the additional purpose of reducing the fines among the seed crystals and effectively narrowing down the seed crystal size distribution. Assuming that the seeds have a uniform size, that no nucleation and breakage occurs, and that all material crystallises on the seed crystals, the required seed crystal mass m_{seed} can be calculated using the seed crystal size l_{seed} the desired final crystal size l_{final} and the cocrystal yield m_{final} [23]:

$$m_{seed} = m_{final} \cdot (l_{seed}/l_{final})^3$$

Under experimental conditions this equation can only function as a guideline and the appropriate seed crystal mass has to be determined experimentally. For the laboratory-scale

experiments it was found that 25% of the calculated seed crystal mass was needed to obtain an l_{final} of around 200 µm using seed crystals with $d_m = 33.2$ µm.

Unseeded antisolvent crystallisation was also carried out with propylene carbonate as solvent in order to determine whether, under more controlled conditions, more compact crystals can be produced. However, no improvement was achieved compared to the initially obtained value (Table 2). No further experiments were carried out with propylene carbonate.

3.2.2 Cooling Crystallisation

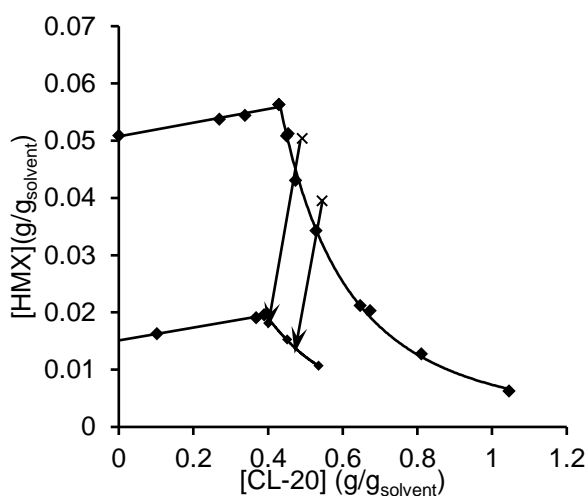


Figure 7: Arrows visualise the crystallisation path in the PSD for cooling crystallisations in ACN from 333.15 K to 293.15 K. x indicates the starting solution compositions.

Externally seeded cooling crystallisations were carried out in ACN from 333.15 K to 293.15 K. It was found that crystallisations with the same solution composition as the antisolvent crystallisations only produced pure cocrystal in about 50 % of the batches. Of six cooling crystallisations conducted in parallel, two to four typically produced fluctuating amounts of HMX and cocrystal, while the others produced pure cocrystal. It is reasonable to assume that the close vicinity of the solution composition to the HMX phase region during the crystallisation facilitated the HMX crystallisation. This is supported by the finding that in one PSD experiment of ACN at 333.15 K multiple solutions with a solution composition in the cocrystal phase region near the boundary to the HMX phase region exhibited non-equilibrium conditions after 5 days, which indicates that initially all cocrystal was dissolved and HMX recrystallised. To prevent HMX impurities the solution composition was adapted to proceed further in the middle of the phase region (Figure 7).

Linear cooling from 333.15 K to 293.15 K within 16.6 h resulted in an average cocrystal yield of 34 mg/g which is only 34 % of the expected yield of

101 mg/g. This indicates that under similar conditions as the antisolvent crystallisation, cooling crystallisation exhibits lower conversion rates. Total crystallisation was achieved with a cooling rate resembling natural cooling within 25 h. Cocrystals with a width-to-height ratio of 1 were obtained.

3.2.3 Batch Reaction Cocrystallization

Batch RC in an intermediate scale was carried out at 333.15 K with ACN and cyclohexanone. Total conversion occurred in ACN within 1 h. Cyclohexanone, however, required the addition of seed crystals, because after 3 h no conversion occurred. Total conversion was achieved within 18 h. This indicates that the total solubility of CL-20 and HMX in cyclohexanone is insufficient to create a nucleation shower, whereas in ACN fast nucleation occurs. 333.15 K was chosen for cooling and antisolvent crystallisation to maximise the cocrystal yield and CL-20 efficiency. For RC, however, the solubility is of lesser importance. Thus, 293.15 K might also be a viable temperature for RC. Due to excessive viscosity no RC at 293.15 K was carried out in cyclohexanone. In ACN, of two identical reaction mixtures, one produced pure irregularly shaped cocrystal within 2 h, whereas the other was interrupted after 18 h, at which point the solid was composed of a mixture of ϵ CL-20, β CL-20, α CL-20 and β HMX. Intermittently gathered samples indicate that at 10 min and 5.5 h reaction time small amounts of cocrystal were formed, however no cocrystal was present in the samples between 10 min and 5 h. To reduce the number of factors that might contribute to this discrepancy, laboratory-scale seeded and unseeded RC were carried out in parallel. Of the five seeded reaction mixtures, two were incompletely transformed, whereas all four unseeded reaction mixtures were incompletely transformed after 24 h. After 48 h, all seeded and none of the unseeded reaction mixtures were completely transformed. It is likely that the low conversion rate and the appearing and disappearing of cocrystal at 293.15 K in ACN is the result of a lower energy benefit of crystallising cocrystal compared to crystallising CL-20 and HMX at 293.15 K compared to 333.15 K and a therefore more labile cocrystal phase region.

As can be seen in Figure 8 (left) and Figure 9 (right), good crystal quality is obtained in both seeded experiments. However, both d_m with 39 μm and 45 μm for the cyclohexanone and ACN experiment are far smaller than the seeding should account for. This shows that m_{seed} must be adjusted specifically to the reaction condition, since after

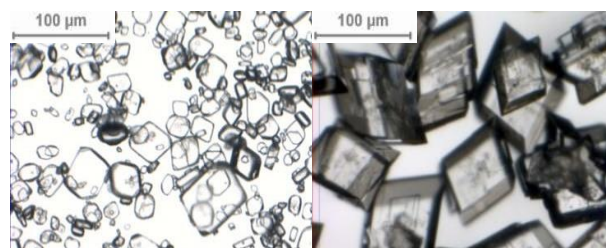


Figure 8: Cocrystals formed in intermediate-scale seeded batch RC in cyclohexanone at 333.15 K (left) and cocrystals formed in intermediate-scale batch RC in ACN at 333.15 K (right).

long reaction times nucleation and attrition have

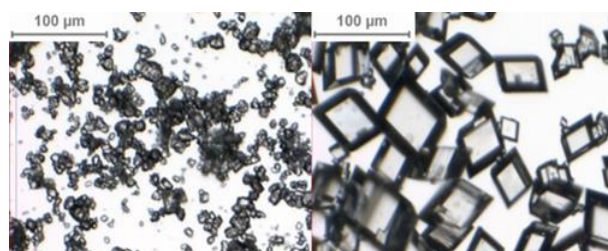


Figure 9: Cocrystals formed in intermediate-scale batch RC in ACN at 293.15 K (left). Cocrystals formed in laboratory-scale batch RC in ACN at 293.15 K (right).

likely occurred in these experiments. More defects are visible in the cocrystals obtained from intermediate-scale batch RC in ACN at 333.15 K which might be caused by the much higher crystallisation rate. The obtained d_m was 83 μm . The width-to-height ratios for batch RC in ACN at 333.15 K, 293.15 K laboratory-scale and cyclohexanone are 1.4, 1.2 and 2.2 respectively.

Based on the varying results for batch RC in ACN at 293.15 K and the higher width-to-height ratio in cyclohexanone, ACN at 333.15 K was chosen as the best condition to produce fine cocrystal. A batch RC scale up in ACN at 333.15 K was undertaken. By directly recycling the reaction solution after solid-liquid-separation, 253 g cocrystal with a combined d_m of 33 μm [24] and width-to-height ratio of 2.7 was produced in three consecutive batches with a CL-20 efficiency of 79%. The difference in particle diameter and width-to-height ratio compared to the previous experiment shows that the size and morphology of the obtained crystals seems to be significantly dependent on the crystallisation conditions.

3.2.4 Evaporation Crystallisation

No evaporation crystallisation was carried out, because no higher CL-20 efficiency and crystal quality is to be expected compared to antisolvent crystallisation. Unlike in antisolvent and cooling crystallisation the theoretical values for cocrystal yield and CL-20 efficiency can be achieved. This, however, requires the crystallisation to start at TP1

and end at TP2. In the beginning phase as well as the final phase of the crystallisation, the solution composition is very close to the phase boundaries, which can facilitate the crystallisation of HMX and CL-20. A more robust evaporation crystallisation in ACN, starting at the same solution composition as the antisolvent crystallisations and ending at the solution composition of 0.90 g CL-20 per g ACN and 0.01 g HMX per g ACN would yield 0.19 g cocrystal per g ACN and a CL-20 efficiency of 26 % which is insignificantly better than the values achieved for antisolvent crystallisation.

4 Conclusion

Table 6: Summary of crystal quality, crystal size, CL-20 efficiency and solution recyclability for different crystallisation methods and conditions

| crystallisation method | crystal quality | 200 μm possible | CL-20 efficiency | solution recyclability |
|------------------------|-----------------|----------------------------|------------------|------------------------|
| antisolvent | + | Yes | 25 % | - |
| cooling | + | Yes | 14 % | + |
| RC at 333.15 K | - | No | >75 % | + |
| RC at 293.15 K | +/- | yes | >70 % | ++ |

It was found that the solubility ratio of the individual cocrystal components serves as a basic tool for roughly judging the achievable cocrystal yield; however, the position of TP1 cannot be predicted based solely on the solubility data for the pure substances. Furthermore, most tested solvents produced cocrystals of undesirable morphology.

In summary, ACN remains the only utilisable solvent of those tested that produces compact CL-20/HMX cocrystal, even though the solubility ratio at TP1 is far from ideal. As a consequence, while antisolvent and cooling crystallisation are capable of producing high-quality cocrystal, they suffer from an insufficient CL-20 efficiency and, in the case of antisolvent crystallisation, additionally from a difficult recycling of the non-crystallised explosive. Batch RC exhibits good CL-20 efficiency, but at temperatures of 333.15 K batch RC gives no control over the product crystal size, and at 293.15 K batch RC leads to varying crystallisation.

Thus, none of the tested crystallisation methods fulfils all of the proposed specifications (Table 6). However, one possible approach to meet the specifications might be to find an intermediate temperature between 293.15 K and 333.15 K for batch RC, where nucleation and crystal growth rate are still low but the cocrystal is thermodynamically more favoured and therefore more reliably formed. Another solution might be semi-batch reaction crystallisation, where HMX and CL-20 are dosed into the reaction mixture as the crystallisation

progresses, thereby keeping the supersaturation on a low level, preventing nucleation and reducing the crystal growth rate. In the course of these experiments the factors influencing the fluctuating width-to-height ratios must also be uncovered. Although the specifications have not yet been met, pure cocrystal with moderate crystal quality and a d_m applicable in PBX can be obtained by batch RC in a reasonable scale. Valuable data can be collected by using this material in PBX test charges.

Acknowledgements

We are grateful for financial support provided by the German Ministry of Defence and the support provided by Dr. Manfred Kaiser at the WTD91.

References

- [1] R. L. Simpson, P.A. Urtiew, D. L. Ornellas, G. L. Moody, K. J. Scribner, D. M. Hoffman, CL-20 performance exceeds that of HMX and its sensitivity is moderate, *Propellants, Explos., Pyrotech.* **1997**, *22*, 5, 249-255
- [2] U. R. Nair, R. Sivabalan, G. M. Gore, M. Geetha, S. N. Asthana, H. Singh, Hexanitrohexaazaisowurtzitane (CL-20) and CL-20-based formulations, *Combust. Explos. Shock Waves* **2005**, *41*, 2, 121-132.
- [3] O. Bolton, L. R. Simke, P. F. Pagoria, A. J. Matzger, High Power Explosive with Good Sensitivity: A 2:1~Cocrystal of CL-20:HMX, *Cryst. Growth Des.* **2012**, *12*, 9, 4311-4314
- [4] N. C. Johnson, CL-20 Sensitivity Round Robin, *Indian Head Division Naval Surface Warfare Center*, **2003**, MD 20640-5035.
- [5] S. Aitipamula, R. Banerjee, A. K. Bansal, K. Biradha, M. L. Cheney, A. R. Choudhury, G. R. Desiraju, A. G. Dikundwar, R. Dubey, N. Duggirala, P. P. Ghogale, S. Ghosh, P. K. Goswami, N. R. Goud, R. R. K. R. Jetti, P. Karpinski, P. Kaushik, D. Kumar, V. Kumar, B. Moulton, A. Mukherjee, G. Mukherjee, A. S. Myerson, V. Puri, A. Ramanan, T. Rajamannar, C. M. Reddy, N. Rodriguez-Hornedo, R. D. Rogers, T. N. G. Row, P. Sanphui, N. Shan, G. Shete, A. Singh, C. C. Sun, J. A. Swift, R. Thaimattam, T. S. Thakur, R. K. Thaper, S. P. Thomas, S. Tothadi, V. R. Vangala, N. Variankaval, P. Vishweshwar, D. R. Weyna, M. J. Zaworotko, 'Polymorphs, Salts, and Cocrystals: What's in a Name?', *Cryst. Growth Des.* **2012**, *12*, 5, 2147-2152
- [6] A) G. R. Desiraju, Crystal and co-crystal, *CrystEngComm* **2003**, *5*, 82, 466

- B) P. Vishweshwar, J. A. McMahon, J. A. Bis, M. J. Zaworotko, Pharmaceutical Co-Crystals, *J. Pharm. Sci.* **2006**, *95*, 3, 499-516
- C) S. L. Childs, G. P. Stahly, A. Park, The Salt-Cocrystal Continuum:~ The Influence of Crystal Structure on Ionization State, *Mol. Pharmaceutics* **2007**, *4*, 3, 323-338
- D) A. D. Bond, What is a co-crystal?, *CrystEngComm* **2007**, *9*, 9, 833
- E) G. P. Stahly, Diversity in Single- and Multiple-Component Crystals. The Search for and Prevalence of Polymorphs and Cocrystals, *Cryst. Growth Des.* **2007**, *7*, 6, 1007-1026
- F) S. Mohamed, D. A. Tocher, M. Vickers, P. G. Karamertzanis, S. L. Price, Salt or Cocrystal? A New Series of Crystal Structures Formed from Simple Pyridines and Carboxylic Acids, *Cryst. Growth Des.* **2009**, *9*, 6, 2881-2889.
- [7] S. R. Anderson, D. J. am Ende, J. S. Salan, P. Samuels, Preparation of an Energetic-Energetic Cocrystal using Resonant Acoustic Mixing, *Propellants, Explos., Pyrotech.* **2014**, *39*, 5, 637-640
- [8] D. Spitzer, B. Risse, F. Schnell, V. Pichot, M. Klaumünzer, M. R. Schaefer, Continuous engineering of nano-cocrystals for medical and energetic applications, *Sci. Rep.* **2014**, *4*, 6575
- [9] C. An, H. Li, B. Ye, J. Wang, Nano-CL-20/HMX Cocrystal Explosive for Significantly Reduced Mechanical Sensitivity, *J. Nanomater.* **2017**, *2017*, 1--7
- [10] S. Sun, H. Zhang, Y. Liu, J. Xu, S. Huang, S. Wang, J. Sun, Transitions from Separately Crystallized CL-20 and HMX to CL-20/HMX Cocrystal Based on Solvent Media, *Cryst. Growth Des.* **2018**, *18*, 1, 77-84.
- [11] M. Ghosh, A. K. Sikder, S. Banerjee, R. G. Gonnade, Studies on CL-20/HMX (2:1) Cocrystal: A New Preparation Method and Structural and Thermokinetic Analysis, *Cryst. Growth Des.* **2018**, *7*, 3781-3793
- [12] B. Gao, W. Dunju, J. Zhang, Y. Hu, J. Shen, J. Wang, B. Huang, Z. Qiao, H. Huang, F. Nie, G. Yang, Facile, continuous and large-scale synthesis of CL- 20/HMX nano co-crystals with high-performance by ultrasonic spray-assisted electrostatic adsorption method, *J. Mater. Chem. A.* **2014**, *2*, 19969-19974
- [13] H. Qiu, R. B. Patel, R. S. Damavarapu, V. Stepanov, Nanoscale 2CL-20/HMX high explosive cocrystal synthesized by bead milling, *CrystEngComm* **2015**, *17*, 22, 4080-4083
- [14] N. Rodríguez-Hornedo, S. J. Nehm, K. F. Seefeldt, Y. Pagán-Torres, C. J. Falkiewicz, Reaction Crystallization of Pharmaceutical Molecular Complexes, *Mol. Pharmaceutics* **2006**, *3*, 3, 362-367
- [15] A) J. E. Field, Hot spot ignition mechanisms for explosives, *Acc. Chem. Res.* **1992**, *25*, 11, 489-496.
- B) Menikoff, R., Pore Collapse and Hot Spots in HMX, *AIP Conference Proceedings*, Portland, Oregon, USA, July 20-25, **2003**, 393-396.
- C) R. H. B. Bouma, W. Duvalois, A. E. D. M. van der Heijden, Microscopic characterization of defect structure in RDX crystals, *J. Microsc.* **2013**, *252*, 3, 263-274
- D) S. M. Walley, J. E. Field, M. W. Greenaway, Crystal sensitivities of energetic materials, *Mater. Sci. Technol.* **2006**, *22*, 4, 402-413
- E) L. Borne, J.-C. Patedoye, C. Spycerelle, Quantitative Characterization of Internal Defects in RDX Crystals, *Propellants, Explos., Pyrotech.* **1999**, *24*, 4, 255-259
- [16] A) D. H. Leung, S. Lohani, R. G. Ball, N. Canfield, Y. Wang, T. Rhodes, A. Bak, Two Novel Pharmaceutical Cocrystals of a Development Compound – Screening, Scale-up, and Characterization, *Cryst. Growth Des.* **2012**, *12*, 3, 1254-1262
- B) R. A. Chiarella, R. J. Davey, M. L. Peterson, Making Co-CrystalsThe Utility of Ternary Phase Diagrams, *Cryst. Growth Des.* **2007**, *7*, 7, 1223-1226
- C) S. Kudo, H. Takiyama, Production method of carbamazepine/saccharin cocrystal particles by using two solution mixing based on the ternary phase diagram, *J. Cryst. Growth* **2014**, *392*, 87-91
- D) S. Boyd, K. Back, K. Chadwick, R. J. Davey, C. C. Seaton, Solubility Metastable Zone Width Measurement and Crystal Growth of the 1:1~Benzoic Acid/Isonicotinamide Cocrystal in Solutions of Variable Stoichiometry, *J. Pharm. Sci.* **2010**, *99*, 9, 3779-3786
- E) X. Sun, Q. Yin, S. Ding, Z. Shen, Y. Bao, J. Gong, B. Hou, H. Hao, Y. Wang, J. Wang, C. Xie, (Solid+liquid) phase diagram for (indomethacin+nicotinamide)-methanol or methanol/ethyl acetate mixture and solubility behavior of 1:1 (indomethacin+nicotinamide) co-crystal at

- T=(298.15 and 313.15)K, *J. Chem. Thermodyn.* **2015**, *85*, 171-177
- [17] D. J. Good, N. Rodríguez-Hornedo, Solubility Advantage of Pharmaceutical Cocrystals, *Cryst. Growth Des.* **2009**, *9*, 5, 2252–2264
- [18] A) E. von Holtz, D. Ornellas, M. F. Foltz, J. E. Clarkson, The Solubility of ϵ -CL-20 in Selected Materials *Propellants, Explos., Pyrotech.* **1994**, *19*, 4, 206-212.
 B) Y. T. Lapina, A. S. Savitskii, E. V. Motina, N. V. Bychin, A. A. Lobanova, N. I. Golovina, Polymorphic transformations of hexanitrohexaazaisowurtzitane, *Russ. J. Appl. Chem.* **2009**, *82*, 10, 1821-1828
 C) L. Svensson, J.-O. Nyqvist, L. Westling, Crystallization of HMX from γ -butyrolactone, *J. Hazard. Mater.* **1986**, *13*, 1, 103-108
 D) J. F. Baytos, B. G. Craig, A. W. Campbell, W. E. Deal, J. J. Dick, R. H. Dinegar, R. P. Engelke, T. E. Larson, E. Marshall, J. B. Ramsay, R. N. Rogers, D. Soran, M. J. Urizar, J. D. Wackerle, *LASL explosive property data* (Eds.: T. R. Gibbs, A. Popolato), Univ of California Press, Berkeley **1980**, p.44
 E) M. E. Sitzmann, S. Foti, C. C. Misener, *Solubilities of high explosives: removal of high explosive fillers from munitions by chemical dissolution*, Naval Ordnance Lab, White Oak, MD, USA, 1973.
- [19] SNPE Safety Data Sheet
- [20] A) A. K. Tiwary, Modification of Crystal Habit and Its Role in Dosage Form Performance, *Drug Dev. Ind. Pharm.* 2001, *27*, 7, 699–709
 B) S. Li, J. Xu, and G. Luo, Control of crystal morphology through supersaturation ratio and mixing conditions, *J. Cryst. Growth* **2007**, *304*, 1, 219-224
- [21] A) A. Alhalaweh, A. Sokolowski, N. Rodríguez-Hornedo, S. P. Velaga, Solubility Behavior and Solution Chemistry of Indomethacin Cocrystals in Organic Solvents, *Cryst. Growth Des.* **2011**, *11*, 9, 3923–3929
 B) S. L. Childs, N. Rodríguez-Hornedo, L. S. Reddy, A. Jayasankar, C. Maheshwari, L. McCausland, R. Shipplett, B. C. Stahly, Screening strategies based on solubility and solution composition generate pharmaceutically acceptable cocrystals of carbamazepine, *CrystEngComm* **2008**, *10*, 7, 856
- [22] By applying high initial supersaturations it is theoretically possible to surpass these values; however, these supersaturations are of no practical use in the described crystallisation experiments.
- [23] A. H. Janse, 1977, Nucleation and crystal growth in batch crystallizers, *PhD Thesis*, Delft, Netherlands
- [24] Laser diffraction measurements are found in the supporting information.

Investigation of Crystallisation Conditions to Produce CL-20/HMX Cocrystal for Polymer-Bonded Explosives

Dirk Herrmannsdörfer*,^[a] Peter Gerber,^[a] Thomas Heintz,^[a] Michael J. Herrmann^[a], Thomas M. Klapötke^[b]

[a] *Energetic Materials Fraunhofer Institute for Chemical Technology ICT Joseph-von-Fraunhofer-Str. 7 76327 Pfinztal, Germany
E-mail: dirk.herrmannsdorfer@ict.fraunhofer.de*

[b] *Department of Chemistry Energetic Materials Research Ludwig-Maximilian University of Munich Butenandtstr. 5 - 13 (Haus D) 81377 Munich, Germany*

Supplementary Images

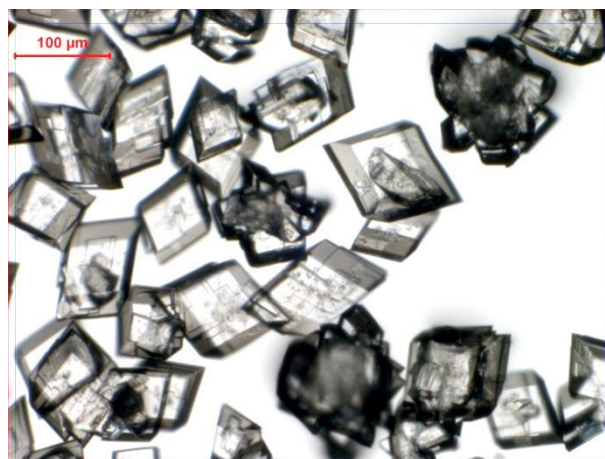


Figure 1: Cocrystal obtained from ACN.

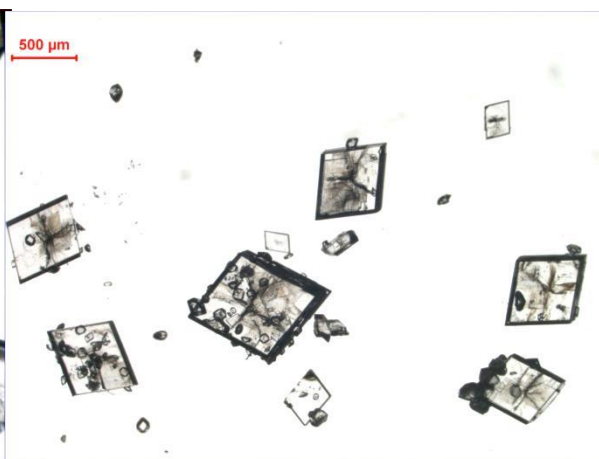


Figure 2: Cocrystal obtained from butane-2,3-dion.



Figure 3: Cocrystal (marked by red circles) obtained from tetramethylurea among other crystals.



Figure 4: Cocrystal obtained from β -butyrolactone.

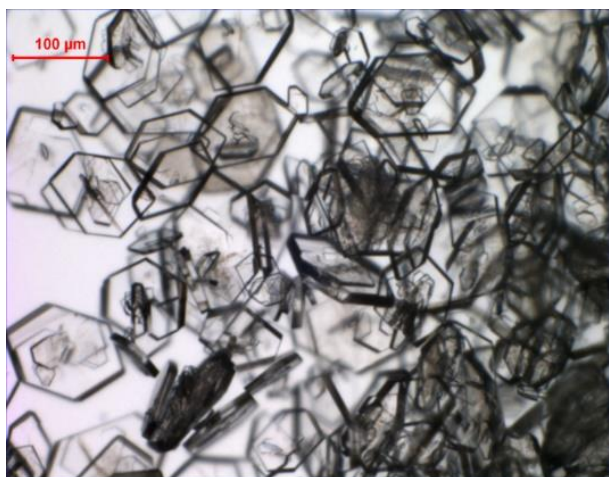


Figure 5: Cocrystal obtained from γ -heptalactone.

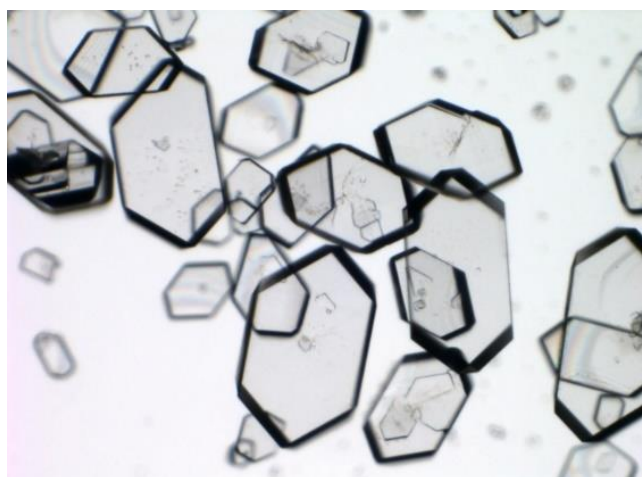


Figure 6: Cocrystal obtained from γ -hexalactone.

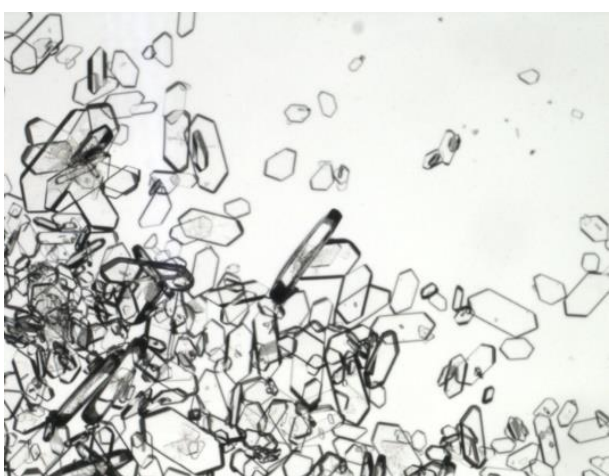


Figure 7: Cocrystal obtained from propylene carbonate.

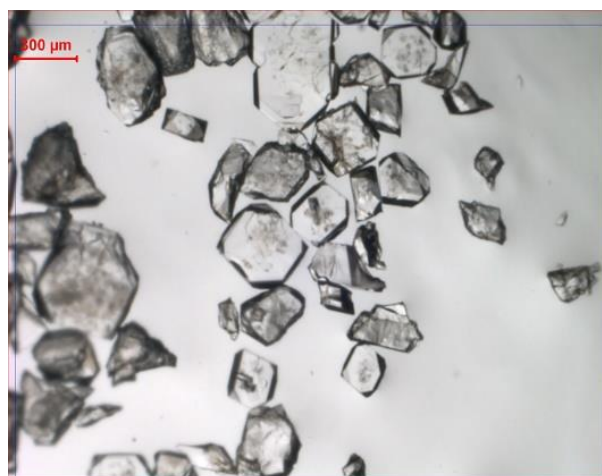


Figure 8: Cocrystal obtained from cyclohexanone.

Supplementary phase solubility diagrams and corresponding solubility data points

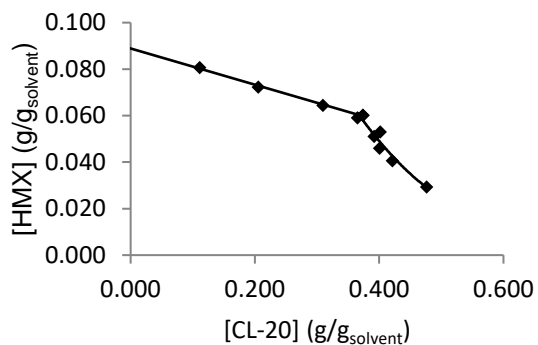


Figure 9: Partially determined PSD for propylene carbonate at 333.15 K.

Table 1: Determined PSD-data of propylene carbonate at 333.15 K

| [CL-20] (g/g) | [HMX] (g/g) | phase region |
|---------------|-------------|---------------|
| 0.111 | 0.081 | HMX |
| 0.206 | 0.072 | HMX |
| 0.310 | 0.064 | HMX |
| 0.365 | 0.059 | TP1 cocrystal |
| 0.374 | 0.060 | cocrystal |
| 0.392 | 0.051 | cocrystal |
| 0.401 | 0.046 | cocrystal |
| 0.402 | 0.053 | cocrystal |
| 0.421 | 0.041 | cocrystal |
| 0.477 | 0.029 | cocrystal |

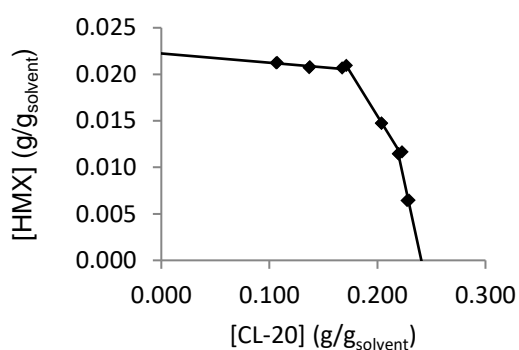


Figure 10: Determined PSD for propylene carbonate/2-propanol 1:1 at 333.15 K.

Table 2: Determined PSD-data of propylene carbonate/2-propanol 1:1 at 333.15 K

| [CL-20] (g/g) | [HMX] (g/g) | phase region |
|---------------|-------------|---------------|
| 0.107 | 0.021 | HMX |
| 0.137 | 0.021 | HMX |
| 0.167 | 0.021 | TP1 cocrystal |
| 0.171 | 0.021 | cocrystal |
| 0.204 | 0.015 | cocrystal |
| 0.219 | 0.011 | Cocrystal |
| 0.223 | 0.012 | TP2 cocrystal |
| 0.228 | 0.006 | CL-20 |

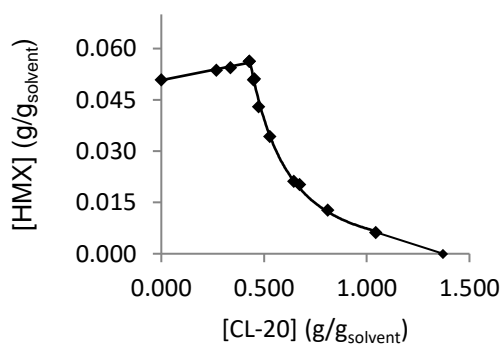


Figure 11: Determined PSD for ACN at 333.15 K.

Table 3: Determined PSD-data of ACN at 333.15 K

| [CL-20] (g/g) | [HMX] (g/g) | phase region |
|---------------|-------------|---------------|
| 0.000 | 0.051 | HMX |
| 0.269 | 0.054 | HMX |
| 0.338 | 0.054 | HMX |
| 0.429 | 0.056 | TP1 cocrystal |
| 0.449 | 0.051 | cocrystal |
| 0.453 | 0.051 | cocrystal |
| 0.474 | 0.043 | cocrystal |
| 0.528 | 0.034 | cocrystal |
| 0.646 | 0.021 | cocrystal |
| 0.673 | 0.020 | cocrystal |
| 0.810 | 0.013 | cocrystal |
| 1.045 | 0.006 | TP2 cocrystal |
| 1.372 | 0 | CL20 |

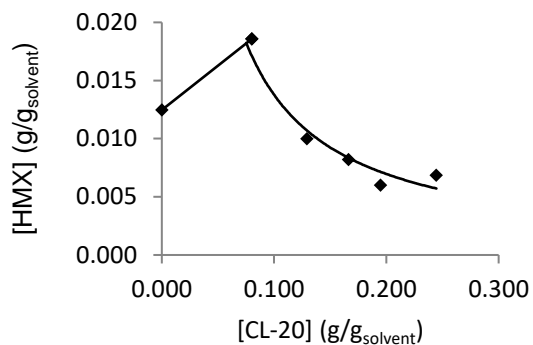


Figure 12: Partially determined PSD for ACN/2-propanol 1:1 at 333.15 K.

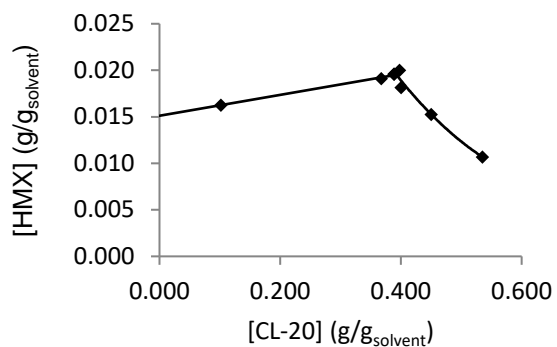


Figure 13: Partially determined PSD of ACN at 293.15K.

Table 4: Determined PSD-data of ACN/2-propanol 1:1 at 333.15 K

| [CL-20] (g/g) | [HMX] (g/g) | phase region |
|---------------|-------------|---------------|
| 0.000 | 0.012 | HMX |
| 0.080 | 0.019 | HMX |
| 0.129 | 0.010 | TP1 cocrystal |
| 0.166 | 0.008 | cocrystal |
| 0.195 | 0.006 | cocrystal |
| 0.245 | 0.007 | cocrystal |

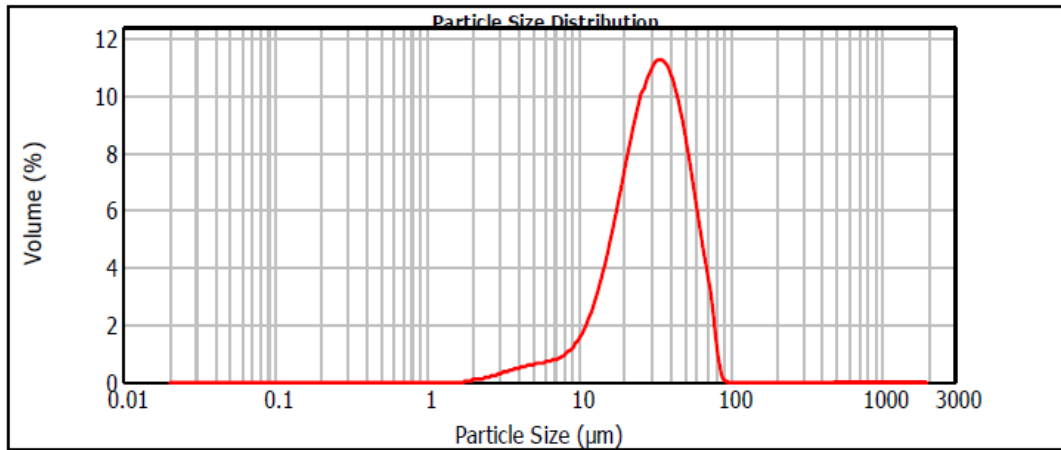
Table 5: Determined PSD-data of ACN at 293.15 K

| [CL-20] (g/g) | [HMX] (g/g) | phase region |
|---------------|-------------|---------------|
| 0.102 | 0.016 | HMX |
| 0.368 | 0.019 | HMX |
| 0.389 | 0.020 | HMX |
| 0.398 | 0.020 | TP1 cocrystal |
| 0.400 | 0.018 | cocrystal |
| 0.450 | 0.015 | cocrystal |
| 0.535 | 0.011 | cocrystal |

Pilot-plant-scale batch RC size distributions

| | | | |
|--|--|---|---------------------------------|
| Particle Name: hmx_1.69_0.1 | Accessory Name: Hydro 2000S (B) | Analysis model: General purpose | Sensitivity: Normal |
| Particle RI: 1.690 | Absorption: 0.1 | Size range: 0.020 to 2000.000 μm | Obscuration: 15.48 % |
| Dispersant Name: Heptane | Dispersant RI: 1.390 | Weighted Residual: 0.661 % | Result Emulation: Off |
| Concentration: 0.0512 %Vol | Span : 1.415 Span84/16 0.5485 | Uniformity: 0.433 | Result units: Volume |
| Specific Surface Area: 0.267 m^2/g | Surface Weighted Mean D[3,2]: 22.448 μm | Vol. Weighted Mean D[4,3]: 33.200 μm | |

d(0.1): 13.374 μm D(0.16) : 16.74 μm d(0.5): 30.841 μm D(0.84) : 50.58 μm d(0.9): 57.002 μm



| Size (μm) | Volume In % | Size (μm) | Volume In % | Size (μm) | Volume In % | Size (μm) | Volume In % | Size (μm) | Volume In % | Size (μm) | Volume In % |
|------------------------|-------------|------------------------|-------------|------------------------|-------------|------------------------|-------------|------------------------|-------------|------------------------|-------------|
| 0.020 | 0.00 | 0.142 | 0.00 | 1.002 | 0.00 | 7.096 | 0.64 | 50.238 | 5.87 | 355.656 | 0.00 |
| 0.022 | 0.00 | 0.159 | 0.00 | 1.125 | 0.00 | 7.962 | 0.76 | 56.368 | 4.60 | 399.052 | 0.00 |
| 0.025 | 0.00 | 0.178 | 0.00 | 1.282 | 0.00 | 8.934 | 0.97 | 63.248 | 3.32 | 447.744 | 0.00 |
| 0.028 | 0.00 | 0.200 | 0.00 | 1.416 | 0.00 | 10.024 | 1.28 | 70.963 | 2.16 | 502.377 | 0.00 |
| 0.032 | 0.00 | 0.224 | 0.00 | 1.589 | 0.00 | 11.247 | 1.73 | 79.621 | 0.42 | 563.677 | 0.00 |
| 0.036 | 0.00 | 0.252 | 0.00 | 1.783 | 0.02 | 12.619 | 2.33 | 89.337 | 0.00 | 632.456 | 0.00 |
| 0.040 | 0.00 | 0.283 | 0.00 | 2.000 | 0.06 | 14.159 | 3.08 | 100.237 | 0.00 | 709.627 | 0.00 |
| 0.045 | 0.00 | 0.317 | 0.00 | 2.244 | 0.10 | 15.887 | 3.96 | 112.468 | 0.00 | 796.214 | 0.00 |
| 0.050 | 0.00 | 0.356 | 0.00 | 2.518 | 0.15 | 17.825 | 4.94 | 126.191 | 0.00 | 893.367 | 0.00 |
| 0.056 | 0.00 | 0.399 | 0.00 | 2.825 | 0.21 | 20.000 | 5.94 | 141.589 | 0.00 | 1002.374 | 0.00 |
| 0.063 | 0.00 | 0.448 | 0.00 | 3.170 | 0.27 | 22.440 | 6.90 | 158.866 | 0.00 | 1124.683 | 0.00 |
| 0.071 | 0.00 | 0.502 | 0.00 | 3.557 | 0.33 | 25.179 | 7.89 | 178.250 | 0.00 | 1261.915 | 0.00 |
| 0.080 | 0.00 | 0.564 | 0.00 | 3.991 | 0.39 | 28.251 | 8.25 | 200.000 | 0.00 | 1415.892 | 0.00 |
| 0.089 | 0.00 | 0.632 | 0.00 | 4.477 | 0.44 | 31.698 | 8.48 | 224.404 | 0.00 | 1588.656 | 0.00 |
| 0.100 | 0.00 | 0.710 | 0.00 | 5.024 | 0.48 | 35.566 | 8.34 | 251.785 | 0.00 | 1782.502 | 0.00 |
| 0.112 | 0.00 | 0.796 | 0.00 | 5.637 | 0.51 | 39.905 | 7.83 | 282.508 | 0.00 | 2000.000 | 0.00 |
| 0.126 | 0.00 | 0.893 | 0.00 | 6.325 | 0.56 | 44.774 | 6.98 | 316.979 | 0.00 | | |
| 0.142 | 0.00 | 1.002 | 0.00 | 7.096 | 0.56 | 50.238 | 6.98 | 355.656 | 0.00 | | |

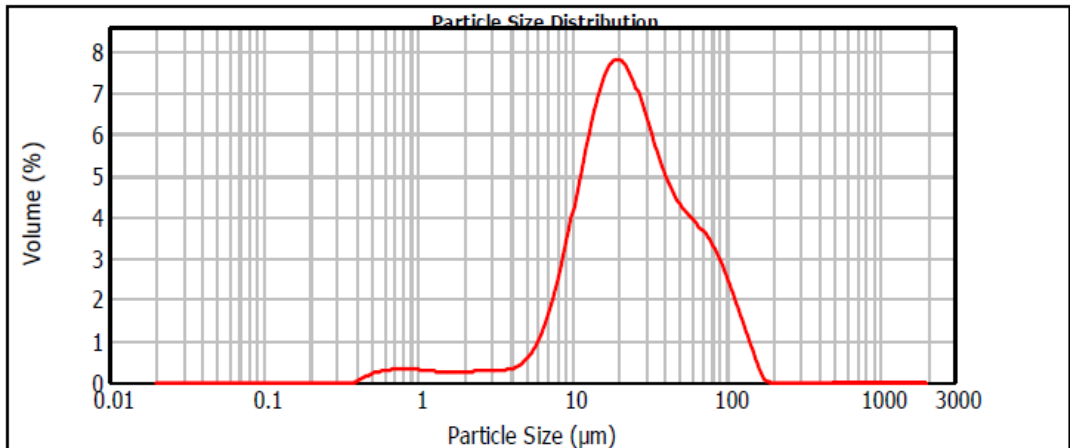
Operator notes: 2 min US 60%

Figure 14: Laser diffraction analysis of the first pilot-plant RC batch.

| | | | |
|---------------------------------------|---|--|---------------------------------|
| Particle Name: hmx_1.69_0.1 | Accessory Name: Hydro 2000S (B) | Analysis model: General purpose | Sensitivity: Normal |
| Particle RI: 1.690 | Absorption: 0.1 | Size range: 0.020 to 2000.000 um | Obscuration: 19.27 % |
| Dispersant Name: Heptane | Dispersant RI: 1.390 | Weighted Residual: 0.443 % | Result Emulation: Off |

| | | | |
|--|---|--|--------------------------------|
| Concentration: 0.0348 %Vol | Span : 2.924 Span84/16 1.0515 | Uniformity: 0.865 | Result units: Volume |
| Specific Surface Area: 0.501 m ² /g | Surface Weighted Mean D[3,2]: 11.985 um | Vol. Weighted Mean D[4,3]: 33.840 um | |

d(0.1): 8.777 um D(0.16) : 11.09 um d(0.5): 23.338 um D(0.84) : 60.18 um d(0.9): 77.007 um



| Size (um) | Volume In % | Size (um) | Volume In % | Size (um) | Volume In % | Size (um) | Volume In % | Size (um) | Volume In % | Size (um) | Volume In % |
|-----------|-------------|-----------|-------------|-----------|-------------|-----------|-------------|-----------|-------------|-----------|-------------|
| 0.020 | 0.00 | 0.142 | 0.00 | 1.002 | 0.22 | 7.096 | 1.50 | 50.238 | 3.14 | 355.656 | 0.00 |
| 0.022 | 0.00 | 0.159 | 0.00 | 1.125 | 0.21 | 7.962 | 2.06 | 56.368 | 2.98 | 399.052 | 0.00 |
| 0.025 | 0.00 | 0.178 | 0.00 | 1.262 | 0.19 | 8.934 | 2.70 | 63.246 | 2.83 | 447.744 | 0.00 |
| 0.028 | 0.00 | 0.200 | 0.00 | 1.416 | 0.18 | 10.024 | 3.41 | 70.963 | 2.64 | 502.377 | 0.00 |
| 0.032 | 0.00 | 0.224 | 0.00 | 1.589 | 0.18 | 11.247 | 4.11 | 79.621 | 2.40 | 563.677 | 0.00 |
| 0.036 | 0.00 | 0.252 | 0.00 | 1.783 | 0.18 | 12.619 | 4.78 | 89.337 | 2.10 | 632.456 | 0.00 |
| 0.040 | 0.00 | 0.283 | 0.00 | 2.000 | 0.19 | 14.159 | 5.31 | 100.237 | 1.74 | 709.627 | 0.00 |
| 0.045 | 0.00 | 0.317 | 0.00 | 2.244 | 0.20 | 15.887 | 5.68 | 112.468 | 1.34 | 796.214 | 0.00 |
| 0.050 | 0.00 | 0.356 | 0.00 | 2.518 | 0.20 | 17.825 | 5.87 | 126.191 | 0.95 | 883.367 | 0.00 |
| 0.056 | 0.00 | 0.399 | 0.05 | 2.825 | 0.20 | 20.000 | 5.85 | 141.589 | 0.55 | 1002.374 | 0.00 |
| 0.063 | 0.00 | 0.448 | 0.12 | 3.170 | 0.21 | 22.440 | 5.64 | 158.866 | 0.17 | 1124.683 | 0.00 |
| 0.071 | 0.00 | 0.502 | 0.17 | 3.557 | 0.23 | 25.179 | 5.29 | 178.250 | 0.00 | 1261.915 | 0.00 |
| 0.080 | 0.00 | 0.564 | 0.21 | 3.991 | 0.27 | 28.251 | 4.85 | 200.000 | 0.00 | 1415.892 | 0.00 |
| 0.089 | 0.00 | 0.632 | 0.23 | 4.477 | 0.35 | 31.698 | 4.39 | 224.404 | 0.00 | 1588.656 | 0.00 |
| 0.100 | 0.00 | 0.710 | 0.24 | 5.024 | 0.49 | 35.566 | 3.97 | 251.785 | 0.00 | 1782.502 | 0.00 |
| 0.112 | 0.00 | 0.796 | 0.24 | 5.637 | 0.72 | 39.905 | 3.61 | 282.508 | 0.00 | 2000.000 | 0.00 |
| 0.126 | 0.00 | 0.893 | 0.24 | 6.325 | 1.06 | 44.774 | 3.34 | 316.979 | 0.00 | | |
| 0.142 | 0.00 | 1.002 | 0.24 | 7.096 | | 50.238 | | 355.656 | 0.00 | | |

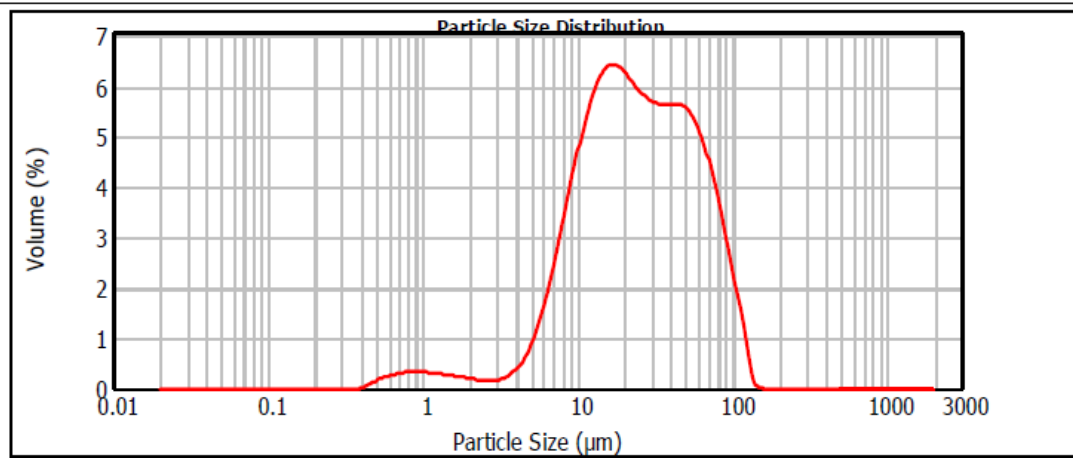
Operator notes: 2 min US 60%

Figure 15: Laser diffraction analysis of the second pilot-plant RC batch.

| | | | |
|---------------------------------------|---|--|---------------------------------|
| Particle Name: hmx_1.69_0.1 | Accessory Name: Hydro 2000S (B) | Analysis model: General purpose | Sensitivity: Normal |
| Particle RI: 1.690 | Absorption: 0.1 | Size range: 0.020 to 2000.000 um | Obscuration: 9.86 % |
| Dispersant Name: Heptane | Dispersant RI: 1.390 | Weighted Residual: 0.486 % | Result Emulation: Off |

| | | | |
|--|---|--|--------------------------------|
| Concentration: 0.0166 %Vol | Span : 2.696 Span84/16 1.0435 | Uniformity: 0.832 | Result units: Volume |
| Specific Surface Area: 0.503 m ² /g | Surface Weighted Mean D[3,2]: 11.930 um | Vol. Weighted Mean D[4,3]: 32.514 um | |

d(0.1): 7.872 um D(0.16) : 9.94 um d(0.5): 23.585 um D(0.84) : 59.16 um d(0.9): 71.462 um



| Size (µm) | Volume In % | Size (µm) | Volume In % | Size (µm) | Volume In % | Size (µm) | Volume In % | Size (µm) | Volume In % | Size (µm) | Volume In % |
|-----------|-------------|-----------|-------------|-----------|-------------|-----------|-------------|-----------|-------------|-----------|-------------|
| 0.020 | 0.00 | 0.142 | 0.00 | 1.002 | 0.24 | 7.096 | 2.17 | 50.238 | 4.12 | 355.656 | 0.00 |
| 0.022 | 0.00 | 0.159 | 0.00 | 1.125 | 0.23 | 7.962 | 2.74 | 56.368 | 3.91 | 369.052 | 0.00 |
| 0.025 | 0.00 | 0.178 | 0.00 | 1.262 | 0.21 | 8.634 | 3.29 | 63.246 | 3.56 | 447.744 | 0.00 |
| 0.028 | 0.00 | 0.200 | 0.00 | 1.416 | 0.19 | 10.024 | 3.82 | 70.963 | 3.11 | 502.377 | 0.00 |
| 0.032 | 0.00 | 0.224 | 0.00 | 1.589 | 0.18 | 11.247 | 4.26 | 79.621 | 2.58 | 563.677 | 0.00 |
| 0.036 | 0.00 | 0.252 | 0.00 | 1.783 | 0.16 | 12.619 | 4.59 | 89.337 | 1.99 | 632.456 | 0.00 |
| 0.040 | 0.00 | 0.283 | 0.00 | 2.000 | 0.16 | 14.159 | 4.78 | 100.237 | 1.43 | 709.627 | 0.00 |
| 0.045 | 0.00 | 0.317 | 0.00 | 2.244 | 0.14 | 15.887 | 4.78 | 112.468 | 1.01 | 796.214 | 0.00 |
| 0.050 | 0.00 | 0.366 | 0.00 | 2.518 | 0.11 | 17.825 | 4.79 | 126.191 | 0.71 | 883.367 | 0.00 |
| 0.056 | 0.00 | 0.399 | 0.00 | 2.825 | 0.12 | 20.000 | 4.67 | 141.589 | 0.51 | 1002.374 | 0.00 |
| 0.063 | 0.00 | 0.448 | 0.03 | 3.170 | 0.12 | 22.440 | 4.67 | 158.866 | 0.36 | 1124.683 | 0.00 |
| 0.071 | 0.00 | 0.502 | 0.08 | 3.567 | 0.15 | 25.179 | 4.51 | 178.250 | 0.26 | 1261.915 | 0.00 |
| 0.080 | 0.00 | 0.564 | 0.15 | 3.991 | 0.23 | 28.251 | 4.38 | 200.000 | 0.18 | 1415.892 | 0.00 |
| 0.089 | 0.00 | 0.632 | 0.19 | 4.477 | 0.35 | 31.698 | 4.29 | 224.404 | 0.13 | 1588.656 | 0.00 |
| 0.100 | 0.00 | 0.710 | 0.24 | 5.024 | 0.55 | 35.566 | 4.25 | 251.785 | 0.09 | 1782.502 | 0.00 |
| 0.112 | 0.00 | 0.796 | 0.24 | 5.637 | 0.83 | 39.905 | 4.25 | 282.508 | 0.06 | 2000.000 | 0.00 |
| 0.128 | 0.00 | 0.893 | 0.25 | 6.325 | 1.20 | 44.774 | 4.26 | 316.079 | 0.04 | | |
| 0.142 | 0.00 | 1.002 | 0.25 | 7.096 | 1.65 | 50.238 | 4.23 | 355.656 | 0.03 | | |

Operator notes:
2 min US 60%

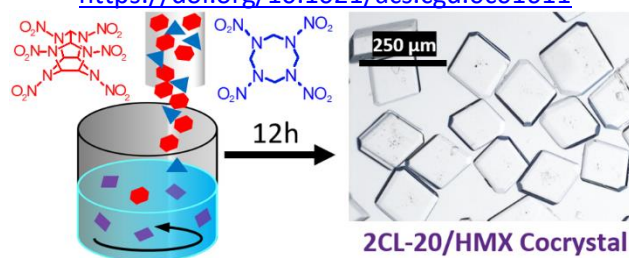
Figure16: Laser diffraction analysis of the third pilot-plant RC batch.

7.2 Semibatch Reaction Crystallization for Scaled-Up Production of High-Quality CL-20/HMX Cocystal: Efficient Because of Solid-Dosing

Dirk Herrmannsdörfer and Thomas M. Klapötke

Crystal Growth & Design **2021**, *21*, 1708-1717

<https://doi.org/10.1021/acs.cgd.0c01611>



The following modifications were made to this paper:

- The journal mandatory American English was corrected to British English

ABSTRACT: CL-20/HMX cocrystal is one of the most promising energetic cocrystals, but scaled-up production was prevented by the large inherent solubility difference of 2,4,6,8,10,12-hexanitro-2,4,6,8,10,12-hexaazaisowurtzitane (CL-20) and 1,3,5,7-tetranitro-1,3,5,7-tetraoctane (HMX) and, therefore, unacceptable CL-20 efficiency. Reaction cocrystallization (aka. Reaction crystallization or slurry technique) has been extensively used as an efficient, straightforward cocrystallization screening method, but only few attempts at utilizing this method for scaled-up cocrystal production have been undertaken and none have realized its full potential. By utilizing solid-dosing and process analytical technology, semibatch reaction cocrystallization (SBRC) provided the first scale up of high-quality CL-20/HMX cocrystal with a particle diameter $D(4,3)$ of 163 μm and a batch size of 100 g. The CL-20 recovery is 63%, which is over two times better than the theoretical recovery rate of the next best method (evaporation crystallization), and the crystal quality is comparable to crystals obtained from controlled antisolvent crystallization. It is shown that SBRC is a valuable crystallization technique for efficient scale up of cocrystal systems whose cofomers exhibit significantly different solubilities.

Introduction

Cocrystallisation has seen increasing interest recently, mostly because of its ability to modify characteristics of the cofomers, such as their bioavailability,¹ permeability,² hygroscopy,³ stability,^{4,5} or sensitivity,^{6,7} without the need for molecular change to the cofomers. This resonated most strongly with the pharmacological sector, as evidenced by the over 150 review papers published on active pharmaceutical ingredient (API) cocrystals over the past decade. Cocrystallisation has also had a significant impact on the field of molecular electronics^{8–11} and energetic materials.^{12–15} The 2:1 CL-20/HMX cocrystal, discovered by Bolton *et al.*,⁶ is one of the most promising energetic cocrystals. It is reported to possess comparable impact sensitivity to HMX and to exceed HMX in terms of detonation velocity because of the better detonation properties of its rather sensitive^{6,16,17} cofomer CL-20. This cocrystal is a promising candidate for succeeding HMX as the state-of-the-art high explosive.

Multiple techniques for producing the cocrystal are presented in the literature: antisolvent crystallisation,^{18–20} cooling crystallisation,¹⁹ spray flash evaporation,^{21,22} spray drying,²³ solvent evaporation,^{6,24,25} ultrasonic spray-assisted electrostatic adsorption,²⁶ liquid-assisted grinding,^{6,18,27} and solution-mediated phase transformation.^{19,24} To test the cocrystal in highly filled polymer-bonded explosive charges, a bimodal size distribution of typically about 20 and 200 μm is required. A crystallisation method is, therefore, needed that can be scaled-up at least to the 100 g

range and can efficiently produce compact crystals of about 200 μm .

Spray drying is considered one of the most desirable methods for the scaled-up production of cocrystals because it is a fast, continuous, one-step process^{28,29} and easy to scale up.³⁰

Cocrystallisation methods that utilise solution-mediated phase transformation such as the slurry technique^{31,32} and batch reaction crystallisation^{29,33} (also called reaction cocrystallization by Rodríguez-Hornedo *et al.*²⁹) have become the most applied cocrystal screening methods³⁴ and are capable of fast and efficient CL-20/HMX cocrystal production in the 100 g-range.^{19,24, b}

While both spray drying and batch reaction cocrystallization can be efficient and easily scalable methods, they are incapable of producing crystals of the desired size and quality. The high initial supersaturation, high nucleation rate, and rapid crystal growth lead to small crystals of poor quality in batch RC,¹⁹ and the even faster solidification during spray drying facilitates the formation of defects and amorphous states.²⁸ The crystal quality is of importance not only in pharmaceutical applications^{35–37} and molecular electronics,^{8,9} but also in the field of energetic crystals because the sensitivity to impact and shock is directly linked to the void fraction and void size of the crystals.^{38–43} Coarse crystals of acceptable quality have only been obtained by controlled cooling or antisolvent crystallisation,¹⁹ but evaporation crystallisation should also be capable of producing high-quality cocrystals. All of these crystallisation techniques suffer from their dependence on the size and position of the cocrystal phase region and the

^b The differentiation between the slurry technique and reaction crystallisation seems artificial because both methods operate strictly within the boundaries of the cocrystal phase region in the ternary phase diagram, and supersaturation of the cocrystal is reached by adding either one^{29,33} or both^{31,32} cocrystal cofomers in a solid form to the solution. From a chemical

standpoint, both methods classify as “reaction cocrystallisation”. Therefore, in this work, the expression “reaction cocrystallization” coined by Rodríguez-Hornedo *et al.* will be used to describe crystallisation experiments where one or more cocrystal cofomer are added to a solution saturated with respect to the cocrystal.

maximum cocrystal yield that can be produced by cooling, antisolvent addition, or solvent evaporation, respectively. The highest CL-20 efficiency (mass of CL-20 found in the cocrystal divided by the total initially dissolved CL-20) that can, therefore, be achieved is 26% for evaporation crystallisation in the only applicable solvent: acetonitrile (ACN).¹⁹ A different crystallisation method was, hence, required that combines the high efficiency of batch RC with the supersaturation control of solution based methods such as cooling, antisolvent, or evaporation crystallisation. This is achievable by SBRC, where the cofomers are added to the solution in a controlled fashion to manage the supersaturation. Despite its obvious benefits, SBRC seems to be a very obscure technique, as only few studies on the formation of cocrystals in this fashion have been published. SBRC in its most literal sense has been carried out by Chen *et al.*⁴⁴ Here the cocrystallisation was induced by partially neutralising sodium benzoate with HCl. The obtained benzoic acid then cocrystallised with the remaining sodium benzoate. Nishimaru, Kudo, and Takiyama have cocrystallised carbamazepine and saccharin by mixing two different eutectic solutions to generate supersaturation of the cocrystal.^{45,46} A similar strategy was employed by Powell *et al.* for cocrystallising *p*-toluenesulfonamide with triphenylphosphine oxide⁴⁷ and urea-barbituric acid.⁴⁸ Because of the addition of the cofomers in dissolved form, this strategy would not be efficient for many cocrystal systems. For the CL-20/HMX cocrystal, only a CL-20 efficiency of 6% could be achieved. Higher efficiencies can only be obtained if the cofomers are added in undissolved form. In this study, we describe the prerequisites for a successful solid-dosing SBRC and the application of process analytical technology (PAT)^{49,50} to improve process efficiency and product quality. The obtained product is compared to crystals obtained from batch RC and antisolvent crystallisation to assess the achieved level of crystal quality.

The phase solubility diagram (PSD) of a cocrystal is an essential tool for the development of SBRC experiments, as it shows the equilibrium solubilities of its solid phases as a function of solution concentration of the cofomers.³³ The PSD of the CL-20/HMX cocrystal in ACN at 333.15 K is displayed in Figure 1. There are multiple phase regions present in the PSD, of which only the regions marked A and B in Figure 1 are relevant for SBRC. In region A, CL-20, HMX, and the cocrystal are undersaturated, no solid phase can form, and the added CL-20, HMX, or cocrystal is dissolved. In region B, the solution is undersaturated with respect to CL-20 and HMX, but supersaturated with

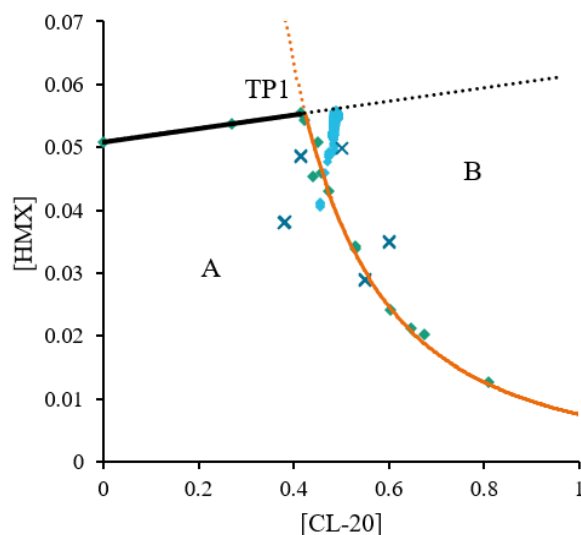


Figure 1. PSD of the CL-20/HMX cocrystal in ACN at 333 K. The straight line represents the HMX solubility curve. The cocrystal solubility curve is displayed in orange. TP1 is the transition point of the phase regions at which the cocrystal and solid HMX are in equilibrium. Green diamonds are solubility measurement points, blue crosses are the infrared (IR) calibration points, and turquoise diamonds are concentrations of SBRC2.

respect to the cocrystal. Here the cocrystal is the only solid phase that is thermodynamically stable. For each SBRC, the solution concentration was adjusted to lie within region A close to the cocrystal solubility curve before the seed crystal addition to ensure partial dissolution of the seed crystals. On the addition of the seed crystals, a concentration on the cocrystal solubility curve is reached. A typical concentration progression of an SBRC is displayed in Figure 1. After the addition of CL-20 and HMX, the concentrations increase until the HMX solubility limit, which also extends into the cocrystal phase region, is reached. If, from this point on, more CL-20 and HMX mixture is added to the solution than is

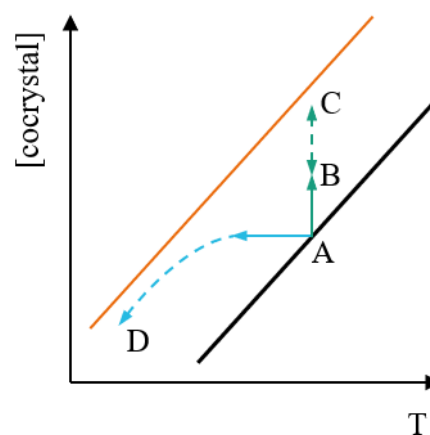


Figure 2. Visualisation of the [cocrystal] and T progression during SBRC (green arrows) and cooling crystallization (teal arrows). The black line represents the cocrystal's solubility curve, and the orange line represents the meta stable zone limit.

deposited on the growing cocrystals, the

concentration will move along the black dashed line to higher [CL-20] and slightly higher [HMX]. During SBRC, the solution concentration can only be located within region B because no CL-20 or HMX supersaturation can be generated.

In SBRC, solid-dosing generates supersaturation in a similar fashion to cooling, antisolvent dosing, or solvent evaporation in the respective crystallisation experiment. This is visualised in Figure 2, where a simplified temperature-dependent solubility diagram of a cocrystal is displayed. During SBRC, solid-dosing increases [cocrystal] along the green vertical line between A and C. In the presence of seed crystals and as long as the metastable zone limit is not exceeded, the seed crystals will grow and the supersaturation will be reduced along the line between C and A. Depending on the dosing rate and the crystallisation rate, an equilibrium supersaturation is reached. If the dosing rate is perfectly matched with the crystallisation rate, a steady state will be reached and [cocrystal] will be stationary. If the dosing rate is increased in discrete steps, [cocrystal] will oscillate between C and B. This is caused by the mismatch between the continuously increasing crystallisation rate and the stepwise increasing dosing rate. For a cocrystal of congruently soluble cofomers, an evaporation crystallisation follows the same trajectory as a solid-dosing SBRC because in evaporation crystallisation experiments, supersaturation is generated by removing solvent, which increases [cocrystal]. In comparison, supersaturation is generated during cooling crystallisation by reduction of the solution temperature. In the presence of seed crystals, crystals will grow with decreasing temperature, and [cocrystal] follows the trajectory of the arrows between A and D.

The LAMBDA Instruments GmbH DOSER 0.2L utilised in this study was chosen because a stepwise dosing program of varying dosing rates and dosing times can be implemented or a dosing rate can be set via external communication by either an analogue or digital signal. Furthermore, it is capable of low dosing rates, can be flushed by pressurised gas to prevent solid agglomeration, and exhibits a slim form factor that is important because of the limited space between the ground glass joints of the 250 mL jacketed vessel. It dispenses the solid by rotating a shaft connected to a cone-shaped polymer cap that exhibits a spiral pattern on the bottom. On rotation, the solid is pushed through an opening in the bottom of the dispenser. The dosing is heavily influenced by the free-flowing capability of the solid. Three solids were utilized for dosing: CL-20 (150 μm), fine HMX (5 μm), and coarse HMX

(300 μm). Only by mixing the utilised HMX coarse to fine at 5:1, reproducible dispensing was achieved. If only fine HMX was used, cavities could form in the solid or the dispensing rate could vary by more than factor 10 within an experiment. If only coarse HMX was used, the solid mixture could trickle through the doser until the hopper was empty even without shaft rotation because of its superior free-flowing capability.

Materials and Methods

Raw Material. The determined chemical purities and commercial sources of the CL-20 and HMX batches are summarised in Table 1. ACN (HPLC grade) was purchased from Carl Roth GmbH, stored over 3 \AA molecular sieve, and used as received.

Table 1. Purity and Commercial Source of the Utilised Solids

| | purity | commercial source; lot number |
|------------|---|----------------------------------|
| CL-20 | 98.3% (^1H NMR) 99.4% (HPLC) | SNPE; 573S98 |
| fine HMX | 98.7% (^1H NMR) 99.3% (HPLC) | Chemring Nobel; NSI 00E 000 E004 |
| coarse HMX | 99.4% (^1H NMR) 99.9% (HPLC) | Eurenco NSO131, lot 20173558 |

In situ ATR-FTIR spectroscopy. Calibration was carried out in 1.5 mL glass vessels. The solid mixture and ACN were weighed, utilising a Kern 770 analytical balance (accuracy 0.1 mg). A strong neodymium magnetic stir bar was inserted to ensure fast dissolution of the solid to prevent regions of high supersaturation. Directly after the weighing of ACN, the vessel was sealed to the ATR probe via o-ring and the vessel was placed in a 333.15 K tempered oil bath that was temperature-controlled via a PT100 temperature probe connected to a heidolph MR Hei-End magnetic stirrer. Care was taken to ensure that no air bubbles surrounded the ATR probe head during measurements. A series of typically 20 measurements at a resolution of 1 cm^{-1} were undertaken. The wavenumber region was 0-4000 cm^{-1} . Typically, only the last 10 measurements were used for the calibration. For each measurement, 20 scans were accumulated. During measurements and between measurements, the probe head and the optical fibre were not moved. Before each series of measurements, a background spectrum was measured against air. The spectra were processed using the Unscrambler X version 10.1. Standard normal variate (SNV) transformation⁵¹ was performed on all spectra to

correct for possible baseline shifts and global intensity variations.⁵² Utilising projection to latent structures (PLS)⁵³ minimised the standard error of calibration.

Experimental Setup. Crystallisation rate determination and SBRC were carried out in a 250 mL flat-bottomed jacketed flask that was temperature-controlled using a Lauda RC6 CP thermostat. No external temperature sensor was utilised, but by prior calibration, the reaction temperature of 333.15 K (± 0.5 K) was achieved by setting the internal thermostat temperature to 335 K. The solid was dispensed by a LAMBDA Instruments GmbH DOSER 0.2L. A slow stream of pressurised air was vented through the solid-doser to prevent cementation of the solid due to ACN vapours. To compensate for the solvent loss because of the air stream, ACN was added during the crystallisation to the reaction vessel utilising a sykam s1610 syringe dosing system. As the central joint of the vessel lid was occupied by the doser unit, no vertically aligned agitator shaft was applicable. Due to the high solid loadings and spatial limitations, no diagonally aligned or eccentric stirrer could be used. The reaction mixture was, therefore, agitated by a specially designed captured magnetic stir bar that was propelled via a heidolph MR Hei-End magnetic stirrer that was also set to 333 K to reduce thermal loss. To reduce particle breakage, the mount of the magnetic stir bar had to be rounded. To prevent rotation of the mount, it had to be fixed by an aluminium rod that was inserted via one of the ground glass joints. The rotation speed was set to 250 rpm. The solution concentration was determined in situ using a Bruker Matrix MF mid-infrared process spectrometer fitted with a Bruker IN350-T diamond ATR immersion probe.

Crystallisation Rate Determination. ACN (82 g, 2.0 mmol) was added to 36.2 g of CL-20 (82.6 mmol) and 1.5 g of HMX (5.1 mmol) in the tempered reaction vessel. After complete dissolution and thermal equilibration, the seed crystals were added to the solution. Then after equilibration, 0.93 g (3.1 mmol) of HMX and 2.79 g (6.4 mol) of CL-20 were added within 30 s. Once a supersaturation of about 1.1 was reached, 0.93 g (3.1 mmol) of HMX and 2.79 g (6.4 mol) of CL-20 were added again two more times. Then the stirrer was removed and the slurry was transferred into a Büchner funnel using a BRAUN omnifix 100 mL syringe without a cannula attached to avoid clogging. The mother liquor was removed, and the product crystals were washed with 30 mL 2-propanol:ACN (8:2), 30 mL 2-propanol:ACN (9:1) and five times with 20 mL of 2-propanol to ensure the total removal of the

mother liquor. The crystals were dried under ambient conditions.

SBRC. ACN (122 g, 2.97 mol) was added to 52.95 g of CL-20 (120.8 mmol) and 5.35 g of HMX (18.1 mmol) in the tempered reaction vessel. After complete dissolution and thermal equilibration, the seed crystals were added to the solution. The concentration was adjusted to ensure about 10% seed crystal dissolution to reduce surface defects that would reduce the crystal quality.^{54,55} After equilibrium was reached, the solid-dosing of a mixture of 90 g of CL-20 (205 mmol) and 30 g of HMX (101 mmol) was started. One hour after all solid was dispensed, the stirrer was removed and the slurry was transferred into a Büchner funnel using a BRAUN omnifix 100 mL syringe. No cannula was attached to avoid clogging. The mother liquor was removed, and the product crystals were washed with 30 mL 2-propanol:ACN (8:2), 30 mL 2-propanol:ACN (9:1), and five times with 20 mL of 2-propanol to ensure the total removal of the mother liquor. The crystals were dried under ambient conditions.

Calculation of Solution Composition and Supersaturation. Solution composition is expressed as the mass ratio [A] of the mass of the individual solids m_A and the solvent mass m_{ACN} as follows:

$$[A] = \frac{m_A}{m_{ACN}}$$

Following the argumentation of Kudo and Takiyama,⁴⁵ the supersaturation of the cocrystal is calculated by dividing [HMX] by the corresponding [HMX*] on the solubility curve. This calculation is possible because for all solution compositions within the cocrystal phase region of CL-20 and HMX in ACN at 333 K the de-supersaturation line from [HMX] through [HMX*] will intersect the CL-20 concentration axis.⁴⁵

Raman Analysis. Raman spectra were obtained utilising a Bruker RFS 100/S Raman spectrometer equipped with a 1064 nm ND:YAG-laser operated at 450 mW and a liquid-nitrogen-cooled germanium detector. The spectra were obtained between 80 and 3500 cm^{-1} with a spectral resolution of 1 cm^{-1} .

Density Measurement. The bulk density was determined using a micromeritics AccuPyc 1340 TEC 10 cm^3 with He 5.0 as the measurement gas. The equilibration pressure change was set to the standard 0.345 hPa. The heating/cooling element was set to 292.95 K for all measurements to achieve an average chamber temperature close to 293.15 K. A calibration of the chamber volumes was carried out before the series of measurements. About 10 g material was weight in using a Kern 770 analytical balance (accuracy 0.1 mg). Three hundred flushing

cycles ensured total sample dryness during the measurement. Between 50 and 300 data points were collected for each measurement. At least two true repeat measurements were carried out for each sample.

Solvent Inclusion Determination. About 50 mg of samples were dissolved in dry dimethylformamide. One microliter of the solution was injected into the Agilent 6890N GC-FID equipped with a DB-624 60 m x 0.25 mm ID x 1.4 μm film column. The split ratio was 10, and the injection port temperature was 503 K. The helium flow was 2 ml min^{-1} , and the column was kept at 323 K for 4 min and then heated up to 353 K with a heating rate of 5 K/min. From 353 K up to 533 K, the heating rate was 20 K/min. The detector temperature was 553 K.

Particle Size Determination. Particle diameters were determined utilising a Malvern Mastersizer 2000 version 5.60 in 2-propanol as dispersion medium. The agitation speed was 2450 rpm. A refractive index of 1.69 was chosen, and the absorption coefficient was selected individually to obtain the best results. Three measurements, each consisting of 10000 individual scans, were averaged.

PXRD Analysis. X-ray powder diffraction measurements were performed on a D8 Advance from Bruker AXS, equipped with a copper tube, two 2.5° Soller collimators, an antiscatter screen, a flip stick stage, and a silicon strip detector (LynxEye). Samples were milled to a particle diameter of less than 10 μm . The reflection range was scanned in 0.01° 2θ steps from 10-42° 2θ . Each measurement was accumulated for 20 s. The data were evaluated using Rietveld analysis based on the structure data reported by Bolton *et al.*⁶

Results and Discussion

In Situ ATR-FTIR Spectroscopy. Fourier transform infrared spectroscopy (FTIR) in combination with attenuated total reflectance (ATR) is an efficient tool for monitoring solution concentrations during crystallisation experiments with high solid loading⁵⁶ and has been used to monitor the solution concentration of both cofomers during cocrystallisation experiments.^{47,57,58} Because of the chemical similarity of CL-20 and HMX and the limited transmittance of the optical fibre, only a small spectral region in which the signals of CL-20 and HMX are strongly superimposed is available for online concentration monitoring (Figure 3). Multivariate analysis^{49,50} was applied to obtain a robust model in face of the presence of the convoluted signals and the substantial signal noise

in the region between 1585 and 1610 cm^{-1} because of low transmittance.

The objective was to monitor the concentration progression of CL-20 and HMX during the solid-dosing of the SBRC independently. Hence, both the HMX and CL-20 concentration were involved in the calibration model. During calibration, it was found that the lever of individual samples in the calibration model becomes excessively large if a calibration of the whole phase region is undertaken. For highest precision, the set of calibration points only envelops part of the cocrystal phase region (Figure 1). Because of the relatively small concentration region for the calibration, only two principal components are needed to achieve an explained variance of 98.4%. The use of only two principal components should increase the robustness of the calibration model. The position of the calibration points was chosen to ensure maximum orthogonality of the [CL-20] and [HMX] values to prevent linear dependency of the

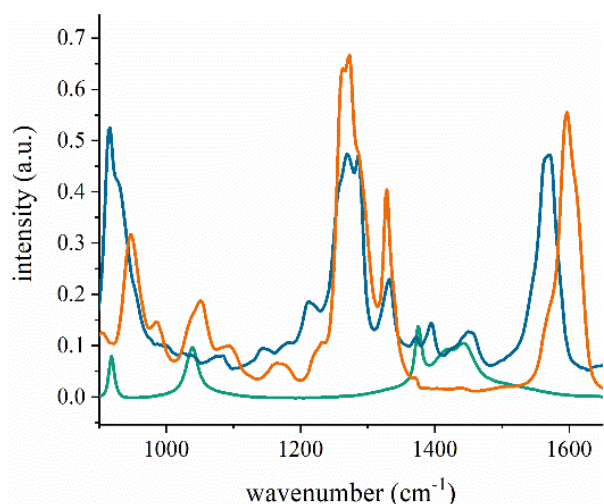


Figure 3. Display of the utilisable wavenumber region for concentration monitoring during SBRC of the CL-20/HMX cocrystal. CL-20 (orange), HMX (blue), and ACN (green).

[HMX] values on the [CL-20] values. The model was validated by predicting the solution concentrations of an older calibration. Four of the old data points lie within the region. On average, an error of 4.2 mg CL-20 g⁻¹ACN and 0.7 mg HMX g⁻¹ ACN was achieved. These errors are sufficiently small for the control of the supersaturation during the SBRC experiments, especially because the HMX concentration is kept at the solubility limit during the entire experiment anyway. Only the CL-20 concentration is, thus, truly important, and a relative error of less than 1% is insignificant. It is, therefore, also less impactful that during the conducted SBRC, [HMX] typically lies outside of the calibrated [HMX] region by 0.005 g/g.

Crystal Growth Rate. Figure 4 presents the concentration progression during the rate determination experiment 1 (RD1). [CL-20] exhibits a sharp sawtooth shape, while [HMX] exhibits plateaus after the addition of solid to the solution. The plateaus occur because the solubility limit for HMX is reached at 0.055 g/g ACN. Undissolved HMX is present during the plateaus. This phenomenon might be very beneficial to the success of an SBRC experiment, as this reduces the supersaturation increase upon solid addition. The supersaturation increases only as the result of the increased CL-20 concentration and the, therefore, shifted equilibration point on the cocrystal solubility curve. This behaviour smoothes the supersaturation progression during solid addition and helps to keep the crystallisation in a steady state. Even though the supersaturation of 1.24 was significantly lower than the previously determined metastable zone width of 1.4, the particle size distribution after the experiment indicated that a substantial amount of nucleation occurred during the experiment. Crystal breakage is the most likely cause because no particles smaller than 20 μm were detected. If

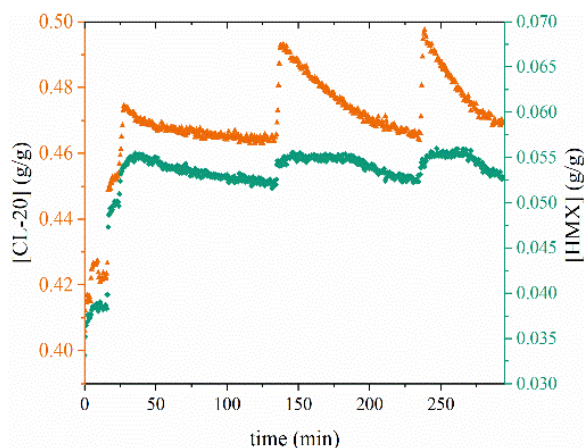


Figure 4. [CL-20] and [HMX] progression during the crystallisation rate determination.

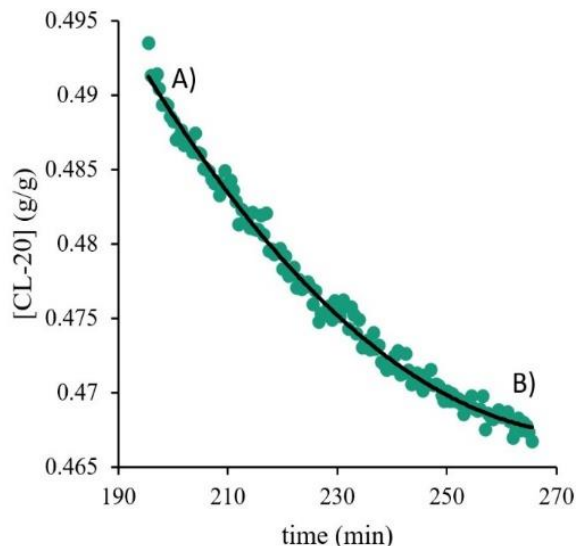


Figure 5. Visualisation of the [CL-20] progression and quadratic regression curve for R_G determination.

significant heterogeneous primary nucleation occurred, finer particles should be present. RD2 was therefore carried out with a

reduced stirrer speed of 150 rpm. The stirrer speed during RC1 was 500 rpm. The [CL-20] progression after the third solid addition is displayed in Figure 5. The significantly coarser product of RD2 indicates that less breakage occurred. Due to the low stirrer speed, the dwell time of the coarser crystals on the bottom of the vessel increased to an unacceptable level that propagated the formation of large, flat crystals. The presence of undissolved HMX could also have an impact on the nucleation rate. Further testing of the nucleation rate in different zones of the cocrystal phase region is required. As the overall crystal growth rate depends on the total crystal surface area, the most reliable data should be obtained from the third solid addition of RD2 because here the total surface area can be calculated from the crystal size distribution determined after the experiment. The overall crystal growth rate R_G can be determined following the formula⁵⁹

$$R_G = \frac{1}{A} \cdot \frac{dm}{dt}$$

where A is the total crystal surface area and dm/dt is the mass rate of deposition. The mass rate of deposition can simply be calculated as⁵⁹

$$\frac{dm}{dt} = \frac{4m_{ACN}}{3} \cdot \frac{d[CL-20]}{dt}$$

The obtained R_G values are summarised in Table 2 for the two [CL-20] values marked in Figure 5.

Table 2. Summary of the data required for calculation of R_G

| | super saturation | m_{ACN} (g) | A (cm ²) | $\frac{d[CL-20]}{dt}$ (min ⁻¹) | R_G (g min ⁻¹ cm ⁻²) |
|----|------------------|---------------|------------------------|--|---|
| A) | 1.20 | 80 | 3013 ^a | -5.77E-04 ^c | -2.04E-05 |
| B) | 1.12 | 80 | 3778 ^b | -8.81E-05 ^c | -2.48E-06 |

^a Calculated from particle size distribution obtained by subtracting the added mass during the third addition.

^b Calculated from particle size distribution.

^c Calculated by differentiation of the second-order regression curve.

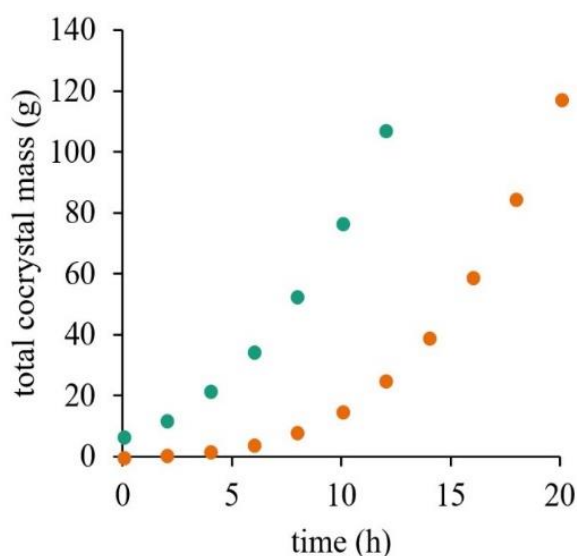


Figure 6. Visualisation of the possible mass increase during SBRC depending on the seed crystal mass and size. Starting from 0.1 g, 20 μm seed crystals (orange) and from 7.5 g, 80 μm seed crystals (green).

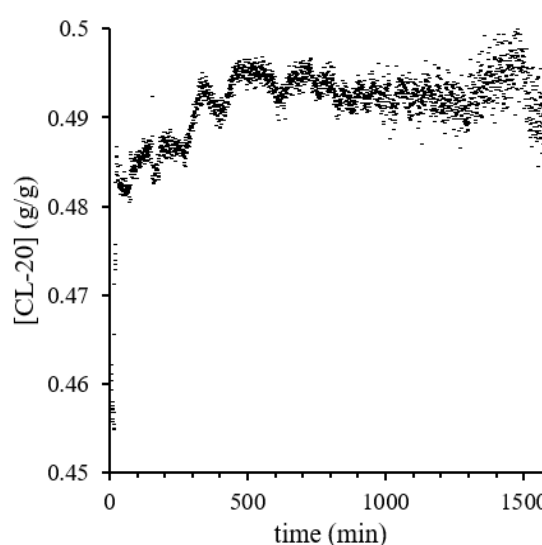
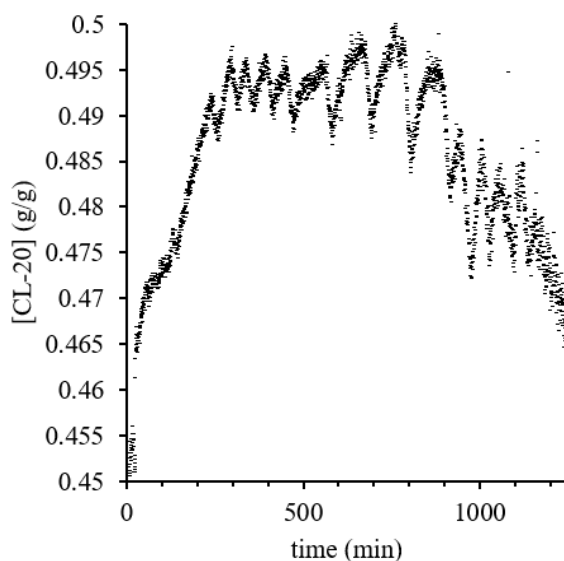


Figure 7. Left: [CL-20] progression during SBRC1. The sawtooth shape is the result of the 20 min. intervals between each 2 h dosing interval (less than 1 h between min. 250 and 500) without solid-dosing, during which the solution concentration drops. Right: [CL-20] progression during SBRC2.

SBRC without Active Dosing Rate Control. Active control of the dosing rate requires the permanent use of a PAT system, the interconnection of the dosing system and the PAT system, as well as the time and effort for the development of the interface software. One way to carry out SBRC without the need for constant PAT application is to set up a dosing program that increases the dosing rate based on a predetermined R_G and the projected total crystal surface area. The solid-dosing rate was calculated based on the R_G value obtained during RD2 for a supersaturation of 1.2. The aim was to produce 100 g of 200 μm crystals. Assuming that the seeds have a uniform size, that no nucleation and breakage occur, and that all material crystallises on the seed crystals, the required seed crystal mass m_{seed} can be calculated using the seed crystal size l_{seed} , the desired final crystal size l_{final} , and the cocrystal yield m_{final} following the formula⁶⁰

$$m_{seed} = m_{final} \cdot (l_{seed}/l_{final})^3.$$

Thus, one can calculate the number of seed crystals and therefore the total seed crystal surface area. Two-hour intervals of constant solid-dosing were chosen. Simulated cocrystal mass progressions for 20 and 80 μm seed crystal sizes are displayed in Figure 6. An exemplary calculation of the dosing rate progression based on the seed crystal mass can be found in the supporting information.

As can be seen in Figure 6, for the desired supersaturation of 1.2 and 20 μm seed crystals, this cocrystal system requires about 19 h to produce 100 g of the product. If 80 μm seed crystals are

utilised, 12 h are required. Based on the size distribution of the utilised seed crystals ($D(4,3)=75.6\ \mu\text{m}$), the seed crystal mass of SBRC1 was calculated to be 7.5 g. This would have resulted in a 12 h crystallisation. Due to a programming error of the solid-doser, however, a supersaturation of 1.2 was only reached after the second dosing interval, which made it necessary to start the program over at this point to prevent increased supersaturations. Furthermore, after around 930 min the solid-dosing rate was reduced most likely because of a leakage of the pressurised air tube that flushes the solid-doser. None of these incidents influenced the crystallisation besides prolonging the experiment by 6 h. The concentration profile of CL-20 during the experiment is shown in Figure 7, left. The final product missed with $163\ \mu\text{m}$ the mark of $200\ \mu\text{m}$. The seed crystal mass was, therefore, reduced to 5 g for SBRC2. Furthermore, the 20 min intervals of no solid-dosing between the dosing intervals were eliminated. Due to constant nucleation, they did not serve to calculate R_G , and the pauses in dosing seem to promote overdosing of the solid once dosing was started again. Because of the reduction of seed crystal mass, the dosing rate also had to be reduced. Seed crystals are partially dissolved to ensure a clean crystal surface, and the exact solution concentration prior to seed crystal addition varies because of varying amounts of condensation on the glass surfaces. Proportionally, more seed crystals might, therefore, be dissolved when less seed crystals are added. The dosing rate was, thus, not reduced by 30% for SBRC2 compared to that for SBRC1, but by around 50%. Even though the solid-dosing was not interrupted, the [CL-20] progression exhibits a sawtooth shape (Figure 7, right). The sharp tooth at 360 min is the result of the change in the dosing rate from 2 to 1. This is necessary because of hardware limitations, as the crystallisation operates at the lowest speed settings of the solid-doser and an average dosing rate of 1.5 cannot be selected. The other dips in [CL-20] are the result of the increasing solid deposition rate with increasing crystal size towards the end of each 2 h interval. Towards the end of the crystallisation the signal noise increases. This is most likely caused by the increase in solid density around the ATR probe head. The larger crystals are harder to suspend and accumulate closer to the bottom where the probe head is situated. ATR-IR is considered to be uninfluenced by solid particles^{56,61,62} because of the shallow penetration depth of the evanescent wave.^{56,63,64} With a sufficient solid loading, however, there was a significant influence in our experiments depending on the crystal size and the agitation rate.

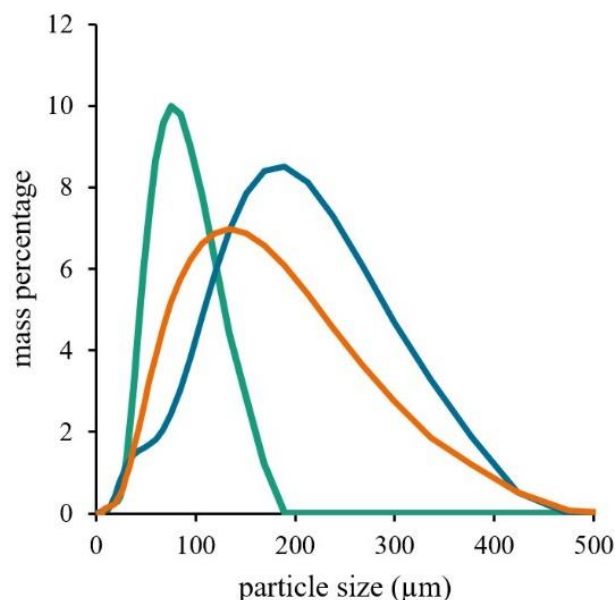


Figure 8. Size distribution determined via laser diffraction of the seed crystals (green), SBRC1 (blue), and SBRC2 (orange).

Even though an increased signal noise is also present in SBRC1, the influence is most likely stronger in SBRC2 because of the overall smaller particle size of $137\ \mu\text{m}$ (Figure 8).

The smaller $D(4,3)$ of SBRC2, with $137\ \mu\text{m}$, compared to that of SBRC1 can partially be explained by the 50% increase of crystallisation time and the, therefore, increased chance of crystal breakage.⁵⁹ The decrease in the crystal size with the decrease in the seed crystal mass indicates that the crystallisation time and the crystal breakage that occurs play a major role in determining the crystal size for this system under the experimental conditions. Preliminary SBRC experiments carried out at a 500 rpm stirrer speed resulted in an even finer product. This indicates that a reduction of stirrer speed can increase the product size for this system. A further reduction of the stirrer speed, from 250 rpm down to 150 rpm for example, is, however, not possible. This was seen during RD2, where at 150 rpm the dwell time of the coarser crystals at the bottom of the vessel increased to an unacceptable level for SBRC. It seems as if a reduction in crystal breakage could only be achieved by redesigning the stirrer unit.

SBRC with Active Dosing Rate Control. The calculation of the dosing rate based on calibration data is a fast and less resource-consuming way of SBRC operation, but this type of operation can have several issues. The dosing rate is calculated based on the calibration of the crystallisation rate, the calibration of the solid-doser unit, and the assumed crystal surface of the seed crystals after partial dissolution. Each of these factors can deviate from the expected value during the actual crystallisation experiment. It is, therefore, very difficult to obtain

exactly the supersaturation aimed at. It is necessary to make allowance for this uncertainty to prevent a nucleation shower because of excess supersaturation. As a result, the supersaturation and, thus, the crystallisation rate might not be optimal, and longer crystallisation times are necessary. If the solution concentration is actively monitored and the solid-doser is linked to a control unit, the dosing rate can be adjusted based on the solution concentration. Thus, by utilising the full potential of PAT, the dosing rate can be adjusted to the solid deposition rate during crystallisation. This could be used to set a specific low supersaturation, which would be relevant, for example, for polymorph control^{65,66} or crystal quality improvement.^{67,68} It, furthermore, facilitates the crystallisation operation in a steady state, which improves the crystal quality and enables one to operate close to the metastable limit to maximise the crystallisation rate. Two possible strategies for automated dosing regulation have been simulated by manual addition of solid to the crystallisation mixture. In CSBRC1, [CL-20] was kept within two concentration limits (hysteresis) as is common with feedback control. In CSBRC2, [CL-20] was regulated hysteresis free as is common for feedforward control.^{69,70} Segments of the two [CL-20] progressions during the experiments are displayed in Figure 9. Because of the lower risk of local supersaturation in CSBRC2, a higher supersaturation was applied. CSBRC1 and 2 are short (about 1.5 h) simulations of possible SBRC experiments with automated active dosing rate control, and no crystalline product was obtained from these tests.

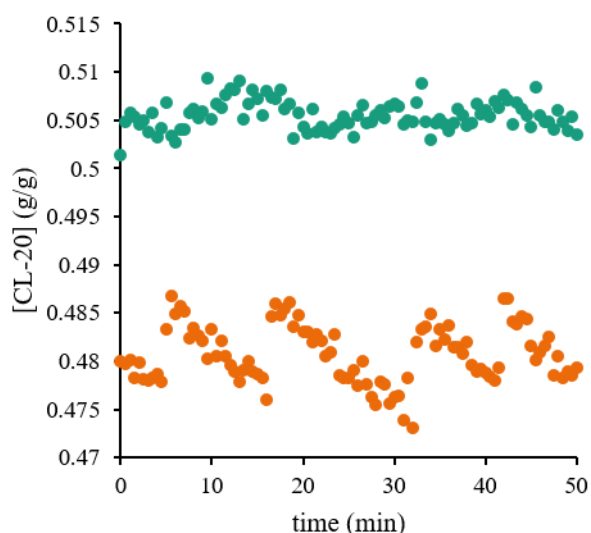


Figure 9. [CL-20] progression during CSBRC1 (orange) and CSBRC2 (green).

These short experiments can be seen as a proof of concept to demonstrate how solid-dosing can be used in conjunction with PAT to automate SBRC and tailor it to the specific needs of the cocrystal system.

Comparison to Existing Crystallisation Methods.

In the following, crystal quality and CL-20 efficiency of SBRC are compared to batch RC and antisolvent crystallisation, because batch RC is the crystallisation method of highest efficiency, while the best crystal quality was achieved by antisolvent crystallisation. The four cocrystal batches compared below are all more than 99.9% pure cocrystal according to Rietveld analysis, and all show no traces of CL-20 or HMX impurities in their Raman spectra. The detection limit of the Raman analysis in this case is 0.5% HMX/CL20. The best way to compare the quality obtained is to compare the crystal morphologies and the amount of inclusions in the crystals. By immersing the crystals in an optically similarly dense liquid, the surface refraction of the crystals is reduced and the internal defects are highlighted (Figure 10).

The crystal density can serve as a tool for assessing the crystal quality in conjunction with the solvent inclusion values and the optical analysis. In Table 3, the solvent inclusion and density values for SBRC1, SBRC2, antisolvent crystallisation, and batch RC experiments are displayed. A more in-depth and statistically sound quality assessment will be published elsewhere. Figure 10 and the values in Table 3 clearly indicate that the SBRC crystal quality is very close to the quality obtained from antisolvent crystallisation. Crystal density and solvent inclusions of antisolvent crystallisation and SBRC are indistinguishable considering the measurement error. The visual analysis of the crystals also shows that no drastic differences exist

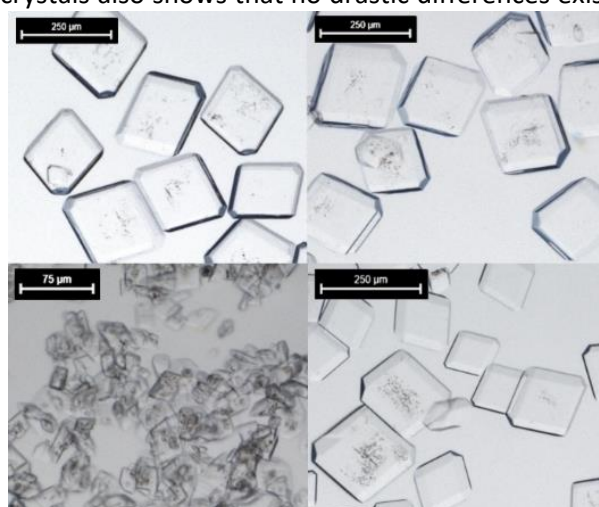


Figure 10. Crystal quality comparison of SBRC1 (top left), SBRC2 (top right), batch RC (bottom left), and antisolvent crystallization (bottom right). The crystals are immersed in a mixture of 1-methyl naphthalene and decan (8:1) to highlight the internal defects of the crystals.

Table 3. Solvent Inclusion and Density Values of Crystal from SBRC and Reference Experiments

| | solvent inclusion (%) | density (g cm ⁻³) |
|-------------|-----------------------|-------------------------------|
| SBRC1 | 0.01 | 1.9545±0.0003 |
| SBRC2 | 0.01 | 1.9544±0.0003 |
| antisolvent | 0.01 | 1.9546±0.0014 |
| batch RC | 0.19 | 1.9533±0.0003 |

in morphology or visual inclusion content between antisolvent and SBRC crystals. The smaller particle size of SBRC2 might be correlated to the layered appearance of the obtained crystals (Figure 10). Some external factors such as humidity or chemical impurities might have induced this crystal morphology. This morphology may facilitate crystal breakage, which would explain the smaller D(4,3).

The CL-20 efficiencies for the major crystallisation techniques capable of producing high-quality cocrystals are presented in Table 4 alongside a qualitative assessment of the solution recyclability (which would increase the method's efficiency, but is not always desired⁷¹). Solid-dosing leads to a 10 times more efficient SBRC experiment than liquid-dosing and SBRC is over two times more efficient than solvent evaporation. The calculations of the SBRC efficiencies and comments on the solution recyclability are found in the supporting information. The CL-20 efficiency of SBRC is dependent on the solid loading. Increasing it would also increase the CL-20 efficiency, but the solid loading is already twice as high as generally recommended for solution crystallisation and higher values might be detrimental to the achievable crystal size.⁵⁹ This value was chosen as a compromise between efficiency and obtainable crystal size.

Table 4. CL-20 Efficiency and Solution Recyclability of Methods for Generating the CL-20/HMX Cocrystal

| crystallisation method | CL-20 efficiency | solution recyclability |
|---------------------------------|------------------|------------------------|
| Liquid-dosing SBRC ^a | 0.06 | - |
| cooling ^b | 0.14 | ++ |
| antisolvent ^b | 0.25 | -- |
| evaporation ^a | 0.26 | + |
| Solid-dosing SBRC | 0.63 | ++ |

^a Calculated value.

^b Experimental value taken from ref 19.

Conclusion

Here we reported the first successful scale up of high-quality coarse CL-20/HMX cocrystal. The obtained particle size of 163 μm and the batch size of 120 g are sufficient for the production of enough cocrystal in an acceptable time frame for the test in

high performance polymer-bonded explosive charges. The crystal quality, as evidenced by the particle density and solvent inclusion values, is close to the crystal quality obtained from laboratory-scale antisolvent experiments. As it stands, SBRC is the most efficient crystallisation technique of the CL-20/HMX cocrystal by a margin of 2.4. It is the only method capable of producing cocrystal of high-quality with an acceptable CL-20 efficiency in the 100 g-range. This technique is easily applicable to other cocrystal systems where high-quality crystals and adjustable crystal size are required and can serve as an efficient way to scale up cocrystal production of cofomers with significant solubility difference.

Supporting information

Efficiency calculation of liquid and solid-dosing SBRC and comment on the solution recyclability dosing rate calculation

FUNDING SOURCE

This work was supported by the German Ministry of Defence.

References

- (1) Blagden, N.; Berry, D. J.; Parkin, A.; Javed, H.; Ibrahim, A.; Gavan, P. T.; Matos, L. L. D.; Seaton, C. C. Current directions in co-crystal growth. *New J. Chem.* 2008, 32 (10), 1659. DOI: 10.1039/B803866J.
- (2) Bolla, G.; Nangia, A. Pharmaceutical cocrystals: walking the talk. *Chem. Commun.* 2016, 52 (54), 8342–8360. DOI: 10.1039/c6cc02943d.
- (3) Raheem Thayyil, A.; Juturu, T.; Nayak, S.; Kamath, S. Pharmaceutical Co-Crystallization: Regulatory Aspects, Design, Characterization, and Applications. *Adv. Pharm. Bull.* 2020, 10 (2), 203–212. DOI: 10.34172/apb.2020.024.
- (4) Landenberger, K. B.; Bolton, O.; Matzger, A. J. Two isostructural explosive cocrystals with significantly different thermodynamic stabilities. *Angew. Chem., Int. Ed. Engl.* 2013, 52 (25), 6468–6471. DOI: 10.1002/anie.201302814.
- (5) Bolton, O.; Matzger, A. J. Improved stability and smart-material functionality realized in an energetic cocrystal. *Angew. Chem., Int. Ed. Engl.* 2011, 50 (38), 8960–8963. DOI: 10.1002/anie.201104164.
- (6) Bolton, O.; Simke, L. R.; Pagoria, P. F.; Matzger, A. J. High Power Explosive with Good Sensitivity: A 2:1 Cocrystal of CL-20:HMX. *Cryst. Growth Des.* 2012, 12 (9), 4311–4314. DOI: 10.1021/cg3010882.
- (7) Landenberger, K. B.; Bolton, O.; Matzger, A. J. Energetic-Energetic Cocrystals of Diacetone Diperoxide (DADP): Dramatic and Divergent

- Sensitivity Modifications via Cocrystallization. *J. Am. Chem. Soc.* 2015, *137* (15), 5074–5079. DOI: 10.1021/jacs.5b00661.
- (8) Jiang, H.; Hu, W. The Emergence of Organic Single-Crystal Electronics. *Angew. Chem., Int. Ed. Engl.* 2020, *59* (4), 1408–1428. DOI: 10.1002/anie.201814439.
- (9) Sun, L.; Zhu, W.; Yang, F.; Li, B.; Ren, X.; Zhang, X.; Hu, W. Molecular cocrystals: design, charge-transfer and optoelectronic functionality. *Phys. Chem. Chem. Phys.* 2018, *20* (9), 6009–6023. DOI: 10.1039/c7cp07167a.
- (10) Wang, Y.; Zhu, W.; Dong, H.; Zhang, X.; Li, R.; Hu, W. Organic Cocrystals: New Strategy for Molecular Collaborative Innovation. *Top. Curr. Chem.* 2016, *374* (6), 83. DOI: 10.1007/s41061-016-0081-8.
- (11) Zhang, J.; Xu, W.; Sheng, P.; Zhao, G.; Zhu, D. Organic Donor-Acceptor Complexes as Novel Organic Semiconductors. *Acc. Chem. Res.* 2017, *50* (7), 1654–1662. DOI: 10.1021/acs.accounts.7b00124.
- (12) Zhang, C.; Cao, Y.; Li, H.; Zhou, Y.; Zhou, J.; Gao, T.; Zhang, H.; Yang, Z.; Jiang, G. Toward low-sensitive and high-energetic cocrystal I: evaluation of the power and the safety of observed energetic cocrystals. *CrystEngComm* 2013, *15* (19), 4003. DOI: 10.1039/c3ce40112j.
- (13) Liu, G.; Wei, S.-H.; Zhang, C. Review of the Intermolecular Interactions in Energetic Molecular Cocrystals. *Cryst. Growth Des.* 2020, *20* (10), 7065–7079. DOI: 10.1021/acs.cgd.0c01097.
- (14) Bu, R.; Xiong, Y.; Zhang, C. π - π Stacking Contributing to the Low or Reduced Impact Sensitivity of Energetic Materials. *Cryst. Growth Des.* 2020, *20* (5), 2824–2841. DOI: 10.1021/acs.cgd.0c00367.
- (15) Bu, R.; Xiong, Y.; Wei, X.; Li, H.; Zhang, C. Hydrogen Bonding in CHON-Containing Energetic Crystals: A Review. *Cryst. Growth Des.* 2019, *19* (10), 5981–5997. DOI: 10.1021/acs.cgd.9b00853.
- (16) Nair, U. R.; Sivabalan, R.; Gore, G. M.; Geetha, M.; Asthana, S. N.; Singh, H. Hexanitrohexaazaisowurtzitane (CL-20) and CL-20-based formulations (review). *Combust., Explos. Shock Waves* 2005, *41* (2), 121–132. DOI: 10.1007/s10573-005-0014-2.
- (17) Johnson, N. C. *CL-20 sensitivity round robin*.
- (18) Anderson, S. R.; am Ende, D. J.; Salan, J. S.; Samuels, P. Preparation of an Energetic-Energetic Cocrystal using Resonant Acoustic Mixing. *Propellants., Explos., Pyrotech.* 2014, *39* (5), 637–640. DOI: 10.1002/prop.201400092.
- (19) Herrmannsdörfer, D.; Gerber, P.; Heintz, T.; Herrmann, M. J.; Klapötke, T. M. Investigation Of Crystallisation Conditions to Produce CL-20/HMX Cocrystal for Polymer-bonded Explosives. *Propellants., Explos., Pyrotech.* 2019, *44* (6), 668–678. DOI: 10.1002/prop.201800332.
- (20) Zhang, S.; Zhang, J.; Kou, K.; Jia, Q.; Xu, Y.; Zerraza, S.; Liu, N.; Hu, R. Investigation on the dissolution behavior of 2HNIW·HMX co-crystal prepared by a solvent/non-solvent method in N,N-dimethylformamide at T = (298.15–318.15) K. *J. Therm. Anal. Calorim.* 2019, *135* (6), 3363–3373. DOI: 10.1007/s10973-018-7502-6.
- (21) Spitzer, D.; Risse, B.; Schnell, F.; Pichot, V.; Klaumünzer, M.; Schaefer, M. R. Continuous engineering of nano-cocrystals for medical and energetic applications. *Sci. Rep.* 2014, *4*, 6575. DOI: 10.1038/srep06575.
- (22) Doblas, D.; Rosenthal, M.; Burghammer, M.; Chernyshov, D.; Spitzer, D.; Ivanov, D. A. Smart Energetic Nanosized Co-Crystals: Exploring Fast Structure Formation and Decomposition. *Cryst. Growth Des.* 2016, *16* (1), 432–439. DOI: 10.1021/acs.cgd.5b01425.
- (23) An, C.; Li, H.; Ye, B.; Wang, J. Nano-CL-20/HMX Cocrystal Explosive for Significantly Reduced Mechanical Sensitivity. *J. Nanomater.* 2017, *2017* (5), 1–7. DOI: 10.1155/2017/3791320.
- (24) Sun, S.; Zhang, H.; Liu, Y.; Xu, J.; Huang, S.; Wang, S.; Sun, J. Transitions from Separately Crystallized CL-20 and HMX to CL-20/HMX Cocrystal Based on Solvent Media. *Cryst. Growth Des.* 2018, *18* (1), 77–84. DOI: 10.1021/acs.cgd.7b00775.
- (25) Ghosh, M.; Sikder, A. K.; Banerjee, S.; Gonnade, R. G. Studies on CL-20/HMX (2:1) Cocrystal: A New Preparation Method and Structural and Thermokinetic Analysis. *Cryst. Growth Des.* 2018, *18* (7), 3781–3793. DOI: 10.1021/acs.cgd.8b00015.
- (26) Gao, B.; Wang, D.; Zhang, J.; Hu, Y.; Shen, J.; Wang, J.; Huang, B.; Qiao, Z.; Huang, H.; Nie, F.; Yang, G. Facile, continuous and large-scale synthesis of CL-20/HMX nano co-crystals with high-performance by ultrasonic spray-assisted electrostatic adsorption method. *J. Mater. Chem. A* 2014, *2* (47), 19969–19974. DOI: 10.1039/C4TA04979A.
- (27) Qiu, H.; Patel, R. B.; Damavarapu, R. S.; Stepanov, V. Nanoscale 2CL-20-HMX high explosive cocrystal synthesized by bead milling. *CrystEngComm* 2015, *17* (22), 4080–4083. DOI: 10.1039/c5ce00489f.
- (28) Alhalaweh, A.; Velaga, S. P. Formation of Cocrystals from Stoichiometric Solutions of Incongruently Saturating Systems by Spray Drying. *Cryst. Growth Des.* 2010, *10* (8), 3302–3305. DOI: 10.1021/cg100451q.

- (29) Rodríguez-Hornedo, N.; Nehm, S. J.; Seefeldt, K. F.; Pagan-Torres, Y.; Falkiewicz, C. J. Reaction crystallization of pharmaceutical molecular complexes. *Mol. Pharmaceutics* 2006, 3 (3), 362–367. DOI: 10.1021/mp050099m.
- (30) Rodrigues, M.; Baptista, B.; Lopes, J. A.; Sarraguça, M. C. Pharmaceutical cocrystallization techniques. Advances and challenges. *Int. J. Pharm.* 2018, 547 (1-2), 404–420. DOI: 10.1016/j.ijpharm.2018.06.024.
- (31) Takata, N.; Shiraki, K.; Takano, R.; Hayashi, Y.; Terada, K. Cocrystal Screening of Stanolone and Mestanolone Using Slurry Crystallization. *Cryst. Growth Des.* 2008, 8 (8), 3032–3037. DOI: 10.1021/cg800156k.
- (32) Zhang, G. G. Z.; Henry, R. F.; Borchardt, T. B.; Lou, X. Efficient co-crystal screening using solution-mediated phase transformation. *J. Pharm. Sci.* 2007, 96 (5), 990–995. DOI: 10.1002/jps.20949.
- (33) Childs, S. L.; Rodríguez-Hornedo, N.; Reddy, L. S.; Jayasankar, A.; Maheshwari, C.; McCausland, L.; Shipplett, R.; Stahly, B. C. Screening strategies based on solubility and solution composition generate pharmaceutically acceptable cocrystals of carbamazepine. *CrystEngComm* 2008, 10 (7), 856–864. DOI: 10.1039/b715396a.
- (34) Chen, J.; Sarma, B.; Evans, J. M. B.; Myerson, A. S. Pharmaceutical Crystallization. *Cryst. Growth Des.* 2011, 11 (4), 887–895. DOI: 10.1021/cg101556s.
- (35) Saleemi, A. N.; Steele, G.; Pedge, N. I.; Freeman, A.; Nagy, Z. K. Enhancing crystalline properties of a cardiovascular active pharmaceutical ingredient using a process analytical technology based crystallization feedback control strategy. *Int. J. Pharm.* 2012, 430 (1-2), 56–64. DOI: 10.1016/j.ijpharm.2012.03.029.
- (36) Simone, E.; Zhang, W.; Nagy, Z. K. Analysis of the crystallization process of a biopharmaceutical compound in the presence of impurities using process analytical technology (PAT) tools. *J. Chem. Technol. Biotechnol.* 2016, 91 (5), 1461–1470. DOI: 10.1002/jctb.4743.
- (37) Douroumis, D.; Ross, S. A.; Nokhodchi, A. Advanced methodologies for cocrystal synthesis. *Adv. Drug Delivery Rev.* 2017, 117, 178–195. DOI: 10.1016/j.addr.2017.07.008.
- (38) Bouma, R. H. B.; van der Heijden, A. E. D. M. The Effect of RDX Crystal Defect Structure on Mechanical Response of a Polymer-Bonded Explosive. *Propellants., Explos., Pyrotech.* 2016, 41 (3), 484–493. DOI: 10.1002/prep.201500222.
- (39) Lindstrom, I. E. Planar Shock Initiation of Porous Tetryl. *J. Appl. Phys.* 1970, 41 (1), 337–350. DOI: 10.1063/1.1658345.
- (40) Maksimowski, P.; Skupiński, W.; Szczygielska, J. Comparison of the Crystals Obtained by Precipitation of CL-20 with Different Chemical Purity. *Propellants., Explos., Pyrotech.* 2013, 38 (6), 791–797. DOI: 10.1002/prep.201300064.
- (41) Baer, M. R. Modeling heterogeneous energetic materials at the mesoscale. *Thermochim. Acta* 2002, 384 (1-2), 351–367. DOI: 10.1016/S0040-6031(01)00794-8.
- (42) Borne, L. Influence of intragranular cavities of RDX particle batches on the sensitivity of cast wax bonded explosives. In *Tenth Symposium (International) on Detonation*, 1993; 286–293.
- (43) Field, J. E. Hot spot ignition mechanisms for explosives. *Acc. Chem. Res.* 1992, 25 (11), 489–496. DOI: 10.1021/ar00023a002.
- (44) Chen, T.-H.; Yeh, K. L.; Chen, C. W.; Lee, H. L.; Hsu, Y. C.; Lee, T. Mixing Effect on Stoichiometric Diversity in Benzoic Acid–Sodium Benzoate Cocrystals. *Cryst. Growth Des.* 2019, 19 (3), 1576–1583. DOI: 10.1021/ACS.CGD.8B01220.
- (45) Kudo, S.; Takiyama, H. Production method of carbamazepine/saccharin cocrystal particles by using two solution mixing based on the ternary phase diagram. *J. Cryst. Growth* 2014, 392, 87–91. DOI: 10.1016/j.jcrysgro.2014.02.003.
- (46) Nishimaru, M.; Kudo, S.; Takiyama, H. Effect of Two Kinds of Supersaturation on Crystal Qualities during Cocrystallization. *J. Chem. Eng. Japan* 2019, 52 (6), 579–585. DOI: 10.1252/jcej.18we281.
- (47) Powell, K. A.; Croker, D. M.; Rielly, C. D.; Nagy, Z. K. PAT-based design of agrochemical cocrystallization processes: A case-study for the selective crystallization of 1:1 and 3:2 co-crystals of p-toluenesulfonamide/triphenylphosphine oxide. *Chem. Eng. Sci.* 2016, 152, 95–108. DOI: 10.1016/j.ces.2016.06.005.
- (48) Powell, K. A.; Bartolini, G.; Wittering, K. E.; Saleemi, A. N.; Wilson, C. C.; Rielly, C. D.; Nagy, Z. K. Toward Continuous Crystallization of Urea-Barbituric Acid: A Polymorphic Co-Crystal System. *Cryst. Growth Des.* 2015, 15 (10), 4821–4836. DOI: 10.1021/acs.cgd.5b00599.
- (49) Chew, W.; Sharratt, P. Trends in process analytical technology. *Anal. Methods* 2010, 2 (10), 1412. DOI: 10.1039/c0ay00257g.
- (50) Pomerantsev, A. L.; Rodionova, O. Y. Process analytical technology: a critical view of the chemometricians. *J. Chemom.* 2012, 26 (6), 299–310. DOI: 10.1002/cem.2445.
- (51) Barnes, R. J.; Dhanoa, M. S.; Lister, S. J. Correction to the Description of Standard Normal Variate (SNV) and De-Trend (DT) Transformations in Practical Spectroscopy with Applications in Food and Beverage Analysis—2 nd Edition. *NIR news* 1994, 5 (3), 6. DOI: 10.1255/nirn.248.

- (52) Tauler, R.; Walczak, B.; Brown, S. D. *Comprehensive Chemometrics: Chemical and Biochemical Data Analysis*; Elsevier, 2009.
- (53) Wold, S.; Sjöström, M.; Eriksson, L. PLS-regression: a basic tool of chemometrics. *Chemom. Intell. Lab. Syst.* 2001, 58 (2), 109–130. DOI: 10.1016/S0169-7439(01)00155-1.
- (54) Sherwood, J. N.; Shripathi, T. Role of dislocations in the growth of single crystals of potash alum. *Faraday Discuss* 1993, 95 (0), 173. DOI: 10.1039/FD9939500173.
- (55) Sherwood, J. N.; Shripathi, T. Evidence for the role of pure edge dislocations in crystal growth. *J. Cryst. Growth* 1988, 88 (3), 358–364. DOI: 10.1016/0022-0248(88)90008-5.
- (56) Togkalidou, T.; Fujiwara, M.; Patel, S.; Braatz, R. D. Solute concentration prediction using chemometrics and ATR-FTIR spectroscopy. *J. Cryst. Growth* 2001, 231 (4), 534–543. DOI: 10.1016/S0022-0248(01)01518-4.
- (57) Gagniere, E.; Mangin, D.; Puel, F.; Valour, J.-P.; Klein, J.-P.; Monnier, O. Cocrystal formation in solution: Inducing phase transition by manipulating the amount of cocrystallizing agent. *J. Cryst. Growth* 2011, 316 (1), 118–125. DOI: 10.1016/j.jcrysgro.2010.12.027.
- (58) Gagniere, E.; Mangin, D.; Puel, F.; Bebon, C.; Klein, J.-P.; Monnier, O.; Garcia, E. Cocrystal Formation in Solution: In Situ Solute Concentration Monitoring of the Two Components and Kinetic Pathways. *Cryst. Growth Des.* 2009, 9 (8), 3376–3383. DOI: 10.1021/cg801019d.
- (59) Hofmann, G. *Kristallisation in der industriellen Praxis*; Wiley-VCH, 2005. DOI: 10.1002/3527602739.
- (60) Janse, A. H. Nucleation and crystal growth in batch crystallizers. Thesis, 1977.
- (61) Dunuwila, D. D.; Berglund, K. A. ATR FTIR spectroscopy for in situ measurement of supersaturation. *J. Cryst. Growth* 1997, 179 (1-2), 185–193. DOI: 10.1016/S0022-0248(97)00119-X.
- (62) Dunuwila, D. D.; Carroll, L. B.; Berglund, K. A. An investigation of the applicability of attenuated total reflection infrared spectroscopy for measurement of solubility and supersaturation of aqueous citric acid solutions. *J. Cryst. Growth* 1994, 137 (3-4), 561–568. DOI: 10.1016/0022-0248(94)90999-7.
- (63) Nagy, Z. K.; Braatz, R. D. Advances and new directions in crystallization control. *Annu. Rev. Chem. Biomol. Eng.* 2012, 3 (1), 55–75. DOI: 10.1146/annurev-chembioeng-062011-081043.
- (64) Ahmad, M.; Hench, L. L. Effect of taper geometries and launch angle on evanescent wave penetration depth in optical fibers. *Biosens. Bioelectron.* 2005, 20 (7), 1312–1319. DOI: 10.1016/j.bios.2004.04.026.
- (65) Kee, N. C. S.; Arendt, P. D.; Tan, R. B. H.; Braatz, R. D. Selective Crystallization of the Metastable Anhydrate Form in the Enantiotropic Pseudo-Dimorph System of L-Phenylalanine using Concentration Feedback Control. *Cryst. Growth Des.* 2009, 9 (7), 3052–3061. DOI: 10.1021/cg8006537.
- (66) Kee, N. C. S.; Tan, R. B. H.; Braatz, R. D. Selective Crystallization of the Metastable α -Form of L-Glutamic Acid using Concentration Feedback Control. *Cryst. Growth Des.* 2009, 9 (7), 3044–3051. DOI: 10.1021/cg800546u.
- (67) Mullin, J. W. *Crystallization*, 4. rev.; Elsevier professional, 2001.
- (68) Kim, D.-Y.; Kim, K.-J. Correlation between quantity of defect and supersaturation in RDX crystallization using γ -butyrolactone and water as solvent. *Chem. Eng. Res. Des.* 2010, 88 (11), 1461–1466. DOI: 10.1016/j.cherd.2009.08.012.
- (69) Oosting, K. W. Simulation of Control Strategies for a Two Degree-of-Freedom Lightweight Flexible Robotic Arm. Thesis, Georgia Institute of Technology, Georgia, 1987.
- (70) Alberts, T.E. Augmenting the Control of A Flexible Manipulator with Passive Mechanical Damping. Thesis, Georgia Institute of Technology, Georgia, 1986.
- (71) Sheikh, A. Y.; Rahim, S. A.; Hammond, R. B.; Roberts, K. J. Scalable solution cocrystallization: case of carbamazepine-nicotinamide I. *CrystEngComm* 2009, 11 (3), 501–509. DOI: 10.1039/b813058b.

Semibatch Reaction Crystallisation for Scaled-up Production of High-Quality CL-20/HMX Cocystal: Efficient because of Solid-Dosing

Dirk Herrmannsdörfer,^{[a]*} Thomas M. Klapötke^[b]

[a] *Energetic Materials Fraunhofer Institute for Chemical Technology ICT Joseph-von-Fraunhofer-Str. 7 76327 Pfinztal, Germany*

[b] *Department of Chemistry Energetic Materials Research Ludwig-Maximilians University of Munich Butenandtstr. 5 - 13 (Haus D) 81377 Munich, Germany*

*Corresponding Author: dirk.herrmannsdoerfer@ict.fraunhofer.de

Content

[Efficiency calculation of liquid dosing SBRC and comment on the solution recyclability](#)

[Efficiency calculation of solid-dosing SBRC and comment on the solution recyclability](#)

[Dosing rate calculation](#)

Efficiency calculation of liquid dosing SBRC and comment on the solution recyclability

Liquid dosing is at least partially limited by the solubilities of the cocrystal cofomers. Assuming no supersaturated solutions are utilised, the maximum efficiency can be achieved by mixing a solutions of composition 0.42 g(CL-20) g⁻¹(ACN) and 0.056 g(HMX) g⁻¹(ACN) and a solution of composition 1.04 g(CL-20) g⁻¹(ACN) and 0.006 g(HMX) g⁻¹(ACN). These are the solution compositions at TP1 and TP2 (Figure S1). Eight mixing ratios were tested to determine the maximum CL-20 efficiency achievable. The solution compositions after mixing c_0 , the solution composition after equilibration c^* and the CL-20 efficiency are displayed in Table S1. The CL-20 efficiency is calculated as:

$$\text{CL-20 efficiency} = (c_0 - c^*) c_0^{-1}$$

Figure S1 presents the solution composition equilibration of the eight solution mixtures. A direct recycling of the solution is not possible, because at c^* [CL-20] and [HMX] are intermediate values between the TP. A refreshing of the solution can either be performed by adding HMX or CL-20 to the solution, or by evaporating the solution until TP2 is reached. Both methods of solution refurbishing require the application of another cocrystallisation technique (solid-dosing SBRC or evaporation crystallisation). The solution of this method is, thus, hard to recycle.

Table S1. Composition and efficiency data of the liquid dosing SBRC

| mixing ratio | $c_0/g\ g^{-1}$ | | $c^*/g\ g^{-1}$ | | CL-20 efficiency |
|--------------|-----------------|-------|-----------------|-------|------------------|
| | CL-20 | HMX | CL-20 | HMX | |
| 9:1 | 0.482 | 0.051 | 0.463 | 0.045 | 4.0% |
| 8:2 | 0.544 | 0.046 | 0.513 | 0.036 | 5.7% |
| 7:3 | 0.606 | 0.041 | 0.567 | 0.028 | 6.5% |
| 6:4 | 0.668 | 0.036 | 0.626 | 0.022 | 6.3% |
| 5:5 | 0.730 | 0.031 | 0.690 | 0.018 | 5.5% |
| 4:6 | 0.792 | 0.026 | 0.758 | 0.015 | 4.2% |
| 3:7 | 0.854 | 0.021 | 0.827 | 0.012 | 3.2% |
| 2:8 | 0.916 | 0.016 | 0.898 | 0.010 | 2.0% |

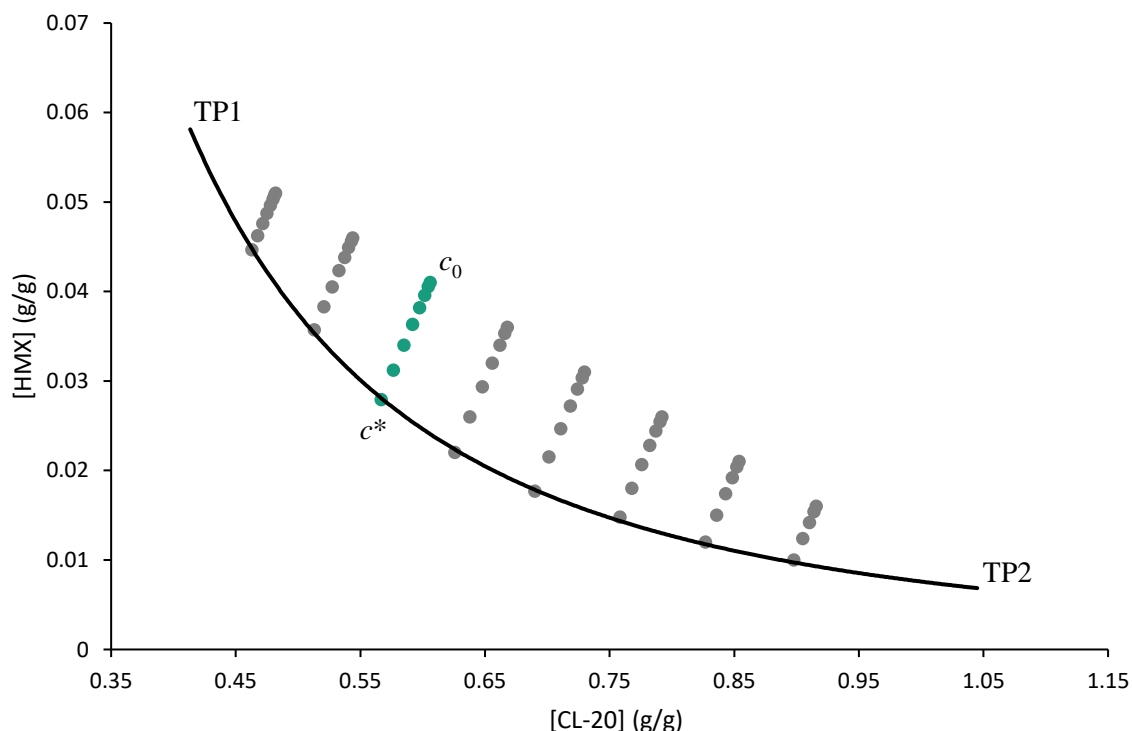


Figure S1: Visualisation of the solution equilibration of the eight solution mixtures. The black curve represents the cocrystal solubility curve. The solution concentration progression of the mixing ratio 7:3 is visualised in green. c_0 is the solution composition after mixture. By crystallisation of the CL-20/HMX cocrystal, the supersaturation is reduced until the solution concentration c^* is reached.

Efficiency calculation of solid-dosing SBRC and comment on the solution recyclability

In contrast to liquid dosing SBRC, solid-dosing SBRC is far less limited by the solubilities of the cocrystal cofomers. The CL-20 efficiency is calculated by dividing the CL-20 found in the obtained cocrystal by the total CL-20 input. For the experiments described in the paper, the total CL-20 input is 148.6 g (53g(solution composition) +5.6g(seed crystals) +90g(solid-dosing)) and the CL-20 found in the obtained cocrystal is 95g (90g(solid-dosing)+ about 4g (seed crystals)). A CL-20 efficiency of 63% is, therefore, reached. After complete crystallisation, the solution composition is c^* . To recycle the solution, it is only required to add ACN until the desired solution concentration is achieved for the desired partial dissolution of the seed crystals. The solution is, thus, easy to recycle.

Dosing rate calculation

In the following, a simplified version of the dosing rate calculation is performed. The following simplifications have been applied. It was assumed that the seed crystals are uniform in size, that the seed crystals are of cubic shape and that no nucleation occurs during the crystallisation experiment. With the exception of the assumption of uniform size of the seed crystals, the other simplifications were also applied to the calculations of the dosing rates of SBRC1. The error arising from ignoring the seed crystal form factor is small, because the same simplification has been applied to the calculation of R_G . The errors cancel each other out to a large degree. To be able to accurately account for nucleation during the experiment requires additional PAT hardware such as an FMBR probe and the application of population balance. For SBRC2, the seed crystal mass was reduced to counteract the increase of crystals.

The calculation is based on the following predefined or predetermined constants.

| product crystal size (cm) | product crystal mass (g) | product crystal density (g cm ⁻³) | seed crystal size (cm) | seed crystal R_G (g min ⁻¹ cm ⁻²) | seed crystal mass (g) | seed crystal # of crystals |
|---------------------------|--------------------------|---|------------------------|--|-----------------------|----------------------------|
| 0.02 | 100 | 1.95 | 0.008 | -2.04E-05 | 6.4 | 6410256 |

Based on these values the total seed crystal surface can be calculated. A feasible way of carrying out the SBRC is to define intervals of constant dosing rate. This eliminates the need for external controllers of the dosing unit. Time intervals of 2 hour were chosen because of the limited number of possible program steps of the solid-doser. With the total crystal surface and the interval time, the dosing rate can be calculated from R_G (Table S2).

Table S2. Calculated data for the determination of the dosing rates during SBRC

| total mass (g) | m (one crystal) (g) | V (one crystal)(cm ³) | crystal size(cm) | A (one crystal) (cm ²) | A_{total} (cm ²) | dosing rate (g h ⁻¹) |
|----------------|-----------------------|-------------------------------------|------------------|--------------------------------------|--------------------------------|----------------------------------|
| 6.4 | 1.0E-06 | 5.1E-07 | 0.008 | 0.0004 | 2462 | 3.0 |
| 12.4 | 1.9E-06 | 9.9E-07 | 0.010 | 0.0006 | 3831 | 4.7 |
| 21.8 | 3.4E-06 | 1.7E-06 | 0.012 | 0.0009 | 5573 | 6.8 |
| 35.4 | 5.5E-06 | 2.8E-06 | 0.014 | 0.0012 | 7706 | 9.4 |
| 54.3 | 8.5E-06 | 4.3E-06 | 0.016 | 0.0016 | 10241 | 12.5 |
| 79.4 | 1.2E-05 | 6.4E-06 | 0.019 | 0.0021 | 13190 | 16.1 |
| 111.7 | 1.7E-05 | 8.9E-06 | 0.021 | 0.0026 | 16559 | 20.3 |

8 Conclusion

Beginning with RQ1, the way towards an answer was concentrated in WP1:

“Suitable analytical methods must be identified or developed in order to be able to quantify and compare the chemical purity, the phase purity and the crystal defects of the crystals from samples even on a laboratory-scale.”

Prior to the work published in the first quality assessment paper (chapter 5.1), the precision limit of the density determined by helium pycnometry was unpublished or even unknown. By identifying the factors influencing the measurements and taking them into account in the data analysis, differences of 0.001 g cm^{-3} can be resolved. This means for the CL-20/HMX cocrystal, samples of a density difference of less than 0.05% are distinguishable. Therefore, a measurement and analysis method for helium pycnometry measurements was established for the first time that enables the differentiation of samples with statistical backing and certainty. This method is tremendously useful for any quality analysis carried out using helium pycnometry in most disciplines. The usefulness of this level of precision for distinguishing the crystal defects of the cocrystal was tested in the second quality assessment paper (chapter 5.2). Here, it was found that the batch RC sample was only about 0.001 g cm^{-3} less dense than the SBRC samples. In combination with the 0.19% solvent inclusion for the batch RC sample, it can be concluded that the too low density difference is the result of higher amounts of gas inclusions in the SBRC samples compared to the batch RC sample. The 0.001 g cm^{-3} higher density of the SBRC4 sample might also be the result of less gas inclusions compared to the other SBRC samples. This shows that the precision of the density measurements achieved is just sufficient for crystal defect analysis of the cocrystal, but only for samples on the pilot plant-scale. This is because a sample mass of approximately 10 g is required to fill the 10 cm^3 sample cup. This is required in order to achieve the determined level of precision. For laboratory-scale samples, only about 1 g is obtained. The measurement error for the 1 cm^3 sample cup is about five times larger for the pycnometer used. Pycnometers specifically designed for smaller samples are available. Assuming that the sampling error and the error due to the barometric pressure drift are transferable, the increased weighing error of 1 g compared to 10 g will result in an overall measurement error of a 1 g sample in such a pycnometer that is twice as high as that of a 10 g

sample in the pycnometer used in this study. But, if sufficient care is taken and a laboratory micro balance is used, the weighing error can be reduced enough that batches on the laboratory-scale should be able to be differentiated with the same precision as batches on the pilot plant-scale. For digital image processing, however, the sample size is of no concern and a high degree of discriminatory power is achieved for each sample. In total, over 3500 crystals from five crystal batches could be quantitatively evaluated. Because of the large number of crystals, the data obtained possess a high explanatory power, even though only a few milligrams of sample are required. The digital image processing could easily determine that the amount of crystal defects in crystals between 150 and $250 \mu\text{m}$ in size is the same for pilot-plant-scale SBRC and laboratory-scale antisolvent crystallisation. But it was also possible to determine that the finer crystals produced by antisolvent crystallisation are of even higher quality. It was, thus, shown in chapters 5.1 and 5.2 that the crystal defects can be quantified sufficiently well, but only digital image processing of photomicrographs could do so also on the laboratory-scale. Chapter 5.2 also showed that the well-established methods $^1\text{H NMR}$, HPLC and GC are suited for the analysis of the chemical purity of the cocrystal batches. The significant solvent inclusion of the batch RC sample and the higher amount of decomposition resulting from the nickel-plated magnetic stir bar for the samples of SBRC1 and SBRC3 were easily detected. All cocrystal batches exhibited fewer impurity signals than the CF in their HPLC chromatograms as well as their ^1H spectra. But they all possess additional signals that are attributed to decomposition products of CL-20. A testimony to the effectiveness of the analytical methods is that from the lower intensity of the decomposition signals and the unexpectedly high relative density of the BRC sample, it can be concluded that the gas inclusions in the crystals of the antisolvent crystallization sample and the SBRC samples are due to the decomposition of the CL-20. A reduction of the crystallisation time should, therefore, reduce the amount of decomposition and gas inclusions and, thereby, improve the crystal density and chemical purity. The level of precision achieved for these methods is sufficient for the quality improvement of the crystallisation methods. This is also true for the Rietveld analysis of the pXRD measurements for assessing the phase purity. All samples are at least 99.9% phase pure, which agrees with the DSC measurements in which no signals were recorded apart from the decomposition. WP1 was, hence, completed

successfully. Sufficiently precise methods were found for the determination of the crystal defects, the chemical purity, and the phase purity. The finding that most samples are indistinguishable by most analysis methods is most likely a testimony to the high reproducibility of the crystal quality of SBRC and the very high overall crystal quality achieved.

The desire to find a solvent and temperature pairing that enables the reproducible and material-efficient cocrystallisation of CL-20 and HMX was concentrated in RQ2 and the corresponding WP2:

“A solvent should be identified either from literature research or experimental work in which CL-20 and HMX are congruently soluble and no solvate formation occurs.”

During the work described in the solubility paper (chapter 6.1) no solvent was found that exhibits a solubility ratio close to the stoichiometric ratio of the cocrystal. Because of the systematic approach to solvent selection, it can be safely stated that the observed solubility difference is the result of the inherent properties of CL-20 and HMX. It can be concluded that most likely no solvent exists that exhibits a favourable solubility ratio of CL-20 and HMX. And it was shown that reports of such beneficial solubility ratios are most likely the result of undetected solvate formation. Given the determined solubility ratios, the strict exclusion of solvate forming solvents from consideration demanded in RQ2 and WP2 can and must be revised. On the one hand, of the ten solvents with the best solubility ratios five are known to form solvates with either HMX or CL-20, and on the other hand, because of the significant solubility difference between HMX and CL-20, it is likely that in the case of a possible CL-20 solvate formation the phase areas in which the cocrystallisation is carried out lies outside of the area in which the solvate can occur as a thermodynamic or kinetic product. Because the cocrystallisation is carried out closer to the HMX phase boundary for reasons of efficiency, only solvents that form HMX solvates should be excluded from considerations. This exclusion can most likely be further restricted to only exclude solvents that form thermodynamically stable HMX solvates. The suitability to form the CL-20/HMX cocrystal was tested for three CL-20 solvate forming solvents in the first crystallisation methods paper (chapter 7.1) together with seven other solvents. Of the three, only acetonitrile was found to be able to form the CL-20/HMX cocrystal reliably. The solvate was never formed in any experiment carried out with HMX, or in any solubility determination.

Dimethyl carbonate did not form the cocrystal at all. The complete phase diagram at 333.15 K was determined and even seed crystals of the cocrystal were converted back to the pure CF. During the five days of equilibration, neither the solvate nor the cocrystal was formed. Only after the solutions were cooled to room temperature did one large solvate crystal grow in one of the solutions over a period of weeks. For this system, the presence of both HMX and dimethyl carbonate seem to hinder each other from forming crystals with CL-20 regardless of the ratio. Butane-2,3-dione yielded only a mixture of CL-20, HMX, and cocrystal in a 72 h equilibration test that started with cocrystal seeds. This indicates a very low conversion rate. The presence of HMX seems to have blocked the formation of the CL-20 solvate for this system. These three cases indicate that no general decision can be made about the utility of solvate forming solvents. The suitability of this type of solvent has to be determined individually. Of all ten solvents tested, acetonitrile has been found to be the most suitable solvent for cocrystallisation in terms of crystal habit, chemical compatibility, and solubility ratio at TP1, although it has a solubility ratio of 10:1 at TP1. This means that WP2 cannot be completed successfully. That acetonitrile can form CL-20 solvates is most likely not of great importance, but because of the solubility ratio at TP1 CL-20 and HMX are incongruently soluble in acetonitrile. This fact and the fact that there is most likely no solvent in which CL-20 and HMX are congruently soluble presented the work on WP3 with additional challenges in order to answer RQ3.

None of the cocrystallisation methods tested in chapter 7.1 were able to combine the three requirements formulated in WP3:

“The crystallisation processes known from the literature are to be tested with regard to which methods are basically capable of delivering high-quality crystals reliably and efficiently.”

While laboratory-scale antisolvent crystallisation could reliably produce high-quality crystals, the CL-20 efficiency of 25% is unacceptable. Laboratory-scale batch RC at 293.15 K could produce high-quality crystals with a CL-20 efficiency of 55%, but not reliably, and pilot plant-scale batch RC at 333.15 K could produce the cocrystal with a CL-20 efficiency of up to 79% reliably, but not of high-quality. None of these results can be improved because the efficiency of the antisolvent crystallisation is severely limited by the solubility ratio at TP1, the reliability of the batch RC at 293.15 K is limited by the small energetic benefit of the cocrystal compared to the CF, and the crystal

quality of the batch RC at 333.15 K is limited by the rapid crystallisation rate caused by the high supersaturation. There could be an intermediate temperature for batch RC for which the energetic benefit is just great enough to enable a reliable cocrystallisation of high-quality co-crystal. But this would still rely on a small energetic advantage of the cocrystal over the CF which would still make the process of forming the cocrystal potentially unreliable. To try for a method that would certainly combine all three positive aspects seemed the more promising route. Thus, solid-dosing semibatch reaction cocrystallisation was developed as described in the second crystallisation method paper (chapter 7.2). By adding the CF to the solution in a controlled manner, as opposed to the complete addition of all CF mass at the beginning of the experiment for batch RC, supersaturation control is achieved. This is very similar to antisolvent, cooling, or evaporation crystallisation, where the antisolvent dosing rate, the cooling rate, or the evaporation rate, determine the level of supersaturation. In contrast to these techniques, the solid dosing renders overheating the solution before the experiment useless. In antisolvent crystallisation, overheating the solution by 10 K suppressed the formation of nuclei during the antisolvent addition. But, because the CF are added in solid form during solid-dosing SBRC, the presumed effect of overheating, the destruction of preformed subcritical molecule clusters, is negated because such clusters are constantly added to the solution. This is possibly the main reason for the smaller than aimed at average particle size of the SBRC batches. Despite this drawback, solid-dosing SBRC combines the supersaturation control of antisolvent crystallisation with the efficiency of batch RC. Because of this, it can produce crystals in the 150-250 μm size range with the same quality as antisolvent crystallisation, but with a CL-20-efficiency similar to batch RC. It is, thus, the only crystallisation technique that produces coarse crystals of the CL-20/HMX cocrystal of sufficient quality and efficiency for its scaled-up production. This method is a promising crystallisation technique for all incongruently soluble cocrystal systems where a high crystal quality of coarse crystals are desired. But for cheap materials, of course, low material efficiency might be acceptable and other methods such as cooling crystallisation may be sufficient.

That liquid-dosing SBRC has been used multiple times in the literature to produce API cocrystals, but solid-dosing SBRC has not been used once might be due to a general aversion against solid-dosing

because it is more difficult to regulate and calibrate than liquid-dosing. But for incongruently soluble cocrystals, the solid-dosing leads to an efficiency gain of about an order of magnitude compared to liquid-dosing.

The development of solid-dosing SBRC concludes WP3 successfully. High-quality crystals can be produced efficiently enough for the scale up of the cocrystal production. WP1 and WP3 were completed favourably, and the efficiency limitation imposed by the impossibility of successfully completing WP2 because of inherent solubility differences was also mitigated by the solid-dosing SBRC.

The proposed research questions are, thus, answered as follows.

RQ1: How can the crystal quality be analysed sufficiently well to allow for the differentiation between and optimisation of the crystallisation methods?

A1: The crystal defects of the CL-20/HMX cocrystal can be analysed sufficiently well by helium pycnometry and digital image processing of photomicrographs of crystals immersed in a liquid of the same optical density. The phase purity is determined easily by Rietveld analysis of pXRD samples, and the chemical purity can be determined sufficiently well by HPLC and ^1H NMR.

RQ2: Which combination of solvent and temperature can produce compact crystals efficiently without the formation of solvates?

A2: No solvent and condition combination could be found that enables one to cocrystallise CL-20 and HMX efficiently in general, and only few solvents (cyclohexanone, ACN and butane-2,3-dione) produce compact crystals. Of these solvents, ACN is the most beneficial despite its potential to form CL-20-solvates.

RQ3: Which crystallisation method can produce high-quality cocrystal efficiently?

A3: Given the inherent solubility difference between CL-20 and HMX, no established crystallisation method could efficiently produce high-quality coarse crystals, but by developing the new cocrystallisation method SBRC using solid-dosing coarse crystal of high-quality can be produced efficiently.

By answering all RQ, all necessary steps were undertaken to formulate a general procedure to work towards a scale up of a, based on the solubility data of the CF, presumed incongruent cocrystal. The procedure can be summarised in these few simple steps:

- The first step in this process is to determine the required level of crystal quality.
 - If a higher level of crystal defects is acceptable, methods such as spray drying or batch RC are an efficient method of generating large quantities of material.
 - If higher qualities are demanded, the next step is to determine the solubilities of the CF in more detail. Furthermore, suitable analysis methods for this cocrystal system and the quality requirements must be identified.
- If a solvent with sufficient solubility can be found that produces compact cocrystals and whose cocrystal phase region includes the stoichiometric solution composition, or a low material efficiency of the more soluble CF is acceptable, antisolvent cocrystallisation, cooling cocrystallisation, or similar techniques can be applied.
- If no solvent can be found that exhibits a beneficial cocrystal phase region, SBRC is the only cocrystallisation method to date that can efficiently produce high-quality cocrystals when the CF are incongruently soluble.

9 Outlook

All WP have been concluded and all RQ answered. For WP1, further refinement of the analysis methods of the chemical purity and the phase purity can certainly increase the level of precision achieved, but for the present samples, the discriminatory power achieved is sufficient. For the crystal defect analysis methods, the enhancement of the density determination of samples on the laboratory-scale would require the acquisition of additional expensive hardware. This seems only reasonable, if much optimisation of crystallisation methods on the laboratory-scale must be carried out. But, the crystal and defect detection of the digital image processing can be honed easily. For

now, more than half of the crystals detected had to be manually excluded after detection because of disturbances to the measurement. This can be greatly improved by stricter exclusion of fine crystals during sample preparation. Furthermore, by increasing the excluded edge area of the crystals, it should also be possible to minimise detection errors resulting from the flattened crystal vertices.

The solubility determinations carried out for WP2 produced strong evidence for the non-existence of a solvent that possesses a beneficial solubility ratio of CL-20 and HMX at least at temperatures below or around 333 K. At higher temperatures, CL-20 and HMX might be congruently soluble in some solvents, but most likely at these temperatures the decomposition of CL-20 will increase to unacceptable levels regarding both the crystal quality as well as the safety. Furthermore, such a solvent might only produce plate-like crystals, as only three of the ten solvents tested produced compact crystals. Solution or solid recycling are, thus, most likely more promising strategies than the search for another solvent or condition to augment the crystallisation method's efficiency.

Both the efficiency and the produces crystal quality of the solid dosing SBRC, developed during the work on WP3, can most likely be further enhanced by improving the crystallisation conditions described in chapter 7.2. A reduction of the crystallisation time is required. This does not only increase the time efficiency, but should also improve the crystal quality because of the reduction in CL-20 decomposition. This can be done by elevating the supersaturation during the process. The metastable zone width of around 1.4 allows a significantly heightened supersaturation compared to the conditions described. A rise in crystallisation rate of factor 10 should be achievable by raising the supersaturation to 1.3 based on the quadratic dependency of the crystallisation rate on the supersaturation. If the crystallisation time can be trimmed down to around 2 hours, the CL-20-efficiency can also be raised by recycling the mother liquor. By recycling the mother liquor twice, the efficiency can be boosted from 61 % to 82 %. The thermal load on CL-20 would then still be only about a quarter compared to the conditions described.

Implementation of these improvements will elevate the usefulness of the methods for the scaled-up production of cocrystals and the quality analysis of crystals in general.

10 Appendix

10.1 List of Publications

1. Herrmannsdörfer, Dirk; Gerber, Peter; Heintz, Thomas; Herrmann, Michael J.; Klapötke, Thomas M., Investigation of Crystallisation Conditions to Produce CL-20/HMX Cocrystal for Polymer-bonded Explosives., *Propellants, Explos., Pyrotech.* **2019** 44 (6), 668-678. (DOI: 10.1002/prop.201800332)
2. Herrmannsdörfer, Dirk; Klapötke, Thomas M., High-Precision Density Measurements of Energetic Materials for Quality Assessment. *Propellants, Explos., Pyrotech.* **2021**, 46, 413–427. (DOI: 10.1002/prop.202000272)
3. Herrmannsdörfer, Dirk; Klapötke, Thomas M., Semibatch Reaction Crystallisation for Scaled-up Production of High-Quality CL-20/HMX Cocrystal: Efficient because of Solid-Dosing. *Cryst. Growth Des.* **2021**, 21, 1708-1717. (DOI: 10.1021/acs.cgd.0c01611)
4. Herrmannsdörfer, Dirk; Stierstorfer, Jörg; Klapötke, Thomas M., Solubility Behaviour of CL-20 and HMX in Organic Solvents and Solvates of CL-20., *Energetic Materials Frontiers.* **2021**, 2 (1), 51-61 (DOI: 10.1016/j.enmf.2021.01.004)
5. Herrmannsdörfer, Dirk; Klapötke, Thomas M., Quality Assessment of the CL-20/HMX Cocrystal Utilising Digital Image Processing., *Propellants, Explos., Pyrotech.* **2021**, 46 (4), 522-529 (DOI: 10.1002/prop.202000341)

10.2 Conference Publications and Presentations

Conference Publications

1. Herrmannsdörfer, Dirk; Herrmann, Michael; Heintz, Thomas, New approaches to the CL-20/HMX cocrystal a less sensitive high power explosive, *46th International Annual Conference of the Fraunhofer ICT 2015*, 107.1-107.9
2. Herrmannsdörfer, Dirk; Herrmann, Michael; Heintz, Thomas, Advanced approaches to the CL-20/HMX cocrystal, *47th International Annual Conference of ICT 2016*, 123.1-123-14
3. Herrmannsdörfer, Dirk; Herrmann, Michael; Heintz, Thomas, Comparison of methods for generating the CL-20/HMX-cocrystal, *48th International Annual Conference of ICT 2017*, 112.1-112.8

Poster Presentations

1. Herrmannsdörfer, Dirk; Herrmann, Michael; Heintz, Thomas, New approaches to the CL-20/HMX cocrystal a less sensitive high power explosive, *46th International Annual Conference of the Fraunhofer ICT 2015*
2. Herrmannsdörfer, Dirk; Herrmann, Michael; Heintz, Thomas, Advanced approaches to the CL-20/HMX cocrystal, *47th International Annual Conference of ICT 2016*
3. Herrmannsdörfer, Dirk; Herrmann, Michael; Heintz, Thomas, Comparison of methods for generating the CL-20/HMX-cocrystal, *48th International Annual Conference of ICT 2017*
4. Herrmannsdörfer, Dirk; Herrmann, Michael; Heintz, Thomas, Comparison of Methods for Generating the CL-20/HMX-Cocrystal, *Produktgestaltung in der Partikeltechnologie 2017*
5. Herrmannsdörfer, Dirk; Herrmann, Michael; Heintz, Thomas, Sensitivity reduction of the CL-20/HMX cocrystal via advanced crystallization process, *49th International Annual Conference of ICT 2018*

Oral Presentations

1. Dirk Herrmannsdörfer, Energetische Cokristalle für Treib- und Explosivstoffe, *DWT: Angewandte Forschung für Verteidigung und Sicherheit in Deutschland 2018*
2. Dirk Herrmannsdörfer, The Way Towards a CL-20/HMX Cocrystal Scale-Up, *50th International Annual Conference of the Fraunhofer ICT 2019*